

Universidade de Évora - Instituto de Investigação e Formação Avançada

Programa de Doutoramento em Ciências da Terra e do Espaço

Área de especialização | Geofísica

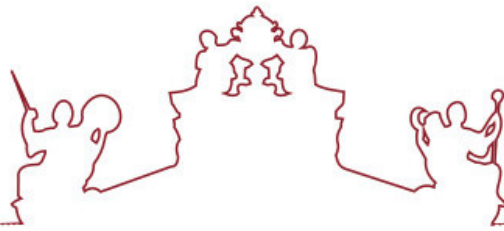
Tese de Doutoramento

Design and Prototyping of a Network-Enabled Low-Cost Low-Power Seismic Sensor Monitoring System

Marco António Azinheira Morais Lourenço Manso

Orientador(es) | Bento António Caldeira
Mourad Bezzeghoud

Évora 2021



Universidade de Évora - Instituto de Investigação e Formação Avançada

Programa de Doutoramento em Ciências da Terra e do Espaço

Área de especialização | Geofísica

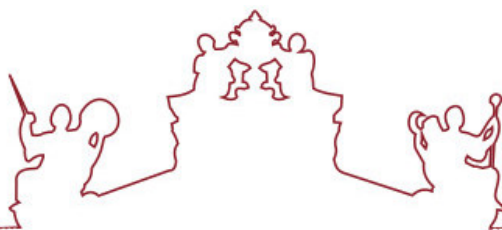
Tese de Doutoramento

**Design and Prototyping of a Network-Enabled Low-Cost
Low-Power Seismic Sensor Monitoring System**

Marco António Azinheira Morais Lourenço Manso

Orientador(es) | Bento António Caldeira
Mourad Bezzeghoud

Évora 2021



A tese de doutoramento foi objeto de apreciação e discussão pública pelo seguinte júri nomeado pelo Diretor do Instituto de Investigação e Formação Avançada:

Presidente | Maria João Costa (Universidade de Évora)

Vogais | Antonio Pazos Garcia (Real Instituto Y Observatorio de la Armada)
Bento António Caldeira (Universidade de Évora) (Orientador)
Carlos Alberto Ferreira de Sousa Oliveira (Instituto Superior Técnico)
José Fernando Borges (Universidade de Évora)
Maria Amelia Ramos Loja (Instituto Superior de Engenharia de Lisboa)
Mouhaydine Tlemcani (Universidade de Évora)
Vicenta Maria Elisa Buforn Peiró (Universidad Complutense de Madrid)

RESUMO

Esta tese explora recentes desenvolvimentos em tecnologias de informação, comunicações e sensores no campo da sismologia. A tese aborda o potencial das redes de monitorização sísmica de elevada densidade na melhoria da resolução da actividade sísmica observada e, conseqüentemente, na melhor compreensão dos processos físicos que estão na base da ocorrência de terremotos.

A tese argumenta que a tecnologia de sistemas de microelectromecânica (MEMS), usada na produção de acelerómetros de pequena dimensão, tem aplicabilidade e elevado potencial no domínio da sismologia. Acelerómetros MEMS já facilitaram a instalação de redes sísmicas de elevada densidade com superior resolução espacial pela Universidade da Califórnia (Rede Sísmica Comunitária) e pela Universidade de Évora (Rede Sísmica de Sensores do Alentejo), esta última ainda em fase de instalação.

Neste contexto, a tese descreve o trabalho conduzido no desenho e desenvolvimento de sistemas de sensores baseados em acelerómetros MEMS. Este trabalho inclui a conceptualização de componentes de arquitectura usados para a implementação de quatro protótipos. Adicionalmente, foram também desenvolvidos os componentes necessários para a operação e gestão da rede de sensores, que inclui servidores dedicados a operar software especificamente desenvolvido neste trabalho.

A tese descreve também a instalação e avaliação de protótipos, usando como base de comparação uma estação sísmica de elevado desempenho, recorrendo inclusivamente à actividade sísmica resultante de dois eventos sísmicos.

A tese conclui que a arquitectura conceptualizada para o sistema sensor e para a rede de sensores demonstrou ser eficaz. Adicionalmente, embora a tecnologia MEMS seja promissora, ainda exhibe limitações que limitam a sua aplicabilidade no domínio da sismologia, especificamente na observação de eventos sísmicos moderados e fortes. Conclui-se também que a instalação de acelerómetros MEMS em conjunto com sismómetros pode trazer benefícios na observação de actividade sísmica. Espera-se também que futuras gerações de acelerómetros MEMS possam ter uma adoção generalizada na sismologia.

Palavras chave: Sismologia, sensores, ambiente, electrónica, internet

ABSTRACT

This thesis exploits advances in information technologies, communications and sensor systems to the field of seismology. It addresses the potential for high-density networks for seismic monitoring aiming to improve the resolution of the recorded seismic activity and, consequently, to improve the understanding of the physical processes that cause earthquakes, as well as to gather more detailed seismic characterisation of studied regions.

It argues that microelectromechanical systems (MEMS) technology, used to produce small size accelerometers, has a potential application in seismology. Indeed, MEMS accelerometers have enabled the deployment of high-density seismic networks capable of monitoring seismic activity with high spatial resolution, such as CalTech's Community Seismic Network (CSN) and University of Évora's SSN-Alentejo, currently in the deployment phase.

In this context, this thesis describes the work conducted to design and develop low-cost seismic sensor systems, based on low-cost MEMS accelerometers. This work includes the conceptualisation of the architectural components that were implemented in four prototypes. Moreover, server-side components, necessary to operate and manage the sensor network, as well as to provide visualisation tools for users, are also developed and presented.

This work also describes the field deployment and evaluation of selected prototypes, using a high-performance seismic station as the reference sensor for comparison, based on generated signals and two recorded seismic events.

It is concluded that the herein conceptualised architecture for the high-dense network and sensor prototypes has been demonstrated to be effective. Moreover, albeit promising, MEMS accelerometers still exhibit performance limitations constraining their application in seismology addressing moderate and strong motion. In addition, MEMS accelerometers characteristics complement seismometers, thus installing MEMS accelerometers with seismometers, may provide additional insights concerning seismic activity and seismology in general. It is also expected that next generation MEMS accelerometers will be capable to compete with traditional seismometers, becoming the *de facto* technology in seismology.

AGRADECIMENTOS

A elaboração deste trabalho contou com o inestimável apoio de pessoas e entidades sem as quais não teria sido possível ser concluído neste formato, conteúdo e abrangência.

Agradeço aos meus orientadores,

Professor Mourad Bezzeghoud

e Professor Bento Caldeira

E também ao Prof. José F. Borges.

Cujo profundos conhecimentos em sismologia, na vertente prática de instrumentação e na observação de eventos sísmicos, associado à vertente humana e de motivação na área, sempre me apresentaram desafios interessantes, permitindo-me beneficiar de lições aprendidas e proporcionando-me poder sempre caminhar sobre um base sólida.

Agradeço também ao projecto SSN-Alentejo (financiado pelo ALT20-03-0145- FEDER-031260), ao Instituto de Ciências da Terra (ICT) e à Fundação para a Ciência e a Tecnologia (FCT) ao permitirem enquadrar este trabalho no âmbito de um projecto e de uma rede mais alargados.

Finalmente, à Bárbara e à Laura, a minha família, pela paciência, apoio e compreensão em prescindirem de tanto tempo e atenção que este trabalho exigiu.

TABLE OF CONTENTS

RESUMO	4
ABSTRACT	5
AGRADECIMENTOS	6
TABLE OF CONTENTS	7
ACRONYMS	11
TABLE OF FIGURES.....	14
TABLE OF TABLES.....	22
1 INTRODUCTION	23
1.1 SEISMOTECTONIC CONTEXT	25
1.2 STRUCTURE OF THIS THESIS	29
2 A BACKGROUND IN THE MONITORING OF SEISMIC ACTIVITY	31
2.1 INTRODUCTION.....	31
2.2 MEASURING GROUND MOTION: FROM GEOPHONES TO ACCELEROMETERS.....	33
2.3 TOWARDS HIGH DENSITY NETWORKS	38
2.4 CONCLUSION	48
3 MEMS ACCELEROMETERS FOR SEISMOLOGY	50
3.1 INTRODUCTION.....	50
3.2 MEMS ACCELEROMETERS FOR SEISMOLOGY	50
3.3 SENSOR RELEVANT PARAMETERS	54
3.4 MEMS ACCELEROMETERS: ANALYSIS AND SELECTION	56
3.5 CONCLUSION	59
4 THE SENSOR SYSTEM	61
4.1 INTRODUCTION.....	61
4.2 ARCHITECTURAL COMPONENTS	61

4.3	ACQUISITION AND PROCESSING BOARD	63
4.3.1	<i>Sensor Component</i>	63
4.3.2	<i>Ancillary Component</i>	63
4.3.3	<i>Power Supply Component</i>	64
4.4	SENSOR SYSTEM APPLICATION LOGIC	64
4.5	CONCLUSION	66
5	SENSOR SYSTEM IMPLEMENTATIONS	67
5.1	INTRODUCTION.....	67
5.2	PROTOTYPE 1: LOW-COST LOW-POWER MULTI-PURPOSE SENSOR SYSTEM.....	67
5.2.1	<i>Components</i>	68
5.2.1.1	Acquisition and Processing Board component	68
5.2.1.2	Sensor Component: Accelerometer	69
5.2.1.3	Sensor Component: Temperature and Humidity.....	69
5.2.1.4	Ancillary Component: Real-Time Clock.....	70
5.2.1.5	Ancillary Component: Persistent Storage	72
5.2.1.6	Power Supply Component.....	73
5.2.2	<i>Prototype Overview</i>	73
5.2.3	<i>Power Analysis and Optimisation</i>	75
5.2.4	<i>Cost Analysis</i>	80
5.3	PROTOTYPE 2: NETWORK-ENABLED LOW-COST SEISMIC SENSOR SYSTEM.....	81
5.3.1	<i>Components</i>	81
5.3.2	<i>Prototype Overview</i>	82
5.3.3	<i>Power Analysis</i>	83
5.3.4	<i>Cost Analysis</i>	84
5.4	PROTOTYPE 3: SMARTPHONE-BASED NETWORK-ENABLED SEISMIC SENSOR SYSTEM.	84
5.5	PROTOTYPE 4: EMULATED SENSOR (TESTING PURPOSES)	86
5.6	NOISE PERFORMANCE COMPARISON	87

5.6.1	<i>Sensor Self-Noise in Dedicated Accelerometers</i>	89
5.6.1.1	ADXL355 Measurements.....	89
5.6.1.2	MPU-6050 Measurements.....	91
5.6.1.3	Sensor Noise in Smartphones and Dedicated Sensors.....	92
5.7	DETECTABILITY.....	94
5.8	CONCLUSION.....	98
6	SENSOR NETWORK: SERVER-SIDE COMPONENTS	100
6.1	INTRODUCTION.....	100
6.2	SERVER COMPONENT.....	101
6.3	SERVER-SENSOR COMMUNICATIONS.....	105
6.4	PLANNING TOOLS FOR LARGE-SCALE DEPLOYMENTS.....	105
6.4.1	<i>Network Load Measurements</i>	106
6.4.2	<i>Server Load Measurements</i>	107
6.4.3	<i>Validation of the Planning Tools</i>	108
6.4.3.1	Experiment Setup.....	108
6.4.3.2	Experiment Results.....	110
6.5	CONCLUSION.....	114
7	DEPLOYMENT AND FIELD TRIALS	116
7.1	INTRODUCTION.....	116
7.2	EXPERIMENT SITE.....	116
7.3	PROTOTYPES SETUP.....	118
7.4	PROTOTYPE MEASUREMENTS.....	119
7.4.1	<i>Generated Data Volumes</i>	120
7.4.2	<i>Observed Sampling rates</i>	120
7.4.3	<i>Observed Noise</i>	132
7.4.4	<i>Observed Signal: 2020-07-28 at 12h UTC</i>	138
7.4.4.1	EVO Reference station measurements.....	138
7.4.4.2	Prototype Measurements.....	140

7.4.4.3	Multiple Sensor Data Analysis.....	147
7.4.5	<i>Frequency Analysis</i>	157
7.4.5.1	DFT Frequency Analysis	157
7.4.5.2	Spectrogram Analysis	160
7.4.6	<i>Probabilistic Power Spectral Density</i>	162
7.4.7	<i>Analysis from Recent Seismic Activity</i>	164
7.4.7.1	Event 1: Magnitude 3.4 (ML) recorded 18-March-2021 at 9h51 (local time).....	165
7.4.7.2	Event 2: Magnitude 2.5 (ML) recorded 24-March-2021 at 14h30 (local time).....	174
7.5	CONCLUSION	183
8	CONCLUSION AND FUTURE WORKS.....	185
9	BIBLIOGRAPHY.....	188
	ANNEX - PAPERS AND PRESENTATIONS	195

ACRONYMS

ADC	Analog-to-digital converter
AnC	Ancillary Component
ANSS	Advanced National Seismic System
APB	Acquisition and Processing Board
BB	Broadband
BOINC	Berkeley Open Infrastructure for Network Computing
CalTech	California Institute of Technology
CPU	Central Processing Unit
CS	Chip Select
CSEM	<i>Centre Sismologique Euro-Méditerranéen</i> (EMSC english acronym)
CSN	Community Seismic Network
CSNPI	CPU Sensor Network Performance Index
DFT	Discrete Fourier Transform
Dint	Data Interface
ECMA	European Computer Manufacturers Association
EEPROM	Electrically Erasable Programmable Read-Only Memory
EEW	Earthquake Early Warning
EMSC	European-Mediterranean Seismological Centre
FBA	Force Balanced Accelerometer
FDSN	Federation of Digital Seismograph Networks
FIFO	first in, first out
FTDI	Future Technology Devices International
GMPE	Ground Motion Prediction Equation
GNSS	Global Navigation Satellite System

GPIO	General Purpose I/O
I/O	Input and Output
I2C	Inter-Integrated Circuit
ICG/NEAMTWS	Intergovernmental Coordination Group for the Tsunami Early Warning and Mitigation System in the North-eastern Atlantic, the Mediterranean and connected seas
ICT	Instituto de Ciências da Terra
IPMA	Instituto Português do Mar e da Atmosfera
ITU	International Telecommunication Union
JSON	JavaScript Object Notation
LAUSD	Los Angeles Unified School District
LED	Light-Emitting Diode
LVT	Lisboa e Vale to Tejo
MAG	Magnitude
MEMS	Microelectromechanical Systems
MISO	Master In; Server Out
MMI	Maximum Intensity
MOSI	Master Out; Server In
NHNM	New High Noise model
NLNM	New Low Noise Model
NTP	Network Time Protocol
ORFEUS	Observatories & Research Facilities for European Seismology
PDF	Probability Density Function
PGA	Peak Ground Acceleration
PPSD	Probabilistic Power Spectral Densities
PREM	Preliminary Reference Earth Model

PSC	Power Supply Component
PSD	Power Spectral Density
QCN	Quake-Catcher Network
RAS	Red Atrapa Sismos
RH	Relative Humidity
RTC	Real-Time Clock
RTC	Real Time Clock
SC	Sensor Component
SCL	Serial Clock
SD	Secure Digital
SDA	Serial Data
SPI	Serial Peripheral Interface
SRAM	Static random-access memory
SSN	Servicio Sismologico Nacional
SSN-Alentejo	Seismic Sensor Network Alentejo
STD	Standard Deviation
TCP/IP	Transmission Control Protocol/Internet Protocol
UI	User Interface
USC	University of Southern California
USGS	United States Geological Survey
UTC	Universal Time Coordinated
WILAS	West Iberia Lithosphere and Asthenosphere Structure

TABLE OF FIGURES

Figure 1 - Map of the Seismic Activity along the western border of the Eurasian (EU) and Nubian (NU) plates, between 1926 and 2020. NA=North American plate. The Arraiolos region is indicated with letter A. Seismicity data is from International Seismological Centre (ISC, 2020). Bathymetry and Topography data are from the GEBCO Grid (2020) The limit between the EU and NU plates is provided by Bird (2003). 25

Figure 2 - Depiction of the impact of the movements between the African and European plates in the Western continental margin of the Iberian Peninsula. Source: (Borges *et al.*, 2001) 27

Figure 3 - Maximum observed intensity map for the 1300–2014 period. Source: (Ferrão *et al.*, 2016)..... 28

Figure 4 - Map of the recorded seismic activity in the Arraiolos Region, Portugal between 1961 and 2018 were it is marked some of the main shocks in region, included the recent seismic sequence associated to the 15 January 2018 shock (M=4.9). Seismic data base: IPMA (Portugal) catalogue. 29

Figure 5 - A Real-time Seismic Noise Analysis System for Monitoring Data Quality and Station Performance. The figure shows LNM and HNM (grey lines) as a function of the period, annotating different types of activities as examples: Minimum, Mode and Maximum recorded values are also presented in red, black and blue respectively (Source: <https://www.iris.edu/gallery3/research/2006proposal/monitoring/McNamaraFig1>)..... 32

Figure 6 - The inertial seismometer - source: (Havskov and Alguacil, 2010) 34

Figure 7 - Amplitude and phase response for a seismometer with a natural frequency of 1 Hz. Curves for various level of damping h are shown. Source: (Havskov and Alguacil, 2010) 35

Figure 8 - The Force Balanced Accelerometer - source: (Havskov and Alguacil, 2010)..... 35

Figure 9 - Frequency response of an accelerometer with natural frequency f_n and reference frequency f_{ref} Source: (Fraden, 2010)..... 36

Figure 10 - A Simple Model of a Capacitive Accelerometer. Source: (D’Alessandro, Scudero and Vitale, 2019) 37

Figure 11 - Effect of a dense array in reconstructing a seismic event: Top: Simulated motion and generated signal in ideal conditions; Middle: Low-density network and reconstructed signal with low resolution; Bottom: High-density network (1000 sensors) and reconstructed signal with high resolution. Source (Clayton *et al.*, 2011).... 39

Figure 12 - Deployment of 5200 stations in the Long Beach area. Red points mark the stations’ location: Source: (Lin *et al.*, 2013) 40

Figure 13 - Snapshots of a sensor recordings of a wavefield emitted by a virtual source (Left image: at 2 sec, Right image: at 4 sec) (Lin *et al.*, 2013) 41

Figure 14 - QCN Sensor 42

Figure 15 - ShakeMap released by the *Red Atrapa Sismos* (RAS), showing an accurate location and magnitude of the event. The red star indicates the estimated event epicenter, and colors indicate estimated peak shaking intensities. Empty circles show the locations reported by the *Servicio Sismológico Nacional* (SSN) and the United States Geological Survey (USGS), respectively. Source: (Dominguez *et al.*, 2015) 43

Figure 16 - CSN: current (red dots) and planned (pink dots) deployments (from <http://csn.caltech.edu/lausd>; accessed 2021-02-21) 45

Figure 17 - Map illustrating the global distribution of MyShake usage. Locations are gathered in clusters showing the number of phones used in MyShake. Source: (Allen, Kong and Martin-Short, 2019) 47

Figure 18 - Different Phases of the Seismic Network in Alentejo (includes the Arraiolos region) and the SSN-Alentejo planned deployment. (A) Temporary seismic network deployed in the Arraiolos region after the earthquake. About 60 connected stations. (B) Current seismic network in the Arraiolos region. Less than 15 connected stations. (C) SSN-Alentejo: planned deployment of additional 60 sensors, resulting in about 75 stations in total. (D) SSN-Alentejo: planned deployment for the Évora city. Sensor density is increased to monitor ground motion activity that may impact cultural heritage and historical buildings. Source: (Manso *et al.*, 2020). The SSN-Alentejo project is funded by the Science Foundation of Portugal (FCT) under grant number ALT20-03-0145-FEDER-031260. 48

Figure 19 - Analog ADXL354/ADXL355 MEMS Accelerometer Dimensions (in mm). Source: www.analog.com 50

Figure 20 - Self-noise analysis of several MEMS accelerometers present in Android phones (Droids), game controllers and Phidget. The NLNM and ANSS Class-A noise floor are shown as reference, showing accelerometers sensor noise above the reference noise. Source: (Evans *et al.*, 2014) 52

Figure 21 - ML4 local earthquake spectra (green line) and average self-noise PSD of a MEMS accelerometer (black dashed line). Peterson's NHNM (red line) shown for reference. Source: (D'Alessandro, Scudero and Vitale, 2019) 53

Figure 22 - Sensor Platform Architecture 62

Figure 23 - High-Level Sensor System Workflow 65

Figure 24 - Arduino Pro Board. Source: Arduino (<https://arduino.cc>) 68

Figure 25 - AM2301 Temperature and Humidity Sensor 70

Figure 26 - RTC DS3231 71

Figure 27 - Micro-SD Module (left) and card (right) 72

Figure 28 - Example of a 8MByte Dataflash Chip 73

Figure 29 - Prototype 1: Sensor System Interconnections 74

Figure 30 - MPU-6050 and RTC DS3231 Hardware Modifications to Reduce Energy Consumption 77

Figure 31 - Prototype 1: Measured Electrical Current for two configurations 78

Figure 32 - Prototype 2: Sensor System Interconnections.....	82
Figure 33 - CSEM LastQuake App (2 images at the left) and MyShake App (2 images at the right)	85
Figure 34 - Prototype 3: Mobile Phone App to record and transmit acceleration measurements. The figure at the right shows an acceleration change clicking the phone screen.....	86
Figure 35 - Prototype 4: Emulated Sensor System	87
Figure 36 - Prototype 4: Generated Periodic Data from Emulated Sensor System	87
Figure 37 - ADXL355 Measured Acceleration Magnitude for different sampling rates. The figure shows signal amplitude peaks varying with the sampling rate.	89
Figure 38 - ADXL355 Measured Standard Deviation for different sampling rates. Higher values indicate a higher sensor self-noise than for lower values.....	90
Figure 39 - MPU-6050 Measured Acceleration Magnitude for different sampling rates	91
Figure 40 - MPU-6050 Measured Standard Deviation for different sampling rates	91
Figure 41 - Measured Standard Deviation for several accelerometers operating at a sampling rate of 100Hz	93
Figure 42 - Accelerometers detectability threshold for accelerometers, depending on the earthquake magnitude and epicentral distance. Only events with PGA (in g) above each black line can be detected by the respective sensor. For example, an M5 event represented by the orange line could be detected by ADXL355 at distances below 200 km, while a LIS3DHH would only detected at distances below 100 km.	95
Figure 43 - ADXL-355 accelerometer detectability threshold when using different sampling rates, depending on the earthquake magnitude and epicentral distance. A M5 event could be detected by ADXL operating at 15Hz, 100Hz and 1kHz at distances below 500 km, 200 km and 100 km, respectively.	97
Figure 44 - Seismic Monitoring System: General View	100
Figure 45 - Server Component: Main Page. Blue dots represent installed sensors. Green dots represent sensors connected to the network. The sensors spatial location represent the planned deployment.....	101
Figure 46 - Server Component: Sensors List. The page shows the sensor unique identification, its description and two buttons granting access to (1) live data and (2) recorded data	102
Figure 47 - Sensor Operations and Data Access	103
Figure 48 - Visualisation of a small sensor network deployment. The figure shows the sensors' location and connection status (green: connected, blue: registered, orange: activity detected). A sensor was coloured in orange because an event was being detected and recorded.	104
Figure 49 - SSN-Project at Github (https://github.com/marcomanso/SSN-alentejo).....	105
Figure 50 - Experiment Setup.....	109

Figure 51 - Network Transmission Rate measured per number of sensors per frequency. It is important to note that measurements pertaining to 100 and 150 sensors at 200Hz and 150 sensors at 100Hz were obtained using formula (6.1).	110
Figure 52 - Example of CPU Usage Provided by Top in Raspberry Pi 3	111
Figure 53 - ServerPC Performance measured based on the percentage of CPU allocated to process sensors' requests	112
Figure 54 - Raspi3 Performance measured based on the percentage of CPU allocated to process sensors' requests	113
Figure 55 - Location of EVO station at MITRA site	116
Figure 56 - STS-2 Instrument Response in frequency (Top) and performance considering the standard model of ambient earth noise defined by Peterson (1993) (Bottom). Source: (STS-2 Datasheet)	117
Figure 57 - Installation of sensor prototypes at MITRA station	118
Figure 58 - "sensor 10" sample period distribution histogram	122
Figure 59 - "sensor 13" measurement rate histogram	123
Figure 60 - "sensor 17" measurement rate histogram	124
Figure 61 - "sensor 17" measurement rate histogram	126
Figure 62 - "sensor 16" measurement rate histogram	128
Figure 63 - "sensor lis3dhh_0002" measurement rate histogram	130
Figure 64 - sensor_10 measurements for 2020-12-09 at 2h (UTC)	132
Figure 65 - sensor_15 measurements for 2020-12-09 at 2h (UTC)	132
Figure 66 - Recorded standard deviation for deployed sensors	134
Figure 67 - Measurements (magnitude value) after subtracting the mean value for deployed sensors while at rest.	135
Figure 68 - Measurements (acceleration magnitude value in (g) after subtracting the mean value) for deployed sensors: zoom in. The LIS sensor exhibits the highest sensor self-noise (represented by the highest variation in amplitude) followed by ADXL at 125 Hz, ADXL 15 Hz and ADXL at 4 Hz (the lowest variation in amplitude).	136
Figure 69 - Sensor measurements per axis: presence of sensor bias in X, Y and Z axis	137
Figure 70 - EVO reference station measurements outlining signals of interest (1), (2), (3) and (4).	139
Figure 71 - Prototype "Sensor 10" with ADXL355 at 125Hz taken at 12h 2020-07-28 during the first 15 minutes. Detections are represented by vertical columns in red. The prototype detects signals (1), (2) and (3) (partially), but not (4). Note that the first peak in signal (3) is missed. Before signal (1), there is also a false detection...	141

Figure 72 - Prototype “Sensor 13” with ADXL355 at 125Hz taken at 12h 2020-07-28 during the first 15 minutes. Detections are represented by vertical columns in red. The prototype detects signals (1), (2) and (3), but not (4). There are four false detections after signal (3). 142

Figure 73 - Prototype “Sensor 17” with ADXL355 at 125Hz taken at 12h 2020-07-28 during the first 15 minutes. Detections are represented by vertical columns in red. The prototype detects signals (1) (partially), (2) and (3), but not (4). There is a false detection before and after signal (1). 143

Figure 74 - Prototype “Sensor 15” with ADXL355 at 15Hz taken at 12h 2020-07-28 during the first 15 minutes. The sensor only shows two detections pertaining to signal (2), missing all others. The prototype only detects two (short) events pertaining to signal (2) missing all others. Given the strength of the signals, it is likely that the sampling frequency was not adequate to measure the signals of interest. This matter is further analysed in subsection 7.4.5. 144

Figure 75 - Prototype “Sensor 16” with ADXL355 at 4Hz taken at 12h 2020-07-28 during the first 15 minutes. The sensor does not show any detection. The prototype misses all signals. Given the strength of the signals, it is likely that the sampling frequency was not adequate to measure the signals of interest. This matter is further analysed in subsection 7.4.5. Moreover, a drift is visible in the magnitude value, indicating that the sensor operation is not adequate for use at this sampling rate. 145

Figure 76 - Prototype “Sensor” with LIS3DHH at 100Hz taken at 12h 2020-07-28 during the first 15 minutes. Detections are represented by vertical columns in red. The prototype detects all signals (1), (2) and partially (3), but misses (4). There is also a false detection before (4). Moreover, the amplitude of the measurements is quite wide, when comparing with the EVO station and the previous sensors. The prototypes’ recorded amplitude is analysed in more detail in section 7.4.4.3. 146

Figure 77 – Time series measurements for Sensors 10, 13 and 17 (using ADXL355 at 125Hz): time window of interest. The three sensors operate at the same frequency and yield similar measurements: however, differences are noted in recorded amplitude and in detection capability (see signals 1 and 3). No sensor detected signal 4. 148

Figure 78 – Time series measurements for Sensors 10, 13 and 17 (using ADXL355 at 125Hz): time window of interest pertaining to signal 2.1. The three sensors operate at the same frequency and yield similar measurements; however, differences are noted in recorded amplitude and in detection capability (see signals 1 and 3). No sensor detected signal 4. 149

Figure 79 – Time series measurements for Sensors 10, 13 and 17 (using ADXL355 at 125Hz): time window of interest pertaining to first event in signal 2.1. The recorded initial amplitude is similar; however, it is noted different attenuation over time: sensor 13 exhibits higher attenuation over time than sensors 10 and 17. The highest difference is visible in the X-axis. 150

Figure 80 - Measurements for sensors LIS3DHH_0002 and ADXL (10, 13, 17): 15 minutes duration 151

Figure 81 - Measurements for sensors LIS3DHH and ADXL355 (sensors 10, 13, 17): zoom in to observe amplitude and time difference. The annotations show a time and amplitude difference among prototypes

pertaining to the same event. In addition to a time delay, LIS3DHH records a signal with an amplitude higher (more than 20x) than ADXL355..... 152

Figure 82 - Measurements for EVO and ADXL355 (sensors 10, 13 and 17). The following is noted: (a) ADXL355 self-noise is higher than EVO's; (b) signal (4) is barely visible and its amplitude is below ADXL355 self-noise (thus is not observable); (c) ADXL355 recorded amplitude is higher than EVO. In particular, signal (1) maximum amplitude is close to the ADXL355 self-noise level; however, sensors 10 and 13 are still able to detect them. 154

Figure 83 - Measurements for EVO and ADXL355 (sensors 10, 13, 17): close look in (2.1) signals of interest. This view allows observing the increase in amplitude in ADXL recorded signal over EVO, as well as a time delay. It is noted that, in some events, ADXL magnitude can be several times (up to 5x) higher than EVO's. See next figure for a more in-depth analysis. 155

Figure 84 - Measurements for EVO and ADXL355 (sensors 10, 13, 17): zoom in to observe amplitude and time difference. The annotations show a time and amplitude difference among prototypes pertaining to the same event. Specifically, ADXL recorded amplitude is about 2x of EVO's. Moreover, ADXL measurements exhibit a time delay of about 200ms in relation to EVO's measurements. 156

Figure 85 - DFT for time interval pertaining to first event in (2.1.1). EVO, sensor 10, sensor 13 and sensor 17 measurements are presented in the first, second, third and fourth row, respectively. The first column presents values recorded for the X-axis, the second column presents values recorded for the Y-axis and the third column presents values recorded for the Z-axis. 159

Figure 86 - Spectrograms related with the first event in signal (2.1.1) for sensors 10, 13 and 17 and EVO. Sensors and EVO consistently show that frequencies between 30 Hz and 40 Hz are more dominant. Where the signal is stronger, EVO shows the presence of a wider range of frequencies (vertical plane of the spectrogram) than the ADXL sensors. The ADXL sensors however keep the presence of frequencies over a longer period of time (horizontal plan of the spectrogram) than EVO (ADXL has a lower signal attenuation factor than EVO). A time difference is also visible between ADXL sensors and EVO. 161

Figure 87 - EVO PPSD (time period 28-July-2020, 1 day). The lines pertaining to NHHM and NLNM are shown. It is also highlighted an area with high probability (centre annotation with yellow arrow indicating about 30% probability of occurrence) and another area (left annotation) where some dispersion in measurements is visible. Importantly, EVO measurements always stay below NHHM and are close to NLNM. 162

Figure 88 - Prototype "Sensor 10" PPSD (time period 29-July-2020, 1 day). The lines pertaining to NHHM and NLNM are shown. Sensor 10 measurements are well above NHHM for the region of interest of the sensor. The amplitude decreases above a 10 seconds period results from the sensor high-pass filter set to remove presence of sensor noise. 163

Figure 89 - Prototype "Sensor lis3dhh_0002" PPSD (time period 29-July-2020, 1 day). The lines pertaining to NHHM and NLNM are shown. Sensor 10 measurements are well above NHHM for the region of interest of the sensor. The amplitude decreases above a 10 seconds period results from the sensor high-pass filter set to remove presence of sensor noise. 164

Figure 90 - Location of the seismic event with 3.4 magnitude (ML) with epicentre 8 km east of Loures (Lisbon district) reported by IPMA. The location of the prototypes is presented in the SSN circle. The prototypes are located at a distance of about 140 km from the epicentre. 165

Figure 91 - EVO recording in the Z axis (HHZ) of a 3.4 magnitude event that occurred at 18-March-2021 for a 100 seconds time window (top), a 60 seconds time window (middle) and a 4-seconds window (bottom). The figure's Y-axis shows the raw amplitude value as recorded by EVO. The P-wave is detected close to 9:51:53 (bottom), followed by the start of the S-wave close to 9:52:05. At 9:53:00, EVO still records level of ground activity above what was recorded before the event. 166

Figure 92 - Overview of acceleration measurements for sensors 10, 13, 17 and, for completeness, 15 over a one hour time window (9:00:00 to 10:00:00 local time). This figure supports the classification of true and false detections of events. Over the set of measurements from sensors 10, 13 and 17, there is only one 'red' vertical line that occurs around the same time and it corresponds to the time of the event. 167

Figure 93 - Overview of acceleration measurements over the three axes for sensor 17 over a 70 seconds time window (9:51:50 and 9:53:20 local time). The X-axis recorded the highest amount of ground motion activity. First detections start at about 9:51:54. The period with strongest activity starts at 9:52:05, continuing until 9:52:15 (the X-axis continues until 9:52:20). In overall, the presence of sensor noise does not allow observing the presence of weak signals after 9:52:20. 168

Figure 94 - Overview of acceleration measurements in the X-axis for sensors 10, 13, 17, 15 and 16 over a 70 seconds time window (9:51:50 and 9:53:20 local time). Detections are marked with a 'red' vertical rectangle. Sensors 10, 13 and 17 perform a first detection at about the same time (9:51:54) and detect the periods of strongest activity. Sensor 13 (middle figure) exhibits a higher damping factor than sensors 10 and 17 (see section 7.4.4) thus has lower detection duration. For completeness, sensors 15 and 16 recordings are also shown, were only sensor 15 performs a single detection at 9:52:10, corresponding to the period of highest activity..... 169

Figure 95 - DFT related with acceleration measurements from sensors 10, 13 and 17 for a time window of 20 seconds (9:52:00 and 9:52:20 local time). The first row refers to the X-axis, the second row to the Y-axis and the third row to the Z-axis. In overall, the DFT shows a somewhat flat response, where irregularities could be attributed to noise, except where clear peaks appear typically close to 10 Hz, 30 Hz and 40 Hz. Additional remarks are presented in the figures. 171

Figure 96 - Spectrograms related with EVO raw measurements for a time window of 20 seconds. The first column refers to EVO X-axis (HHE), the second column to EVO Y-axis (HHN) and the third column to EVO Z-axis (HHZ). In overall, the recorded signal show predominant frequencies around 10 Hz..... 172

Figure 97 - Spectrograms related with acceleration measurements from sensors 10, 13 and 17 for a time window of 20 seconds (9:52:00 and 9:52:20 local time). The first column refers to the X-axis, the second column to the Y-axis and the third column to the Z-axis. In overall, the recorded signal produces frequency gains predominantly around 10 Hz and 40 Hz. Additional remarks are presented in the figures..... 173

Figure 98 - Location of the seismic event with 2.5 magnitude (ML) with epicentre 8 km north-northwest of Viana do Alentejo (Évora district) reported by IPMA. The location of the prototypes is presented in the SSN circle. The prototypes are deployed at a distance of about 10 km from the epicentre..... 174

Figure 99 - EVO recording in the Z-axis (HHZ) of a 2.5 magnitude (ML) for a 45-seconds window (top), a 12-seconds time window (middle) and a 3-seconds window (bottom). The figure's Y-axis shows the raw amplitude value as recorded by EVO. The event starts with the arrival of the P-wave at 14:29:39 (bottom), followed by the S-wave at about 14:29:41. At 14:30:00 (top), EVO still records ground activity above what was present before the event..... 175

Figure 100 - Overview of acceleration measurements for sensors 10, 13, 17 and, for completeness, 15 over a one hour time window (14:00:00 to 15:00:00 local time). This figure supports the classification of true and false detections of events. Over the three set of measurements, there is only one 'red' vertical line that occurs at the same time and it corresponds to the time of the event..... 176

Figure 101 - Sensor_17 acceleration measurements over a 20-seconds time window (14:30:15 and 14:30:35 local time). Detections are marked with a 'red' vertical rectangle. The event is detected in all axes after 14:30:16, with strongest amplitude above 2mg for all axes. The X-axis exhibits the highest acceleration amplitude and detection over time. 177

Figure 102 - Overview of acceleration measurements in the X-axis for sensors 10, 13, 17, 15 and 16 over a 20 seconds time window (14:30:15 and 14:30:35 local time). Detections are marked with a 'red' vertical rectangle. Sensor 10 performs the first detection, followed by sensors 13 and 17. After 14:30:17, all these sensors detect ground motion activity until about 14:30:25 (followed by periods of change in reported activity). After 14:30:30, no sensor reports any activity. Sensor 13 (middle figure) exhibits a higher damping factor than sensors 10 and 17 (see section 7.4.4) thus has lower detection duration. Sensor 15 only detect an event close to 14:30:20, while sensor 16 does not detect any event..... 178

Figure 103 - DFT related with acceleration measurements from sensors 10, 13 and 17 for a time window of 15 seconds (14:30:15 and 14:30:30 local time). The first row refers to the X-axis, the second row to the Y-axis and the third row to the Z-axis. In overall, the DFT shows a somewhat flat response, where irregularities could be attributed to noise, except where clear peaks appear typically close to 10 Hz, 20 Hz, 30 Hz and 40 Hz. Additional remarks are presented in the figures. 180

Figure 104 - Spectrograms related with EVO raw measurements for a time window of 15 seconds. The first column refers to EVO X-axis (HHE), the second column to EVO Y-axis (HHN) and the third column to EVO Z-axis (HHZ). In overall, the recorded signal show predominant frequencies around 10 Hz (in the X and Z EVO axes) and 10 Hz, 20 Hz, 30 Hz and 35 Hz in the Y-axis (EVO HHN). 181

Figure 105 - Spectrograms related with acceleration measurements from sensors 10, 13 and 17 for a time window of 15 seconds (14:30:15 and 14:30:30 local time). The first column refers to the X-axis, the second column to the Y-axis and the third column to the Z-axis. In overall, the recorded signal produces frequency gains predominantly around 10 Hz, 20 Hz and 30 Hz. Additional remarks are presented in the figures. 182

TABLE OF TABLES

Table 1 - Seismic Wave Period and Frequencies per Type of Activity. Based on Havskov and Ottemoller (2010)	33
Table 2 - Purpose and Characteristics of Different Types of Sensors. Based on (Havskov and Ottemoller, 2010)	37
Table 3 - MEMS Accelerometers: parameters and target values	56
Table 4 - Analysis and Evaluation of 27 MEMS Accelerometers.....	57
Table 5 - Prototype 1: Components and Interfaces	74
Table 6 - Arduino Pro Energy Savings.....	76
Table 7 - Arduino Pro Energy Overall Savings (estimated).....	76
Table 8 - Prototype 1 Configuration 1 Power Consumption Results	79
Table 9 - Prototype 1 Configuration 2 Power Consumption Results	79
Table 10 - Prototype 1: Platform cost (in Euros).....	80
Table 11 - Prototype 2: Architecture Components	81
Table 12 - Prototype 2: Interfaces	83
Table 13 - Prototype 2: Platform cost (in Euros).....	84
Table 14 - ADXL355 Measured Standard Deviation: minimum recorded value, mean value and delta value (difference between mean and minimum value).	90
Table 15 - MPU-6050 Measured Standard Deviation: minimum recorded value and mean value.....	92
Table 16 - Measured Standard Deviation for several devices: minimum recorded value and mean value.....	93
Table 17 - Server Implementations for the Experiments.....	109
Table 18 - Sensor Network Transmission Rate (KiB/s) measured per number of sensors per frequency	110
Table 19 - Prototypes used for analysis	118
Table 20 - Sensor data volume size per sensor and sampling rate over one hour of operation.....	120
Table 21 - Sample rate overall results	131
Table 22 - Sensor measurements at rest	133

1 INTRODUCTION

Seismic events can be extreme and severe threats to humanity, causing a heavy death toll, serious destruction and damage. Being no exception, the Iberian Peninsula and the North of Africa - part of the Ibero-Maghrebian region between the Gulf of Cadiz and Algeria - share the Eurasian–Nubian plate boundary that corresponds to a well-defined narrow band of seismicity, where large earthquakes occur (Ousadou and Bezzeghoud, 2019).

Helping to understand these phenomena, seismic networks have been deployed in increasing numbers, filling in gaps in the global coverage and improving our understanding of the physical processes that cause earthquakes. Portugal, in particular, has made a significant effort to develop the Broadband Portuguese seismic network integrating seismological stations from various institutions supporting real-time monitoring of the earthquake activity (Caldeira *et al.*, 2007). In an effort to overcome the limitations of the National Network (IPMA) where the rate of seismicity is higher, a regional network was deployed in December 1995 (Carrilho *et al.*, 2021) providing important data for seismicity studies (Carrilho *et al.*, 2004b; Carrilho *et al.*, 2021). The most recent network upgrade, which led to the current network deployment status, started in 2005. The main objectives of the upgrade were to: 1) Improve the quality of the data acquisition in key stations, also equipped with strong-motion sensors; 2) Implement high quality digital transmission; 3) Install real-time monitoring at the Operational Centre; 4) Implement automatic signal detection and automatic association of detections, event location and magnitude evaluation; 5) Develop a rapid earthquake information system for civil protection authorities; 6) Install a capability for the automatic archive of recorded data; 7) Develop high-level products (e.g. seismic bulletins, shakemaps, regional moment tensor); 8) Contribute to international monitoring efforts (e.g., International Federation of Digital Seismograph Networks (FDSN), Observatories & Research Facilities for European Seismology (ORFEUS), European-Mediterranean Seismological Centre (EMSC), Intergovernmental Coordination Group for the Tsunami Early Warning and Mitigation System in the North-eastern Atlantic, the Mediterranean and connected seas (ICG/NEAMTWS)); and 9) Maintain and provide data for scientific research (Carrilho *et al.*, 2021).

Between 2010 and 2012, the West Iberia Lithosphere and Asthenosphere Structure (WILAS) project integrated a temporary network of 20 sensors in the Portuguese national network resulting in a total of 55 stations spaced on average by 50 km (Veludo *et al.*, 2017; Custódio *et al.*, 2014). These stations continuously recorded measurements at frequencies up to 100 Hz, thus collecting a large volume of high-quality data of densely distributed broadband stations

that can be used to image the Earth's inner structure with unprecedented resolution (Palomeras *et al.*, 2014). More recently, the Arraiolos seismic network (in Alentejo) was deployed comprising 14 broadband stations (CMG 6TD, 30s) of the Institute of Earth Sciences of Évora, Portugal (Instituto de Ciências da Terra or ICT) and temporarily extended with 21 short-period stations (CDJ, 2.0 Hz) of the Dom Luiz Institute of Lisbon, Portugal (Instituto Dom Luiz or IDL) within a 20 km radius (Wachilala *et al.*, 2019; Carrilho *et al.*, 2021).

Continuing the trend to increase seismic monitoring resolution by deploying more seismic stations, the United States deployed several very high density seismic networks with the capability to record the propagation of seismic activity in high resolution. This methodology allowed displaying seismic wave propagations in space and time (i.e., evolutive *Shakemaps*): in 2001 and 2002, the California Institute of Technology (CalTech) deployed more than 5200 stations spaced by 100 meters with the main purpose to conduct seismic survey to better define the Long Beach oilfield (Inbal, Clayton and Ampuero, 2015). In addition, CalTech's established the Community Seismic Network (CSN), an earthquake monitoring system based on a dense array of low-cost acceleration sensors (more than 1000) aiming to produce block-by-block strong shaking measurements during an earthquake (see <http://csn.caltech.edu/>, last accessed 2020/08/14). The University of Southern California's (USC) Quake-Catcher Network (QCN) began rolling out 6000 tiny sensors in the San Francisco Bay Area, being part of the densest networks of seismic sensors ever devoted to study earthquakes in real time (see <https://quakecatcher.net/>, last accessed 2020/08/14).

High density networks also present several challenges for the state-of-the-practice in seismology. According to Addair *et al.* (2014), traditional techniques in seismology use a processing paradigm that was developed in the 1980s when average computer processing power was a tiny fraction of what is commonly available now. The huge data volume generated by high density networks demands for research on the application of data intensive processing techniques, like big data and artificial intelligence (e.g., clustering, pattern-matching and correlation), in seismology.

A high dense network-enabled seismic network operating in the principle of “live” data brings the opportunity to explore new applications in seismology, including real-time earthquake detection, more accurate characterisation (high resolution) of strong ground motion and the generation of *Shakemaps* in near real-time.

A high dense deployment is planned for the Alentejo region, given that it exhibits low to moderate seismic activity. However, a recent recorded event with a $M_L=4.9$ (the biggest

recorded earthquake in the area) raised a number of questions concerning the tectonic characterisation of this region, thus requiring increased monitoring of seismic activity in high resolution. The seismotectonic context of the region of interest for this thesis is introduced next.

1.1 Seismotectonic Context

This subsection contains excerpts from (Manso et al. 2020).

Along the border between the Eurasian-Nubian plates, in the section that extends from the islands of the Azores to the Strait of Gibraltar and the Ibero-Maghrebian region, different tectonic contexts are distinguished. The interaction between Iberia and Africa results in a complex region located in the western part of the boundary between the Eurasian and Nubia plates. The seismic activity within the region thus results from the transition from an oceanic border (from the Azores to the Gorringe Bank NE Atlantic), to a continental limit where Iberia and Africa collide (see Figure 1).

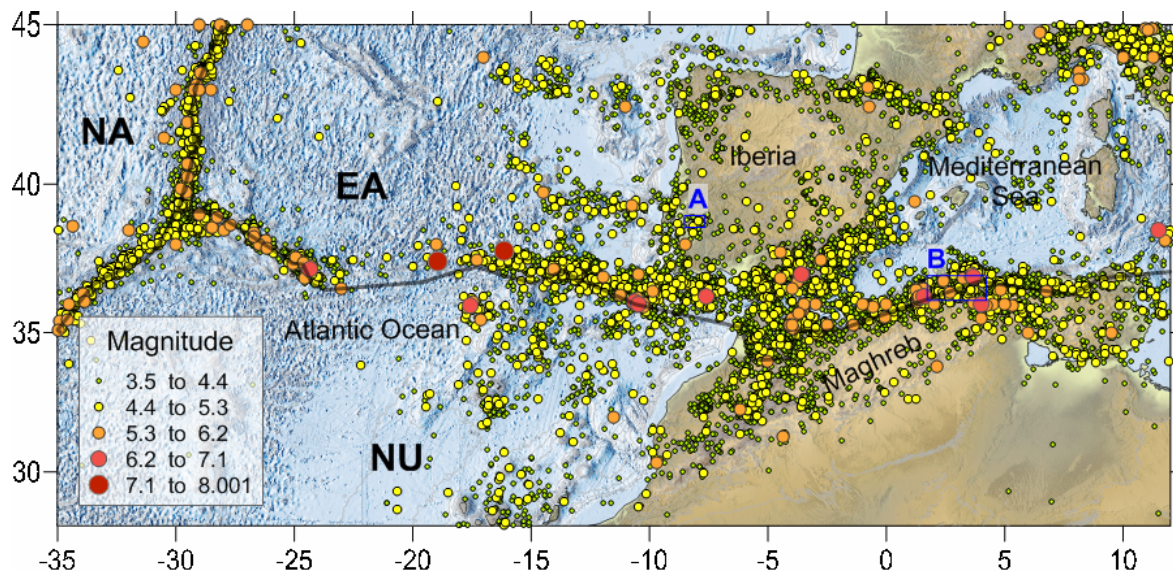


Figure 1 - Map of the Seismic Activity along the western border of the Eurasian (EA) and Nubian (NU) plates, between 1926 and 2020. NA=North American plate. The Arraiolos region is indicated with letter A. Seismicity data is from International Seismological Centre (ISC, 2020). Bathymetry and Topography data are from the GEBCO Grid (2020) The limit between the EA and NU plates is provided by Bird (2003).

The plate boundary is very well defined in the oceanic part, from the Azores islands along the Azores-Gibraltar fault to west of the Strait of Gibraltar (approximately 12° W). From 12° W to 3.5° E, including the Ibero-Maghrebian region and extending to the western part of Algeria, the

border is more diffuse and forms a wide area of deformation (ex: Bezzeghoud and Buforn, 1999; Borges *et al.*, 2001; Buforn *et al.*, 2004; Borges *et al.* 2007).

The characteristics of the seismicity recorded in the region, suggests the division of the western part of the Eurasia-Nubia limit, from the Middle Atlantic crest - in the west, to Algiers - in the east, in six zones (see Buforn *et al.*, 2004; Bezzeghoud *et al.*, 2014): These zones are characterized by a faulting mechanism variability based on seismicity and focal mechanisms (Bezzeghoud *et al.*, 2014).

Portugal, in particular, can be considered to have a moderate seismicity characterized by small events ($M < 5.0$) and occasional moderate/large/major ($M \geq 5$) earthquakes (Borges *et al.*, 2001), including the 1755 earthquake ($M = 8.5$) - the strongest recorded earthquake to have occurred in the western part of Europe – followed by a tsunami that devastated areas on the coasts of Portugal, Spain, and Morocco (Grandin *et al.*, 2007a; Grandin *et al.*, 2007b; Pro *et al.*, 2013). More recently, on January 2018, the region of Arraiolos was struck by a ML 4.9 earthquake, being felt with a maximum intensity (MMI) of VI in Aldeia da Serra (Matias *et al.*, 2019; Wachilala *et al.*, 2019; Araújo *et al.*, 2020; Carrilho *et al.*, 2021).

From Borges *et al.* (2001) and illustrated in Figure 2, the western continental margin of the Iberian Peninsula is deeply affected by the movements between the African and European plates and can be divided in two main regions of complex bathymetry separated by the Nazaré submarine valley (NV): the **northern region** comprises the Galicia Bank (GB), the Vigo (VS) and Porto (PS) seamounts and few small submarine valleys. The **southern region** has smaller seamounts and larger submarine valleys: Tejo (TV), Sado (SV) and São Vicente (SV) submarine valleys. Westwards of cape of São Vicente (CSV) is the Gorringe Bank (GB), one of the main seismogenic areas for the Iberian Peninsula and North Africa region. It is located in the border between the Nubia and Eurasia plates, within the Azores-Gibraltar fault.

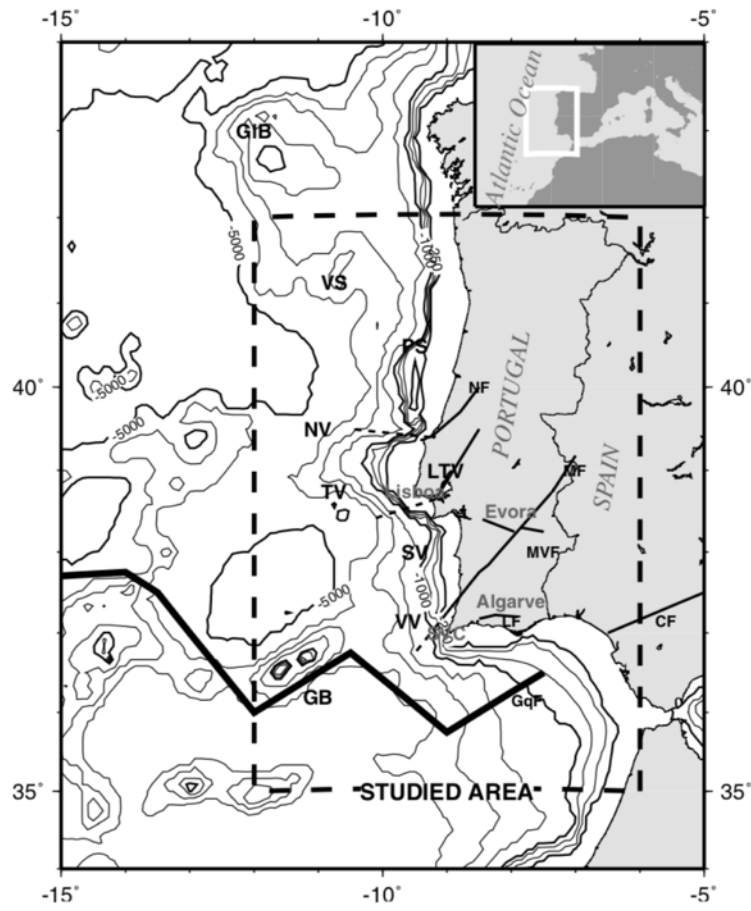


Figure 2 - Depiction of the impact of the movements between the African and European plates in the Western continental margin of the Iberian Peninsula. Source: (Borges *et al.*, 2001)

Consequently, the seismicity of the Portuguese territory increases in intensity from north to south, with a spatial distribution concentrated in the south and its adjacent Atlantic margins. A distribution map of the maximum seismic intensity felt on Portugal between 1300 and 2014 is depicted in Figure 3 showing that the zones with intensities between VI and VII are concentrated around Évora, the LTV region, the southern part of Lisbon, and along the Algarve coast. (Ferrão *et al.*, 2016).

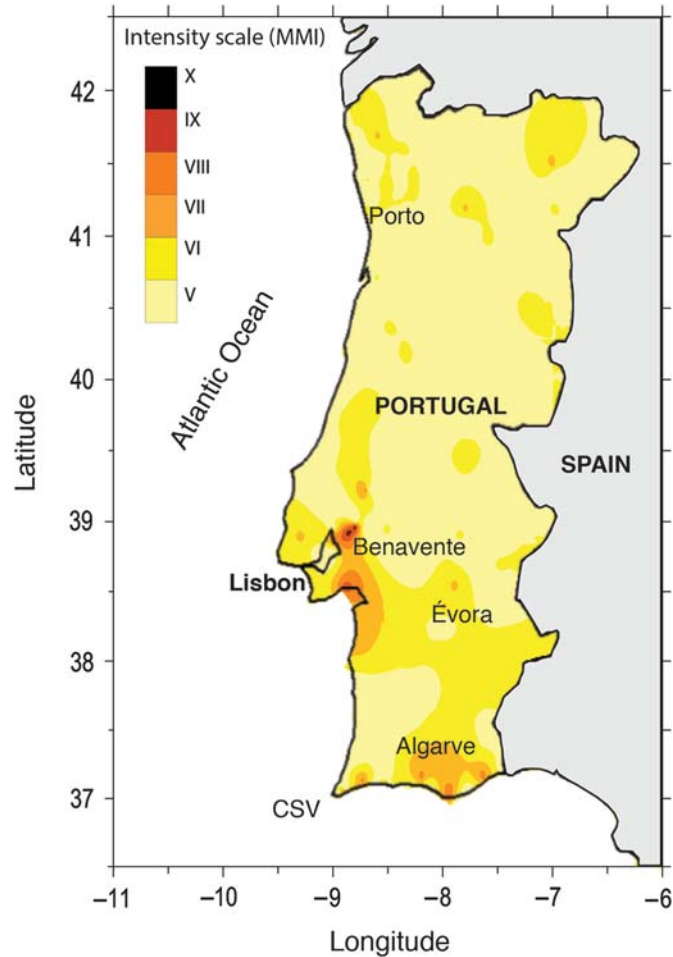


Figure 3 - Maximum observed intensity map for the 1300–2014 period. Source: (Ferrão *et al.*, 2016)

An area of interest for this work is Arraiolos that is located in the north of Évora (Portugal). The Arraiolos region was affected by an earthquake that occurred on the 15th of January 2018 with a $ML=4.9$ located at a depth of 11km. This was the biggest recorded earthquake in the area. A mapping of the seismic activity registered in the area between 1961 and 2018 is illustrated in Figure 4.

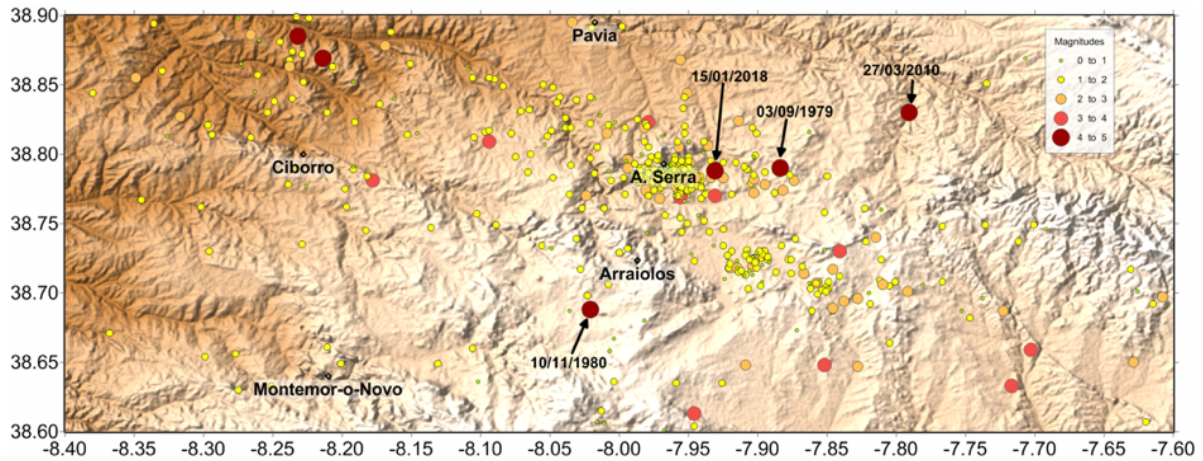


Figure 4 - Map of the recorded seismic activity in the Arraiolos Region, Portugal between 1961 and 2018 were it is marked some of the main shocks in region, included the recent seismic sequence associated to the 15 January 2018 shock (M=4.9). Seismic data base: IPMA (Portugal) catalogue.

The recent seismic events (including the aftershocks) recorded in Arraiolos has raised a number of interesting questions about the tectonic characterisation of this region. The seismic activity in the region has been historically moderate, being assumed to be generated by the slow plate movement of Iberia. Geological and seismological studies have been conducted in the region (Wachilala *et al.* 2019; Araújo *et al.* 2018, 2020; Matias, *et al.* 2019; Carrilho *et al.*, 2021), however the seismotectonic interpretations have been difficult to derive from existing tectonic knowledge and seismic data. The known mapped faults in the region do not seem to be linked to the recently observed seismic activity, thus the identification of its probable associated faults is yet to be resolved. Given the increased - previously unknown – degree of seismotectonic complexity of the region, it becomes necessary to improve the seismic and tectonic knowledge of this region by deploying additional seismic sensors, increase the resolution of the recorded seismic activity and, consequently, produce a more detailed seismic characterisation of the region, including tomographic study (Hamak *et al.*, 2020).

1.2 Structure of this Thesis

This thesis exploits advances in information technologies, communications and sensor systems to the field of seismology.

Section 2 starts with a background in the monitoring of seismic activity, presenting basic conceptual (mechanical) seismometers and their operating principles, to then introduce

broadband stations and the recent microelectromechanical systems (MEMS) used to produce small size accelerometers with a potential application in seismology.

Section 3 addresses specifically MEMS accelerometers, starting by describing their potential in seismology and other application domains, followed by a selection of accelerometers, based on identified relevant parameters, to be used in prototypes built during this work.

Section 4 presents the architecture of a sensor seismic system, describing its main hardware and software components necessary for its operation.

Section 5 presents four prototypes implemented as part of this work, which includes: a low-cost low-power multi-purpose sensor system; a network-enabled low-cost seismic sensor system, a smartphone-based seismic sensor system and an emulated sensor (used for testing purposes). In this section, a first assessment of the prototypes' noise characteristics and detectability capability is also presented.

Section 6 introduces server-side components that are necessary for the overall system operation, including sensor measurements storage, sensor management and data visualisation. Since this thesis deals with high-density deployments, analytical tools to assist planning and deployment are also presented.

Section 7 describes the final stage of work consisting in the deployment and evaluation of prototypes, using a high-performance seismometer as reference instruments. The evaluation includes sampling rate stability, sensor bias, noise characteristic assessment, signal detection capability and frequency analysis. It concludes with the analysis of two seismic events observed by the deployed prototypes.

Section 8 presents the conclusion of this thesis, also recommending future work.

Section 9 lists the bibliography used in this work.

During the elaboration of this thesis, three papers, two journal publications and four presentations were done with the aim to disseminate and share generated knowledge and ideas on the topics of high-density seismic networks and application of MEMS accelerometers for seismology. The list of papers and presentations is given in Annex "Papers and Presentations".

2 A BACKGROUND IN THE MONITORING OF SEISMIC ACTIVITY

2.1 Introduction

Seismology *studies seismic waves and what they tell us about the structure of Earth and the physics of earthquakes* (Shearer, 2009). Since the early 1800s, the theory of elastic wave propagation (in complex media like the Earth's crust) began to be developed by Cauchy, Poisson, Stokes, Rayleigh, and others who described the main wave types to be expected in solid materials. In the early 1900s, H. F. Reid, an American geophysicist, studied survey lines across the fault taken before and after the 1906 San Francisco earthquake. His analysis led to the **elastic rebound theory** that forms the fundamental hypotheses of seismology. The theory characterizes the internal forces and deformations in geological material with specific elastic properties (i.e., an elastic solid), caused by the accumulation of strain energy due to the movement between two sides of a fault. When surpassing the material's cohesion, it ruptures, releasing high amounts of accumulated energy and generating seismic waves that cause ground motion. The location of the rupture is the focus point of the seismic activity and it is called the **hypocenter**. Seismic waves are radiated from the focus point and include **compressional** and **shear** waves (termed body waves since they travel through solid volumes, thus in the interior of the Earth) and **surface** waves, which travel along free surfaces. Since compressional waves travel faster than shear waves and are thus the first to arrive, they are often called **primary or P waves**, whereas the later arriving shear waves are called **secondary or S waves** (Shearer, 2009).

The seismic waves' travel time is given by the Preliminary Reference Earth Model (PREM) (Dziewonski and Anderson, 1981):

- **P waves** velocity varies between 8 and 14 km/s.
- **S waves** velocity varies between 4 and 7 km/s.
- **Surface waves** consist of multiply reflected and super-imposed S-waves (i.e., Love waves) or a combination of P and S-waves (i.e., Rayleigh waves) travelling at velocities around 3.5 and 4.5 km/s (Havskov and Ottemoller, 2010).

Seismic waves are a result of seismic events (or earthquakes). Earthquakes can result, for example, from “high” amplitude motions resulting from the release of high amounts of accumulated energy (e.g., on tectonic faults, explosions or volcanic eruptions).

Earthquakes therefore are not just "ground motion". In fact, the ground is continuously at unrest, which from a seismological perspective consists in "unwanted" noise in seismic activity and is called "Earth's seismic background noise".

In 1993, Peterson published a comprehensive **standard model of ambient earth noise**, identifying **new low noise model (NLNM)** and **new high noise model (NHNM)** (Peterson, 1993) also revealing dominant features resulting from natural microseisms (periods between 1 and 20 sec., peaking at 5 and 18 sec.), urban noise (e.g., traffic, machinery and other human activity observable at low periods (0.1-1s) and the Earth tides (at semi-diurnal and diurnal periods). Peterson's noise model identifies the Power Spectral Density (PSD) associated with NLNM and NHNM. Figure 5 shows a probability density function (PDF) example for the transportable array station TA 109C in southern California, where it is presented the LNM, HNM and features resulting from various types of activity.

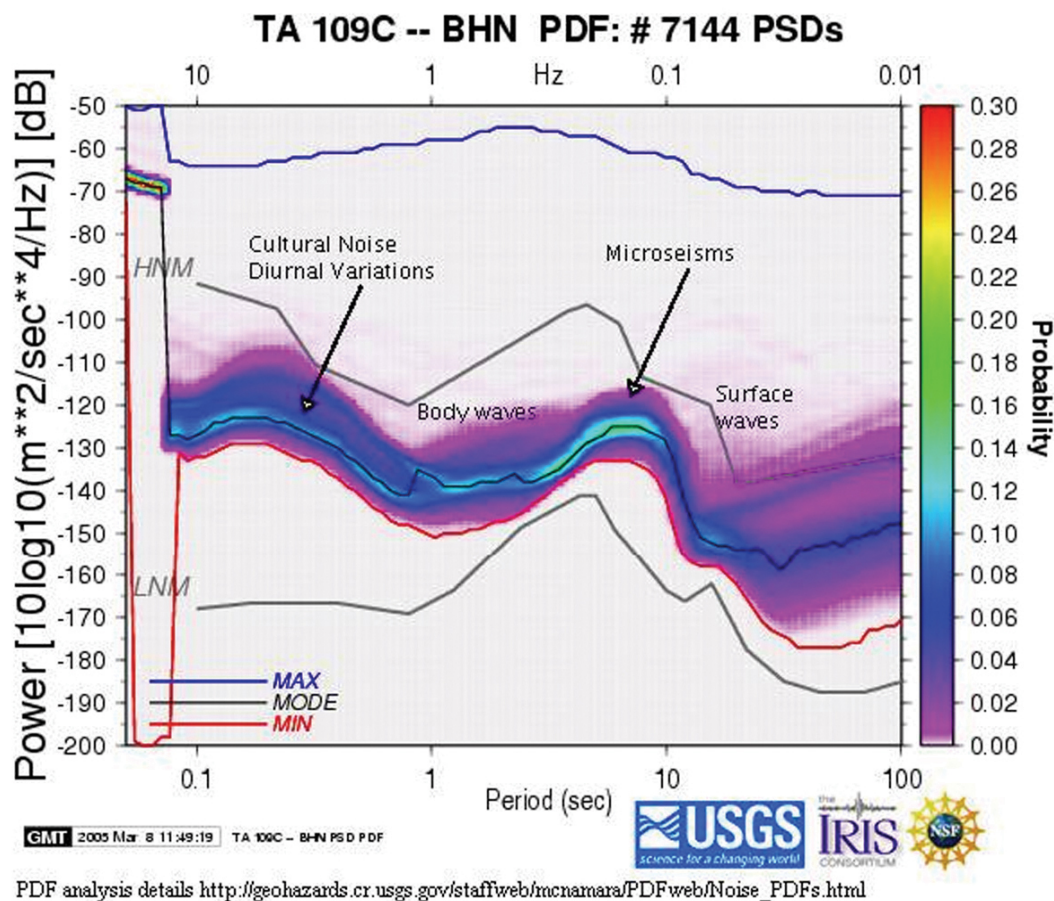


Figure 5 - A Real-time Seismic Noise Analysis System for Monitoring Data Quality and Station Performance. The figure shows LNM and HNM (grey lines) as a function of the period, annotating different types of activities as examples: Minimum, Mode and Maximum recorded values are also presented in red, black and blue respectively (Source: <https://www.iris.edu/gallery3/research/2006proposal/monitoring/McNamaraFig1>)

As shown in Figure 5, different types of activities generate different motion characteristics as presented in Table 1, based on (Havskov and Ottemoller, 2010). It can be seen that earth tides exhibit high periods (thus very low frequencies) while P and S waves (including earthquakes) exhibit low periods. It is important to understand these characteristics so that appropriate instruments are developed allowing observation of the activities of interest.

Table 1 - Seismic Wave Period and Frequencies per Type of Activity. Based on Havskov and Ottemoller (2010)

Period (sec.)	Frequency (Hz)	Type of Activity
>10k	$<10^{-4}$	Earth tides
1k – 10k	$10^{-4} – 10^{-3}$	Earth free oscillations, earthquakes
100 – 1k	$10^{-3} – 10^{-2}$	Surface waves, earthquakes
10 – 100	$10^{-2} – 0.1$	Surface waves, P and S waves, earthquakes with $M>6$
0.1 – 10	0.1 – 10	P and S waves, earthquakes with $M>2$ Urban noise (e.g., traffic, machinery and other human activity)
< 0.1	> 10	P and S waves, earthquakes, $M<2$

2.2 Measuring Ground Motion: from geophones to accelerometers

Seismic waves cannot be measured from direct observations, thus the work of seismologists relies on observations and measurements taken by instrumentation, specifically, seismic sensors (or seismometers) that produce seismograms, i.e., ground motion recordings. Ground motion can be described as displacement, velocity or acceleration done in a moving reference frame. Consequently, the principle of the seismic sensor (i.e., **inertial sensor**) is that a mass must move relative to the reference in response to ground motion. The relative motion will be a function of the ground's motion.

An example of a simple inertial seismometer is illustrated in Figure 6.

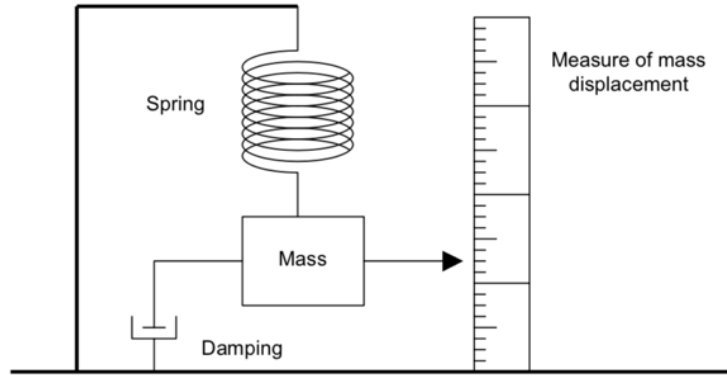


Figure 6 - The inertial seismometer - source: (Havskov and Alguacil, 2010)

As described in (Havskov and Alguacil, 2010), the simple inertial seismometer can be represented as a “mass-spring-damper” system in the form of the following second-order differential equation:

$$\ddot{z} + 2h\omega_0\dot{z} + \omega_0^2z = -\ddot{u} \quad (1.1)$$

Where

\ddot{u} is the ground acceleration,

z is the displacement of the mass m relative to the earth,

ω_0 is the resonant angular frequency of the mass–spring system, calculated as

$$\omega_0 = \sqrt{k/m},$$

being k the spring constant and h is the seismometer damping constant calculated as $h = d/2m\omega_0$, being d the friction constant.

Such a system exhibits an amplitude and phase frequency response, as illustrated in Figure 7. Different responses are presented considering different levels of damping (h). Lowering damping increases the frequency response and sensitivity of the system, however it also produces a peak in the response function at the resonant frequency.

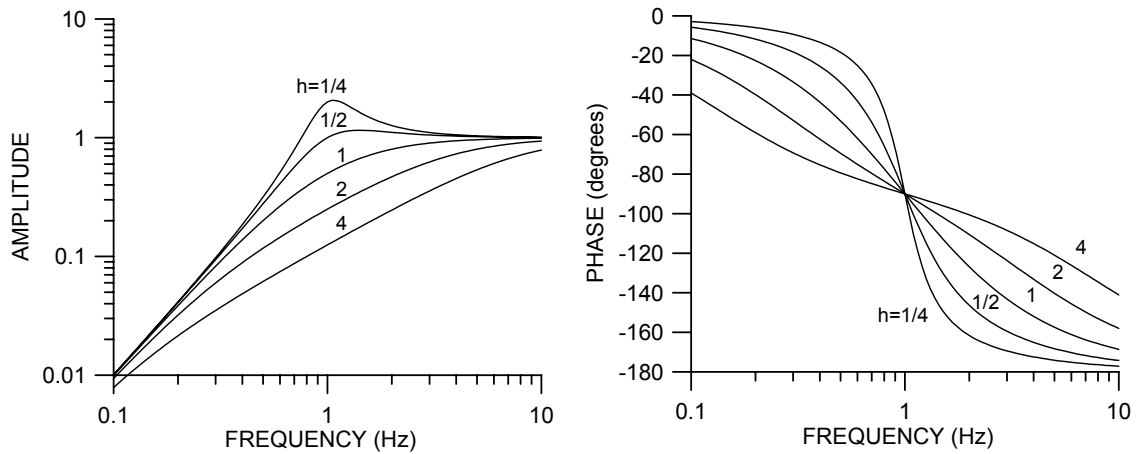


Figure 7 - Amplitude and phase response for a seismometer with a natural frequency of 1 Hz. Curves for various level of damping h are shown. Source: (Havskov and Alguacil, 2010)

Seismometer sensitivity and response were greatly improved by means of a **Force Balanced Accelerometer (FBA)** that has a feedback coil that exerts a force (inversely) proportional to the acceleration of the mass (resulting from ground motion). The mechanism tries to prevent the mass from moving at all with respect to the frame, generating a current that opposes any motion of the mass. By measuring the current, a measure linearly proportional to the external acceleration can be obtained, thus the sensor directly measures acceleration. See Figure 8 for a depiction of a FBA.

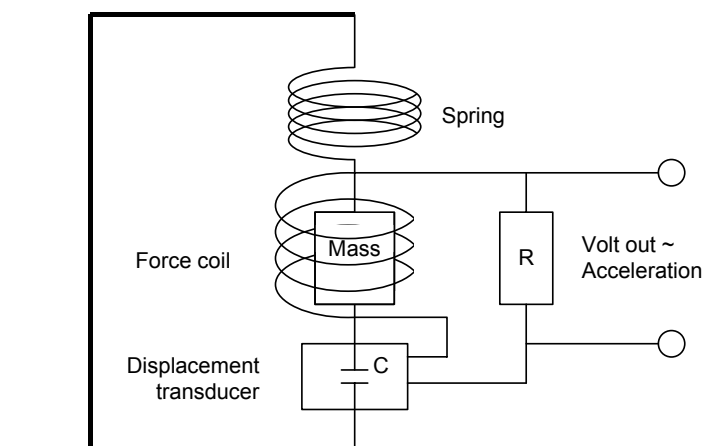


Figure 8 - The Force Balanced Accelerometer - source: (Havskov and Alguacil, 2010)

The FBA principle is used in most modern **broadband (BB) sensors**, that is, sensors recording seismic activity over a large frequency band (e.g., between 0.01 and 50 Hz) (Havskov and Alguacil, 2010).

Accelerometer sensors have also been explored for purposes of seismic monitoring. They give a simple response as their output is linearly proportional to the acceleration and have no phase shift. Accelerometers have typically a natural (resonance) frequency of about 1kHz and reference frequency of 100Hz or more. Ideal accelerometers exhibit a flat frequency response close to the natural frequency. See Figure 9 for an example.

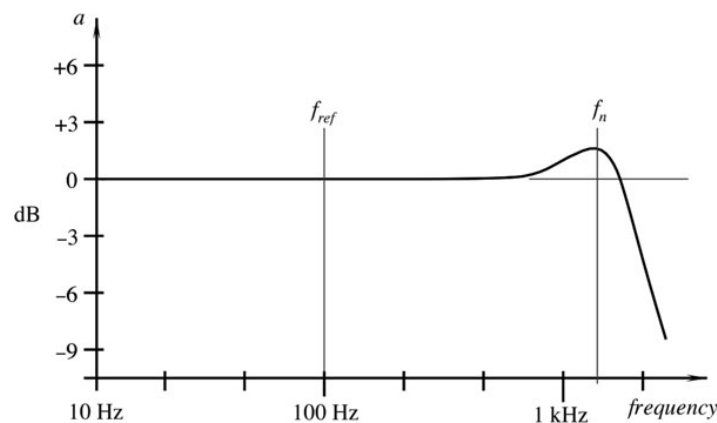


Figure 9 - Frequency response of an accelerometer with natural frequency f_n and reference frequency f_{ref} Source: (Fraden, 2010)

Recent developments in MEMS have enabled the mass production of small size accelerometers with potential applications in numerous areas, including seismology. From the various types available, capacitive accelerometers are the most popular. They are based on spring-mass system placed on a silicon substrate as depicted in Figure 10 (D'Alessandro, Scudero and Vitale, 2019). When subjected to an acceleration, the inertial mass shifts cause a (proportional) change in the capacitance. By measuring the capacitance change, the acceleration can be calculated.

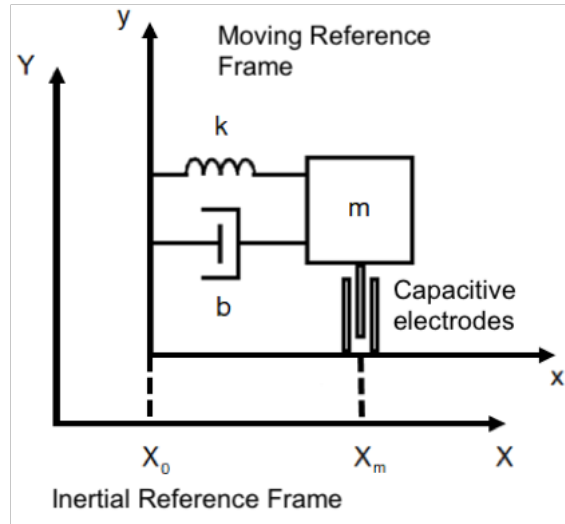


Figure 10 - A Simple Model of a Capacitive Accelerometer. Source: (D’Alessandro, Scudero and Vitale, 2019)

MEMS accelerometers’ small size (effectively having a very small mass) result in higher amplitude and frequency range than BB sensors, but also exhibit higher noise at low frequencies. In fact, the “high” sensor noise present in MEMS accelerometers is one of their most limiting features for seismological applications. While improvements in MEMS technology will continue to occur over the next years, at the time of the writing of this thesis, trade-offs need to be made when choosing the type of equipment to employ for seismological purposes.

Seismic Activity and Suitable Sensors

Table 2 presents the sensor types suitability in monitoring seismic activity.

Table 2 - Purpose and Characteristics of Different Types of Sensors. Based on (Havskov and Ottemoller, 2010)

	Passive short period (SP) sensors	Active BB sensors	MEMS Accelerometers
Main purpose	Local earthquakes. Global observations of P waves.	Suited for all seismological observations. Global observations	Retrieve unclipped observations near the earthquake. Can replace SP sensors for local earthquakes. Supports very high frequencies. Not suited for low frequencies (<1Hz) and weak motion (M<2).
Frequency Range	Linear bandwidth to velocity is 1.0–100 Hz	Linear bandwidth for velocity: 0.01–50 Hz	Linear for acceleration in frequency band 0–1000 Hz Sensor noise limits their application, especially at low frequencies.

Presently, BB sensors are the instruments of choice for seismologists. The main barrier for the adoption of MEMS accelerometers mainly lies in the presence of low frequency noise: their high level of instrumental self-noise – that increases as frequency decreases – makes them unsuitable for the study of low frequency weak-motion forces (Evans *et al.*, 2014) (Farine, Thorburn and Mougénot, 2003).

On the other hand, in the presence of strong seismic activity, BB sensors are more likely to saturate (clip) than MEMS accelerometers. In fact, in these circumstances, MEMS accelerometers have been demonstrated to outperform local BB sensors (see section 3) (Farine, Thorburn and Mougénot, 2003).

MEMS-based accelerometers complement traditional seismology sensors by measuring strong ($M > 3$) and high frequency seismic waves. Their capability allows for recording strong ($M > 6$) regional earthquakes at a distance of few hundreds of km, and even moderate ($M \sim 3$) local earthquakes at a distance of the order of some tens of km (D'Alessandro, Scudero and Vitale, 2019). Importantly, given the MEMS low cost, robustness (capable to measure and/or sustain high acceleration values), self-calibration capability (resulting from their ability to measure the gravity acceleration component) and low maintenance requirements, they gathered a suitable set of specifications to enable the deployment of high dense seismic sensor networks (Manso *et al.*, 2017). The analysis and application of MEMS accelerometers are a central element of this study and are further described in section 3. Next, efforts in deploying high density seismic sensor networks are presented.

2.3 Towards High Density Networks

This subsection contains excerpts from (Manso, Bezzeghoud and Caldeira, 2017)

The technology applied to sensors and sensor platforms has evolved in a strong and fast pace over the last years, resulting in increased performance, reduced energy consumption, improved connectivity, miniaturization and reduced cost. These innovations bring to scientific communities and experimenters promising prospects such as the deployment of large sensor networks for "live" (online and real-time) monitoring of seismic activity with high spatial resolution.

Figure 11 presents a visually representation of the effects of a seismic array with different densities in reconstructing a seismic event. In this regard, large scale high density sensor networks have been deployed aiming to bring to the field of seismology high resolution geo-referenced measurements.

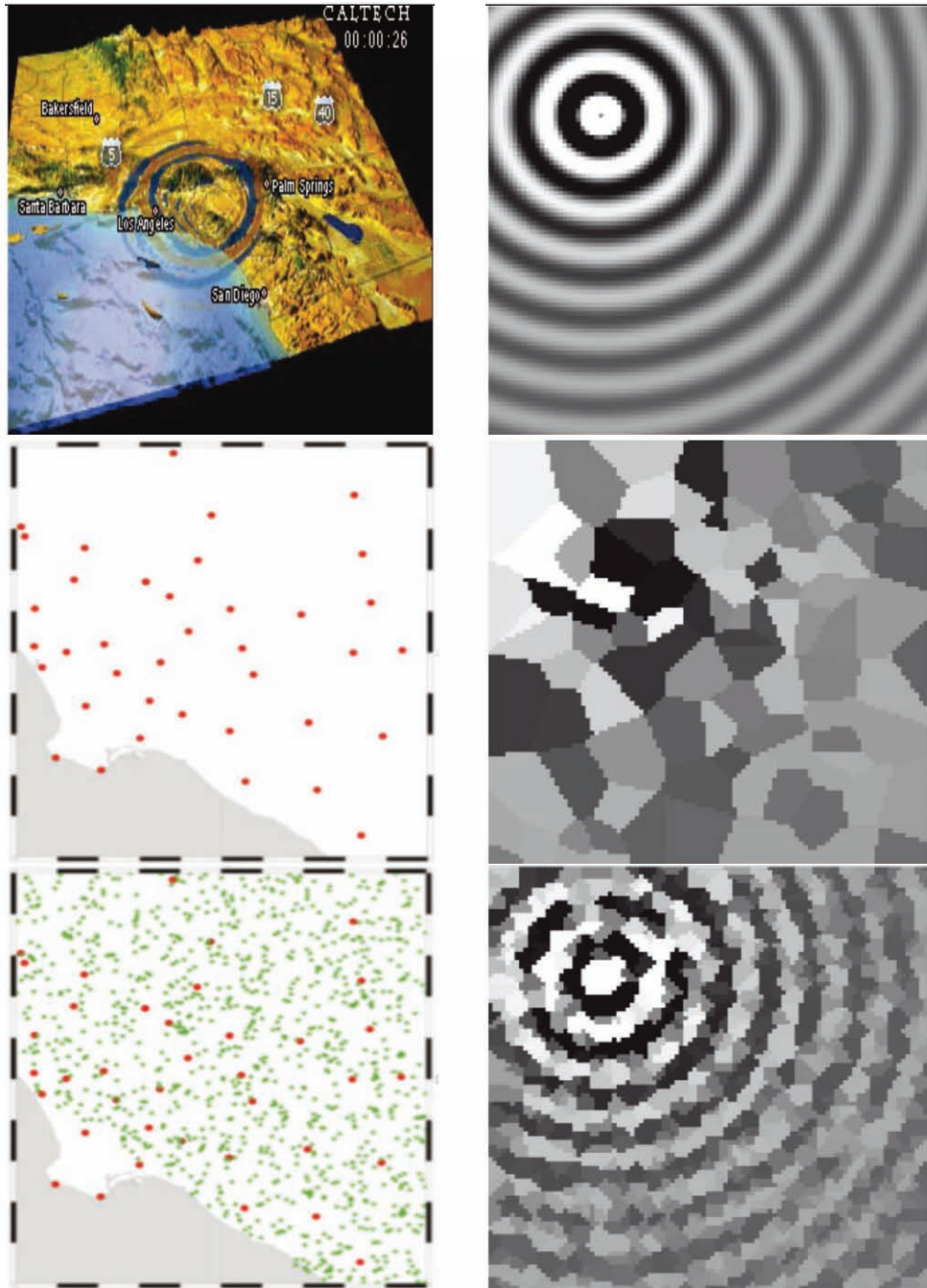


Figure 11 - Effect of a dense array in reconstructing a seismic event: Top: Simulated motion and generated signal in ideal conditions; Middle: Low-density network and reconstructed signal with low resolution; Bottom: High-density network (1000 sensors) and reconstructed signal with high resolution. Source (Clayton *et al.*, 2011)

These networks measure seismic activity with high resolution and, by correlating the signal with time and space, allow for example the production of *shakemaps* directly from observations. High-density sensor networks can be relevant to other fields as well. Indeed, studies have taken place to demonstrate the detection of important geospatial events such as

earthquakes and hazardous radiation, where sensor data correlation improved data quality and brought additional insights (Liu, 2013). Additionally, it is foreseen the potential to identify precursor signals associated with earthquakes (Manso *et al.*, 2011), a capability that can be used for "early-warning" applications and thus to alert populations and reduce the time to respond to a disaster.

Next are presented cases of high-density deployments.

5200-sensor network deployed in the Long Beach area

Between January and June 2011, more than 5200 high-frequency (10-Hz corner frequency) velocity sensors, with an average spacing close to 100m, were deployed in the Long Beach area as part of a petroleum industry survey (Lin *et al.*, 2013; Inbal *et al.*, 2015). The main purpose was to better define the area, including construction of a high-resolution 3D shallow crustal structure. Figure 12 shows the region and density of the seismic network.

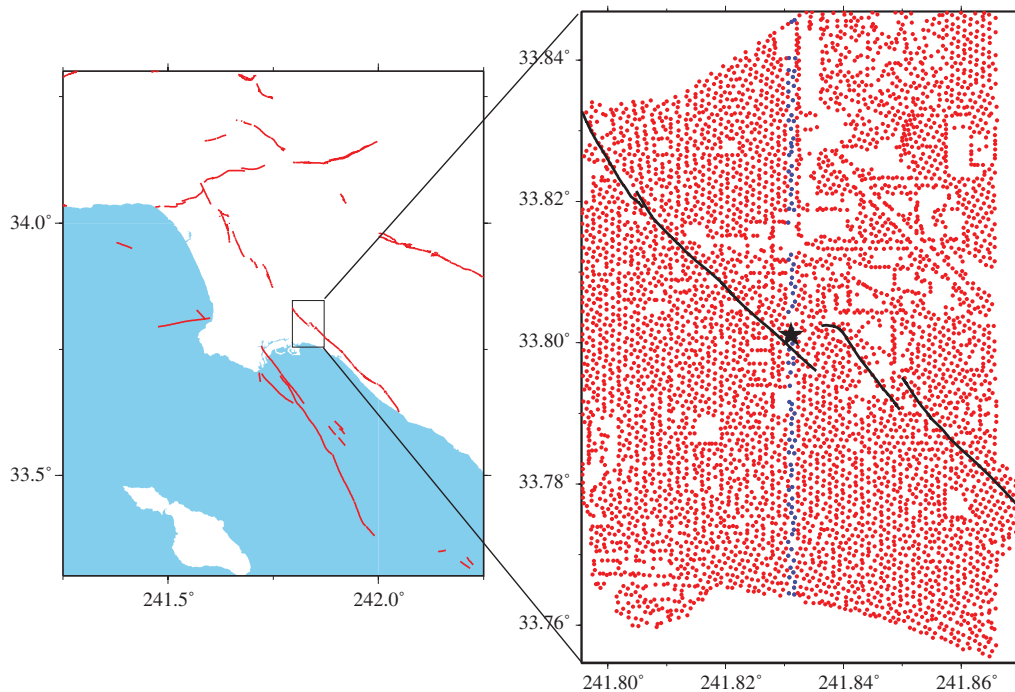


Figure 12 - Deployment of 5200 stations in the Long Beach area. Red points mark the stations' location: Source: (Lin *et al.*, 2013)

The study concluded that the resulting 3D model showed a clear correlation with the known geologic features and could be used to complement traditional active source studies. The network was capable to measure the seismic wavefield propagation over space and time, as it

can be visualized in Figure 13 (two snapshots taken at 2 and 4 seconds after an event). Moreover, the 3D velocity model could also be useful for hazard assessment and fault zone studies.

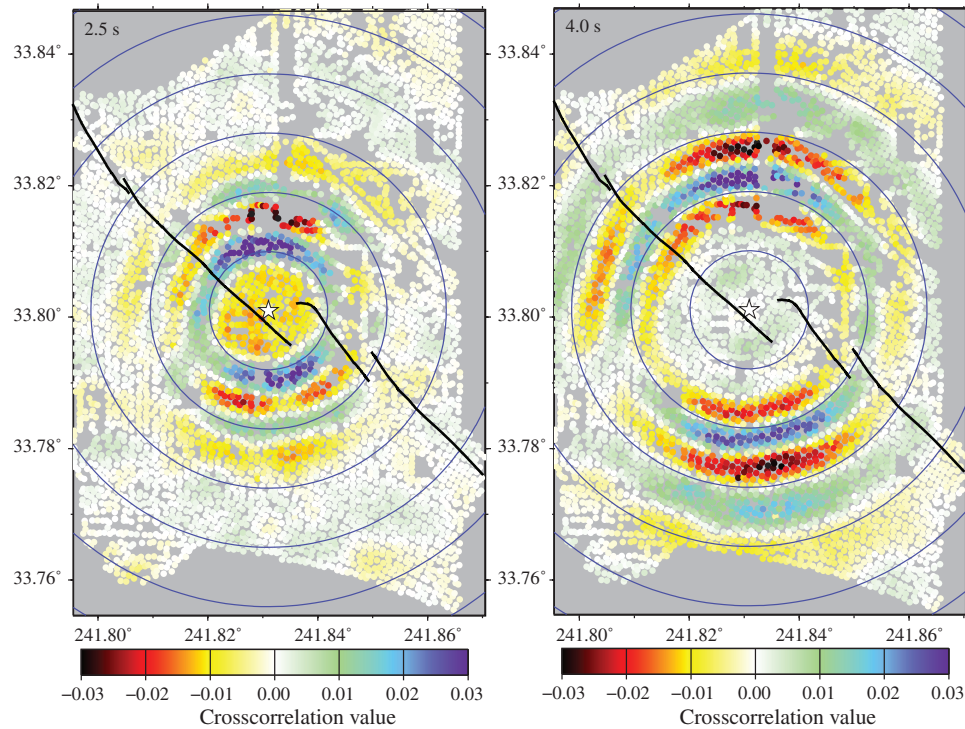


Figure 13 - Snapshots of a sensor recordings of a wavefield emitted by a virtual source (Left image: at 2 sec, Right image: at 4 sec) (Lin *et al.*, 2013)

The Long Beach high-density deployment was a pioneering effort that demonstrated the high-resolution observation and reconstruction of seismic activity.

University of Southern California's (USC) Quake-Catcher Network (QCN)

The University of Southern California's (USC) Quake-Catcher Network (QCN) *is a seismic network that implements distributed/volunteer computing with the potential to provide critical earthquake information by filling in the gaps between traditional seismic stations* (Cochran *et al.*, 2009). Initially, it started to exploit data produced by accelerometers pre-installed in computers and now uses USB-connected MEMS accelerometers (preferred source) and mobile phone accelerometers (see Figure 14). The system communicates via the Berkeley Open Infrastructure for Network Computing (BOINC) (Anderson, 2004).

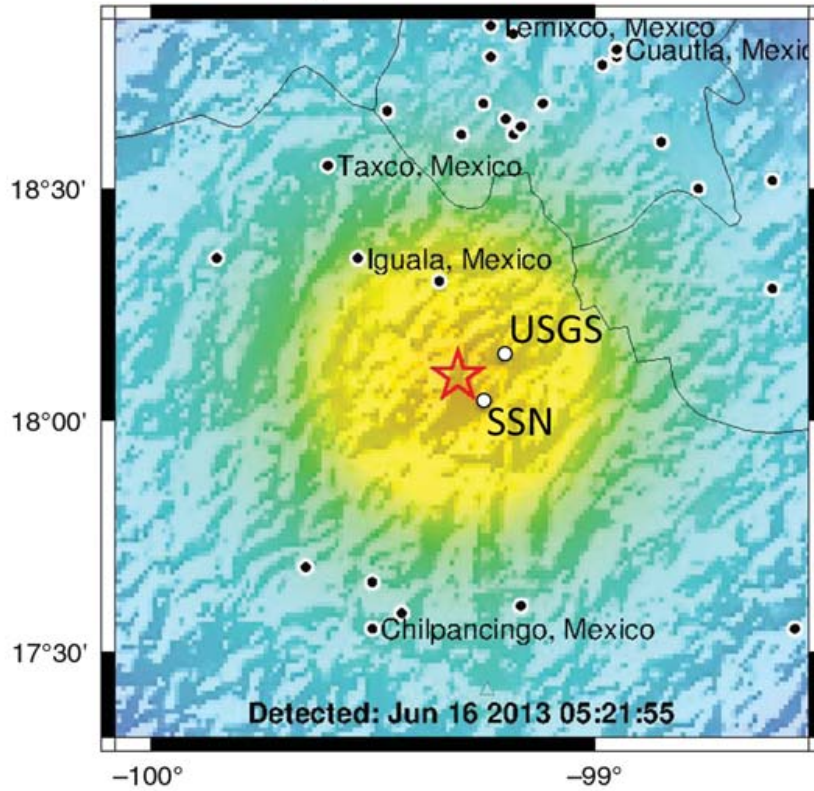


Figure 14 - QCN Sensor

QCN exhibited the following features and limitations:

- QCN sensors can only record strong motion.
- QCN sensors require a USB connection and a computer.
- The computer needs to run local software (i.e., BOINC drivers) and requires a network connection.

In Dominguez *et al.*, (2015), it was demonstrated the QCN's capability to stream real-time data through the Internet and produce intensity *Shakemaps* after an earthquake, as illustrated in Figure 15.



PERCEIVED SHAKING	Not felt	Weak	Light	Moderate	Strong	Very strong	Severe	Violent	Extreme
POTENTIAL DAMAGE	none	none	none	Very light	Light	Moderate	Moderate/Heavy	Heavy	Very Heavy
PEAK ACC.(%g)	<.17	.17-1.4	1.4-3.9	3.9-9.2	9.2-18	18-34	34-65	65-124	>124
PEAK VEL.(cm/s)	<0.1	0.1-1.1	1.1-3.4	3.4-8.1	8.1-16	16-31	31-60	60-116	>116
INSTRUMENTAL INTENSITY	I	II-III	IV	V	VI	VII	VIII	IX	X+

Figure 15 - ShakeMap released by the *Red Atrapa Sismos* (RAS), showing an accurate location and magnitude of the event. The red star indicates the estimated event epicenter, and colors indicate estimated peak shaking intensities. Empty circles show the locations reported by the *Servicio Sismologico Nacional* (SSN) and the United States Geological Survey (USGS), respectively. Source: (Dominguez *et al.*, 2015)

In Europe, a collaboration was initiated with the European-Mediterranean Seismological Centre (EMSC) that *deployed a QCN server for the Euro-Med region*. EMSC has 3 deployment areas: Thessaloniki (Greece); Patras (Greece) and Martinique Islands (French Lesser Antilles) (see EMSC QCN page¹).

EMSC initiated an effort to recruit volunteers to join the project and thus increase the number of deployment sites; however, the website reports no participants (see <https://www.emsc-csem.org/service/QCN/>).

¹ Link: <https://www.emsc-csem.org/Earthquake/225/EMSC-Quake-Catcher-Network> (Last update: 21 July 2015 at 14:09 UTC)

CalTech's Community Seismic Network (CSN)

CalTech's established the Community Seismic Network (CSN) by 2009, consisting in an earthquake monitoring system based on a dense array of low-cost acceleration sensors aiming to produce block-by-block measurements of strong shaking during an earthquake. As stated in the CSN website², its mission is to:

- Provide maps of maximum shaking immediately following a major earthquake to help direct first responders.
- Monitor health and safety of structures.
- Create zonation maps of populated areas.

CSN is constituted by many sensor systems and a cloud-based server, using the Internet as communication platform. Currently, the sensor system is comprised by 3-axis class-C MEM accelerometer Phidget 1043³ and Raspberry-Pi 3b (Linux micro-computer).

In 2015, CSN was described as a 500-element network located in the Los Angeles area of California, in the USA (Clayton *et al.*, 2015). The expansion plan throughout the Los Angeles region consists in deploying sensors in schools by involving the Los Angeles Unified School District (LAUSD). The expansion started with 100 schools and was later supplemented with additional 200 campuses. The plan is to reach all 1000 campuses of LAUSD and extend to other public and private schools in the region (4000 campuses in total). Figure 16 depicts the initial, actual and planned CSN deployments.

² <http://csn.caltech.edu>

³ See: <https://www.phidgets.com/?&prodid=31>

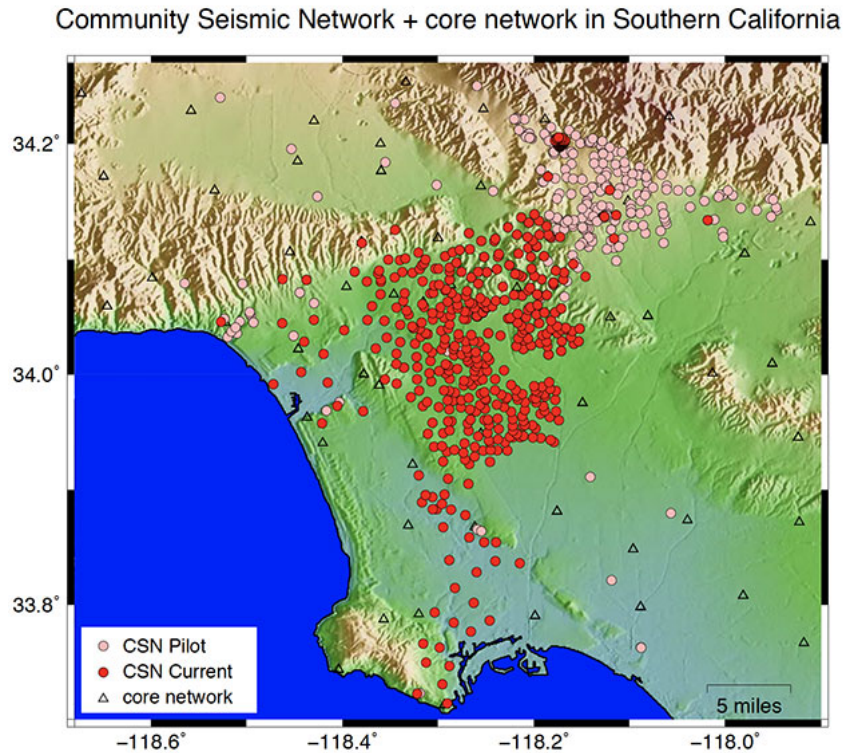


Figure 16 - CSN: current (red dots) and planned (pink dots) deployments (from <http://csn.caltech.edu/lausd/>; accessed 2021-02-21)

Since its inception, the CSN has evolved over the years, providing valuable lessons learned related with community-based sensor deployments:

- The first sensor versions required a computer to be connected to retrieve sensor data and send them to the CSN servers. This was problematic due to a number of aspects: concerns with installing and running external software applications, support various operating systems, computer downtime, among other. Current deployments have sensor systems that operate autonomously.
- The sensor system connects to the Internet using a wired connector. Alternative versions were built using solar power and 3G wireless communications, however this increased manufacturing, operation and maintenance costs. Moreover, issues were noted with using wireless connection (including Wi-Fi), since they are less reliable.
- The utilization of smartphones was experimented, namely using the built-in accelerometer and developing an App. However, (1) considering that phones are often moving, the quality of the produced data was inferior to the one provided by a fixed accelerometer, (2) its continued use in sampling acceleration data increased battery

power consumption (thus decreasing the autonomy time of the phone) and (3) it raised several privacy concerns (i.e., disclose of location data, possibility to profile a user's activity behaviour). Findings can be seen in (Faulkner *et. al.* 2014).

- The first deployments saturated the network or server-side components whenever an event was observed. The server-side software was adapted to allow dynamic deployment of instances if demand arose (e.g., rapid increases in the numbers of picks (high accelerations) during earthquakes). To decrease the network load, at an initial stage, the CSN processes data at the edge of a sensor network, then it continues processing in the network and cloud.

Importantly, in addition to seismological and educational purposes, deployments in schools consider the integration with disaster and emergency response situations, thus contributing to improve safety and well-being of society in overall. Monitoring the peak acceleration at each campus provides a synoptic view of the entire LAUSD system and hence can be used by emergency responders to plan their response.

MyShake Platform: Leveraging on Mobile Phones

The MyShake Platform is an operational framework to provide earthquake early warning (EEW) to people in earthquake-prone regions. It is built on existing smartphone technology to detect earthquakes and issue warnings (Allen, Kong and Martin-Short, 2019).

Over 300 thousand people around the globe have downloaded the MyShake app, however the number of active users (i.e., active phones connected) only peaked at 25 thousand.

Based on empirical observations, the team involved in MyShake claims that the platform allows earthquakes to be detected, located, and the magnitude estimated up to 7 seconds after the origin time (Allen, Kong and Martin-Short, 2019). The on-phone earthquake detection algorithm is able to trigger and recognize earthquake ground motions from:

- M5 earthquakes can be detected out to ~250 km.
- M4 earthquakes can be detected out to ~150 km.
- M3 earthquakes can be detected out to ~50 km.

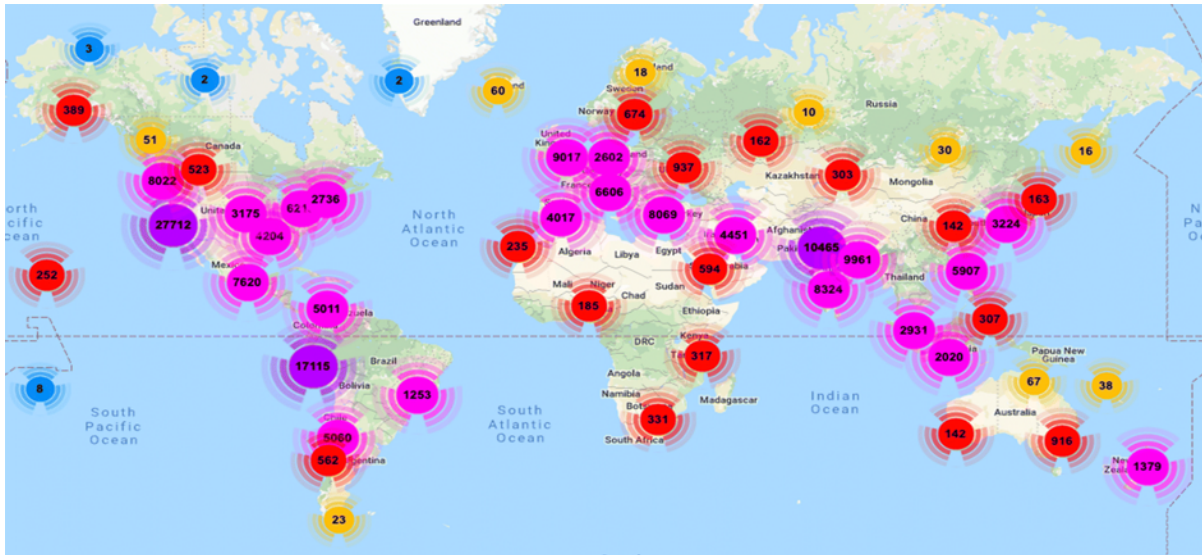


Figure 17 - Map illustrating the global distribution of MyShake usage. Locations are gathered in clusters showing the number of phones used in MyShake. Source: (Allen, Kong and Martin-Short, 2019)

SSN Alentejo

The Seismic Sensor Network Alentejo (SSN-Alentejo) developed by ICT brings to fruition the densest seismic sensor network ever deployed in Portugal. This novel network aims to improve the characterisation of seismic activity in the region and to improve earthquakes' assessment. Planned for 2020 and 2021, SSN-Alentejo aims to deploy a monitoring network of 60 sensors to generate significant volumes of live data and advance seismology knowledge. The sensors are distributed in a mesh configuration spaced on average 10 km and covering an area of about 5000 square kilometres. The density proposed for the network abides to the findings of Clayton *et al.* (2011). Furthermore, as recommended by Evans *et al.* (2003), the project opts for a cost-effective network configuration, combining high-performing broadband stations and low-cost sensors.

SSN-Alentejo represents a reinforcement of sensing and monitoring capabilities, enabling the opportunity to explore, for the first time in Portuguese territory, the high-resolution observation of seismic activity. In particular for the Arraiolos region in Portugal, it is important to overcome existing limitations in monitoring seismic activity by deploying additional seismic sensors, increasing the resolution of the recorded seismic activity and, consequently, producing a more detailed seismic characterisation of the region (see section 1.1). This is a necessary step to improve the seismic and tectonic knowledge in the regions.

The evolution of the seismic network in Arraiolos and planned deployments for SSN-Alentejo are presented in Figure 18 (Manso *et al.*, 2020).

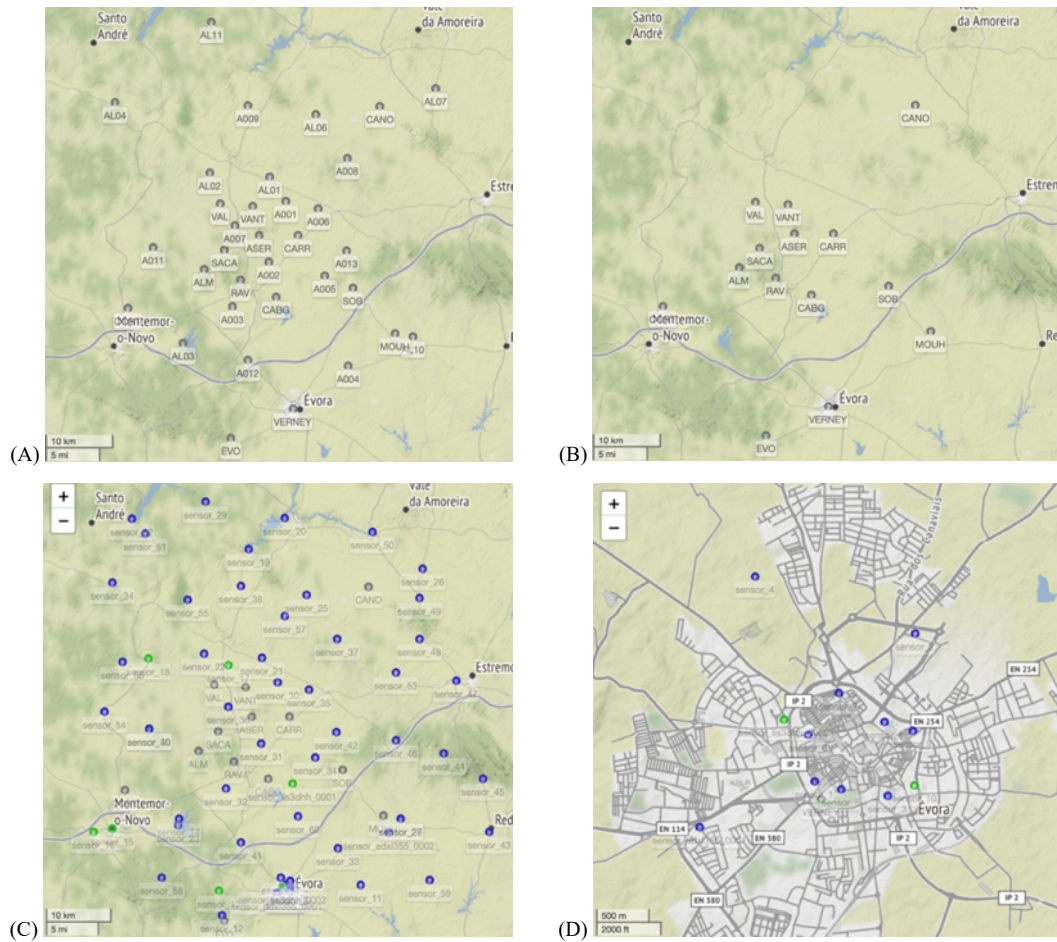


Figure 18 - Different Phases of the Seismic Network in Alentejo (includes the Arraiolos region) and the SSN-Alentejo planned deployment. (A) Temporary seismic network deployed in the Arraiolos region after the earthquake. About 60 connected stations. (B) Current seismic network in the Arraiolos region. Less than 15 connected stations. (C) SSN-Alentejo: planned deployment of additional 60 sensors, resulting in about 75 stations in total. (D) SSN-Alentejo: planned deployment for the Évora city. Sensor density is increased to monitor ground motion activity that may impact cultural heritage and historical buildings. Source: (Manso *et al.*, 2020). The SSN-Alentejo project is funded by the Science Foundation of Portugal (FCT) under grant number ALT20-03-0145-FEDER-031260.

2.4 Conclusion

In this section, the fundamentals of seismology were introduced, followed by a classification of the mechanic waves frequency (and period) band as a function of the source type. Over the last years, techniques employed to observe and record seismic events have significantly progressed, where broadband seismometers became the *state-of-the-art* equipment used in seismology. Recently, MEMS-based accelerometers have also started to be explored given their high amplitude measurement, high frequency range, small size and affordability, but the

presence of sensor noise limits their application. In this regard, MEMS-based accelerometers can complement traditional seismology sensors, especially for the observation of strong motion events, and have enabled the deployment of high-density seismic sensor networks, as in the case of USC's QCN, CalTech's CSN and ICT's SSN-Alentejo. Importantly, high-density seismic sensor networks measure seismic activity with "high resolution" and, by correlating the signal with time and space, they allow, for example, the production of *shakemaps* directly from observations. The application of MEMS accelerometers in seismology aiming high-density deployments are thus central elements of this thesis and are further described in the following sections.

3 MEMS ACCELEROMETERS FOR SEISMOLOGY

3.1 Introduction

In the last years, sensors and sensing network technology evolved at a strong fast pace, resulting in improved performance (resolution, sensibility and processing capacity), operation (energy efficiency, operation time) and connectivity (broadband communications), at significant cost reduction. These innovations bring scientists promising prospects and, recently, low-cost MEMS accelerometers demonstrated the capability to generate relevant data for seismic analysis in dense deployment contexts.

MEMS technology has enabled the mass production of small sized accelerometers with potential applications in numerous areas, including seismology. Their small size (made of small components in the order of μm) and their "simple" manufacturing process makes them low-cost.

3.2 MEMS Accelerometers for Seismology

Capacitive accelerometers, in particular, are highly popular due to the reduced cost, a simple structure and the ability to integrate the sensor close to the readout electronics. They are based on a spring-mass system placed on a silicon substrate, as illustrated in Figure 10. When subjected to an acceleration, the inertial mass shifts, causing a (proportional) change in the capacitance. By measuring the capacitance change, the acceleration can then be calculated. Figure 19 shows the dimensions of Analog ADXL354/ADXL355 MEMS Accelerometer.

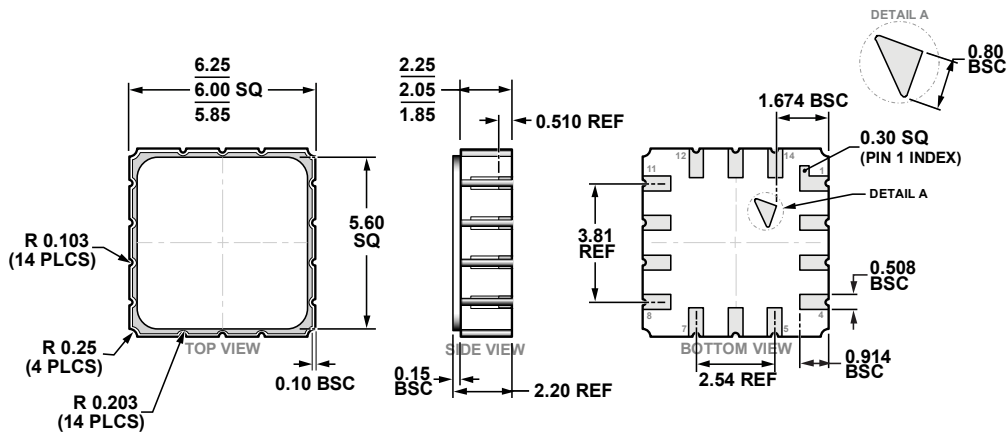


Figure 19 - Analog ADXL354/ADXL355 MEMS Accelerometer Dimensions (in mm). Source:

www.analog.com

The application of MEMS accelerometers to seismology has found several fields of application, including (Scudero *et al.*, 2018):

- i) seismological study and earthquake observation,
- ii) seismic activity monitoring networks, and
- iii) seismic surveys.

Triaxial MEMS accelerometers are already used to augment existing seismic networks, essentially filling in gaps present in high-quality sensors, as described in section 2.

Early efforts explored the presence of accelerometers in computers that, connected to a distributed computing network, could be used to build QCN, a network of sensors to detect and monitor earthquakes (Cochran, 2009).

As the underlying technologies to build connected MEMS systems became more accessible and affordable, several efforts are currently using dedicated MEMS sensors to build dense seismic sensor networks, as the case of CSN and the urban MEMS seismic network in the Acireale Municipality (Sicily, Italy) (D'Alessandro, Luzio and D'Anna, 2013).

In order to better understand the applicability and limitations of MEMS for purposes of seismology, several teams have analysed their performance under numerous conditions. In this respect, it is important to define the following performance categories, as per Advanced National Seismic System (ANSS) guidelines (ANSS, 2008; Evans *et al.*, 2014):

- Class A refers to the highest performance, state-of-the-art instrumentation, presently for accelerometers with useful **resolution of about 22–24 bits peak-to-peak over 2 to 4g ranges (sensor roughly US\$2000–4000)**.
- Class B can be illustrated by the NetQuakes instrument (GeoSIG model GMS-18) that is an **effectively 16-bit (vertical) and 18-bit (horizontal) instrument over 3g ranges** (sensor roughly US\$500–1000).
- Class C is the lowest performance level, potentially usable by ANSS and has useful resolution from about 12 to 16 bits, typically over 2g ranges (sensor roughly US\$100–200).

As presented in Figure 20, Evans *et al.* (2014) analysed several class-C MEMS present in consumer products and prototype boards, namely: Android smartphones (i.e., Droids); Gulf Coast Data Concepts (GCDC; gcdaconcepts.com); JoyWarrior model 24F14 accelerometers used in game controllers (“JWF14”; Code Mercenaries Hard- und Software GmbH, codemerccs.com); O-Navi LLC (o-navi.com) used in game controllers; Phidgets (phidgets.com) models 1043 and 1043. The figure also presents the vault noise recorded at the USGS

Albuquerque Seismological Laboratory that is close to the NLNM. All analysed MEMS exhibited sensor noise *well above the site noise, which made the coherence method and even night recording unnecessary. Instead, all of the sensor output is attributed to instrument noise.* Main limitations resulted from **insufficient resolution, low sample rates and high sensor self-noise**. Indeed, the small MEMS physical size means it effectively has a very small inertial mass, making it pervious to noise (electronic or mechanical), especially at low frequencies. On the other hand, it makes it suitable to measure "very high" frequencies (above hundreds of Hz).

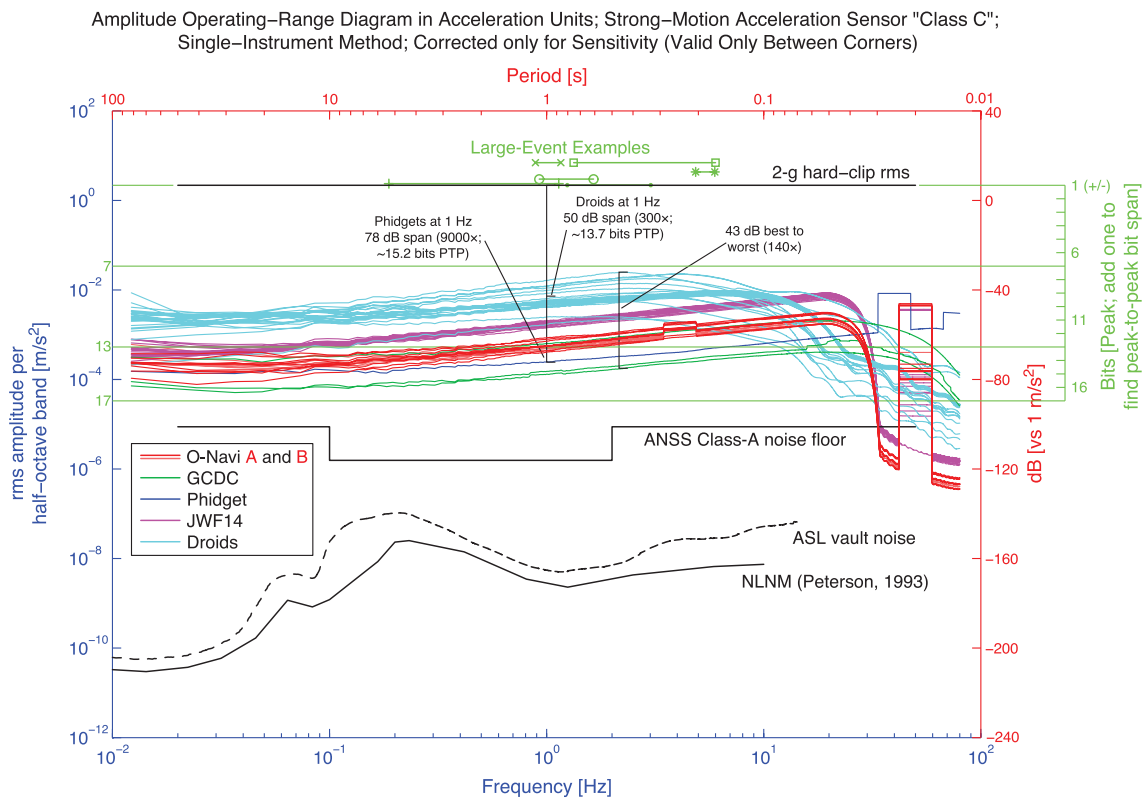


Figure 20 - Self-noise analysis of several MEMS accelerometers present in Android phones (Droids), game controllers and Phidget. The NLNM and ANSS Class-A noise floor are shown as reference, showing accelerometers sensor noise above the reference noise. Source: (Evans *et al.*, 2014)

Despite their limitations, it is generally accepted that MEMS-based accelerometers complement traditional seismology sensors by measuring strong ($M > 3$) and high frequency seismic waves. Their capability allows for recording strong ($M > 6$) regional earthquakes at a distance of few hundreds of km, and even moderate ($M \sim 3$) local earthquakes at a distance of the order of some tens of km. This is a result of the generated ground motion's amplitude (and resulting acceleration) being several times higher than the MEMS self-noise. D'Alessandro,

Scudero and Vitale (2019) illustrates a MEMS accelerometer capability by recording a ML 4 event that occurred at a distance of 35 km, being noted that the signal is well above Peterson's NHNM.

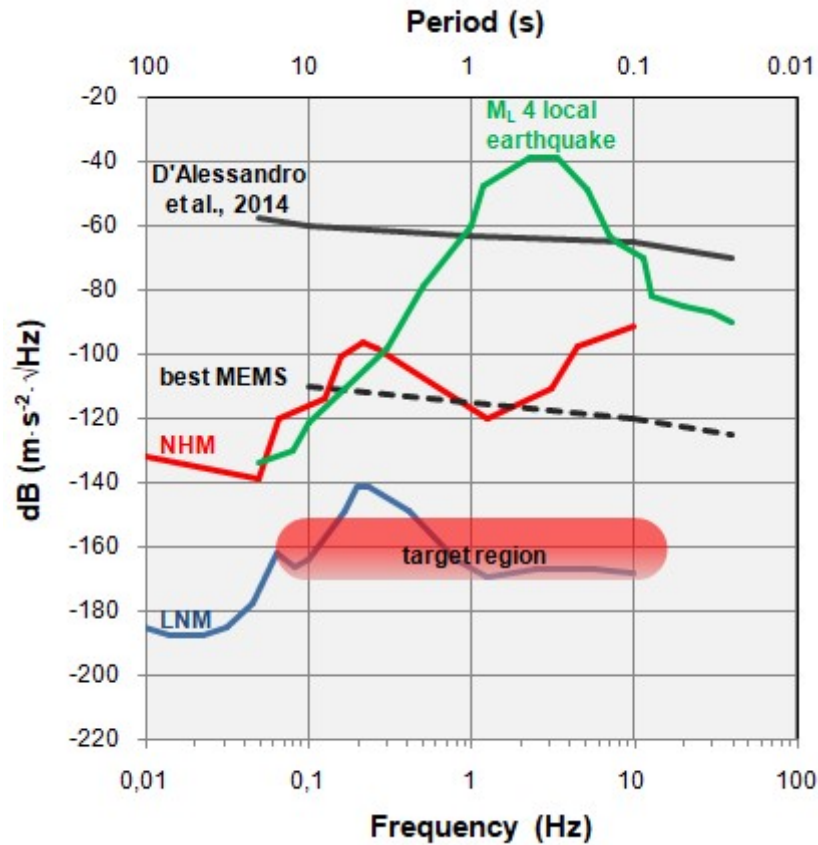


Figure 21 - ML4 local earthquake spectra (green line) and average self-noise PSD of a MEMS accelerometer (black dashed line). Peterson's NHNM (red line) shown for reference. Source: (D'Alessandro, Scudero and Vitale, 2019)

For purposes of seismology, and as presented by Manso *et al.* (2017), state-of-the-art low-cost MEMS-based accelerometers:

- provide adequate sensitivity, noise level, and range (measured in g) to be applicable to earthquake strong motion acquisition ($M > 3$), thus also limiting the "resolution" capability. However, the high level of instrumental self-noise that increases as frequency decreases limits their application in the study of low frequency weak motion forces (Evans *et al.*, 2014; Farine *et al.*, 2003).
- are well fit to measure high frequency (> 40 Hz) ground motion (Farine *et al.*, 2003) since their resonant frequency (typically above 1 kHz) is far above the seismic band pass.

- measure the gravity acceleration component that provides a useful reference for sensitivity calibration and tilt measurement.
- have high acceleration ranges (several g) and are capable of sustaining high acceleration (several hundred g) without being damaged.
- when compared with seismometers, such as geophones, may have an advantage in detecting weak high frequency signals, while geophones may have the advantage in detecting weak signals at low frequencies.
- can have useful applications such as earthquake early warning, seismic hazard map and security applications (Pakhomov *et al.*, 2005).

3-axis MEMS accelerometers are already used to augment existing seismic networks, essentially filling in the gaps between higher quality sensors (Evans *et al.* 2003). Furthermore, MEMS technology will surely continue to evolve and it is expected that their performance on weak low frequency signals will improve:

- Homeijer *et al.* (2014) have shown MEMS performance comparable to reference seismometers, where its self-noise level during low seismic background conditions.
- Schiefer and Bono (2009) developed a calibration methodology for low frequencies and
- Laine and Mougnot (2014) presented a new generation of MEMS-based digital sensor with a low noise floor at low frequencies (<5Hz).

Thus, MEMS' relevance in seismology is expected to increase in the coming years.

3.3 Sensor Relevant Parameters

There is a wide range of MEMS accelerometers available in the market for various purposes and addressing different applications, including automobile, computer, mobile phones and video game industries. The applications dictate the characteristics that a MEMS should exhibit. Seismology is mostly interested in measuring small ground motions at low frequencies (e.g., distance teleseismic events), while sometimes dealing with moderate to large local events having medium and strong ground motions at high frequencies (see Table 2). It is quite challenging for seismometers to cope with such a wide range of signals, inevitably having to setup compromises between sensitivity and range: even broadband seismic sensors with a 160 dB dynamic range will clip [in non-teleseismic distances] in a magnitude 9 earthquake event (whose maximum dynamic range is around 220dB) (Tunc *et al.*, 2012). Installing strong-

motion accelerometers helps overcoming this limitation and thus provide valuable measurement data for seismologists.

In this regard, when selecting MEMS accelerometers for seismological purposes, the following parameters should be taken into account⁴:

- **Range:** Specifies the minimum and maximum acceleration values it can measure. It is often represented relative to earth standard gravity g (e.g., $\pm 2g$).
- **Resolution:** Specifies both (i) the degree to which a change can be detected and (ii) the maximum possible value that can be measured. In case of a digital sensor, it is expressed in *bits*. For example, a sensor with 16-bits resolution is able to quantify 65,536 possible values. If the scale is set to $\pm 2g$ (hence, a 4g range) the minimum possible change that can be detected is about $61\mu g$.
- **Sensitivity:** Specifies the ratio of the sensor's electrical output to mechanical input thus representing the smallest absolute amount of change that can be detected by a measurement. It is typically used in analogue sensors. It can be measured in V/g or in counts/g.
- **Noise density:** Accelerometers are subject to noise generated by electronic and mechanical sources. Given their small size (thus, having a small inertial mass), accelerometers exhibit "high" noise at low frequencies. The noise density is often represented in terms of power spectral density (PSD) and is expressed as g/\sqrt{Hz} . It varies with the measurement bandwidth: when multiplied by it, the resulting value represents the minimum acceleration values that can be resolved.
- **Bandwidth:** Specifies the frequency range that the sensor operates in. It is limited to the natural resonance frequency of the mechanical structure of the accelerometer itself, which is typically very high ($>kHz$).
- **Sample rate:** Specifies the number of measurements (samples) per second.

Moreover, for purposes of high dense deployments, other factors are relevant, such as:

- **Size:** Specifies the physical characteristics of the sensor. MEMS accelerometers are supplied embedded in small chips (order of mm).
- **Power Consumption:** Specifies the required power to operate. Usually is very low (order of μA).

⁴ For more details, see also Endevco Technical Paper 328 "Practical understanding of key accelerometer specifications" accessible at: https://www.endevco.com/contentStore/mktgContent/endevco/dlm_uploads/2019/02/TP328.pdf.

- **Cost:** Refers to the cost to purchase a MEMS accelerometer. Prices vary according to the sensor performance. Cost tends to decrease as new (improved) models are launched every year.

3.4 MEMS Accelerometers: Analysis and Selection

Several commercially available MEMS accelerometers were analysed in order to assess the most suitable ones for a high dense network. Table 3 presents accelerometer's parameters and associated target values for seismic purposes. The target values follow recommendations for class-C or above (ANSS, 2008).

Table 3 - MEMS Accelerometers: parameters and target values

Parameter	Target	Notes
Range	2g	Increasing range reduces sensitivity. It is thus advisable to select a small value.
Resolution	16-bit or above.	-
Noise density	Below $100\mu\text{g}/\sqrt{\text{Hz}}$ (below $400\mu\text{g}/\sqrt{\text{Hz}}$ acceptable for prototyping and testing).	This is a critical parameter that is currently the main limiting factor in the application of MEMS in seismology. The target value reflects the current state-of-the-art of the low-cost MEMS market.
Bandwidth (and sample rate)	100 Hz or above (sample rate of 200 sps).	Increasing the bandwidth increases the noise density.

In the context of high-dense networks, it is also important to consider factors that impact overall cost, including manufacturing and assembling aspects. As such, the assessment considers the following requirements:

- **Digital sensor**, facilitating direct data read (i.e., no need for an analogue-to-digital converter, no need for any signal pre-conditioning or pre-processing, signal is less exposed to external noise).
- **Purchase cost** (for 3-axis measurements).

Two other important parameters are intrinsic in most MEMS and are not differentiable:

- **Size** (MEMS accelerometers are embedded in very small chips, in the order of mm).
- **Power** (MEMS accelerometers operate using small currents, in the order of mA or less).

Resorting to online resources and marketplaces, several MEMS accelerometers were analysed based on openly available information, such as product datasheets. Information pertaining to sensors from the following companies was analysed:

- Analog Devices (source: <https://analog.com>).
- Applied Measurement Australia (source: <https://appliedmeasurement.com.au>).
- Bosch Sensortec (source: <https://www.bosch-sensortec.com>).
- Colibrys (source: <https://www.colibrys.com>).
- Endevco (source: <https://endevco.com>).
- Freescale (now NXP) (source: <https://www.nxp.com>).
- Invensense (source: <https://www.invensense.com>).
- Kionix (source: <https://www.kionix.com>).
- Phidgets (source: <https://www.phidgets.com>).
- Silicon Designs (source: <https://www.silicondesigns.com>).
- STMicroelectronics (source: <https://www.st.com>).

From an initial list of about 50 sensors, 27 were selected as presented in Table 4. The following colour codes are used:

- In the sensors: GREEN: sensor meeting requirements; ORANGE: sensor meeting requirements for prototyping.
- In the parameters: GREEN: parameter meets or is above the target value; RED: parameter does not meet the target value; ORANGE: parameter is close to meet the target value.

Table 4 - Analysis and Evaluation of 27 MEMS Accelerometers

Manufacturer	Sensor Name	price (\$USD)	Digital	nbr axis	Resolution (bits) or Sensitivity (V/g)	Noise Density	Bandwidth (Hz)	1g	1.5g	2g	3g	4g	8g	16g	Notes
Analog Devices	ADXL313	-	Y	-	10-bit	150µg/√Hz	-								
Analog Devices	ADXL355	35	Y	3	20-bit	25µg/√Hz	4000Hz			X		X	X		Has temperature sensor
Analog Devices	ADXL354	-	N	-	-	20µg/√Hz	-			X		X	X		
Analog Devices	ADXL362	-	Y	-	12-bit	175µg/√Hz	-			x		x	x		
Analog Devices	ADIS16210		Y		16-bit	248µg/√Hz	-								

Manufacturer	Sensor Name	price (\$USD)	Digital	nbr axis	Resolution (bits) or Sensitivity (V/g)	Noise Density	Bandwidth (Hz)	1g	1.5g	2g	3g	4g	8g	16g	Notes
Analog Devices	ADIS16003		Y	2	12-bit	110 μ g/ \sqrt Hz	-								
Analog Devices	BMI160	-	Y	9	16-bit	300 μ g/ \sqrt Hz	12.5 - 1600			X		X	X	X	
A.M.A.	4332		N	3	1V/g	8 μ g/ \sqrt Hz	0 - 20			X					
Bosch	BMA180	2.5	Y	3	14-bit	200 μ g/ \sqrt Hz	0.2 - 300	X	X	X	X	X	X	X	
Bosch	BMA456	40	Y	-	16-bit	120 μ g/ \sqrt Hz	-			X		X	X	X	
Colibrys	VS1002	-	N	1	1350 mV/g	7 μ g/ \sqrt Hz	0 - 1000			X					
Colibrys	SF2006	-	N	1	0.8 \pm 0.08 V/g	11 μ g/ \sqrt Hz	0 - 1000								
Endevco	7290A	-	N	-	1V/g	100 μ V	0 - 15			X					
Endevco	MMA8452Q	-	Y	-	12-bit	126 μ g/ \sqrt Hz	1.56 - 800								
Freescale / NXP	MMA7455	2	Y	3	8-bit	-	125, 250			X		X	X		
Freescale / NXP	MMA7660	3	Y	3	6-bit	-	1 - 120		X						
Freescale / NXP	MMA8451Q	2	Y	3	14-bit	99 μ g/ \sqrt Hz	1.56 - 800			X		X	X		
Invensense	MPU-6050	1.5	Y	6	16-bit	400 μ g/ \sqrt Hz@10Hz	1.25 - 40			X		X	X	X	
Invensense	MPU-9250	-	Y	9	16-bit	300 μ g/ \sqrt Hz	5 - 260			X		X	X	X	
Kionix	KX123-1039	-	Y	3	16-bit	750 μ g/ \sqrt Hz@50Hz	0.781 - 25.6k			X		X	X		
Kionix	KMX62G	-	Y	9	16-bit	750 μ g/ \sqrt Hz@50Hz	0.781 - 25.6k			X		X	X	X	
Phidgets	1044	140	Y	9	16-bit	280 μ g	1 - 250			X			X		Discontinued
Phidgets	1044_1	120	Y	9	16-bit	N/A	497 Hz (~250 sps)			X			B		Contains gyroscope and compass. Has a backup accelerometer (8g)
Phidgets	1041_0	40	Y	3	16-bit	N/A (\pm 2.5mg)	(62.5 sps)						X		
Silicon Designs	2460 / 2466	-	N	-	2V/g	10 μ g/ \sqrt Hz	0 - 300			X					
ST	LIS3DHH	7	Y	-	16-bit	45 μ g/ \sqrt Hz	235 or 440								
ST	LIS344ALH	2.5	N	-	-	50 μ g/ \sqrt Hz	-			X					

Table 4 shows a wide variety of sensors and associated characteristics. In addition to digital sensors, it was decided to keep a few analogue sensors for future reference, given their interesting characteristics regarding noise density (e.g., A.M.A. 4332, Colibrys VS1002 and SF2006, Silicon Designs 2460/2466).

A few of the analysed MEMS accelerometers seem to be targeted for consumer products (e.g., cars, mobile phones, game controllers), where low resolution and high noise might be acceptable.

Looking into the analysed digital sensors, two sensors are highlighted:

- the Analog ADXL355, the best performing 3-axis digital sensor given its high resolution (20-bit), noise density (expressed as PSD) of $25\mu\text{g}/\sqrt{\text{Hz}}$ and moderate cost ($\sim 35\text{€}$).
- followed by ST Electronics LIS3DHH with high resolution (16-bits), noise density (PSD) of $45\mu\text{g}/\sqrt{\text{Hz}}$ and low cost ($\sim 7\text{€}$).

It is worth mentioning two additional sensors:

- Freescale MMA8451Q that, despite the insufficient resolution (14-bit), exhibits a low noise density ($99\mu\text{g}/\sqrt{\text{Hz}}$), making it an interesting option when considering strong motion.
- Phidgets 1044_1 that is quite popular among seismologists (see CSN in section 2.3), offering interesting performance in most characteristics and including other sensors, like a compass and a magnetometer.

Invensense MPU-6050 is also considered for prototyping and evaluation purposes, given its reasonable performance and very low cost. However, its high noise density makes it unfit for seismic deployments.

3.5 Conclusion

In the last years, sensors and sensing network technology evolved at a strong fast pace, resulting in improved performance and connectivity at significant cost reduction. MEMS accelerometers in particular have demonstrated the capability to generate relevant data for seismic analysis in dense deployment contexts. This section presented an analysis of the application of MEMS accelerometers in seismology, including their capability in detecting and measuring seismic activity. It is shown that MEMS accelerometers exhibited sensor noise well above the site noise. However, and despite their limitations, it is generally accepted that they can complement traditional seismology sensors in measuring strong motion.

Several MEMS accelerometers were analysed based on available specifications, being highlighted the following sensors:

- the Analog ADXL355, the best performing 3-axis digital sensor given its high resolution (20-bit), noise density of $25\mu\text{g}/\sqrt{\text{Hz}}$ and moderate cost ($\sim 35\text{€}$).
- followed by ST Electronics LIS3DHH with high resolution (16-bits), noise density (PSD) of $45\mu\text{g}/\sqrt{\text{Hz}}$ and low cost ($\sim 7\text{€}$).
- Freescale MMA8451Q that, despite the insufficient resolution (14-bit), exhibits a low noise density ($99\mu\text{g}/\sqrt{\text{Hz}}$), making it an interesting option when considering strong motion.
- Phidgets 1044_1 offering interesting performance in most characteristics and including other sensors like a compass and a magnetometer.

4 THE SENSOR SYSTEM

This section is based on the presentation *Low-Power Low-Cost Sensor Platform for Seismic and Environmental Monitoring* (Manso *et al.*, 2016) and the article journal *Design and Implementation of a Network Enabled High-Throughput MEMs-based Seismic Sensor* (Manso *et al.*, 2017).

4.1 Introduction

In this section, it is presented the design of a MEMS-based sensor system to measure ground motion (more specifically, acceleration) that operates autonomously, is network-enabled and is capable to deliver high data throughput. The sensor system contains the sensor component, as well as additional components in order to achieve the functionalities required to operate in a network-enabled environment. The platform shall:

- deliver the capability to function autonomously (i.e., no need to connect to external computers to operate).
- connect to an IP-based network; and
- be low cost.

4.2 Architectural Components

The architecture outlining main components for the sensor system is presented in Figure 22 and described next.

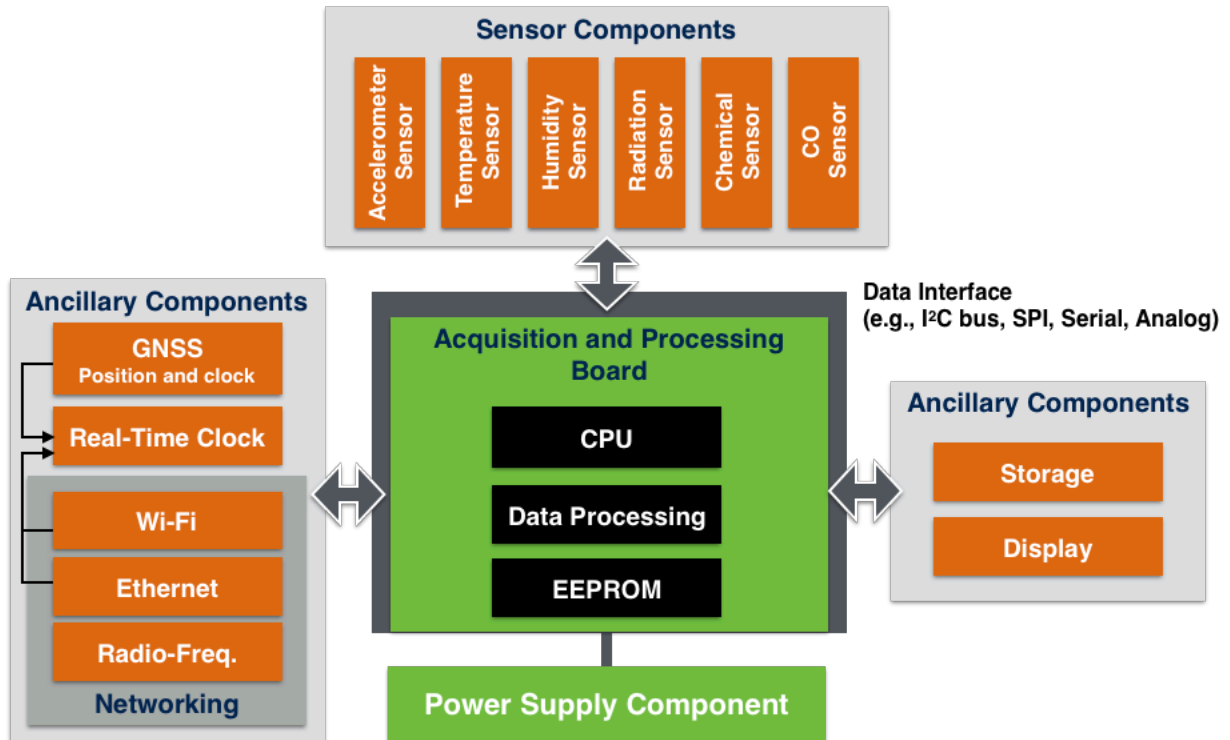


Figure 22 - Sensor Platform Architecture

The following main components are defined:

- The **Acquisition and Processing Board (APB)** is the core component of the platform that deals with data acquisition, processing and overall control and synchronisation of all system components.
- The **Sensor Component (SC)** provides the capability to measure the physical variable(s) of interest. The architecture is designed to allow using multiple sensors.
- The **Ancillary Component (AnC)** provides additional necessary or useful functions for the platform. These include e.g., real-time clock, networking, display and high-capacity data storage.
- The **Power Supply Component (PSC)** provides energy to the platform so that all electrical components can function.

In addition, a **Data Interface (DInt)** (grey lines and arrows) is depicted to refer to data exchange capability between components. It can consist in e.g., I2C (Inter-Integrated Circuit), Serial Interface, Serial Peripheral Interface (SPI) and analogue to digital interface.

The components are described next.

4.3 Acquisition and Processing Board

The Acquisition and Processing Board (APB) is the core component of the platform that deals with data acquisition, processing and overall control of the system. It includes capabilities to exchange data (input and output (I/O)) with the various platform components (such as sensors) and can be programmed to execute specific code instructions, including data processing (e.g., filters and corrections). Furthermore, it provides clock synchronization and can also provide power supply to other components. The constituent parts relevant for a sensor platform are the Central Processing Unit (CPU), which ensures correct program execution, peripherals control and interrupt handling; the Data Processing, which consists in the code instructions that handle specific sensor (or sensors) data; and the Electrically Erasable Programmable Read-Only Memory (EEPROM) for persistent (non-volatile) data storage.

The APB must be designed as to achieve the required sampling speed, amount of local signal processing and power consumption.

4.3.1 Sensor Component

The SC purpose is to measure the physical quantity of interest and to transmit the output variable associated to the measure. In this regard, the SC provides the function and purpose of the system.

There is a wide variety of sensors made for a broad spectrum of purposes, ranging from environmental monitoring to industrial applications and home appliances. For seismology, the main variable of interest is ground motion, which can be measured using accelerometer sensors (see section 3 for a review).

4.3.2 Ancillary Component

The Ancillary Component (AnC) purpose is to provide additional functions that are necessary for the proper functioning of the platform. These can include:

- Time precision component, which purpose is to provide accurate and precise tracking of date and time timing. Examples are Real-Time Clock (RTC) and Global Navigation Satellite System (GNSS) components.
- Persistent Storage component, which purpose is to save sensor system data (especially measurements) over time. Examples are SD card readers and memory chips.

- Networking components, which purpose is to communicate with external systems. Examples are Wi-Fi components.
- Display (and User Interface (UI)) component, which purpose is to show relevant information to human users. Examples are LED screens and buttons.

Note that some ancillary components might provide multiple functions. For example: GNSS components can be used for both time synchronisation and location; Networking components can provide time synchronisation if connected to the Internet or dedicated time providers.

4.3.3 Power Supply Component

The Power Supply Component (PSC) deals with providing the necessary power for the system to operate. It can rely on existing infrastructures (e.g., electrical grid) and include self-sufficient capabilities, like a rechargeable battery and solar panels.

In the context of high dense deployments, including remote sites, it is important to seek low-power consumption in order to maximise operation time to prevent loss of data in cases of energy blackouts.

4.4 Sensor System Application Logic

The application logic governs the functioning of the sensor system. It deals with setup and configuration of all components, manage connection status and handle sensor data. In case the sensor system incorporates advanced computing capabilities, it can also be used to perform local data processing and filtering functions in order to optimise system-level functions, like compressing data to reduce network traffic and the servers' workload.

A simplified high-level software workflow is depicted in Figure 23 and is explained next. Optional blocks are presented in dark background. The workflow has two main sections “Initialisation” and “Main Loop”. These, together with the most relevant logic blocks, are explained next.

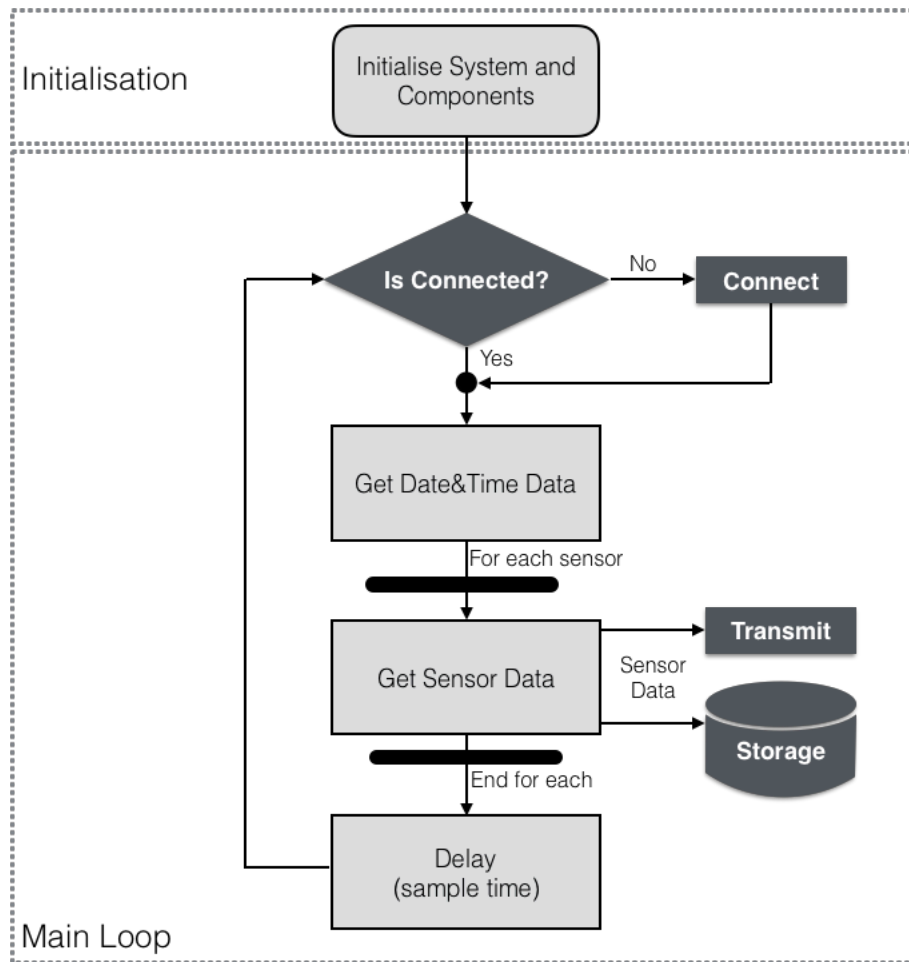


Figure 23 - High-Level Sensor System Workflow

Initialisation

The initialisation block is the starting point of the application logic. It only runs at power up. It handles the configuration of the APB and all connected components, including sensors (e.g., calibration and sample rate), storage (if present), connection ports and connectivity protocols. The initialisation can also be used to configure parameters that will contribute to a low-power mode operation.

Main Loop

The main loop performs the continuous functions related with the sensor system operation. Its main operational purposes are to (1) retrieve the current date and time, (2) collect data from the sensor components and (3) store and/or transmit data from the sensor component.

The main loop also deals with checking the correct operation of the system. For instance, verifies the connectivity state, reconnecting if needed.

The optional blocks (dark coloured) are optional, as per architecture specifications (see Figure 22). For example, a sensor operating in offline mode (no online connection) can store sensor measurements in local storage, while an always connected sensor transmits sensor data and does not need local storage.

The main loop runs continuously. The retrieval of sensor data is done periodically (depending on the desired sample rate). If a low-power operation is targeted, it is possible to set the system in low-power mode between sensor readings in order to save energy.

It is important to have a precise time control of the main loop in order to deliver the expected sample rate. This requires proper setup of the sensor component and APB instructions of the main loop.

4.5 Conclusion

In this section, it was presented the sensor system design for a MEMS-based accelerometer system. Its main architectural components include the following:

- The **Acquisition and Processing Board** that is the core component of the platform dealing with data acquisition, processing and overall control and synchronisation of all system components.
- The **Sensor Component** that provides the capability to measure the physical variable(s) of interest. The architecture is designed to allow using multiple sensors.
- The **Ancillary Component** that provides additional necessary or useful functions for the platform. These include e.g., real-time clock, networking, display and high capacity data storage.
- The **Power Supply Component** that provides energy to the platform so that all electrical components can function.

The functioning of the sensor system is governed by the application logic that deals with setup and configuration of all components, manage connection status and handle sensor data. The application logic for the sensor system was presented consisting in an “Initialisation” section, dealing with the initialisation of the sensor system, and a “Main Loop” section, running continuously to handle sensor measurements.

The architecture and its components are abstract and described in functional terms, allowing different choices for its realisation. The next section presents several implemented prototypes, following the architecture herein defined.

5 SENSOR SYSTEM IMPLEMENTATIONS

5.1 Introduction

The architecture defined in section 4 provides a general design guidance for the implementation of sensor systems for specific purposes.

As part of this work, several implementations were experimented and analysed targeting different objectives, as follows:

- Prototype of a low-cost low-power multi-purpose sensor system capable to operate autonomously, targeting deployments over long periods of time (order of months).
- Prototype of a low-cost network-enabled seismic sensor system.
- Prototype of a network-enabled seismic sensor application running on mobile phones.
- Prototype of an emulated seismic sensor for testing purposes.

This section finalises by presenting a noise comparison between the different prototypes and an analysis of their detectability capabilities in seismology.

5.2 Prototype 1: Low-cost low-power multi-purpose sensor system

This section is based on the presentation Low-Power Low-Cost Sensor Platform for Seismic and Environmental Monitoring by (Manso et al., 2016)

The first prototype targets a sensor system aiming to comply with the following requirements:

- Multi-purpose system, capable to collect multiple parameters of interest. More specifically, the defined purpose is environmental monitoring and seismic activity, thus, the following shall be measured: ambient temperature, ambient humidity and ground motion.
- Capability to locally store sensor data (with capacity for several months of data).
- Low-power system (below 1 Watt on average) aiming to operate autonomously over long periods of time (order of months).
- Low-cost system (below 25€).

Note this implementation does not target a connected (network-enabled) system. The selection of the architecture components is presented next.

5.2.1 Components

5.2.1.1 Acquisition and Processing Board component

A suitable platform for the APB is the low-power Arduino Pro (3.3v version) operating at 8MHz. The board (see Figure 24) includes a power connector allowing to directly connect an external battery.



Figure 24 - Arduino Pro Board. Source: Arduino (<https://arduino.cc>)

The Arduino Pro board has the following main characteristics (from <https://www.arduino.cc/en/Main/ArduinoBoardPro>):

- Microcontroller: ATmega328.
- Operating voltage: 3.3v.
- Clock speed: 8MHz.
- Flash memory: 32KB.
- SRAM: 2KB.
- EEPROM: 1KB.
- Digital I/O Pins: 14.
- Maximum DC current: 100mA (overall) and 40mA (per I/O pin).
- Wide range of low-level communications supported, such as, I2C and SPI.

In normal operation, the platform has an operating current of 4.24mA that can be significantly reduced to about 0.47mA (sleep mode) and 0.30mA (power down). Removing the power led further reduces the operating current in 0.170mA.

The Arduino platform is also supported by a large community and has many open-source libraries and tools available (including a high-level programming editor), resulting in the support of a wide range of devices. The board can be programmed using a Future Technology Devices International (FTDI) serial board configured for 3.3v. Programming is performed using the Arduino IDE (<https://www.arduino.cc/en/Main/Software>) and C/C++ programming language.

A software program was developed and uploaded to the board, following the design principles defined in 4.4.

5.2.1.2 Sensor Component: Accelerometer

The selected accelerometer for this prototype is the MPU-6050 (see section 4 for its specifications).

An important feature of this device is that it collects samples autonomously (independently of the APB) and stores them in a local FIFO⁵ (first in, first out) buffer, while the APB can be put to sleep in order to save power.

The MPU-6050 operating current while sampling acceleration is 500 μ A (in normal operation), 20 μ A (if sample rate at 5Hz) and 5 μ A (sleep mode). It is worth mentioning that the MPU-6050 also includes a Gyroscope, which has been used to explore the relevance of rotational components in seismology. However, since the use of the Gyroscope has an energy cost of 3.3mA (almost 10x the accelerometer), it will not be used in this implementation.

5.2.1.3 Sensor Component: Temperature and Humidity

The chosen environmental sensor chosen is the AM2301 digital temperature and humidity sensor that is connected to a 8-bit microcontroller. The sensor is presented in Figure 25.

⁵ FIFO is a method for organizing and managing a data list. When accessing data, the first element of the list is retrieved. Any data added to the list is put to the end of the list.

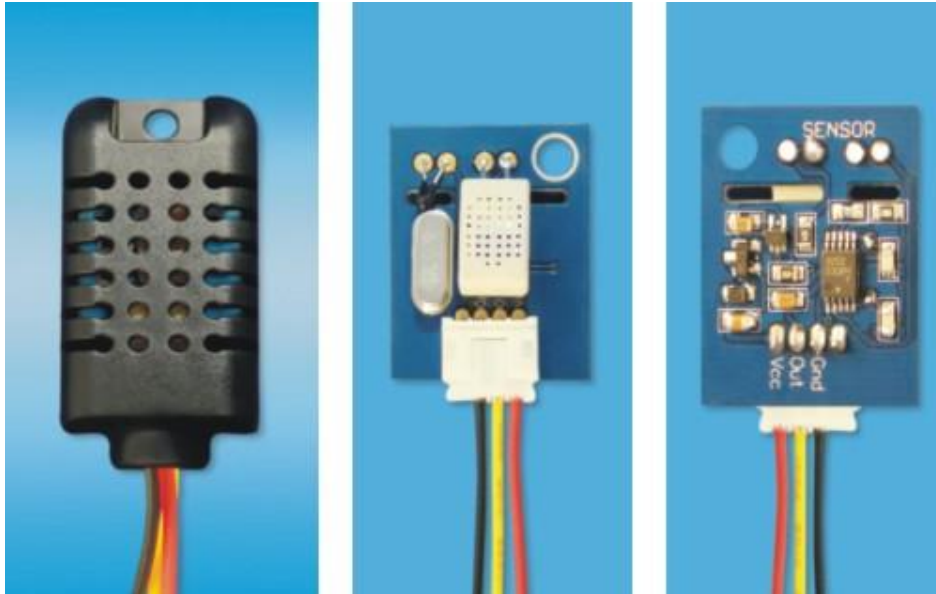


Figure 25 - AM2301 Temperature and Humidity Sensor

The AM2301 specifications⁶ are:

- Temperature measuring range: -40°C to $+80^{\circ}\text{C}$ (0.1°C resolution, $\pm 0.5^{\circ}\text{C}$ maximum error).
- Relative Humidity (RH) measuring range: 0% to 99.9%RH ($0.1\%RH$ resolution, $\pm 5\%RH$ maximum error).
- Operating current (not including data bus): $10\mu\text{A}$ (dormant), $500\mu\text{A}$ (measuring); turn on current is 8mA for about 1 second.
- Sample period: 2 seconds.
- Single-bus (one wire) interface that requires a pull-up resistor between the data connector and V_{cc} . A $10\text{k}\Omega$ resistor is used for this purpose.

5.2.1.4 Ancillary Component: Real-Time Clock

Given the requirement about long-term deployment for the sensor system, it is required to resort to an ancillary component to maintain precise tracking of date and time. Simply put, without it, if the system resets or powers down, the date and time is also reset (goes back to epoch

⁶ Aosong(Guangzhou) Electronics Co.,Ltd. Temperature and humidity module. AM2301 Product Manual. www.aosong.com

time⁷). Moreover, the Arduino internal clock is not designed for precision and will drift from actual time as it operates.

In order to keep track of time, a real-time clock (RTC) is used.

The selected component is the RTC DS3231 (see Figure 26) given that it has an integrated temperature-compensated crystal oscillator and crystal. The RTC provides time accuracy even if the APB is powered down, since it is powered by a cell battery.



Figure 26 - RTC DS3231

Its main features are the following⁸:

- Clock accuracy adjusted with an integrated temperature-compensated crystal oscillator (TCXO) and crystal: maintains ± 2 minutes per year accuracy from -40°C to $+85^{\circ}\text{C}$. Despite this compensation, the clock might exhibit an unacceptable time drift unless it is adjusted periodically.
- Energy consumption: 0.2mA in normal operation and $0.11\mu\text{A}$ in sleep mode.
- Can operate with a cell battery.
- Uses the I2C bus digital interface.
- Maintains seconds, minutes, hours, day, date, month, and year information. The date at the end of the month is automatically adjusted for months with fewer than 31 days, including corrections for leap year (valid up to 2100).

⁷ See <https://www.unixtimestamp.com>

⁸ See Maxim Integrated RTC DS3231 available at: <https://www.maximintegrated.com/en/products/analog/real-time-clocks/DS3231.html>

5.2.1.5 Ancillary Component: Persistent Storage

Similarly to the decision of including an RTC, the requirement about long-term deployment for the sensor system requires a persistent storage component to store sensor data.

Micro-SD cards are a possible choice: they support hot-swap (can be plugged-in and removed without the need to shut down the platform), they have high data capacity (several Gygabytes); and they are relatively low cost (<5€ for a 16GB card). SD cards however require a relatively high amount of current to operate: up to 100mA to 200mA in write cycles according to specifications (SD group, 2013); several μ As while in sleep mode. It is noted that energy consumption values greatly vary between SD cards – see (SD group, 2013 and Mallon E. and Beddows P., 2014). Techniques will be used to reduce energy consumption, including minimising access to the SD card (keeping it in sleep mode as much as possible) and optimizing write operations.

For this prototype, a 6-Pin Micro SD Card Module and a 2GB micro-SD card (see Figure 27) is used to implement the persistent storage component.

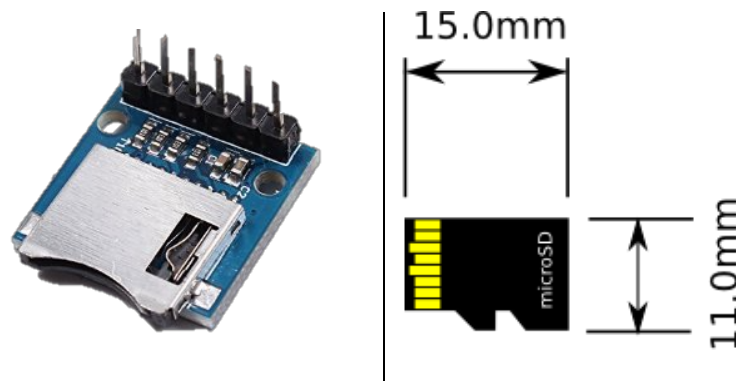


Figure 27 - Micro-SD Module (left) and card (right)

An alternative solution for persistent storage that consumes less energy is dataflash chips: they can store several MBytes and support at least 100k program/erase cycles⁹.

⁹ See Adesto Technologies DataFlash®|Serial Flash Brochure. Available at http://www.adestotech.com/wp-content/uploads/all_DFSF.pdf



Figure 28 - Example of a 8MByte Dataflash Chip

Typical current consumptions are 11mA while in active read/write mode, 25 μ A in standby mode, 3 μ A in deep power down and 0.4 μ A in ultra-deep power down mode¹⁰. A 4MB costs about 5€, however, when compared with SD cards, the price per MB is significantly higher, the capacity is significantly lower and they do not support *hot-swap*.

Therefore, the utilisation of SD cards is recommended, unless the power requirements for the particular deployment cannot be met.

5.2.1.6 Power Supply Component

The requirement on remote long-term operation might result in sensor systems deployed in areas without existing energy infrastructure, thus requiring autonomous energy sources like a battery component. For the designed system, it will be determined the energy consumption requirements and subsequently the required battery energy capacity.

5.2.2 Prototype Overview

The sensor platform integrating components previously described is depicted in Figure 29. The schematics were build using the Fritzing tool¹¹.

¹⁰ See Adesto Technologies. AT45DB321E 32-Mbit DataFlash (with Extra 1-Mbits), 2.3V Minimum SPI Serial Flash Memory. Available at <http://www.adestotech.com/wp-content/uploads/doc8784.pdf>

¹¹ See <http://fritzing.org/>

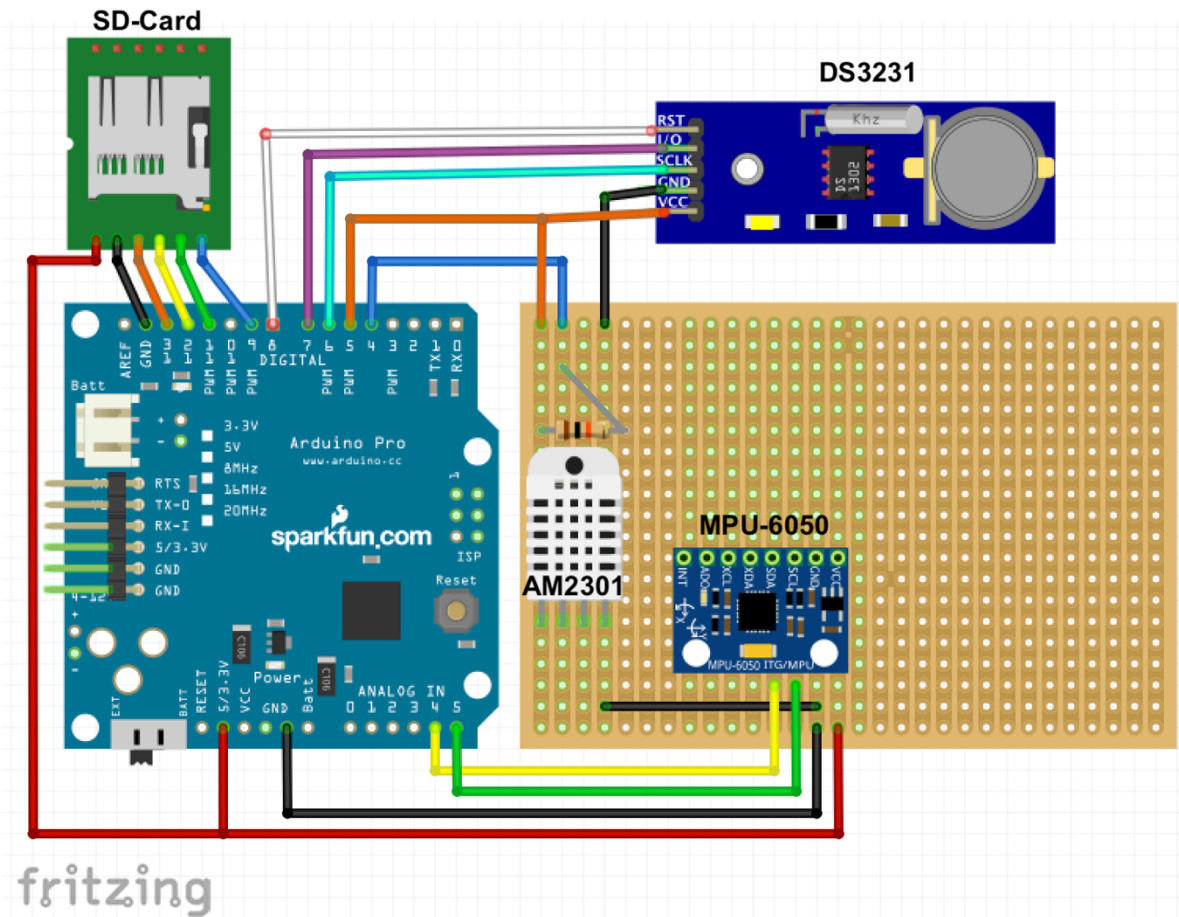


Figure 29 - Prototype 1: Sensor System Interconnections

The interface connections between the devices and the APB are detailed in Table 5.

Table 5 - Prototype 1: Components and Interfaces

Component	Interface	Ports
MPU-6050	I2C	A4 (SDA), A5 (SCL) Note that the module has pull-up resistors required by the I2C.
AM2301	One wire	4 (Data). Note the 10kΩ pull-up resistor required by the interface.
DS3231	Three wire	6 (Clock), 7 (I/O), 8 (Reset)
SD module	SPI	9 (CS), 11 (MOSI), 12 (MISO), 13 (Clock)

In addition, the Arduino digital port 5 is used to power supply and control (switch on and off) the AM2301 and RTC components in order to reduce power consumption. The Arduino digital ports can supply up to 40mA that is sufficient to power these components.

The Arduino is programmed in order to be able to communicate with devices (initialisation, setting up, data extraction and storage), ensure proper sampling time and optimize system power consumption (e.g., change between low-power and normal mode).

The application logic follows the described in section 4.4, having the “Initialisation” and “Main Loop” blocks. Note that the system is not network connected, thus the blocks related with connectivity are not applicable. It is also noted that low-power functions are explored for the Arduino Pro and the MPU-6050 sensor as follows:

- The Arduino operation mode is set to "sleep mode" in between sensor sample collections.
- The MPU-6050 uses its internal FIFO list to store acceleration samples, allowing to lower the Arduino's wake cycle (thus reducing overall energy consumption).

5.2.3 Power Analysis and Optimisation

Several configurations, optimisations and improvements are made in order to reduce the power consumption, as described next. The presented data was measured with the sensor system in operation mode.

APB

The Arduino Pro (version 3.3v at 8MHz) consumes:

- 4.24mA in normal operation mode.
- 0.57mA in sleep mode.

A method used to reduce power consumption is to put the board in sleep mode for as much time as possible, only waking it up when necessary (e.g., read and store sensor data).

In addition, several configurations were performed during initialisation resulting in a few energy savings as described below and presented in Table 6 (note that energy savings were measured during sleep mode operation):

- Disable brown-out, saves 0.01mA.
- Disable ADC, saves 0.09mA
- Put unused general purpose input/output (GPIO) pins in low state mode, saves 0.10mA.

In overall, the energy consumption was reduced in 0.20mA.

Table 6 - Arduino Pro Energy Savings

Arduino Pro, USB 3.3v@8MHz	Operation Mode	Current (mA)	Impact (mA)
Power ON	Normal	4.24	-
Power Save	Sleep	0.57	-3.67
- Brown-out Disable	Sleep	0.56	-0.01
- Turn-off ADC	Sleep	0.48	-0.09
- Pins in LOW state	Sleep	0.47	-0.10
- Power LED removal (*)	Normal	4.07	-0.17

The board also has a power LED that if be removed would result in a saving of 0.170 mA. This modification was not performed in the prototype, thus this aspect of energy saving is an estimated value.

As presented in Table 7, in overall, the estimated energy consumption was reduced in 9% (3.87mA) in normal operation mode and 65% (0.20mA) in sleep mode.

Table 7 - Arduino Pro Energy Overall Savings (estimated)

Operation Mode	Current (mA)	Impact (%)
Normal	3.87	9 %
Sleep	0.20	65 %

Sensor and Ancillary Components

Despite what is reported in the components' specifications, the actual power consumption of the used components is above what is reported in the datasheet since they come in PCBs that contain additional electrical components like LEDs and voltage converters that consume additional energy.

Additional hardware modifications could be used, as shown in Figure 30¹², specifically the removal of two LEDs and no dissipation from unnecessary resistors, which could result in a reduction of about 0.3mA. Note that these were not performed in the implemented prototype.

¹² Source: online articles (1) <https://bengoncalves.wordpress.com/2015/10/02/arduino-power-down-mode-with-accelerometer-compass-and-pressure-sensor/> (2) <https://www.raspberrypi-spy.co.uk/2015/05/adding-a-ds3231-real-time-clock-to-the-raspberry-pi/>

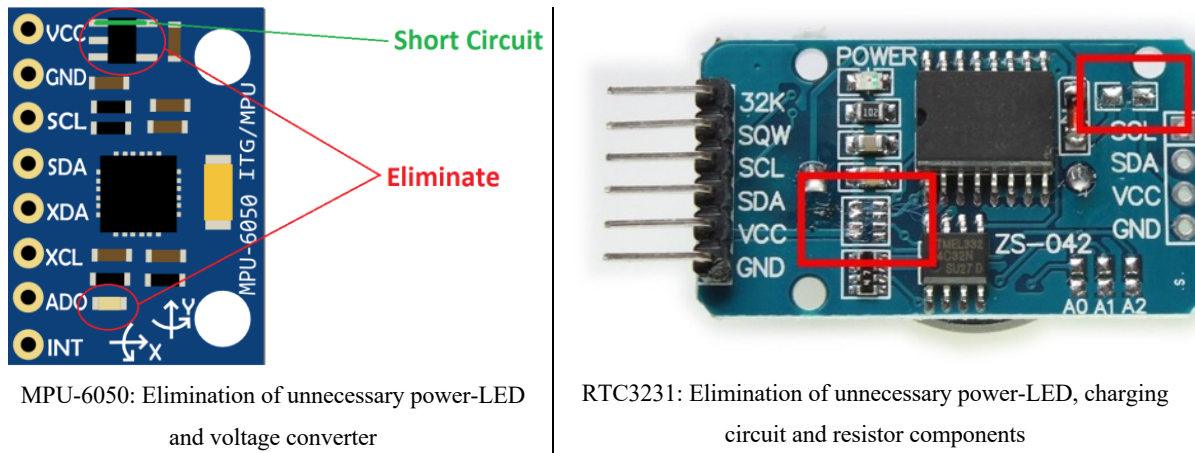


Figure 30 - MPU-6050 and RTC DS3231 Hardware Modifications to Reduce Energy Consumption

Finally, the most energy savvy component is the SD card, especially when performing write operations. Specifications vary between manufacturers and models, including the implemented power saving methods, making selection and analysis difficult. The prototype reduces the number of SD card operations, but a significant impact in energy consumption is expected.

Next, actual energy measurements related with the sensor prototype are presented and analysed.

Energy Measurements

As previously described, the prototype operates in two main modes:

- **Normal operation**, where the APC is active (read and store sensors data) and all components are active.
- **Low power operation**, where the APC is in sleep mode and the power supply to some components is disabled (namely, the RTC and the AM2301).

The MPU-6050 is set to operate in low power but continuous mode (3-axis acceleration measurements with a specific sample rate), taking advantage of its internal FIFO list. The SD card has its own power management functions (not controlled by the ACP).

The power consumption analysis is based on the amount of electrical current used by the APC. An oscilloscope is used to measure the current.

For this experiment, two different configurations are analysed:

- **CONFIGURATION 1**: the MPU-6050 frequency is set to 100Hz.
- **CONFIGURATION 2**: the MPU-6050 frequency is set to 5Hz.

The parameter with most influence on the overall energy consumption is the MPU-6050 sampling rate: it determines the wake-sleep cycles of the APC and sets the amount of necessary SD card write operations. The higher the sampling rate, the higher the wake cycle and SD card write operations.

The measured electrical current is presented in Figure 31. The measurements refer to 1 wake-sleep cycle operation.

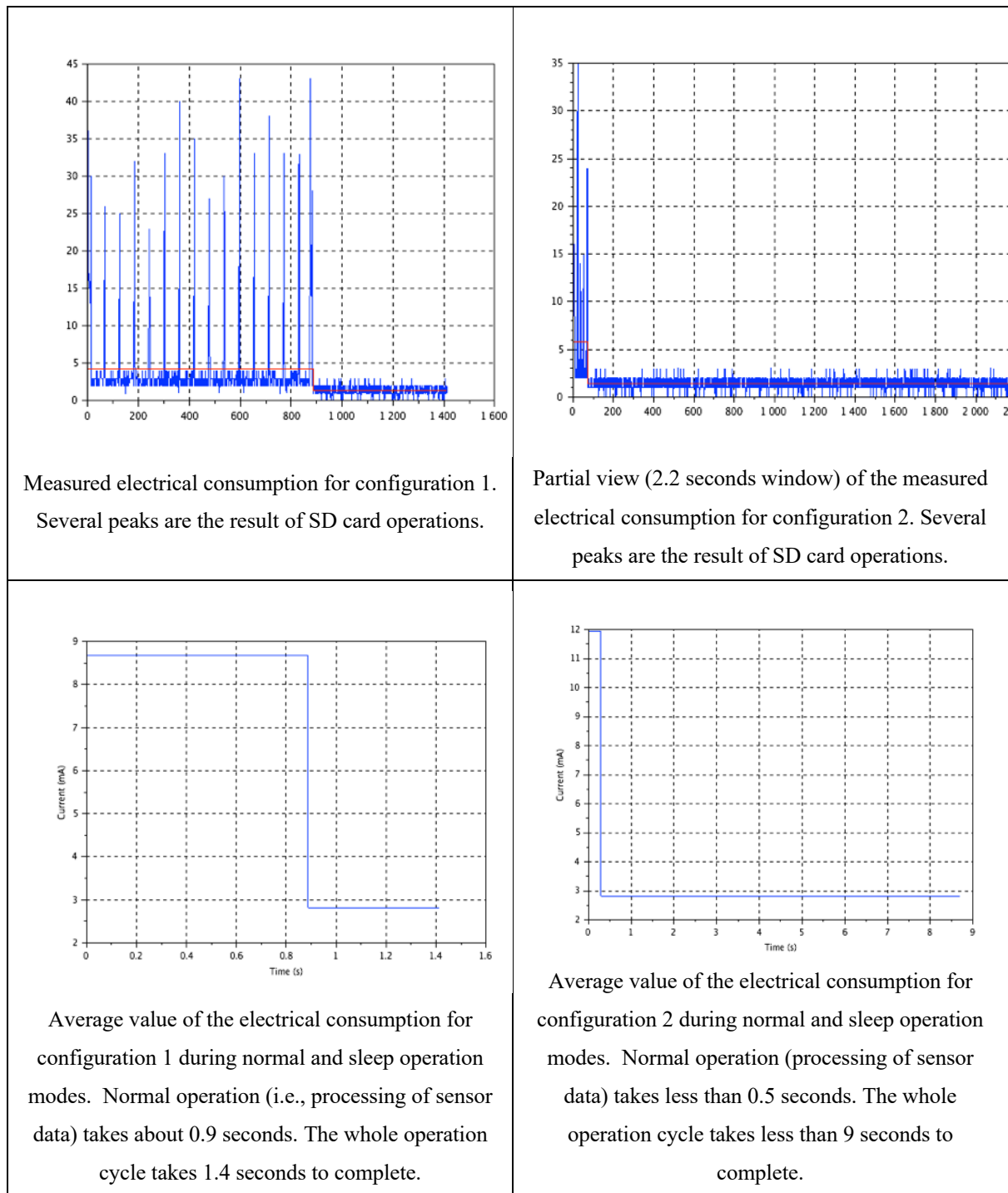


Figure 31 - Prototype 1: Measured Electrical Current for two configurations

In order to calculate the average current consumption $I_{average}$ for the platform the following formula is used:

$$I_{average} = \frac{I_{wake_mode} \times time_{wake_mode} + I_{sleep_mode} \times time_{sleep_mode}}{time_{wake_mode} + time_{sleep_mode}} \text{ (units A)} \quad (5.1)$$

Where:

- I_{wake_mode} is the current value while in wake mode.
- $time_{wake_mode}$ is the amount of time (in seconds) while in wake mode.
- I_{sleep_mode} is the current value while in sleep mode.
- $time_{sleep_mode}$ is the amount of time (in seconds) while in sleep mode.

The power consumption results are presented in Table 8 and Table 9 for CONFIGURATION 1 and CONFIGURATION 2, respectively. Note that the prototype uses a supply voltage of 3.3v.

Table 8 - Prototype 1 Configuration 1 Power Consumption Results

@100Hz	mA	mW	time (ms)
ACTIVE	8.68	28.64	900
SLEEP	2.82	9.31	500
AVERAGE/TOTAL	6.59	21.74	1400

Table 9 - Prototype 1 Configuration 2 Power Consumption Results

@5Hz	mA	mW	time (ms)
ACTIVE	11.90	39.27	300
SLEEP	2.82	9.31	8000
AVERAGE/TOTAL	3.15	10.39	8300

CONFIGURATION 1 is active for most of the cycle time (0.9s representing 64.3% of the cycle) at 28.64mW and sleeping for 0.5s (35.7% of the cycle), resulting in a total 21.74mW power consumption.

CONFIGURATION 2 is active for a small part of the cycle (0.3s representing 3.6% of the cycle) at 39.27mW and sleeping for 8s (96.4% of the cycle), resulting in a total 10.39mW power consumption.

If using a battery with 10Ah capacity, prototype 1 operating in CONFIGURATION 1 would function for more than 2 months and prototype 1 operating in CONFIGURATION 2 would function for more than 4 months. If additional optimisations would be performed (e.g., remove unnecessary components and replace the SD Card with a Dataflash Chip), the operating time could be further extended.

5.2.4 Cost Analysis

The price in Euros for the platform is below 25€, as detailed in Table 10. Note that prices were obtained in the year of 2016. The Arduino Pro and the micro-SD card represent 36% and 20% of the total platform cost, respectively. Note that this version uses a DC transformer to supply power to the platform.

Table 10 - Prototype 1: Platform cost (in Euros)

Component	€	Supplier
Arduino Pro Mini 3.3v	9.08	Sparkfun Electronics
MPU-6050	2.50	Amazon Spain
AM2301	2.58	eBay
RTC DS1302	1.29	eBay
Micro SD module	0.65	eBay
Micro SD card	5.00	Retail store
DC 4.3v Transformer	3.00	Retail store
CR2032 battery cell	0.30	IKEA (bulk of ten, unit cost)
Misc (resistors, wires, ...)	0.50	eBay
TOTAL	24.91	

5.3 Prototype 2: Network-enabled low-cost seismic sensor system

This section is based on the presentation Low-Power Low-Cost Sensor Platform for Seismic and Environmental Monitoring by (Manso et al., 2016)

The first prototype achieved the requirements on sensor data storage and low-power, however the lack of connectivity limits access to data to offline mode, which discards real-time applications.

The second sensor implementation targets a sensor system for seismological applications that is designed to operate in "live" mode. It shall comply with the following requirements:

- Capability to collect seismic activity (i.e., ground acceleration).
- Network-Enabled capability, allowing to connect to IP-networks and stream sensor data.
- Low-cost system (less than 25€).

It is noted that this implementation does not target a low power system.

Next, the selection of the architecture components is presented.

5.3.1 Components

Following the general design presented in section 4, the components constituting the sensor system are the following: Acquisition and Processing Board, Storage, Networking, Sensor, Real-Time Clock (RTC) and Power Supply. The chosen components are presented in Table 11.

Table 11 - Prototype 2: Architecture Components

Component	Architecture Component
ESP8266	Acquisition and Processing Board (32-bit processor at 80MHz); Storage (internal flash, between 512KiB and 16MiB); Networking (integrated TCP/IP protocol stack, Wi-Fi)
MPU-6050 (see section 3) or LIS3DHH (see section 3) or ADXL355 (see section 3)	MEMS Accelerometer
Internal clock synchronised with NTP	Real-Time Clock
3.3v Power Supply Board	Power Supply
I2C Bus	Data Interface (connecting the ESP8266 to the MPU-6050)

For the APB, the ESP8266 (more specifically, the NodeMCU that uses the ESP8266 related ESP-12E model) is selected because it provides: a fast and programmable microcontroller (operates at 80 or 160 MHz); Storage capabilities (embedded flash up to 4MiB); Networking capabilities (via its embedded Wi-Fi chip). RTC time synchronisation is achieved by means of Network Time Protocol (provided by a NTP server). NTP can keep time accuracy of all machines within the same subnet within one millisecond (NTP, 2003). Nonetheless, if additional time precision is required, a GNSS receiver can be added (GNSS can provide time accuracy of 0.1 ms^{13}).

The ESP8266 also supports a wide range of libraries, in large part provided by the Arduino community.

Concerning the accelerometer, three options are used: MPU-6050, LIS3DHH and ADXL355 (see section 3). A performance evaluation is performed later in this section.

5.3.2 Prototype Overview

The sensor system overview, including components' interconnections, are presented in Figure 32. The pin connections between the components are presented in Table 12. Note that the depicted accelerometer is the MPU-6050. The data interface used is the I2C Digital Interface.

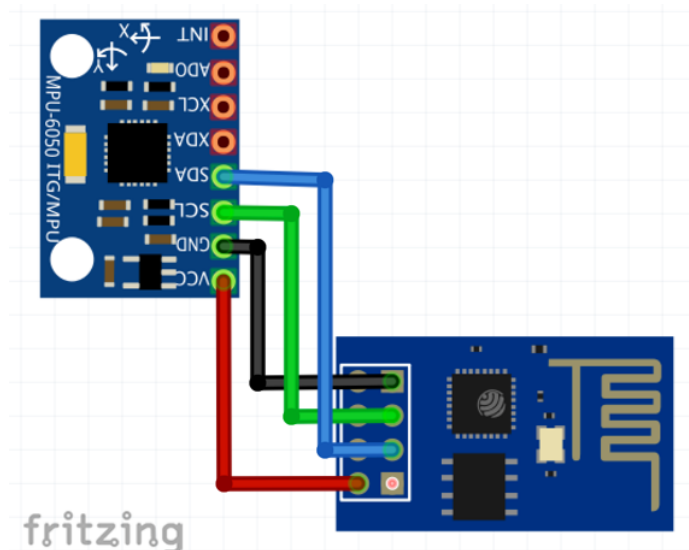


Figure 32 - Prototype 2: Sensor System Interconnections

¹³ See <https://www.atomic-clock.galleon.eu.com/support/ntp-time-server-accuracy.html>

Table 12 - Prototype 2: Interfaces

Interface	ESP Pin	MPU Pin
I ² C SDA	Pin 0	SDA
I ² C SCL	Pin 2	SCL

Comparing with the previous one, prototype 2 is greatly simplified, benefitting from having a small APB embedding several components. Furthermore, being network-enabled, it allows using NTP for time synchronisation and decreases the storage requirements (only needs to temporarily store measurements in case of loss of connectivity).

The application logic follows the one described in section 4.4, having the “Initialisation” and “Main Loop” blocks. Note that this prototype is designed to be network enabled, thus the main aim of the local storage is to prevent data loss by keeping sensor measurements while the network connectivity is not available. Long-term sensor data storage should be done by a server component (described in section 6).

5.3.3 Power Analysis

Prototype 2 is designed to rely in existing network and power infrastructure. In this regard, the design does not seek power consumption optimisation. Nonetheless, an analysis of the power requirements to operate is presented, which may be useful in case the system needs to be temporarily battery operated.

Analysing the ESP8266 specifications¹⁴, the power requirements in normal operation mode (i.e., active mode) vary between 56 mA and 170 mA, being significantly higher than prototype 1 (see Table 6). This is mostly caused because of the energy requirements of wireless communications (Wi-Fi mode).

A few methods could be applied to reduce overall power consumption as follows¹⁵:

- Put ESP8266 in light-sleep (0.9 mA consumption) or deep-sleep mode (0.010 mA consumption) whenever possible (e.g., in between sensor measurements).

¹⁴ See https://www.espressif.com/sites/default/files/documentation/0a-esp8266ex_datasheet_en.pdf

¹⁵ See <https://www.instructables.com/id/ESP8266-Pro-Tips/>

- Consider that "waking up" causes a network reconnection, which can take about 3 seconds. The reconnection time can be reduced if static IP address is used. Nonetheless, overall calculations should be made to assess the feasibility to cope with timeouts.
- Disabling Wi-Fi when not necessary: right before going to sleep and at the start of the "waking up" operation.

5.3.4 Cost Analysis

The price in Euros for the platform using the MPU-6050 is close to 10€, however a power-bank is added to ensure continuity of operations in case of power failure. The overall cost is therefore 15.50 € as detailed in Table 13.

Table 13 - Prototype 2: Platform cost (in Euros)

Component	€	Supplier
ESP8266 (NodeMCU board)	5	Amazon Spain
MPU-6050	2.50	Amazon Spain
DC 5v Transformer	3.00	Retail store
Power Bank (5Ah)	5	Amazon Spain
TOTAL	15.50	

Note that the ADXL355 cost is above 30€. Thus, selecting this component greatly increases the overall system cost.

5.4 Prototype 3: Smartphone-based network-enabled seismic sensor system

Mobile phones have a ubiquitous presence in the developed world. The International Telecommunication Union (ITU) reports over 105 mobile subscriptions per 100 habitants (ITU, 2020). Statista estimates that the total number of smartphone users in 2020 will reach 3.5 billions¹⁶. Smartphones, in particular, incorporate several technologies (e.g., fast processing, local display, local storage, communications, cameras, gyroscopes, compass,

¹⁶ See <https://www.statista.com/statistics/330695/number-of-smartphone-users-worldwide/>

accelerometers, battery power), having evolved to become multi-purpose devices. Given their wide reach and flexibility, their utilisation for purposes of seismology has been explored. The application of smartphones in seismology was mentioned in section 2.3 specifically in QCN, CSN and MyShake. Despite its limitations and privacy concerns, smartphones allowed detecting and locating strong-motion earthquakes ($>M3$).

Mobile phones are also a convenient channel to inform and alert citizens concerning earthquake activity. This feature is used, for example, by MyShake (Allen, Kong and Martin-Short, 2019) and CSEM's LastQuake¹⁷. See Figure 33 for screenshots.

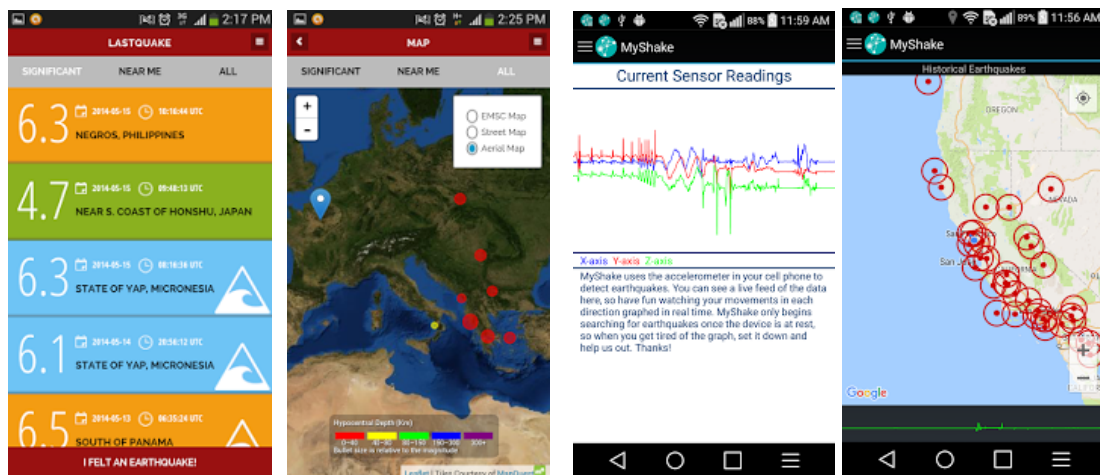


Figure 33 - CSEM LastQuake App (2 images at the left) and MyShake App (2 images at the right)

Prototype 3 exploits the capabilities of a smartphone to develop an integrated platform (i.e., accelerometer, CPU, local storage, display and UI, battery, communications) capable to collect acceleration data and transmit it via a network. The prototype also uses the phone screen to convey information to the user. See Figure 34 for snapshots of the App for prototype 3.

¹⁷ See <https://www.emsc-csem.org/service/application/>

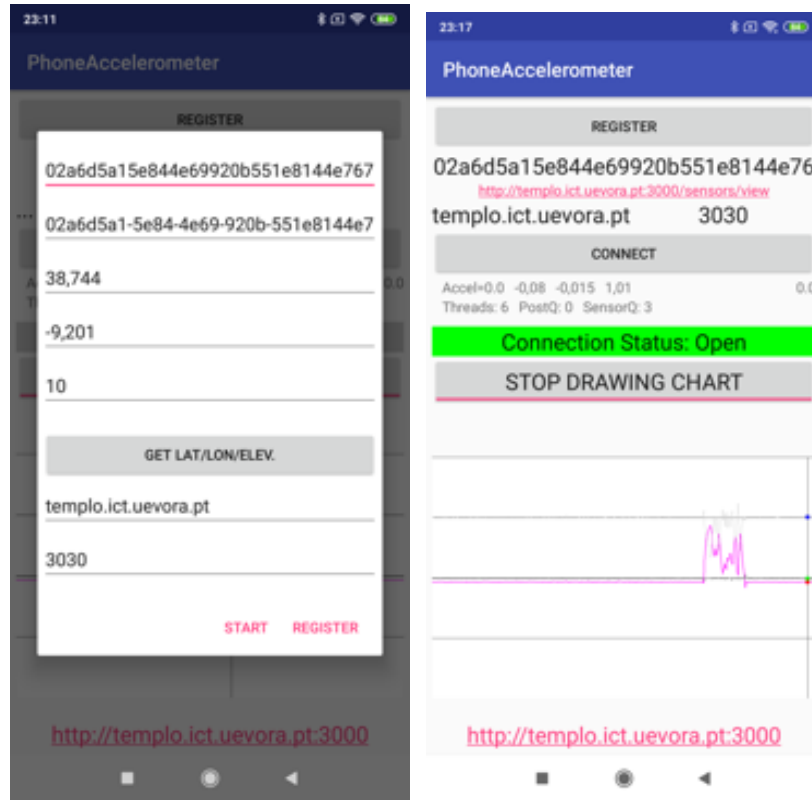


Figure 34 - Prototype 3: Mobile Phone App to record and transmit acceleration measurements. The figure at the right shows an acceleration change clicking the phone screen.

Evans *et al.* (2014) analysed the performance of several smartphone accelerometers, noting most are unacceptable per general ANSS guidance, however also pointing that *analog instruments of significantly lower resolution were used for some decades and produced much useful information*. Smartphone accelerometers may find useful applications, such as generating reliable pictures of regional seismicity and strong shaking and generations of earthquake-safety building codes.

5.5 Prototype 4: Emulated Sensor (testing purposes)

For purposes of testing the capabilities of the overall system, a prototype of a sensor emulator is developed. The prototype is network-enabled and streams (1) random data or (2) periodic data following a sinus function. The user can set parameters such as: frequency, range and amount of variability (i.e., scale to apply in random number, in %) in case of random data. The emulated prototype mimics the operation of a real sensor system. It runs on a command line (see Figure 35), allowing to easily deploy a high number of instances for testing purposes (see section 6).

```
#####
Sensor is "Test sensor phone006" (sensor_key= sensor_phone0006 )
-- variability amount: 0.5
-- frequency: 100.0
-- range: 2g (scale is 1 )

    1 - Register (new) Sensor
    2 - Update Sensor
    3 - Delete Sensor

    5 - Start RANDOM STREAMING (will loop forever)
    6 - Start SIN STREAMING (will loop forever)

    0 - QUIT

Option>6
Connect to: ws://193.137.179.141:3030/sensor_phone0006
f=83(Hz) -----*-----|-----*-----|-----*-----█
```

Figure 35 - Prototype 4: Emulated Sensor System

The generated data as received by a sensor portal is shown in Figure 36.

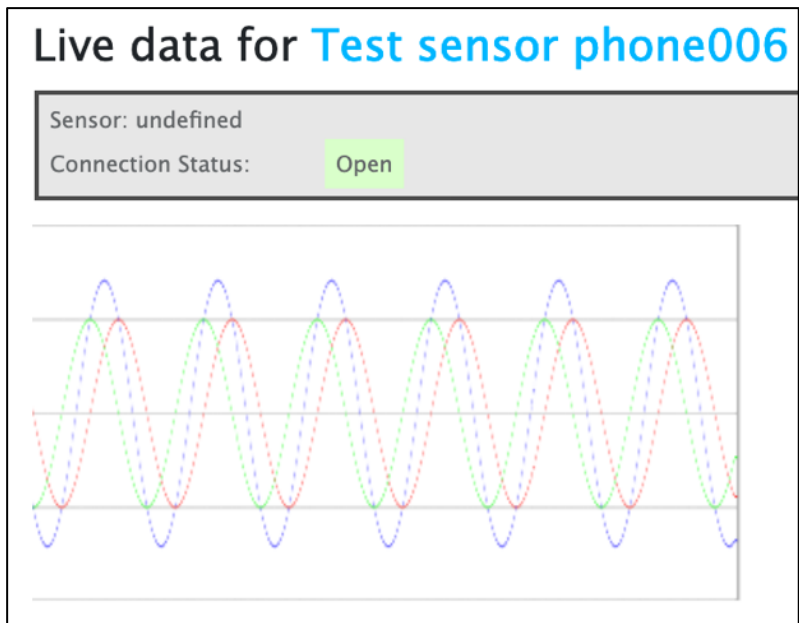


Figure 36 - Prototype 4: Generated Periodic Data from Emulated Sensor System

5.6 Noise Performance Comparison

This section is based on the paper On-Site Sensor Noise Evaluation and Detectability in Low Cost Accelerometers presented at SENSORNETS 2021 by (Manso and Bezzeghoud, 2021)

Section 3 presented an overview of MEMS accelerometers, describing their application for seismology, also mentioning as a main limitation the presence of sensor noise that is originated

from the sensor's electrical and mechanical components. In this subsection, an indication of sensor noise is measured by deploying and collecting acceleration data from several accelerometers (used in prototypes described earlier in this section) while at rest position. The sensor noise assessment is made by calculating the standard deviation of the signal (calculated using a “moving window” of 100 samples). The lower the standard deviation, the lower the sensor noise.

The standard deviation is calculated using the well know formula 5.2:

$$\sigma = \sqrt{\sum \frac{(x_i - \mu)^2}{N}} \quad (5.2)$$

Where:

i is the sample number,

x_i is the measurement related with sample i ,

μ is the mean value and

N is the sample size.

The environment where accelerometers are installed might be affected by external factors (e.g., traffic or seismic activity), which can be registered by accelerometers and should be excluded from the sensor noise analysis. In order to exclude these “signals” from “noise”, a threshold logic is defined and implemented as follows:

```

let  $\sigma(n)$  be the standard deviation related with sample window n
let  $\sigma_{min}$  be the registered minimum standard deviation for the running period

if (  $\sigma(n) > \sigma_{min} . Threshold$  ) then
    is signal
else
    is noise
endif

```

The first part of the analysis uses dedicated accelerometers operating at different bandwidth, while the second part compares the sensor noise in dedicated accelerometers and consumer smartphones. Note that this analysis assumes a “quiet” environment, thus the presence of background environmental noise is not taken into account.

5.6.1 Sensor Self-Noise in Dedicated Accelerometers

An indication of sensor noise is measured in two dedicated accelerometers, namely:

- **Analog ADXL355**, a 3-axis digital sensor with 20-bit resolution, noise density of $25\mu\text{g}/\sqrt{\text{Hz}}$. (source: <https://analog.com>).
- **Invensense MPU-6050** with 16-bit resolution, noise density of $400\mu\text{g}/\sqrt{\text{Hz}}$. (source: <https://www.invensense.com>).

Based on the specifications, the ADXL355 sensor noise is substantially lower (16x less) than the MPU-6050. Moreover, sensors are setup to work at different bandwidth in order to observe its effect in sensor noise.

The results are presented next.

5.6.1.1 ADXL355 Measurements

The ADXL355 is setup to operate in three different sampling rates: 15Hz, 100Hz and 1KHz. The measured magnitude¹⁸ acceleration values subtracted by the average (in g) are presented in Figure 37. As it can be seen, the magnitude of the acceleration increases with the sampling rate.

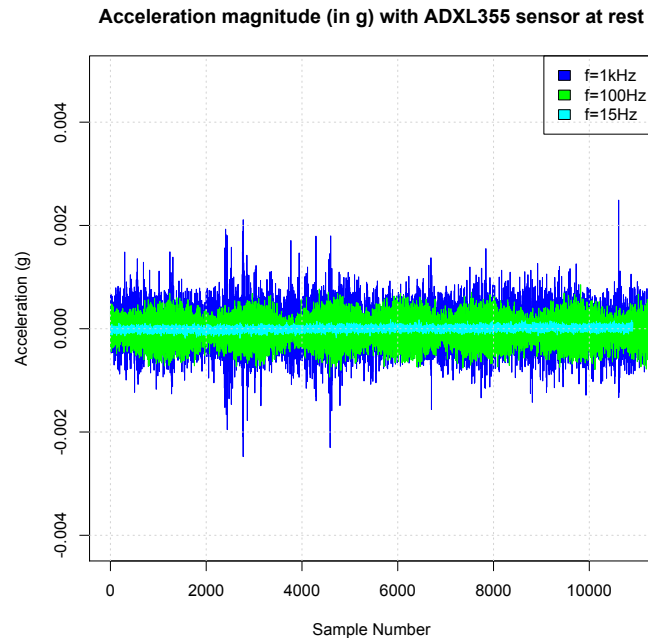


Figure 37 - ADXL355 Measured Acceleration Magnitude for different sampling rates. The figure shows signal amplitude peaks varying with the sampling rate.

¹⁸ The acceleration magnitude is the length of the acceleration vector, calculated from the three-axis acceleration values.

In order to measure the variation of sensor measurements around the mean value, the standard deviation is used. The measured standard deviation for ADXL-355 is presented in Figure 38 and Table 14. Two types are considered for analysis: σ_{min} that represents the “sample window” with lowest sensor noise, and σ_{mean} that provides an indication of the average value of all included σ .

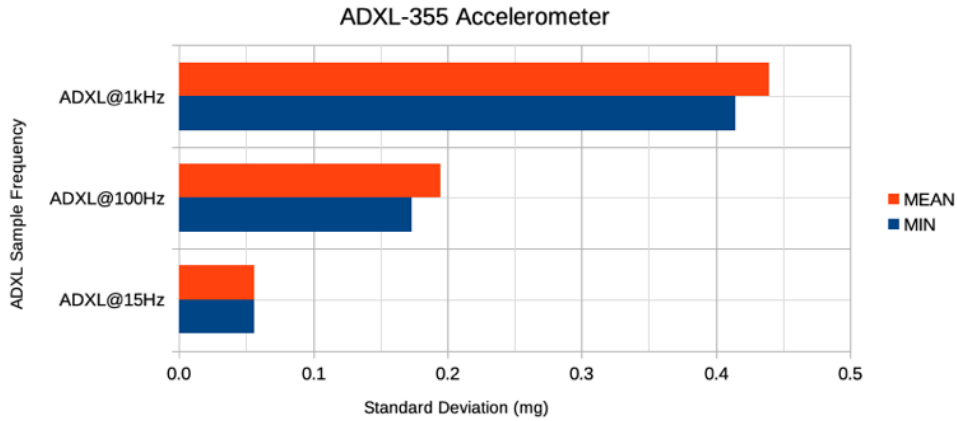


Figure 38 - ADXL355 Measured Standard Deviation for different sampling rates. Higher values indicate a higher sensor self-noise than for lower values.

Table 14 - ADXL355 Measured Standard Deviation: minimum recorded value, mean value and delta value (difference between mean and minimum value).

ADXL355	σ_{MIN} (mg)	σ_{MEAN} (mg)	Δ (mg)
1000 Hz	0.4143	0.4394	0.0252
100 Hz	0.1734	0.1950	0.0217
15 Hz	0.0555	0.0563	0.0008

As expected, increasing the sample frequency increases sensor noise, resulting in higher dispersion in measurements and thus in a higher standard deviation. The lowest standard deviation value (0.0555mg) was recorded at 15Hz (the lowest sample frequency used) and the highest standard deviation value (0.4143 mg) was recorded at 1KHz. This trend is also present in the difference (Δ) between σ_{mean} and σ_{min} .

5.6.1.2 MPU-6050 Measurements

The MPU-6050 is setup to operate in three different sampling rates: 5Hz, 10Hz and 100Hz. The measured magnitude acceleration values subtracted by the average (in g) are presented in Figure 39. Once again, the magnitude of the acceleration increases with the sampling rate.

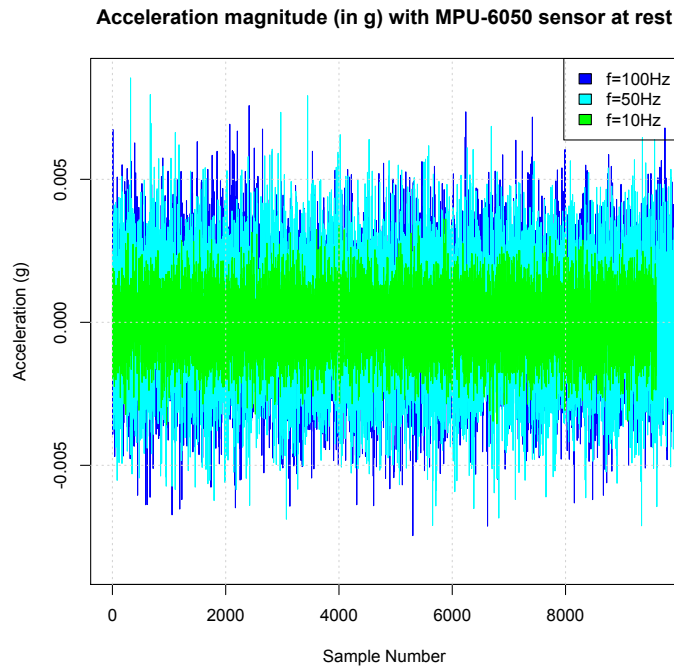


Figure 39 - MPU-6050 Measured Acceleration Magnitude for different sampling rates

The measured standard deviation for MPU-6050 is presented in Figure 40 and Table 15. As previously, the analysis considers σ_{min} and σ_{mean} .

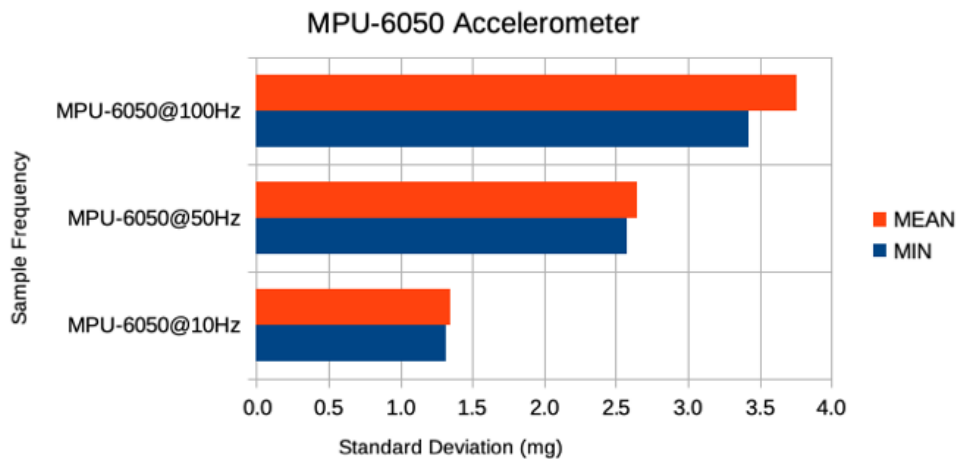


Figure 40 - MPU-6050 Measured Standard Deviation for different sampling rates

Table 15 - MPU-6050 Measured Standard Deviation: minimum recorded value and mean value.

MPU-6050	σ_{MIN} (mg)	σ_{MEAN} (mg)	Δ (mg)
100 Hz	3.4253	3.7606	0.3354
50 Hz	2.5713	2.6515	0.0802
10 Hz	1.3122	1.3472	0.0350

Again, sensor noise increases with the sample frequency: the lowest standard deviation value (1.3122 mg) was recorded at 10Hz (the lowest sample frequency used) and the highest standard deviation value (3.4253 mg) was recorded at 100Hz. This trend is also present in the difference between σ_{mean} and σ_{min} . Moreover, the standard deviation value can also be used to compare sensor noise between different accelerometers: Table 14 and Table 15 show that, at a sampling rates of 100Hz, the MPU-6050 standard deviation value is higher (about 20x higher) than ADXL-355, as expected from their respective datasheets.

A comparison between different accelerometers sensor noise is given next.

5.6.1.3 Sensor Noise in Smartphones and Dedicated Sensors

An indication of sensor noise is measured for different accelerometers, including those present in consumer smartphones, operating at the same sampling rate (100Hz) for purposes of comparing the associated sensor noise. The following devices were analysed:

- A TCL mobile phone.
- A Xiaomi mobile phone.
- A CAT mobile phone.
- Invensense MPU-6050 (used in section 5.5.1.1).
- ST LIS3DHH dedicated accelerometer.
- Analog ADXL-355 (used in section 5.5.1.2).

The results are presented next.

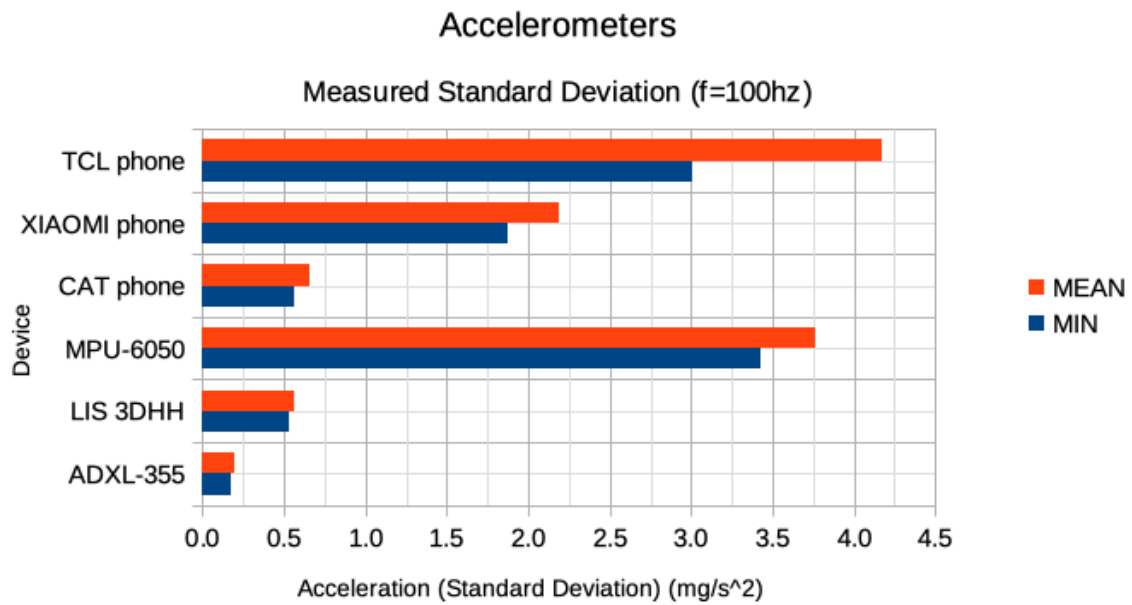


Figure 41 - Measured Standard Deviation for several accelerometers operating at a sampling rate of 100Hz

Table 16 - Measured Standard Deviation for several devices: minimum recorded value and mean value.

Accelerometers	σ_{MIN} (mg)	σ_{MEAN} (mg)
TCL phone	3.0115	4.1707
XIAOMI phone	1.8716	2.1893
CAT phone	0.5595	0.6563
MPU-6050	3.4253	3.7606
LIS 3DHH	0.5270	0.5634
ADXL-355	0.1734	0.1950

The developed method yields an indication of sensor noise, which is sensor specific. As shown in Figure 41 and Table 16, the dedicated accelerometer ADXL-355 yields the lowest minimum standard deviation (0.1734 mg), followed by the LIS 3DHH (0.5270 mg), the CAT phone (0.5595 mg). The TCL phone and the MPU-6050 yield the highest values, with 3.0115 mg and 3.4253 mg, respectively. It is also pertinent to note the disparity between the mean and the minimum value of standard deviation for the TCL phone, indicating that the minimum value for standard deviation alone is not sufficiently robust to assess sensor noise in actual deployments.

The presented analysis of sensor noise observed in different types of accelerometers, successfully developing a method to measure noise on-site and in-operation. The method produces an indication of sensor noise based on the measured standard deviation. It yields results consistent with sensors specifications (i.e., ADXL-355, LIS 3DHH and MPU-6050) or, when not available, with the observations. Importantly, the method adapts to the sensor’s characteristics (e.g., sensor noise), allowing to identify the occurrence of relevant events (i.e., presence of signal), without necessarily knowing *a priori* the sensor specification (noise is calculated with the sensor in-operation). In addition, this method also adapts to changing circumstances, such as “noise” alterations caused by subtle changes in sensor characteristics (resulting from e.g., small displacements or temperature change). When considering a high-density deployment, logistic and maintenance aspects can represent serious bottlenecks, unless the system supports adaptive capabilities, as those here described.

5.7 Detectability

This section is based on papers High-density seismic network for monitoring Alentejo region (Portugal) and Mitidja basin region (Algeria) by (Manso et al., 2020) and On-Site Sensor Noise Evaluation and Detectability in Low Cost Accelerometers presented at SENSORNETS 2021 by (Manso and Bezzeghoud, 2021)

A key aspect in using accelerometers for seismic purposes is determining their sensitivity to detect and measure seismic events, which can have different magnitudes. Introduced in Manso et. al (2020) and further explored in Manso and Bezzeghoud (2021), herein it is presented in equation (5.3) an estimation of the detectability threshold (*DetecT*) of accelerometers, considering their self-noise level, as measured in 5.6, multiplied by *C*, a constant that is used to increase the assurance that measurements are above noise level:

$$DetecT = \sigma_{accelerometer} \cdot C \quad (5.3)$$

C is arbitrary and should be chosen taking into account the probability of classifying false positives or false negatives in the observed signal.

The sensor self-noise is assumed as white-noise (i.e., random signal with equal intensity at different frequencies, thus exhibiting constant power spectral density) outputting

measurements following a normal distribution, where the average is its maximum value. Based on the recorded standard deviation, the probability of a given measurement to be signal (and not noise) can be determined, for example using the normal distribution. Future work could address the application of this method to detect seismic events, comparing it to more traditional techniques like Short Time Average (STA) over Long Time Average (LTA).

Considering a typical Ground Motion Prediction Equation (GMPE) - proposed by Atkinson (2015) - and the resulting Peak Ground Acceleration (PGA), the accelerometers detectability threshold, depending on the earthquake magnitude and epicentral distance, is presented in Figure 42 when using $C=5$ in (5.3).

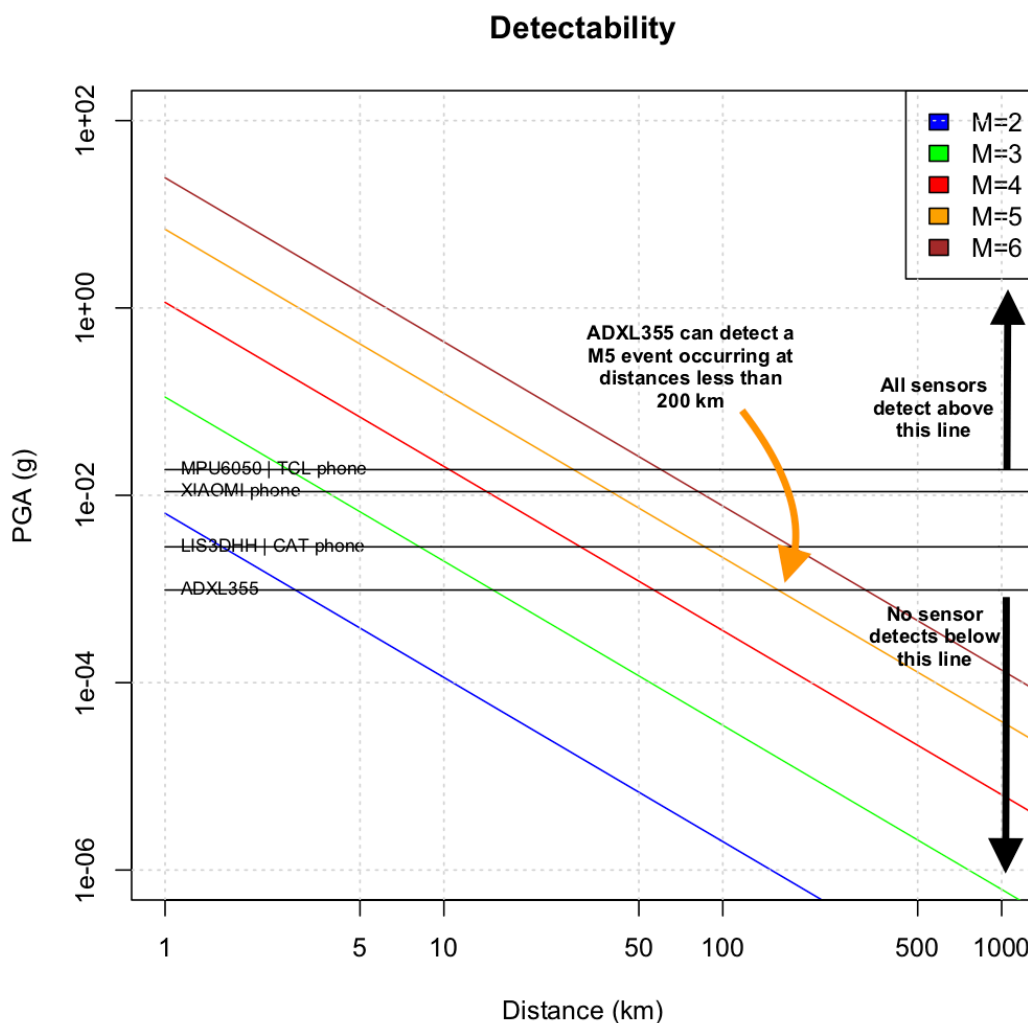


Figure 42 - Accelerometers detectability threshold for accelerometers, depending on the earthquake magnitude and epicentral distance. Only events with PGA (in g) above each black line can be detected by the respective sensor. For example, an M5 event represented by the orange line could be detected by ADXL355 at distances below 200 km, while a LIS3DHH would only detected at distances below 100 km.

The formula to calculate the PGA as a function of magnitude (M) and event distance (R)¹⁹ is from Atkinson (2015) and is presented in (5.4).

$$\log_{10} PGA_{m/s^2} = (c_0 + c_1 \times M + c_2 \times M^2 + c_3 \times \log_{10} R) \quad (5.4)$$

Coefficients c are selected for PGA, as follows:

- $c_0 = -2.378$
- $c_1 = 1.818$
- $c_2 = -0.1153$
- $c_3 = -1.752$

The ADLX-355 is the sensor with the lowest *DetecT*, being capable to detect earthquakes with $M=3$ and $M=5$ at a distance larger than 10 km and 100 km, respectively. Both the MPU-6050 and TCL phone exhibit similar performance and should be able to detect earthquakes with $M=3$ and $M=5$ at a distance of about 2 km and 20 km, respectively.

The ADXL-355 accelerometer exhibited the best performance based on the measured sensor noise, thus further analysis is presented. ADXL-355 detectability threshold changes with the chosen sampling rate, as illustrated in Figure 43.

¹⁹ R is an effective point-source distance that includes near-source distance-saturation effects using an effective depth parameter (Atkinson, 2015)

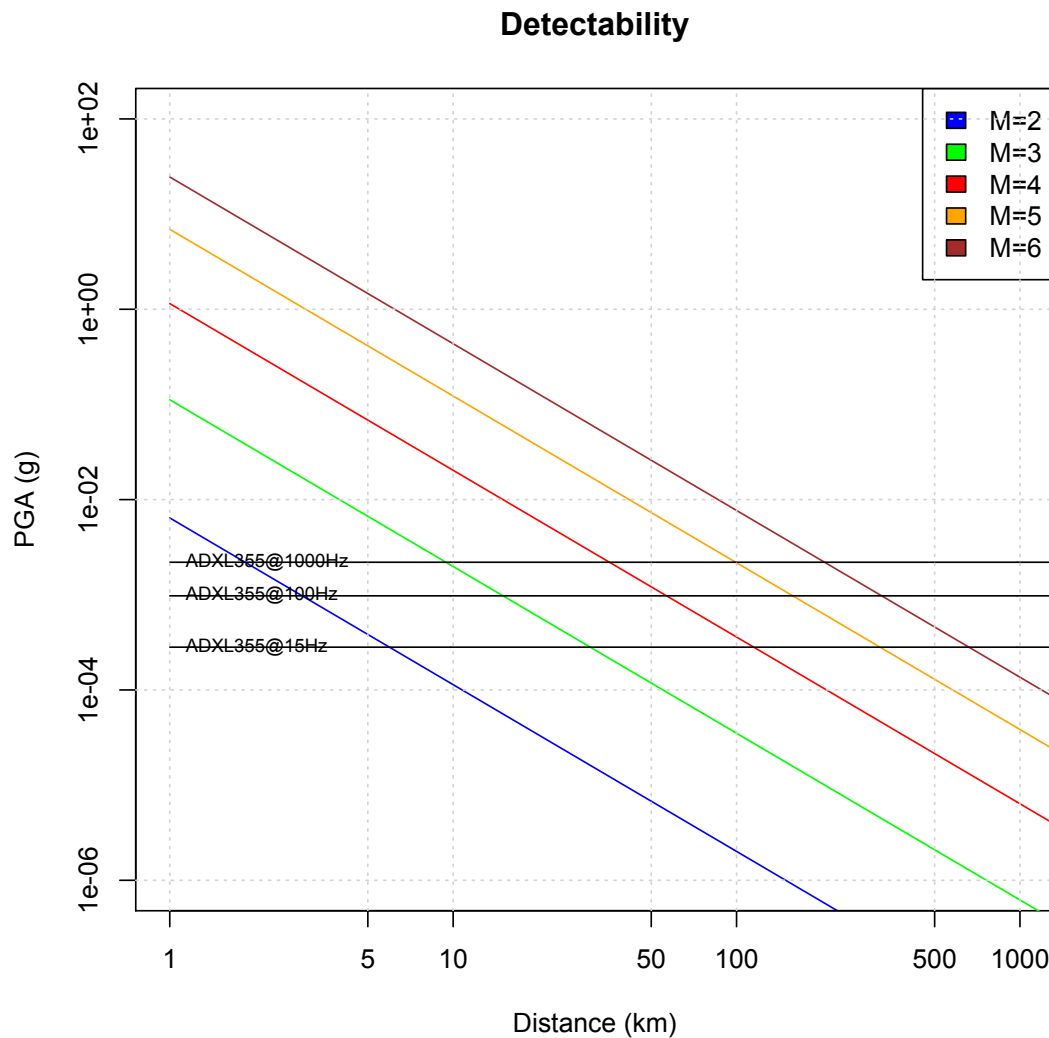


Figure 43 - ADXL-355 accelerometer detectability threshold when using different sampling rates, depending on the earthquake magnitude and epicentral distance. A M5 event could be detected by ADXL operating at 15Hz, 100Hz and 1kHz at distances below 500 km, 200 km and 100 km, respectively.

For a M=3 event, the ADXL-355 would be able to detect it at a distance of about 30 Km if operating at a 15Hz frequency, or about 10 Km if operating at a 1000Hz frequency.

For a M=5 event, the ADXL-355 at 15Hz would be able to detect it at a distance of about 300 Km.

While these findings suggest that lowering sampling rate might benefit detectability, it should be considered that the selection of sampling rate depends on the observed signal characteristics. For example, seismic events occurring at short distances might exhibit a strong presence of high frequencies (above 15 Hz) that will be missed by sensors operating at low sampling rates. As such, a careful trade-off analysis should be made when choosing a sensor sampling rate.

These findings are preliminary and a more thorough analysis, including comparing results with a seismological reference station, is conducted in section 7.

5.8 Conclusion

This section described the work in the realisation of four sensor system prototypes, following the general design of section 4. The prototypes addressed different objectives, as follows:

- Prototype of a low-cost low-power multi-purpose sensor system capable to operate autonomously, targeting deployments over long periods of time (order of months).
- Prototype of a low-cost network-enabled seismic sensor system.
- Prototype of a network-enabled seismic sensor application running on mobile phones.
- Prototype of an emulated seismic sensor for testing purposes.

In the context of high-density networks, a network-enabled capability is fundamental for “live” data and near real-time operations. As such, the network-enabled seismic sensor system and the mobile phones running the seismic sensor application are analysed further.

A method to measure noise on-site and in-operation was defined to produce an indication of sensor noise, based on the measured standard deviation, without necessarily knowing *a priori* the sensor specification (noise is calculated with the sensor in-operation). Importantly, the method adapts to the sensor’s characteristics (e.g., sensor noise), allowing to identify the occurrence of relevant events (i.e., presence of signal). In addition, this method also adapts to changing circumstances, such as “noise” alterations caused by subtle changes in sensor characteristics (resulting from e.g., small displacements or temperature change). When considering a high-density deployment, logistic and maintenance aspects can represent serious bottlenecks unless the system supports adaptive capabilities, as those here described.

The method was applied to the following sensor systems:

- Dedicated sensor systems ADXL355 and MPU-6050 operating at different sampling rates.
- Dedicated sensor systems and smartphones operating at the same sampling rate.

The method yielded results consistent with sensors specifications or, when not available, with the observations. Specifically, the ADXL355 exhibited the lowest sensor noise from all sensor systems. Moreover, it could be observed that sensor noise decreased with the sampling rate. The developed method also allowed differentiating sensor noise between dedicated sensors and smartphones.

This section finalised by presenting an estimation of the detectability threshold (*Detect*) of accelerometers, considering their noise level, as measured above. The estimation suggests that the ADLX-355 is the sensor with the lowest *Detect*, being capable to detect earthquakes with $M=3$ and $M=5$ at a distance larger than 10 km and 100 km respectively.

Although promising, these findings are preliminary for a more thorough analysis including comparing results with a seismological reference station is recommended. This analysis is conducted in section 7.

6 SENSOR NETWORK: SERVER-SIDE COMPONENTS

This section is based on the paper Design and Evaluation of a High Throughput Seismic Sensor Network. Tools for Planning, Deployment and Assessment, presented at SENSORNETS 2017 by (Manso et al., 2017)

6.1 Introduction

This section introduces the server-side components that are part of the sensor network, whose main tasks are to manage the connected sensor systems, receive and store data from the sensor systems and provide access mechanisms to stored data from sensor systems.

The server-side components shall support a large-scale deployment. Thus, a **server cluster implementation** is envisaged to ensure scalability and distribute load over multiple processors and computers. In order to support deployment, planning tools are also developed and presented at the end of the section.

Ultimately, system resources (sensors and servers) will be accessible globally over the World Wide Web (i.e., Internet) relying on many of the latter's components (e.g., routers and gateways). It is not the scope of this work to describe these; hence, for simplicity purposes, the Internet and its components are treated as means to exchange information and are depicted as a cloud. It is also assumed that sensors are able to connect to servers. A general view of the system is presented in Figure 44. The sensor platform was described in section 5. The server components are described next.

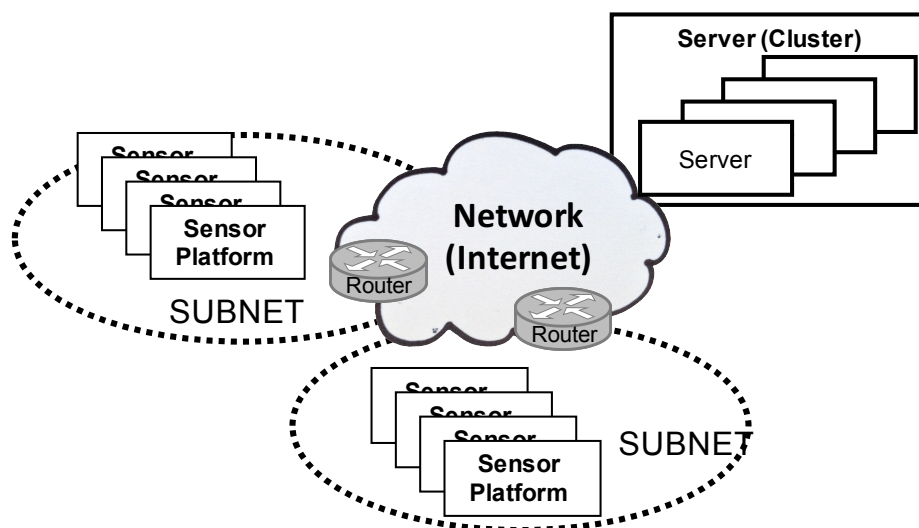


Figure 44 - Seismic Monitoring System: General View

6.2 Server Component

The implemented server component collects and stores data received from connected sensors. Optionally, it can also run a NTP server allowing to time-synchronize sensors.

The server runs a server application (supporting HTTP) that can be accessed by sensors over a local network or the Internet and send measured data. The server code is implemented in *node.js* since its event-driven and non-blocking I/O model delivers high performance and scalability. It is also highly integrated with Internet-based technologies and supports multi-core technology. As mentioned above, multiple servers can be deployed and co-exist in a cluster-like environment.

Each server provides a web-browser view, allowing users to visualise and manage the network.

As illustrated in Figure 45, the main page of the server shows a map with the location of the sensors. It also provides navigation options at the top of the screen.

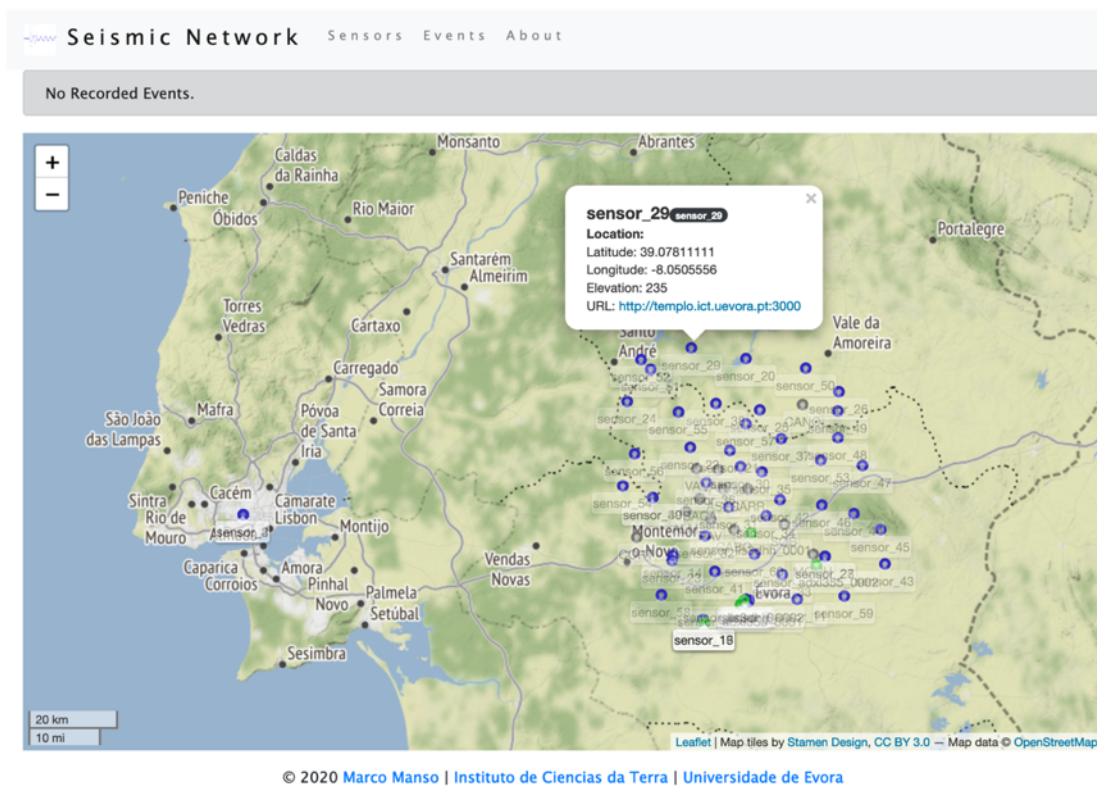


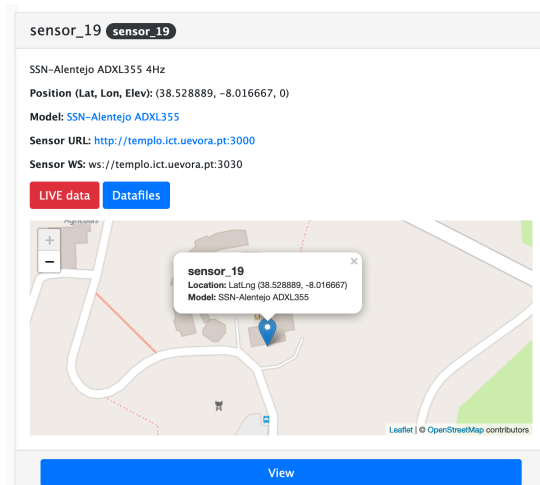
Figure 45 - Server Component: Main Page. Blue dots represent installed sensors. Green dots represent sensors connected to the network. The sensors spatial location represent the planned deployment.

The list of sensors can be visualised in the sensors list page, as shown in Figure 46.

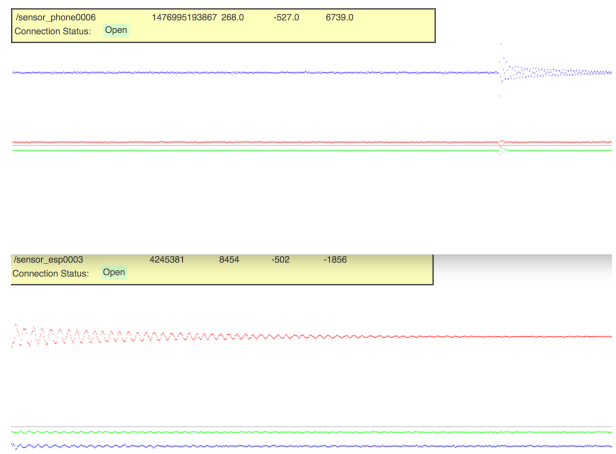
sensor_1	sensor_1	SSN-Alentejo ADXL355	LIVE Data	Datafiles
sensor_10	sensor_10	SSN-Alentejo ADXL355 125Hz	LIVE Data	Datafiles
sensor_11	sensor_11	SSN-Alentejo ADXL355	LIVE Data	Datafiles
sensor_12	sensor_12	SSN-Alentejo ADXL355	LIVE Data	Datafiles
sensor_13	sensor_13	SSN-Alentejo ADXL355 125Hz	LIVE Data	Datafiles
sensor_14	sensor_14	SSN-Alentejo ADXL355	LIVE Data	Datafiles
sensor_15	sensor_15	SSN-Alentejo ADXL355 15Hz	LIVE Data	Datafiles
sensor_16	sensor_16	SSN-Alentejo ADXL355 4Hz	LIVE Data	Datafiles
sensor_17	sensor_17	SSN-Alentejo ADXL355 125Hz	LIVE Data	Datafiles
sensor_18	sensor_18	SSN-Alentejo ADXL355 15Hz	LIVE Data	Datafiles
sensor_19	sensor_19	SSN-Alentejo ADXL355 4Hz	LIVE Data	Datafiles
sensor_2	sensor_2	SSN-Alentejo ADXL355 125Hz	LIVE Data	Datafiles
sensor_20	sensor_20	SSN-Alentejo ADXL355	LIVE Data	Datafiles
sensor_21	sensor_21	SSN-Alentejo ADXL355	LIVE Data	Datafiles
sensor_22	sensor_22	SSN-Alentejo ADXL355	LIVE Data	Datafiles

Figure 46 - Server Component: Sensors List. The page shows the sensor unique identification, its description and two buttons granting access to (1) live data and (2) recorded data

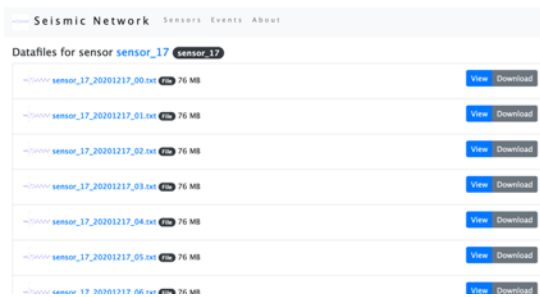
Shown in Figure 47, sensors can be selected, visualised, edited and deleted. Moreover, sensors' data can be visualised online (live data) and offline (recorded data).



Sensor page showing its location and access to the sensor's main information areas: live data and recorded data.



Example of sensor live data visualisation



Accessing sensor's recorded data



Visualising sensor's recorded data

Figure 47 - Sensor Operations and Data Access

The server also supports visualisation and data processing tools exploiting “live” sensor data. Users (*clients*) can use Internet Browsers to access the SSN-Alentejo server and visualise the location of sensors, as well as their connection status.

Figure 48 illustrates a simulated scenario of 10 deployed sensors in Évora.

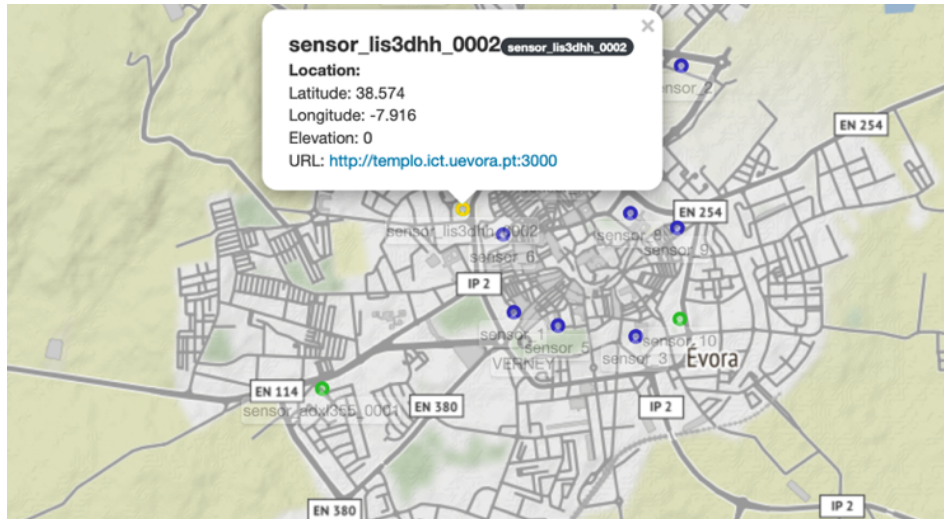


Figure 48 - Visualisation of a small sensor network deployment. The figure shows the sensors' location and connection status (green: connected, blue: registered, orange: activity detected). A sensor was coloured in orange because an event was being detected and recorded.

Note that sensors are displayed as a circle over a map, thus allowing to visualise their location in space. A colour code is used as follows:

- Green: the sensor is connected and providing data.
- Orange: the sensor has triggered a seismological event.
- Blue: the sensor is registered but is not providing data.

The figure shows two connected sensors (green colour), seven registered sensors (blue colour) and one sensor detecting an event (orange colour).

As part of this thesis, a SSN-Alentejo project was created at GitHub with the following address:

- <https://github.com/marcomanso/SSN-alentejo>

The project contains the server source-code, as well as two examples of sensor emulators (described in section 5.5). See Figure 49.

The screenshot shows the GitHub repository page for `marcomanso/SSN-alentejo`. The repository is private and has 172 commits. The commit history table is as follows:

File	Commit Message	Time Ago
<code>.idea</code>	updated sensor data format	12 months ago
<code>seismicSensorEmulator</code>	initial commit of existing code	15 months ago
<code>seismicSensorEmulatorPy</code>	test statistical functions	11 months ago
<code>seismicWebPlatform</code>	fast commit changes	4 months ago
<code>.gitignore</code>	Added sensor certificate support. Added sensor emulator in python	15 months ago
<code>README.md</code>	updated README	15 months ago

The README.md content is as follows:

```

SSN-alentejo

Repository for SSN-Alentejo

It contains the following modules:

• seismicWebPlatform: web portal for SSN-Alentejo. It is built in node.
• seismicSensorEmulator: simple sensor emulator that emulates a sensor generating random data. It is built in node.

This project started as part of Marco's PhD to build a high density sensor network. This work was extended and funded by the Science Foundation of Portugal (FCT) under grant number ALT20-03-0145- FEDER-031260.

```

The right sidebar shows the following information:

- About:** Repository for SSN-Alentejo. Includes a Readme link.
- Releases:** No releases published. Includes a link to "Create a new release".
- Packages:** No packages published. Includes a link to "Publish your first package".
- Languages:** A chart showing the following distribution: JavaScript 81.8%, HTML 12.4%, Python 4.7%, and Other 1.1%.

Figure 49 - SSN-Project at Github (<https://github.com/marcomanso/SSN-alentejo>)

6.3 Server-Sensor Communications

The communications between sensors and server(s) fully rely on Internet-based technologies. The base protocol used is the ubiquitous Internet Protocol (IP). Considering the need to support a high sensor throughput, which produces measurements with a frequency up to 200Hz, the *websocket* protocol (Fette and Melnikov, 2011) is selected due to its capability to handle high data throughput and its easy integration with Internet-based technologies.

6.4 Planning Tools for Large-Scale Deployments

In this subsection, tools that assist in the planning and design of large-scale sensor system deployments are introduced. Their aim is to:

- **Plan the deployment of network components** (e.g., routers serving sensor systems), by estimating the amount of generated network traffic and identifying potential congestion points.

- **Plan the deployment of server components**, by calculating the expected CPU load required to handle connected sensor systems and determining the maximum recommended number of sensors that should be connected to a server.

The planning tools resort to two types of measurements: Network load and Server load. They shall allow planners to assist the design of a network involving a high number of high-throughput sensors and servers, providing a method to determine the recommended (and highest) number of connected sensors a server (or a cluster of servers) can support.

6.4.1 Network Load Measurements

The network load measurements are related to the actual network transmission rate as a function of the number of sensors and their measurement frequency.

Defined as Sensor Network Transmission Rate (*SNTR*) and measured in KiB/s, it increases proportionally with the number of sensors connected and their sampling rate. This relation can be approximately described and generalised according to formula (6.1).

$$SNTR = \sum_{Sensors} SMsgSize \times SFreq(sensor) \quad (6.1)$$

Where:

- *SNTR* is the amount of data (in KiB/s) transmitted per second.
- *SMsgSize* is the size (in KiB) required to transmit a single sensor measurement. It also includes protocol overheads (in the case of IP is 0.14KiB per message).
- *SFreq* is the sampling rate (in Hz) of the respective sensor.

The *SNTR* provides an indication of the network data throughput that is required to comply with a sensor network configuration.

Since the network planner is limited to the throughput capacity of the network (via a network access point), the following options are available:

- If the sensor frequency and message size cannot be changed, calculate the maximum number of sensors that can be connected to a single network access point.
- If the number of network access points is limited, determine the recommended sampling rate for the connected sensors.

- From a development point of view, reduce the message size by applying techniques such as compression.

6.4.2 Server Load Measurements

The server load measurements are related to the amount of work that is placed in the server concerning the operation of the connected sensors.

The server performance is assessed based on the percentage of CPU (%CPU or $Server_{CPU_LOAD}$, expressed in percentage) allocated to process all sensors' requests, which varies according to the number of sensors and their sample frequency (both used to determine the $SNTR$). Other parameters, like memory allocation and storage operations (i.e., hard-disk write and read), are not significant in the assessment process.

The formula to determine the expected server $Server_{CPU_LOAD}$ when handling an arbitrary number of sensors (exhibiting a known $SNTR$) is presented in (6.2).

$$Server_{CPU_LOAD} = \frac{SNTR}{CSNPI} \times 100\% \quad (6.2)$$

The CPU Sensor Network Performance Index" ($CSNPI$) value (units KiB/s) is server dependent and it is a quantity that represents a server capacity to process sensor network data. It has to be determined for the specific server platform to use in the planned deployment.

Thus, increasing the number of sensors causes the $SNTR$ to increase, which in turn increases the CPU load. A CPU load above 100% means the server is not capable to provide the workload required, likely resulting in the loss of sensor messages. Moreover, the target CPU load should not be above 60% in order to ensure enough CPU reserves to execute additional tasks or handle peak loads.

Importantly, knowing the $CSNPI$ (which is an intrinsic characteristic of the server) and the $SNTR$ (which is a characteristic of the sensor), the recommended number of sensors to connect to a specific server in order to achieve a specific CPU load percentage can be determined according to (6.3) presented next.

$$n_{CPU_LOAD\%} = \frac{CPU_LOAD\%}{100\%} \times \frac{CSNPI}{SNTR} \quad (6.3)$$

Where:

- $n_{CPU_LOAD\%}$ is the calculated number of sensors to connect to the server in order to achieve a CPU load percentage of $CPU_LOAD\%$.
- $CPU_LOAD\%$ is the target value for the CPU load percentage.

Note that sensors should be homogeneous, that is, produce the same type of messages and operate with the same frequency.

6.4.3 Validation of the Planning Tools

In this subsection, it is described a set of experiments conducted to assess the performance of the sensor network system based on collected empirical data. The derived analysis and observations also allow validating the planning methods and tools previously defined.

6.4.3.1 Experiment Setup

The evaluation of the sensor network system considers several connected sensors exhibiting various data throughputs (up to 200Hz sensor data frequency, i.e., the highest frequency of the selected accelerometer).

The experiment setup is depicted in Figure 50. In this setting, all components are part of the same local network. Multiple sensors are deployed. The server component is accessible via the *websocket* protocol. To collect sensor data, the server runs a *node.js* application that is capable to distribute, as needed, sensor requests to the available CPU cores, thus fully exploiting its processing capabilities.

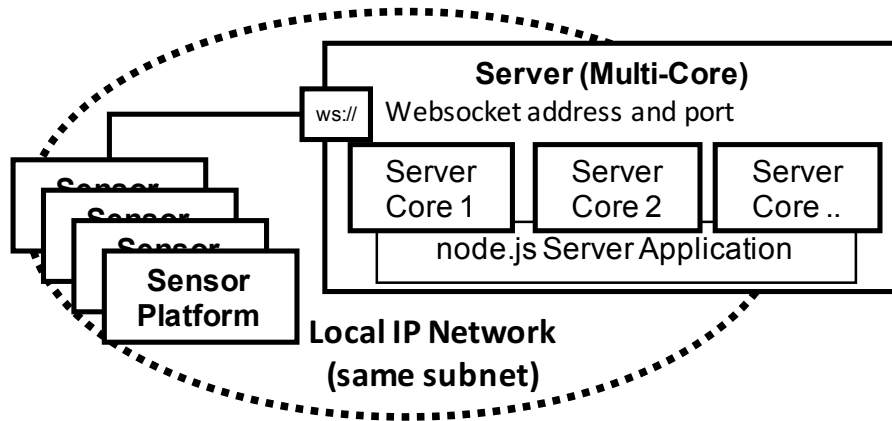


Figure 50 - Experiment Setup

The sensors used in this experiment are simulated using the prototype described in section 5.5. The simulator produces an equivalent data throughput of a real sensor. Moreover, multiple simulated sensors can be easily created and deployed. In this way, the behaviour of a large sensor network can be reproduced.

To conduct the experiments, two server platforms having different characteristics were deployed. Their main characteristics are presented in Table 17.

Server	Main Characteristics
Server PC (ServerPC)	Intel Core 2 Duo 64-bit (dual core) 2.33GHz Built-in Ethernet OS: Ubuntu Server 16.04.1 LTS (Xenial Xerus, Linux Kernel 4.4) 64-bit
Raspberry Pi 3 (Raspi3)	CPU: ARMv8 64-bit quad-core 1.2GHz Built-in Ethernet OS: Raspian (Debian Jessie, Linux Kernel 4.4) 32-bit

Table 17 - Server Implementations for the Experiments

For each server implementation, different sensor network configurations are setup and deployed as follows:

- Number of sensors: 1, 5, 10, 25, 50, 75, 100 and 125.
- Sensor sampling rate: 10, 50, 100 and 200 Hz.

6.4.3.2 Experiment Results

Following the setup described above, several simulated deployments were conducted, allowing the collection of data regarding network throughput and CPU load. Results are presented net.

Network Transmission Rate

The actual network transmission rate (in KiB/s) is measured as a function of the number of sensors and their measurement frequency. For this purpose, it is used the "System Monitor" tool provided by Ubuntu.

The results are presented in Table 18 and Figure 51.

Table 18 - Sensor Network Transmission Rate (KiB/s) measured per number of sensors per frequency

# Sensors	200Hz	100Hz	50Hz	10Hz
1	25	12	6	1.4
5	130	62	30	7
10	268	124	60	13
25	760	310	150	34
50	1420	630	310	68
75	2050	1024	450	100
100	2840*	1420	620	136
150	4100*	1950*	780	170

Network Transmission Rate as a function of frequency. Estimated values are marked with (*)

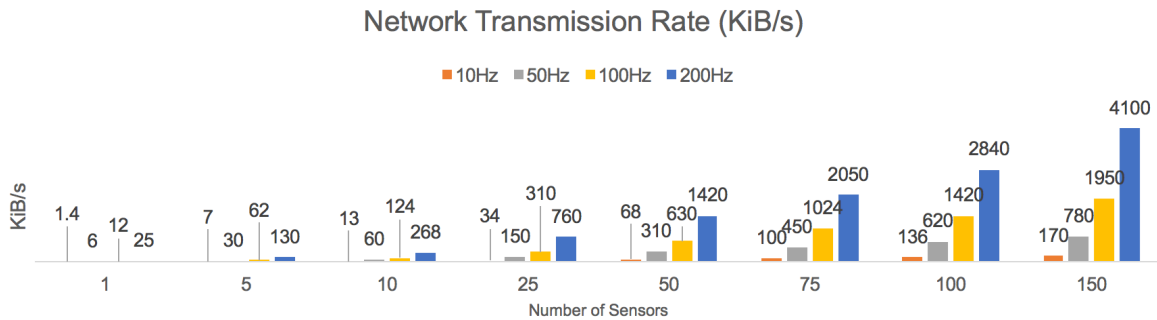


Figure 51 - Network Transmission Rate measured per number of sensors per frequency. It is important to note that measurements pertaining to 100 and 150 sensors at 200Hz and 150 sensors at 100Hz were obtained using formula (6.1).

As expected, the transmission rate increases proportionally with the number of sensors and their frequency.

It can also be verified that formula (6.1) provides predictions that are close to the measured values, as exemplified below:

- 10 sensors at 10Hz produce 13KiB/s against 14KiB/s given by the formula.
- 75 sensors at 200Hz produce 2050KiB/s against 2100KiB/s given by the formula.
- 100 sensors at 200Hz produce 2080KiB/s against 2800 KiB/s given by the formula.
- 10 sensors at 100Hz produce 124KiB/s against 140 KiB/s given by the formula.
- 25 sensors at 200Hz produce 760KBi/s against 700KiB/s given by the formula.

The SNTR is useful to determine the server workload (as presented next) and the network capacity requirements.

Server Performance

The server performance is assessed based on the percentage of CPU (%CPU) allocated to process all sensors' requests, which varies according to the number of sensors and their sample frequency (both used to determine the *SNTR*). The lower the %CPU the better is the server performance. Average allocations above 60% should be avoided to ensure a *healthy* server operation.

Figure 52 shows the %CPU allocation provided by the *top* application running on the *Raspi3*. It is visible the 4 instances of *nodejs* handling sensor requests. At the moment the snapshot was taken, the overall CPU usage was 22.3% CPU. Note that applications not related with the monitoring system also consume resources (*top* included).

```
top - 22:12:17 up 1 day, 29 min, 4 users, load average: 0.86, 0.25, 0.08
Tasks: 154 total, 1 running, 153 sleeping, 0 stopped, 0 zombie
%Cpu(s): 16.7 us, 5.6 sy, 0.0 ni, 76.4 id, 0.0 wa, 0.0 hi, 1.4 si, 0.0 st
KiB Mem: 882780 total, 391408 used, 491372 free, 39128 buffers
KiB Swap: 102396 total, 0 used, 102396 free. 208028 cached Mem
```

PID	USER	PR	NI	VIRT	RES	SHR	S	%CPU	%MEM	TIME+	COMMAND
20724	pi	20	0	70288	18100	7752	S	30.6	2.1	0:08.61	nodejs
20720	pi	20	0	70452	17796	7844	S	18.3	2.0	0:05.66	nodejs
20721	pi	20	0	70448	18544	7840	S	18.3	2.1	0:21.74	nodejs
20722	pi	20	0	70456	17828	7844	S	17.8	2.0	0:05.74	nodejs
14835	root	20	0	0	0	0	S	5.9	0.0	0:01.63	kworker/u8+
78	root	-51	0	0	0	0	D	3.0	0.0	0:31.53	irq/92-mmc1
22094	pi	20	0	5112	2520	2140	R	1.0	0.3	0:00.83	top

Figure 52 - Example of CPU Usage Provided by Top in Raspberry Pi 3

Next, the measurements for the two server platforms selected are presented.

(a) ServerPC Performance

The *ServerPC* performance measurements are presented in Figure 53.

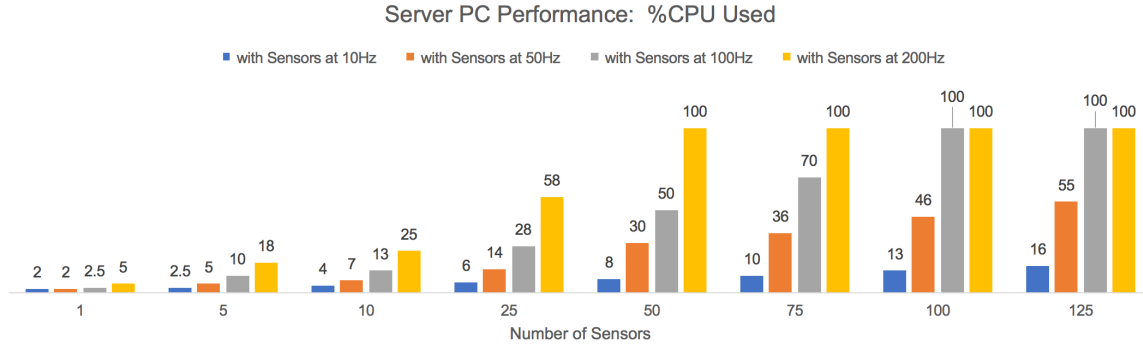


Figure 53 - ServerPC Performance measured based on the percentage of CPU allocated to process sensors' requests

As expected, increasing the number of sensors and/or sensors' frequency increases the %CPU. Based on the performance measurements, the relation is proportional and can be approximately described according to the following formula:

$$Server_{CPU_LOAD} = \frac{SNTR}{1310} \times 100\% \quad (6.4)$$

Where:

- $Server_{CPU_LOAD}$ is the percentage of CPU (%CPU) allocated to process all sensors' request.
- $SNTR$ is described in (6.1).
- 1310 is the value that characterizes this server capability to handle network sensor data (units are KiB/s). This value is called $CSNPI$ or CPU Sensor Network Performance Index.

From Figure 53, the recommended maximum number of connected sensors to a single *ServerPC* (i.e., %CPU less than 60%) are 25, 50 and 125 if, respectively, frequencies of 200Hz, 100Hz and 50Hz are used. Thus, for this system, the recommended number of sensors can be obtained from (6.5):

$$n_{\text{recommended}} = \frac{CPU_Load_{\text{recommended}} \times 1310}{SMsgSize \times SFreq \times 100} \quad (6.5)$$

Where $n_{\text{recommended}}$ is the maximum number of sensors recommended.

For example, if deploying sensors operating at a 10 Hz sampling rate (each generating 1.4KiB/s, as shown in Table 18), the number of sensors that *ServerPC* may support targeting a CPU load no higher than 60% can be calculated from (6.5) as follows:

$$n_{60\%} = \frac{60\%}{100\%} \times \frac{1310}{1.4} = 561.4$$

A single *ServerPC* may support in good *health* 561 sensors operating at 10Hz.

(b) Raspi3 Performance

The Raspi3 performance measurements are presented in Figure 54.

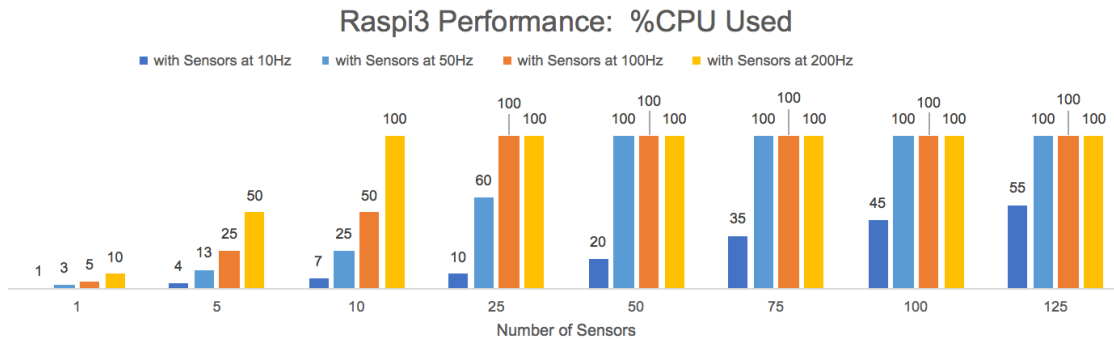


Figure 54 - Raspi3 Performance measured based on the percentage of CPU allocated to process sensors' requests

Similar to the *ServerPC*, a relation can be established and described according to formula (6.4), using the respective CSNPI that characterises the specific platform that was obtained from the performance measurements.

The formula for the Raspi3 is presented in (6.6).

$$Server_{CPU_LOAD} = \frac{SNTR}{280} \times 100\% \quad (6.6)$$

The variables in (6.6) are the same as in (6.4). Note that the Raspi3 CSNPI value (i.e., 280) is almost 5 times lower than the ServerPC CSNPI (i.e., 1310), thus one can conclude that it copes with 5 times less sensors.

From Figure 54, the recommended maximum number of connected sensors to a single *Raspi3* are 5, 10, 25 and 125 if, respectively, frequencies of 200Hz, 100Hz, 50Hz and 10Hz are used. Using formula (6.3) and using sensors at 10 Hz (each generating 1.4KiB/s, as shown in Table 18), the number of sensors that Raspi3 may support targeting a CPU load no higher than 60% can be calculated using (6.5) as follows:

$$n_{60\%} = \frac{60\%}{100\%} \times \frac{280}{1.4} = 120$$

A single Raspi3 may support in good *health* 120 sensors operating at 10Hz.

(c) Generalisation

The formula to determine the expected server CPU load (i.e., $Server_{CPU_LOAD}$) when handling an arbitrary number of sensors (exhibiting a known $SNTR$) is presented in (6.2). The load is determined based on the CSNPI value, which can be determined for any server platform.

The methods and tools presented in this subsection are useful to assist the design of a network involving a high number of high-throughput sensors and servers, allowing to determine the recommended (and highest) number of connected sensors a server (or a cluster of servers) can support, based on the sensors' message size and frequency.

6.5 Conclusion

This section presented the implemented server-side components that are part of the sensor network. The server component collects and stores data received from connected sensors. It also allows managing and visualising the network and its data. Importantly, multiple servers can be deployed, each managing a cluster of sensors, thus ensuring scalability and distributed load over multiple processors and computers, necessary for high-density deployment scenarios.

This section also introduced tools to assist in the planning and design of large-scale sensor system deployments. The planning tools resort to two types of measurements: Network load and Server load. The tools were validated resorting to experiments conducted to assess the performance of the sensor network system based on collected empirical data. The experiments involved the deployment of two different types of servers and sensor prototype simulators (described in section 5.5).

The developed tools support planners in the design of a network involving a high number of high-throughput sensors and servers, providing a method to determine the recommended (and highest) number of connected sensors a server (or a cluster of servers) can support. Conversely, these tools can also be used to determine the network and server requirements based on the number of sensors that shall be deployed.

7 DEPLOYMENT AND FIELD TRIALS

7.1 Introduction

In this section, it is presented the results of field trials involving prototypes developed in section 5. For this purpose, the MITRA site shown in Figure 55, close to Évora is chosen, given that it hosts the EVO station, a high-performing seismometer that will be used as reference instrument in comparing and assessing measurements obtained with the developed prototypes.

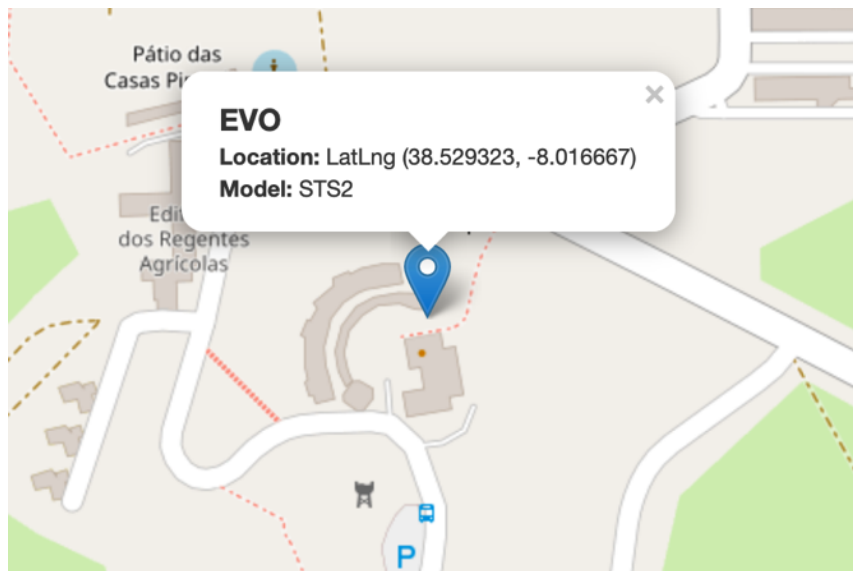


Figure 55 - Location of EVO station at MITRA site

7.2 Experiment Site

The MITRA site (Fig. 54) has a reference class-A station named EVO that will be used to compare the performance between the prototypes.

The EVO seismometer model is “STS-2/N” manufactured by “Streckeisen”. As per datasheet (STS-2 Datasheet), the station measures velocity over 3-axis (X, Y and Z) with frequency response displayed in Figure 56. The station exhibits a flat response between $\sim 0.02\text{Hz}$ and 10Hz and can be extended to 50Hz ($\pm 1.5\text{dB}$ thus within 15% in amplitude). Importantly, considering the standard model of ambient earth noise defined by Peterson (1993), the STS-2 noise characteristics are below the low noise model.

STS-2 VELOCITY RESPONSE

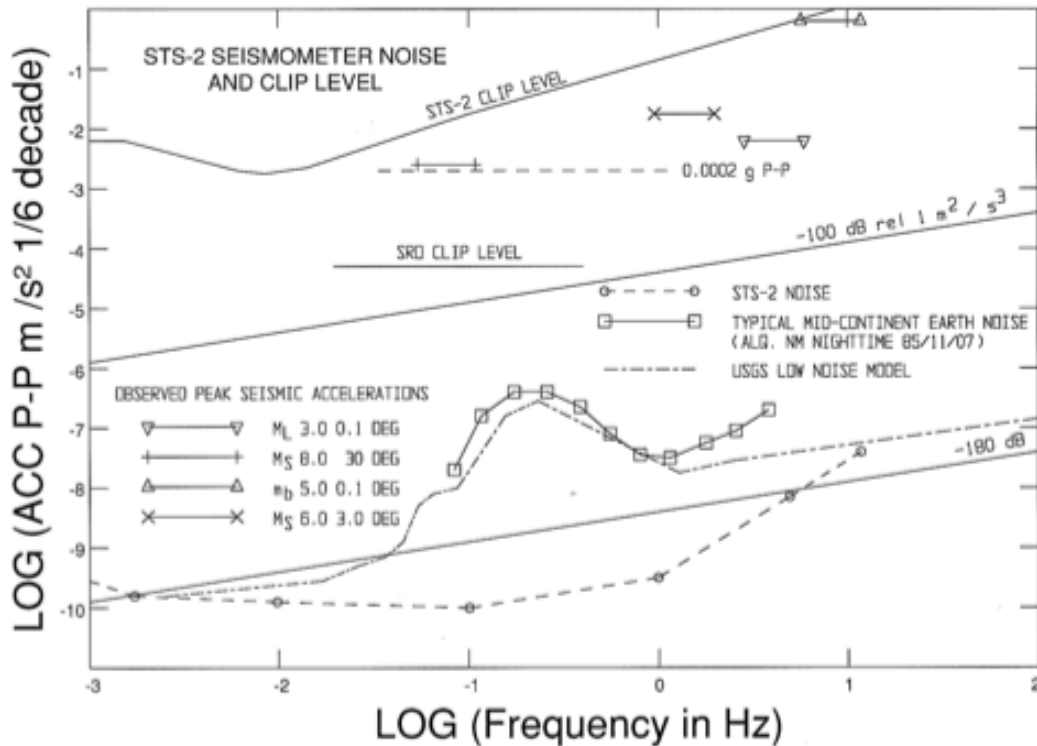
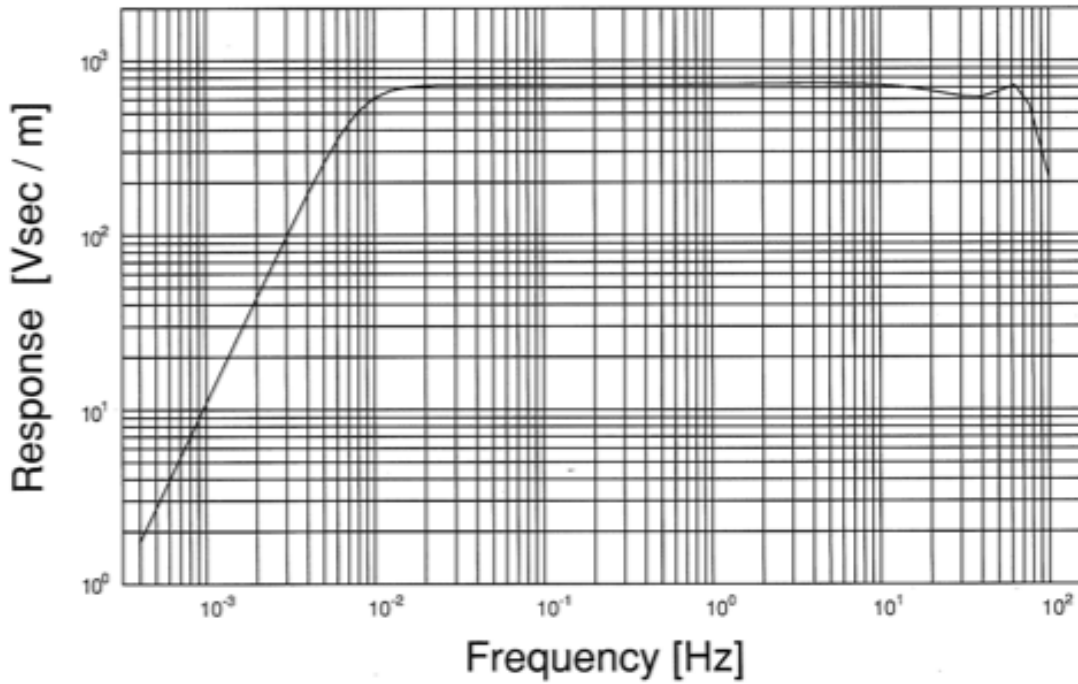


Figure 56 - STS-2 Instrument Response in frequency (Top) and performance considering the standard model of ambient earth noise defined by Peterson (1993) (Bottom). Source: (STS-2 Datasheet)

7.3 Prototypes Setup

Sensor prototypes following the design in section 5.2 (prototype 2) were developed and deployed at the MITRA site (Figure 55 and Figure 57).



Figure 57 - Installation of sensor prototypes at MITRA station

For the purposes of this analysis, the used prototypes are presented in Table 19.

Table 19 - Prototypes used for analysis

Prototype name	MEMs sensor	Frequency
Sensor 10	ADXL355	125Hz
Sensor 13	ADXL355	125Hz
Sensor 17	ADXL355	125Hz
Sensor 15	ADXL355	15Hz
Sensor 16	ADXL355	4Hz
Sensor lis3dhh_002	LIS3DHH	100Hz

The prototypes were installed on 28th July 2020. The prototypes are connected to a server hosted by the University of Évora. The sensors sent the measurement readings in real-time to the server using a Wi-Fi Access Point at MITRA.

Next, an analysis of the sensors characteristics and performance is presented, addressing the following aspects:

- Prototype generated file size volumes.
- Prototype sampling rate stability.
- Sensor measurement bias.
- Sensor noise characteristic.
- Sensor signal detection, in comparison with reference sensor EVO.
- Sensor frequency analysis.
- Probabilistic Power Spectral Density analysis.

7.4 Prototype Measurements

The prototypes operate at a pre-defined sampling rate, generating the following data per sample:

- time in seconds (since unix epoch²⁰).
- microseconds of time.
- acceleration in standard gravity g for X, Y and Z (represented as floats).
- CPU clock time in milliseconds.

Time (seconds and microseconds) is obtained using NTP (see section 5). Since the NTP precision may vary depending on the network conditions, the “CPU clock time” is also included to allow a precise track of time, while NTP time provides time synchronisation (at system level, that uses multiple sensors).

An example of the information stored per sample is given below:

```
{ "sensor_id": "sensor_15", "time_epoch_sec": 1603904399, "time_micro": 946000,
  "accel_x": -0.01077734375, "accel_y": -0.01930859375, "accel_z": 0.988640625,
  "cpu_time_ms": 13449529 }
```

Given that the work involves the use of prototypes, a verbose output is used²¹. The sample information is JSON formatted as per ECMA standard (ECMA, 2013) given its easy portability and use for Internet-based platforms, however at the cost of volume and performance.

²⁰ The Unix epoch is 00:00:00 UTC on 1 January 1970 (see: https://pubs.opengroup.org/onlinepubs/9699919799/xrat/V4_xbd_chap04.html)

²¹ For example, the miniSEED format contains metadata information (e.g., station information) and measurements in sequential order, assuming a stable sampling rate. miniSEED is also stored in binary format.

The prototypes' generated data are stored in text files, each containing measurements pertaining to one hour of operation according to the following format:

```
<sensor_id>_<year><month><day>_<hour>.txt
```

Thus, a file generated by “sensor_10” at noon (UTC time), date 28th July 2020 would be:

```
sensor_10_20200728_12.txt
```

7.4.1 Generated Data Volumes

The generated data volume as a function of the sensor sampling rate is presented in Table 20. As expected, size increases with the sampling rate, where a sensor operating at 125Hz require about 72MB per hour. Sensor data is stored in plain text format that can be compressed using *gzip*²², which is highly efficient for this type of files, resulting in more than 10x size reduction.

Table 20 - Sensor data volume size per sensor and sampling rate over one hour of operation

Prototype Sensor	Sampling Rate (Hz)	File size (uncompressed) (approx. value)	File size (compressed) (approx. value)
ADXL355	125	72MB	6MB
ADXL355	15	9.6MB	827KB
ADXL	4	2.3MB	175KB
LIS3DHH	100	61MB	3.3MB

7.4.2 Observed Sampling rates

The prototypes are setup to operate at a specific sampling rate. However, there may occur deviations due to a number of factors like network instability (causing loss of measurements) or the prototype main loop (see 4.3) taking a higher delay than planned (which could be caused by internal maintenance functions of the ESP8266 chip).

The actual measurement sampling period (in ms) for the different prototypes was determined by calculating the difference between time of successive samples. Subsequently, a histogram

²² <https://www.gzip.org/>

is generated showing the total number of samples that occurred at specific periods. The ideal outcome would be to have all samples (100%) having the expected measurement period.

The results are presented next. The interpretation of obtained results is given at the end of the subsection.

Sensor_10 with ADXL355 accelerometer operating at a sampling rate of 125Hz (P=8ms)

Prototype “sensor_10” was setup to operate at a frequency of 125Hz (period=8ms). Several files were analysed yielding similar results, being herein presented results for the measurement file related to 9th December 2020 at 2am.

The obtained histogram function is shown in Figure 58. A total of 449,062 measurements were processed, where most measurements (52.7%) occurred within the expected period of 8ms, with 19.5% with 9ms and 13.1% with 7ms. A small percentage of samples (14.7%) occurred outside this range.

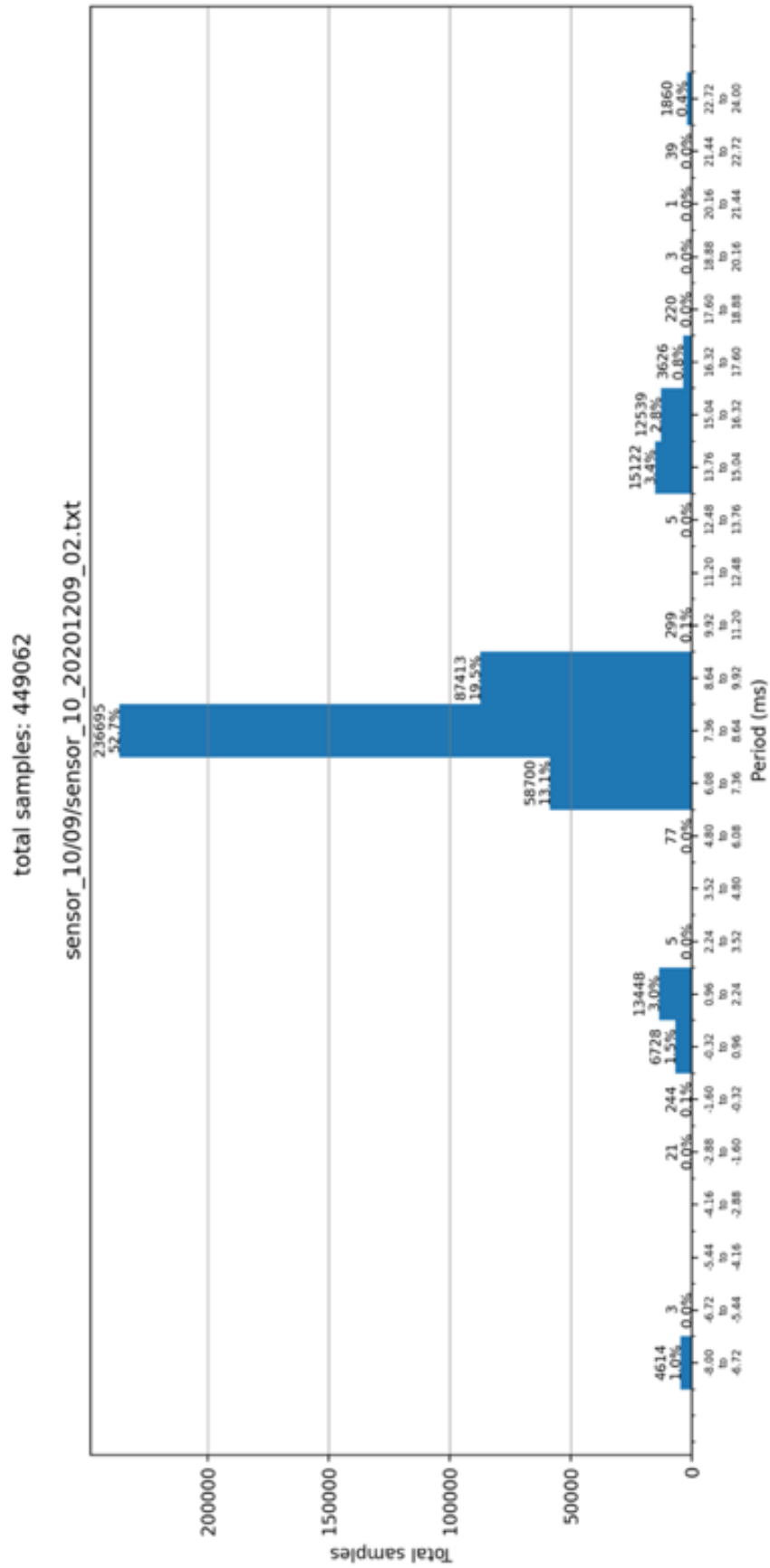


Figure 58 - “sensor 10” sample period distribution histogram

For completeness, results of sensor_13 and sensor_17, both operating with a 125Hz sample frequency, are also presented in Figure 59 and Figure 60.

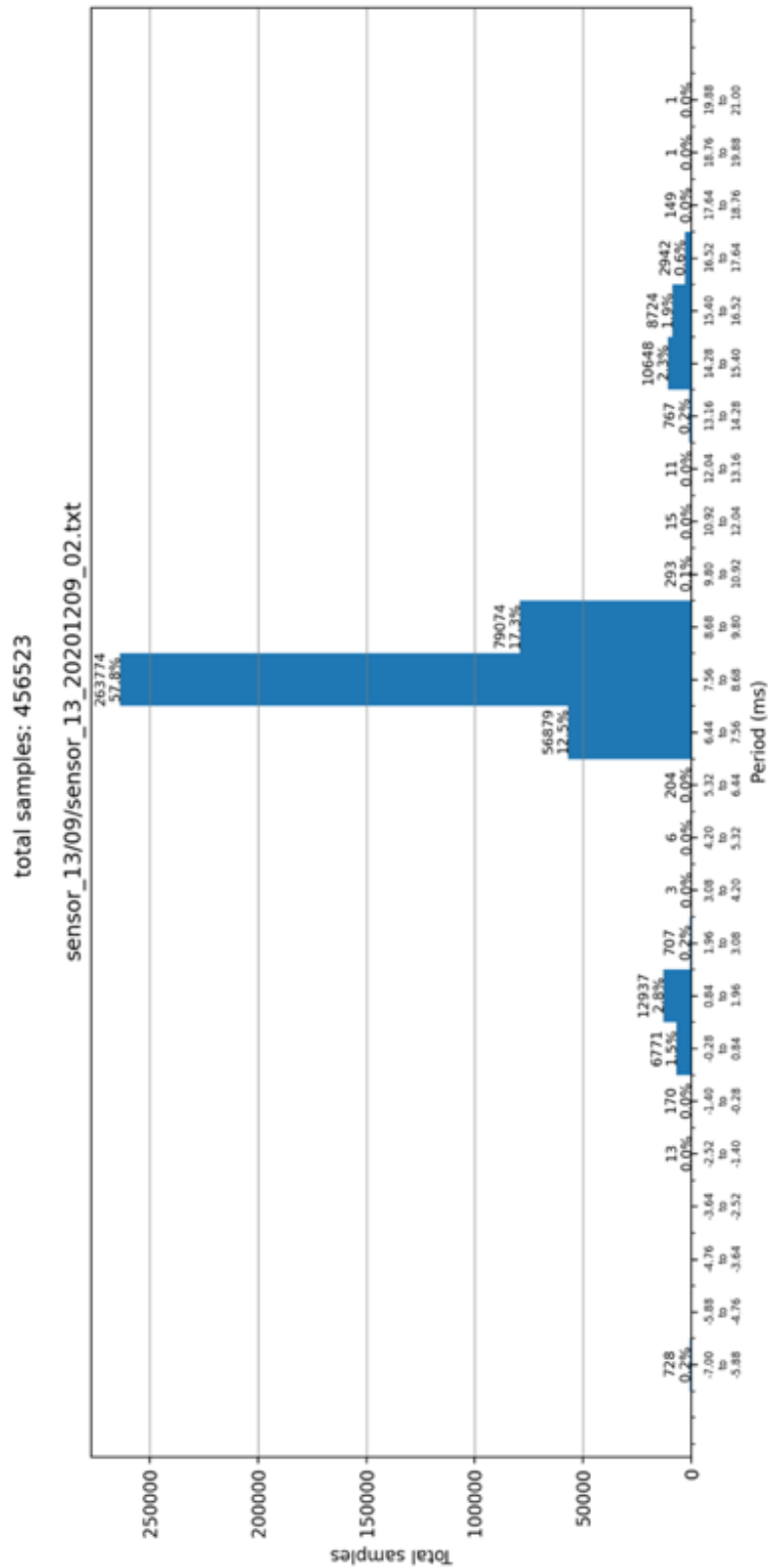


Figure 59 - “sensor 13” measurement rate histogram

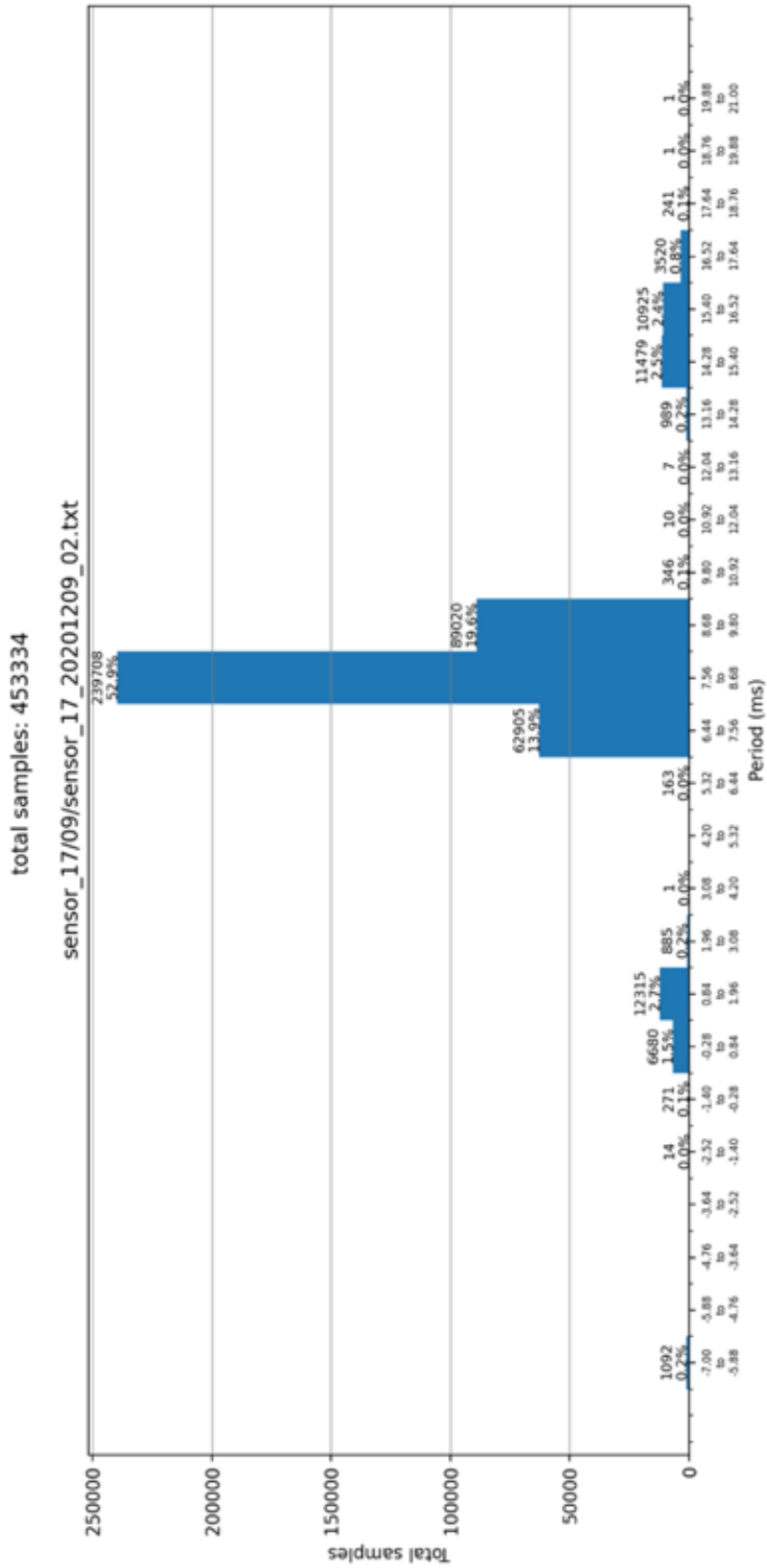


Figure 60 - “sensor 17” measurement rate histogram

sensor_15 with ADXL355 accelerometer operating at a sampling rate of 15Hz (P=67ms)

Prototype “sensor_15” was setup to operate at a frequency of 15Hz (period=67ms). The same analysis process as defined for “sensor_10” was followed, being herein presented results for the measurement file related to 9th December 2020 at 2am.

The obtained histogram function is shown in Figure 61. A total of 56979 measurements were processed, where almost all measurements (98.5%) occurred within the expected period of 67ms. A small percentage of samples (1.5%) occurred outside this range.

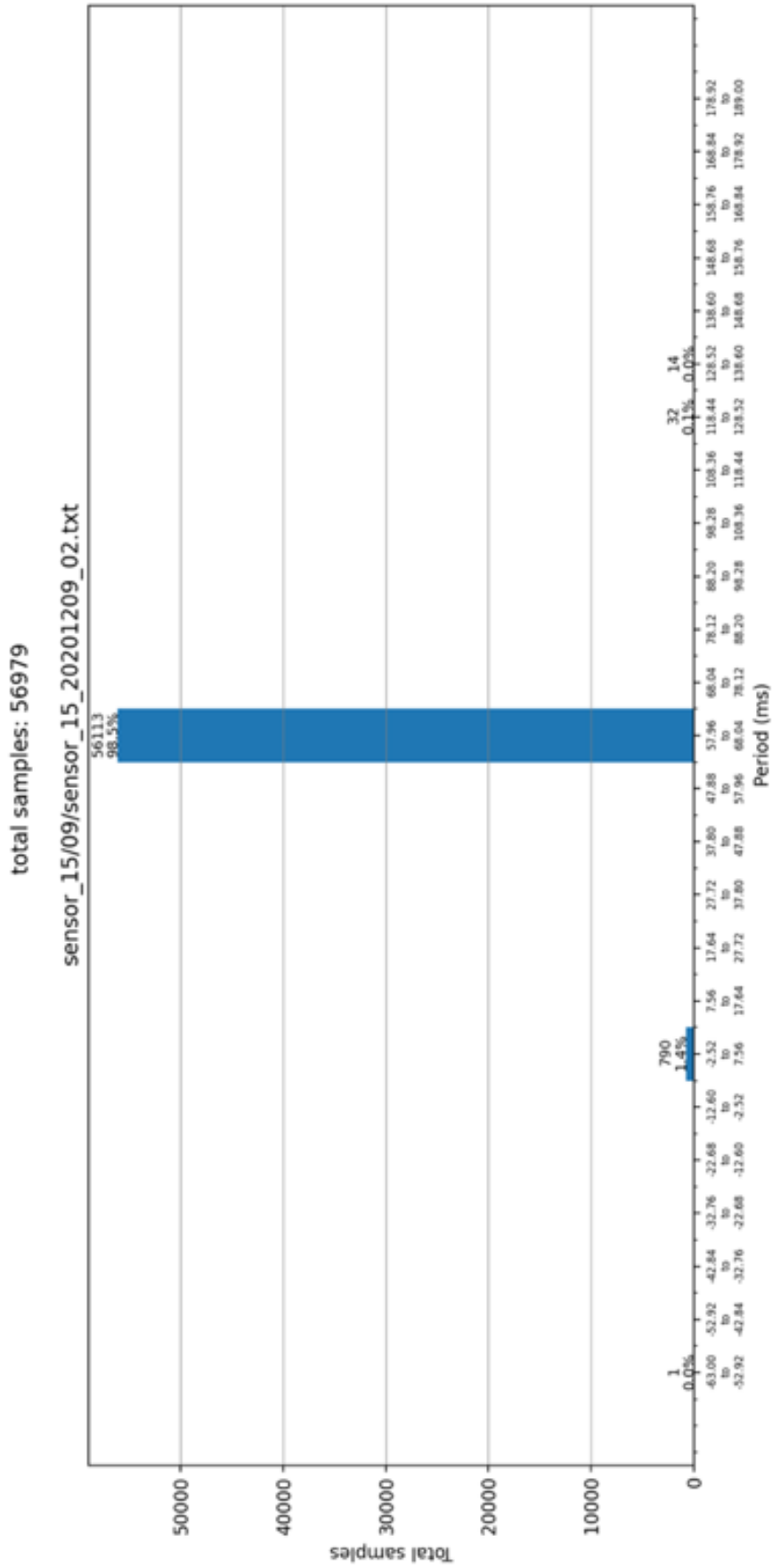


Figure 61 - “sensor 17” measurement rate histogram

sensor_16 with ADXL355 accelerometer operating at a sampling rate of 4Hz (P=250ms)

Prototype “sensor_16” was setup to operate at a frequency of 4Hz (period=250ms). The same analysis process as defined for “sensor_10” was followed, being herein presented results for the measurement file related to 9th December 2020 at 2am.

The obtained histogram function is shown in Figure 62. A total of 14055 measurements were processed, where almost all measurements (97.6%) occurred within the expected period of 250ms. A small percentage of samples (2.4%) occurred outside this range.

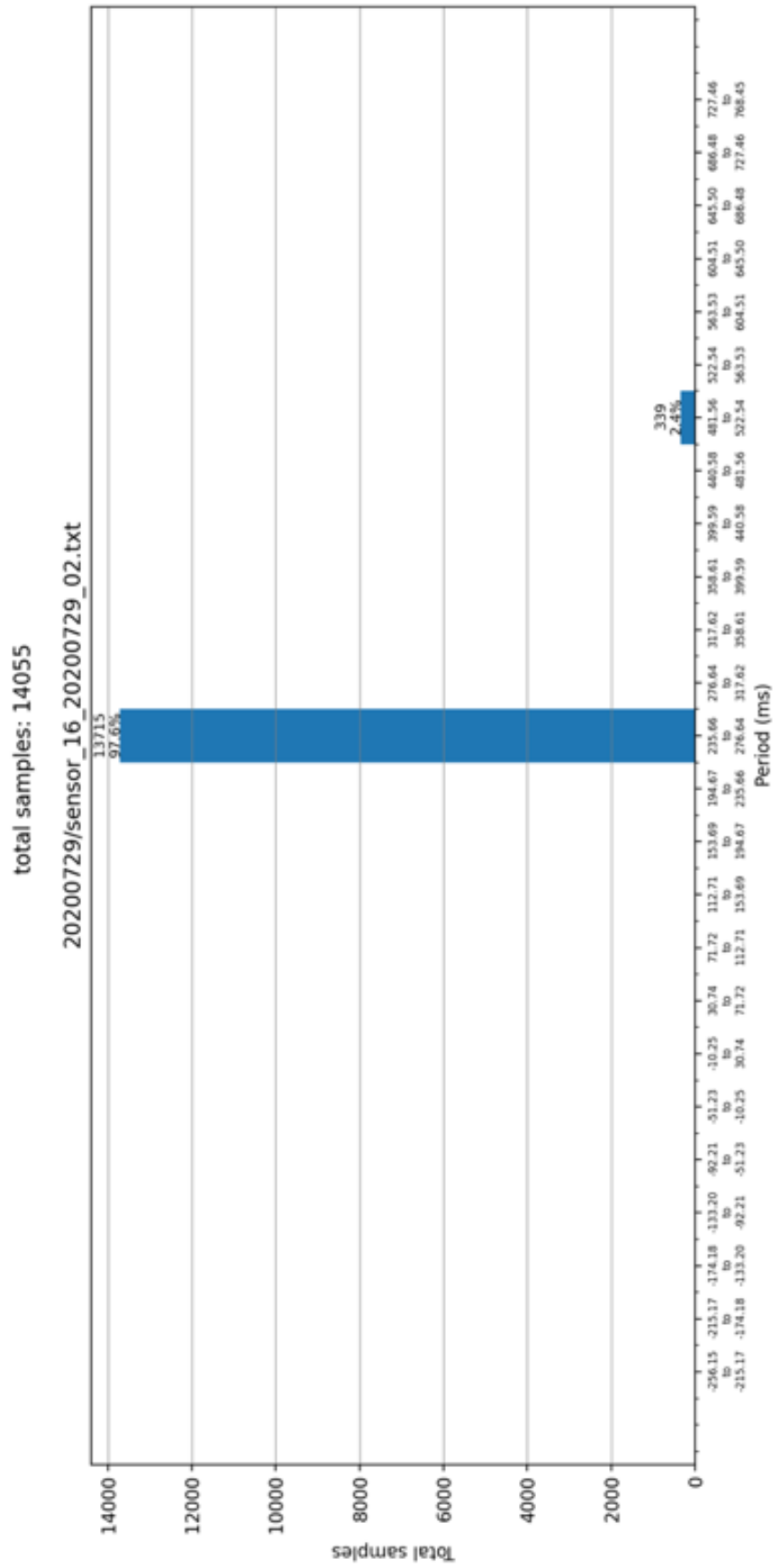


Figure 62 - “sensor 16” measurement rate histogram

sensor_lis3dhh_002 with LIS3DHH accelerometer operating at a sampling rate of 100Hz (P=10ms)

Prototype “sensor_lis3dhh” was setup to operate at a frequency of 100Hz (period=10ms). The same analysis process as defined for “sensor_10” was followed, being herein presented results for the measurement file related to 9th December 2020 at 2am.

The obtained histogram function is shown in Figure 63. A total of 356669 measurements were processed, where most measurements (52.8%) occurred within the expected period of 10ms, while 27.9% occurred around 11ms and 19% occurred around 9ms. It is noted that a FIFO was not used for the LIS.

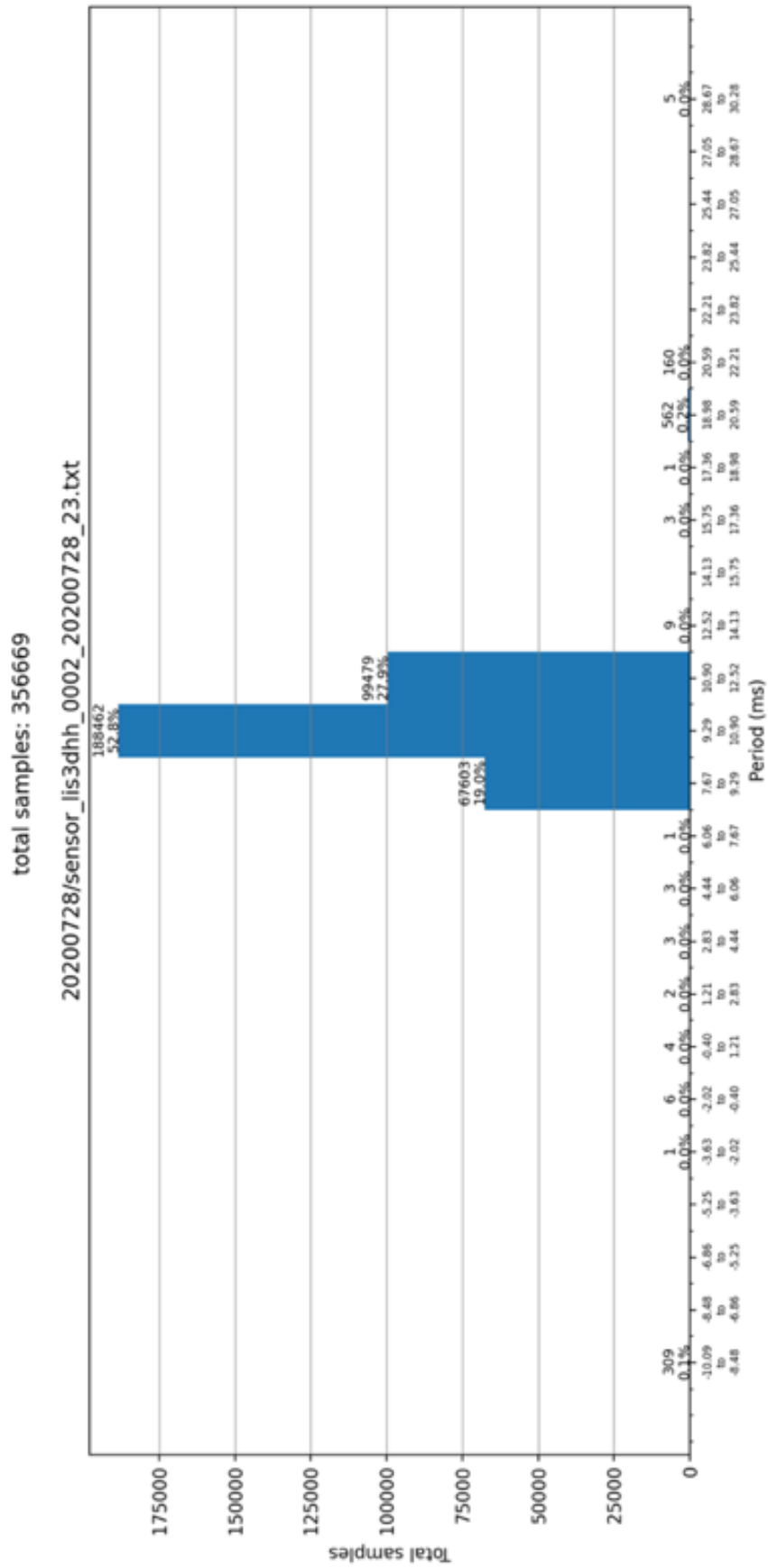


Figure 63 - "sensor lis3dhh_0002" measurement rate histogram

Summary

Table 21 presents a summary of the results obtained in the sample rate analysis. It can be seen that the prototype yields stable results for ADXL operating with lower sample rates (i.e., 4Hz and 15Hz). For high sample rates, the prototype exhibits a good accuracy for the LIS at 100Hz (52.8% within the expected value, more than 99% if considering a small ± 2 ms deviation) and the ADXL at 125Hz (52.7% within the expected value, more than 85% if considering a small ± 2 ms deviation).

Table 21 - Sample rate overall results

Sensor Prototype	Total Samples	% Samples at correct frequency	% Samples with delay (± 1 frequency)	% Samples outside frequency
ADXL@125Hz	449062	52.7%	32.6%	14.7%
ADXL@15Hz	56979	97.6%	-	2.4%
ADXL@4Hz	14111	98%	-	2%
LIS@100Hz	356669	52.8%	46.9%	0.3%

Given the prototype targets seismological applications, considering the frequencies of interest presented in Table 1 and Table 2, the prototypes should target sample rates of 100Hz or above. However, it is important to further reduce variations in sampling rate.

Since the sensor prototypes' measurements are read via the software implemented in the APB "main loop" (see section 4.4), circumstances may occur where APB background tasks need to perform administrative tasks (e.g., in the case of the ESP8266 network housekeeping or reconnection) thus interrupting the sensor application logic. Although a FIFO list is implemented in the prototype allowing to queue measurements even when the application logic is interrupted, minor time delays (in the milli- or microseconds order) occur, which explains the observed variations. Future prototype versions should seek (1) multi-core CPU architecture for the APB, allowing running dedicated tasks without risk of interruption, (2) faster CPU and (3) independent dedicated hardware for reading sensor measurements.

7.4.3 Observed Noise

Complementing the analysis in section 5.6.1, the sensor noise was also measured in the MITRA site for all installed sensors. The measurement files used to perform noise analysis were selected where no relevant seismic activity was detected. For illustration purposes, measurements collected from sensors 10 and 15 for selected time periods are presented next.

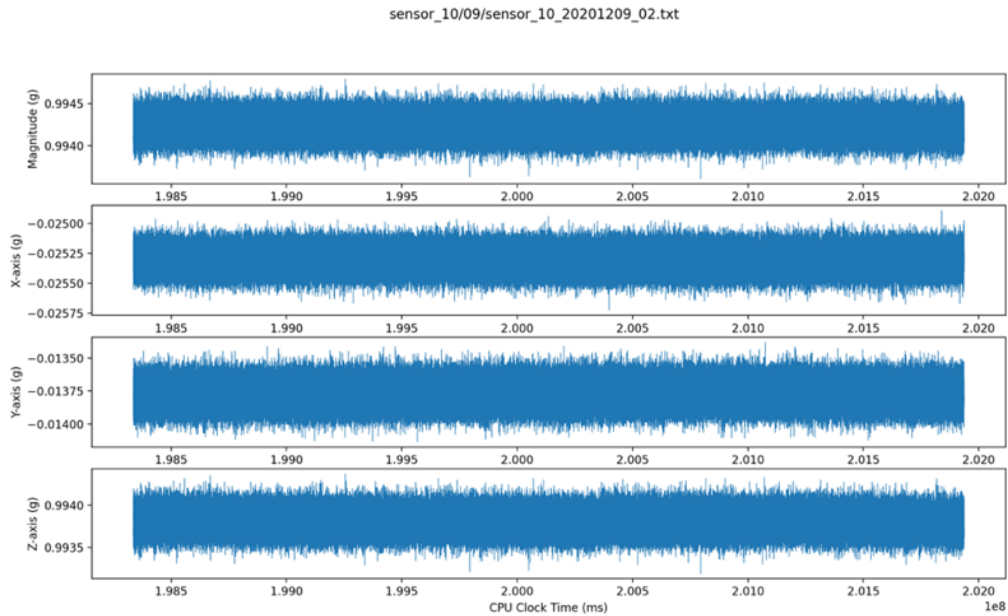


Figure 64 - sensor_10 measurements for 2020-12-09 at 2h (UTC)

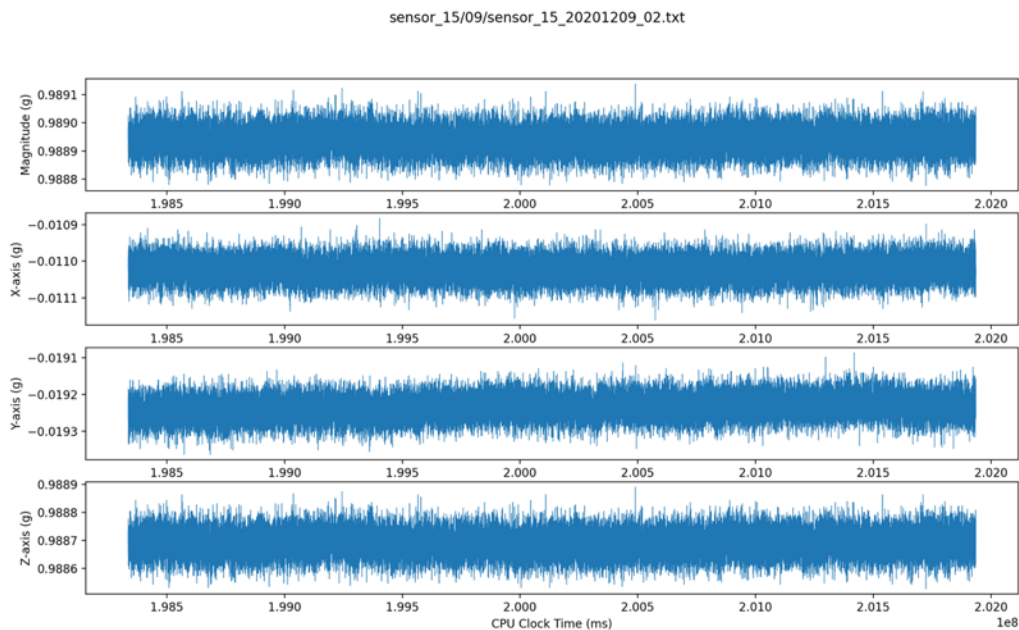


Figure 65 - sensor_15 measurements for 2020-12-09 at 2h (UTC)

The sensor measurements at rest are presented in Table 22. These include:

- Acceleration (acc.) magnitude (Acc. MAG in g).
- Mean acceleration value for axis X, Y and Z (Mean X, Y and Z in g).
- Acceleration standard deviation for the acceleration magnitude (STD MAG in mg).
- Acceleration standard deviation for each axis X-Y-Z (STD X, Y and Z in mg).

Table 22 - Sensor measurements at rest

	Acc. MAG (g)	Mean X (g)	Mean Y (g)	Mean Z (g)	STD (MAG) (mg)	STD X (mg)	STD Y (mg)	STD Z (mg)
sensor_10 (f=125Hz /P=8ms)	0.990	-0.030	-0.010	0.990	0.120	0.084	0.085	0.120
sensor_13 (f=125Hz /P=8ms)	0.990	-0.010	0.000	0.990	0.122	0.084	0.084	0.120
sensor_17 (f=125Hz /P=8ms)	1.010	-0.010	-0.020	1.010	0.124	0.082	0.083	0.124
Sensor_15 (f=15Hz, P=67ms)	0.990	-0.010	-0.020	0.990	0.044	0.030	0.031	0.044
Sensor_16 (f=4Hz, P=250ms)	1.010	0.000	-0.010	1.010	0.023	0.015	0.015	0.023
LIS3DHH002 (f=100Hz, P=10ms)	0.990	0.010	0.000	0.990	0.394	0.321	0.343	0.394

Concerning sensor noise, being proportional to the standard deviation value (see STD (MAG) in mg), it can be seen that for ADXL it increases with sampling rate: 0.023mg at 4Hz, 0.044mg at 15Hz and 0.120mg at 125Hz. LIS exhibits the highest noise with 0.394mg at 100Hz. These values are consistent with those reported in section 5.6.1, albeit slightly inferior indicating an environment with lower background noise. Recorded standard deviation for sensors is also presented in Figure 66.

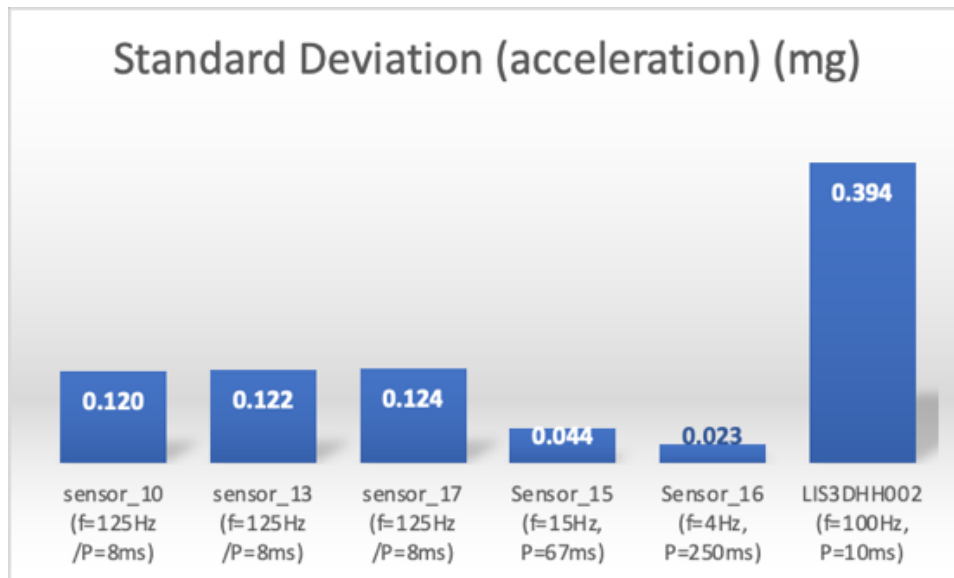


Figure 66 - Recorded standard deviation for deployed sensors

Sensor noise can be clearly visualised by superimposing several sensor readings over time, after subtracting the mean value, as depicted in Figure 67 and Figure 68. It is clear that prototype LIS (in blue) exhibits a higher signal amplitude than prototypes with sensors 10, 13 and 17 (operating with ADXL355 at 125Hz). Sensor 16, having the lowest sampling rate, exhibits the lowest amount of noise.

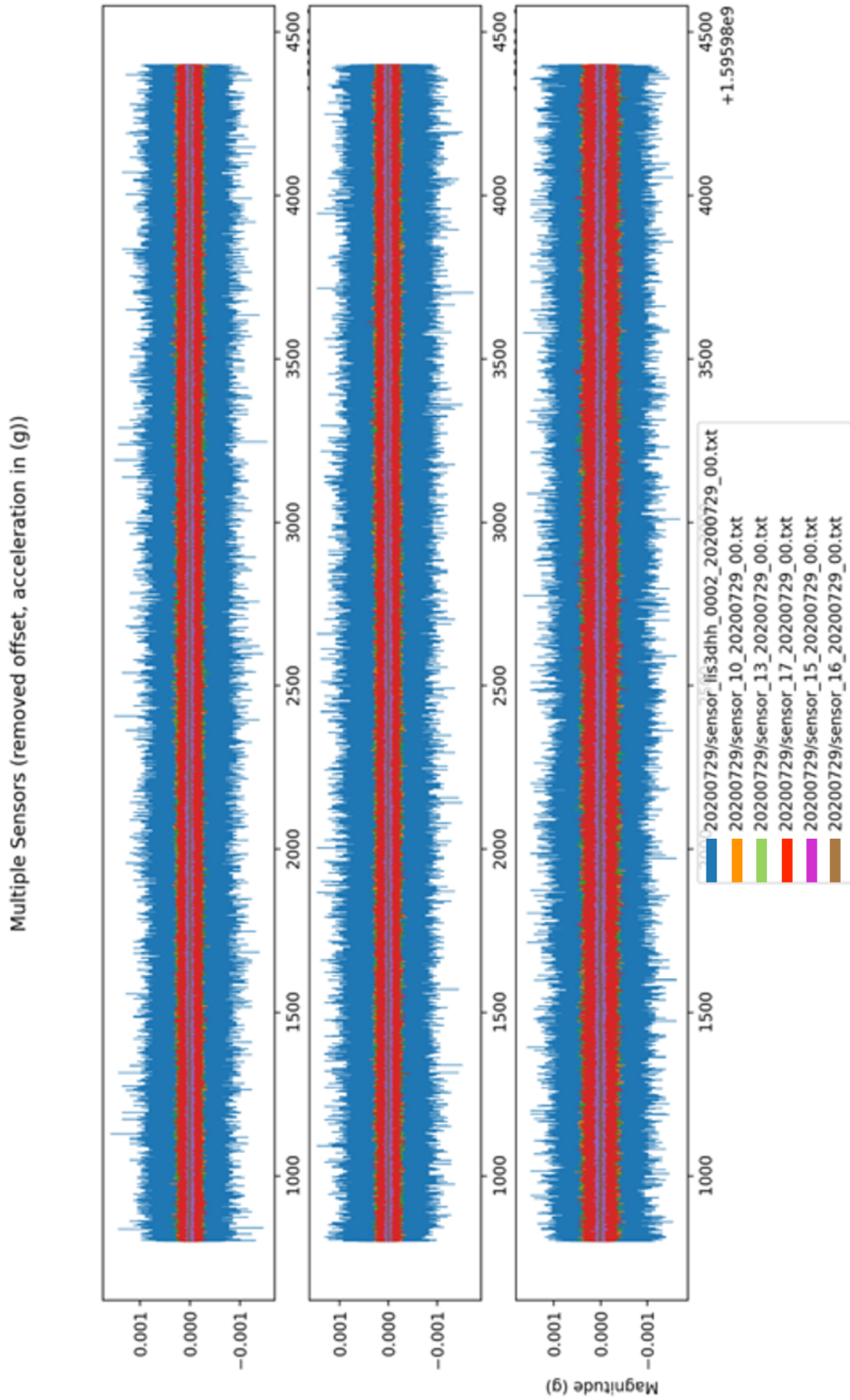


Figure 67 - Measurements (magnitude value) after subtracting the mean value for deployed sensors while at rest.

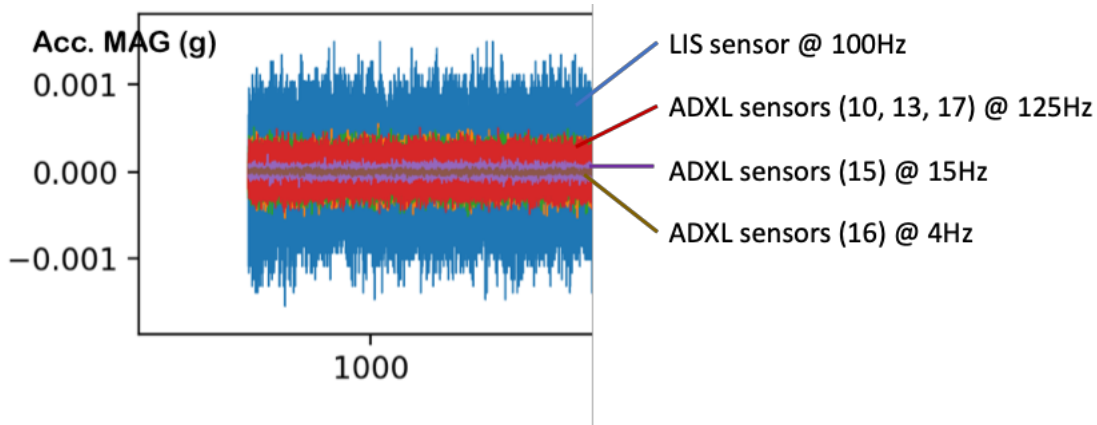


Figure 68 - Measurements (acceleration magnitude value in (g) after subtracting the mean value) for deployed sensors: zoom in. The LIS sensor exhibits the highest sensor self-noise (represented by the highest variation in amplitude) followed by ADXL at 125 Hz, ADXL 15 Hz and ADXL at 4 Hz (the lowest variation in amplitude).

Concerning acceleration measurements at rest, ideally all prototypes should provide the same values in X-Y-Z and a magnitude value of $1g^{23}$. Moreover, since sensors were installed horizontally, having the sensor's relative Z-axis aligned with gravity, ideally, Z measurements should be 1 g while X and Y measurements should be zero. However, from Figure 69 and Table 22, it can be seen that the magnitude value ranges vary in the X-axis (between -0.02 and 0.01), Y-axis (between -0.02 and 0.01) and Z-axis (between 0.99 and 1.01) among different prototypes. It is worth to mention that no specific calibration took place when installing sensors, thus observing minor offsets were expected. These offsets were removed before analysing the signals. Importantly, since the aim is to deal with large scale deployments and manual calibration is a time-consuming process, automatic on-site in-operation calibration techniques should be developed in future work.

²³ Accelerometers provide readings in bits, which number depends on the sensor resolution. For example, per axis, ADXL355 provides a 20-bit resolution while LIS3DHH provides 16-bit resolution. Thus, to harmonise readings across sensors, values are expressed as *float* value in g.

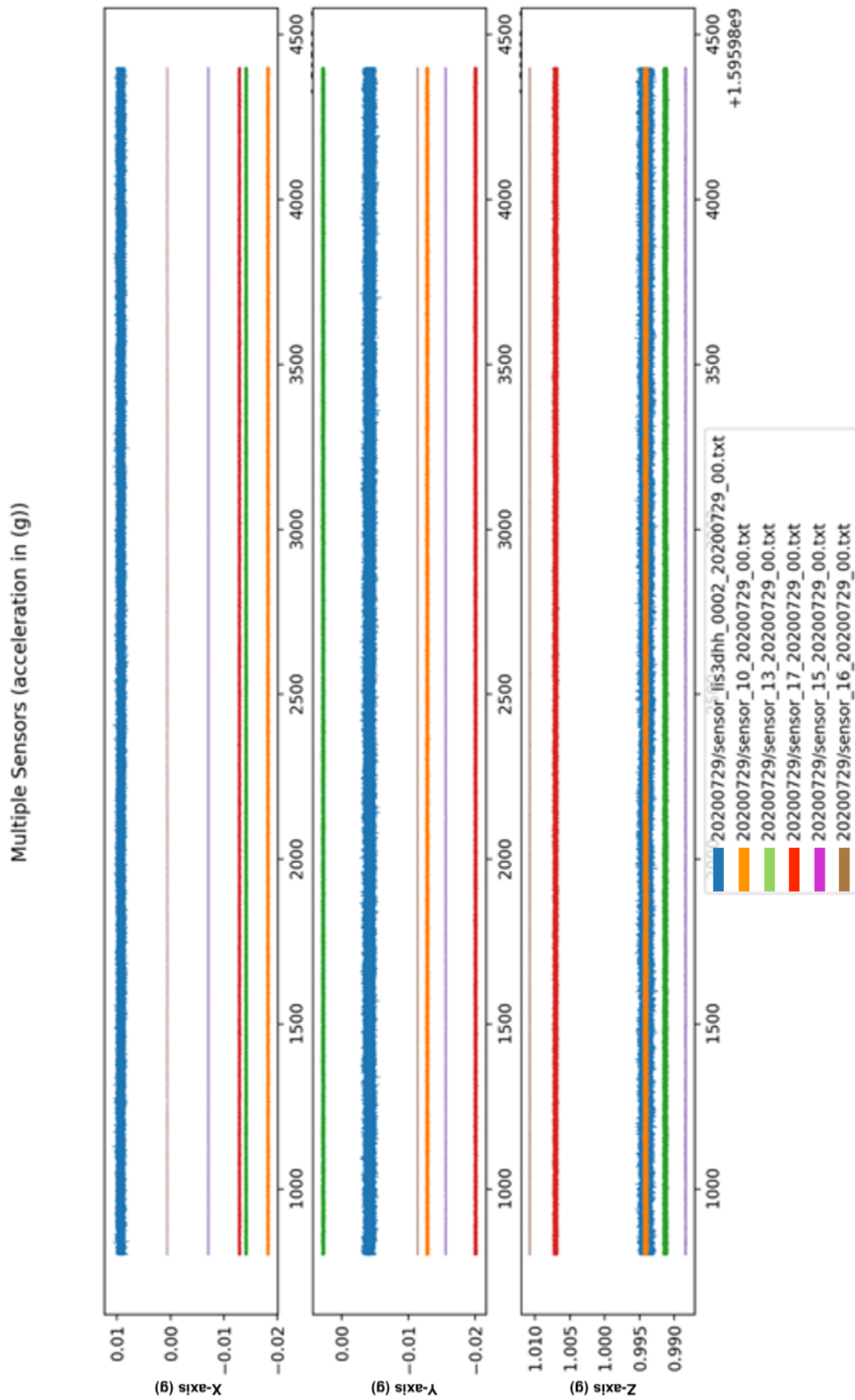


Figure 69 - Sensor measurements per axis: presence of sensor bias in X, Y and Z axis.

7.4.4 Observed Signal: 2020-07-28 at 12h UTC

The prototypes were installed at MITRA at the 28th July 2020 around 12h (UTC time). After installation, signals were “generated” for testing purposes.

The purpose of the exercise is twofold:

- First, to test the capability of the prototypes to detect generated signals. The criteria to discriminate “signal” from “noise” follows the methods presented in 5.6 and 5.7, using formula (5.3) with $C = 4^{24}$.
- Secondly, to compare prototype measurements against a high-quality seismic station (EVO) installed at MITRA station.

The results per prototype are presented next.

Note that in this analysis the prototype acceleration measurements are converted to (m/s²) units to allow comparison with EVO.

7.4.4.1 EVO Reference station measurements

EVO station measurements for the period of interest are presented in Figure 70. For analysis purposes, the vertical axis (Z) is chosen given it is the axis exhibiting the highest amplitude. **Note that EVO acceleration values are expressed as m/s².** The following time windows are outlined to illustrate in more detail measurements in signals of interest resulting from perturbations caused inside or close to the building where sensors were installed: the first (1) results from perturbations caused outside the building; the second (2) refers to strong perturbations caused in the pillar where the sensors were installed, where subwindow (2.1.1) shows in more detail that the first signals include three acceleration moments; the third (3) refer to perturbations caused inside a room next to the sensors; the fourth (4) shows perturbations caused by jumping outside the building where sensors were installed. Thus, signals 2 and 3 are strong signals, followed by 1 and then 4.

²⁴ A lower value than in section 5.7 is used to increase the sensor detectability, however increasing probability of having false positives

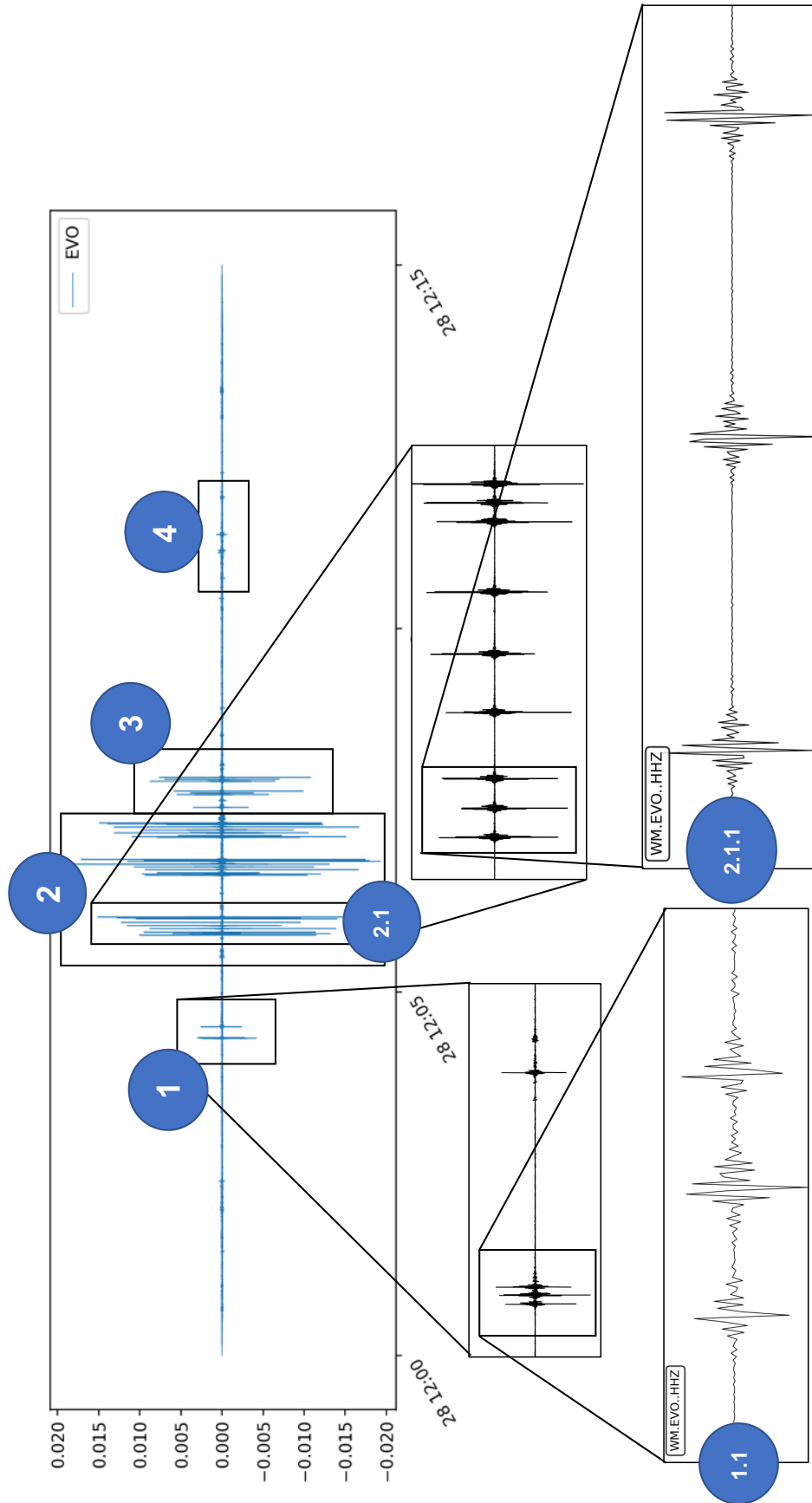


Figure 70 - EVO reference station measurements outlining signals of interest (1), (2), (3) and (4).

7.4.4.2 Prototype Measurements

Z-axis measurements collected by deployed prototypes within the relevant time window are presented next.

The following is noted: measured signals are drawn in blue colour; detections are represented in red vertical lines. Detections are calculated using the Detectability techniques described in section 5.7. For convenience, the “signal of reference” (i.e., measurements from EVO) are presented above the prototype measurements, facilitating the identification of detected signals. Annotations are presented facilitating interpretation of results. All acceleration measurements are presented in m/s^2 .

Prototype “Sensor 10”

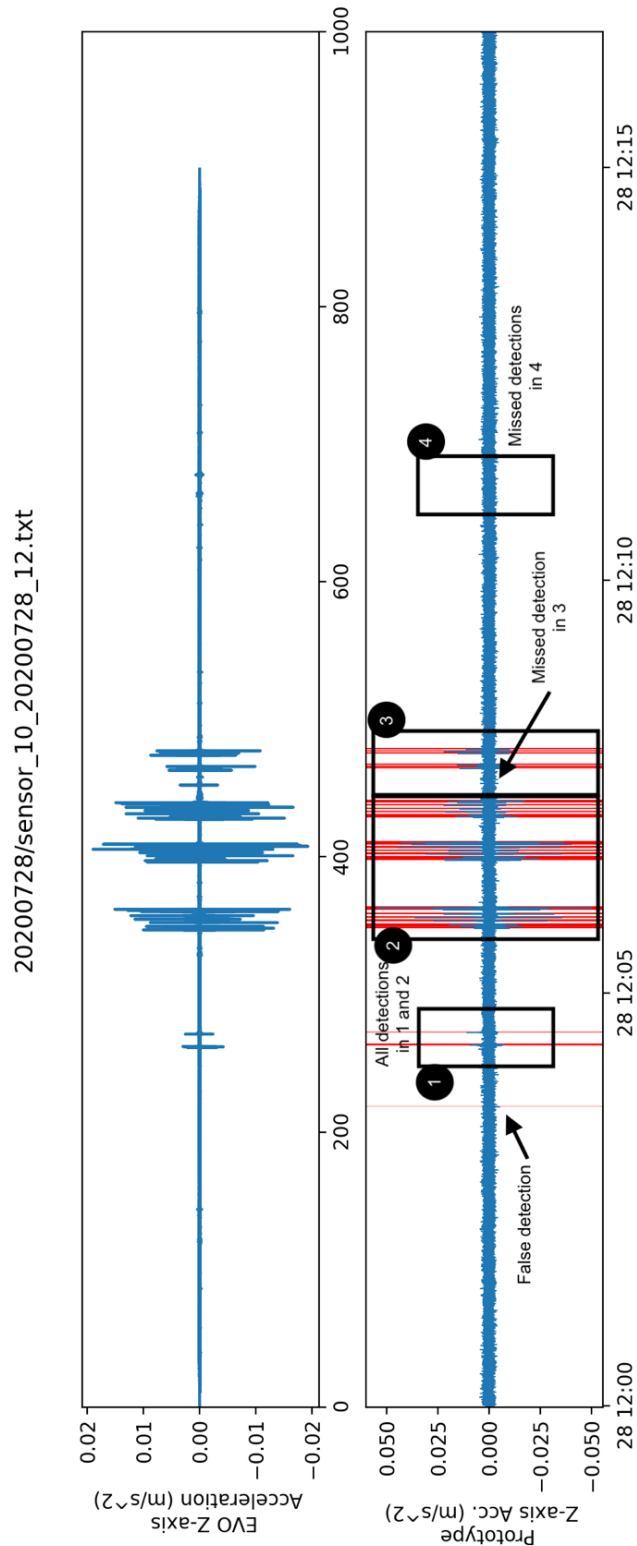


Figure 71 - Prototype “Sensor 10” with ADXL355 at 125Hz taken at 12h 2020-07-28 during the first 15 minutes. Detections are represented by vertical columns in red. The prototype detects signals (1), (2) and (3) (partially), but not (4). Note that the first peak in signal (3) is missed. Before signal (1), there is also a false detection.

Prototype “Sensor 13”

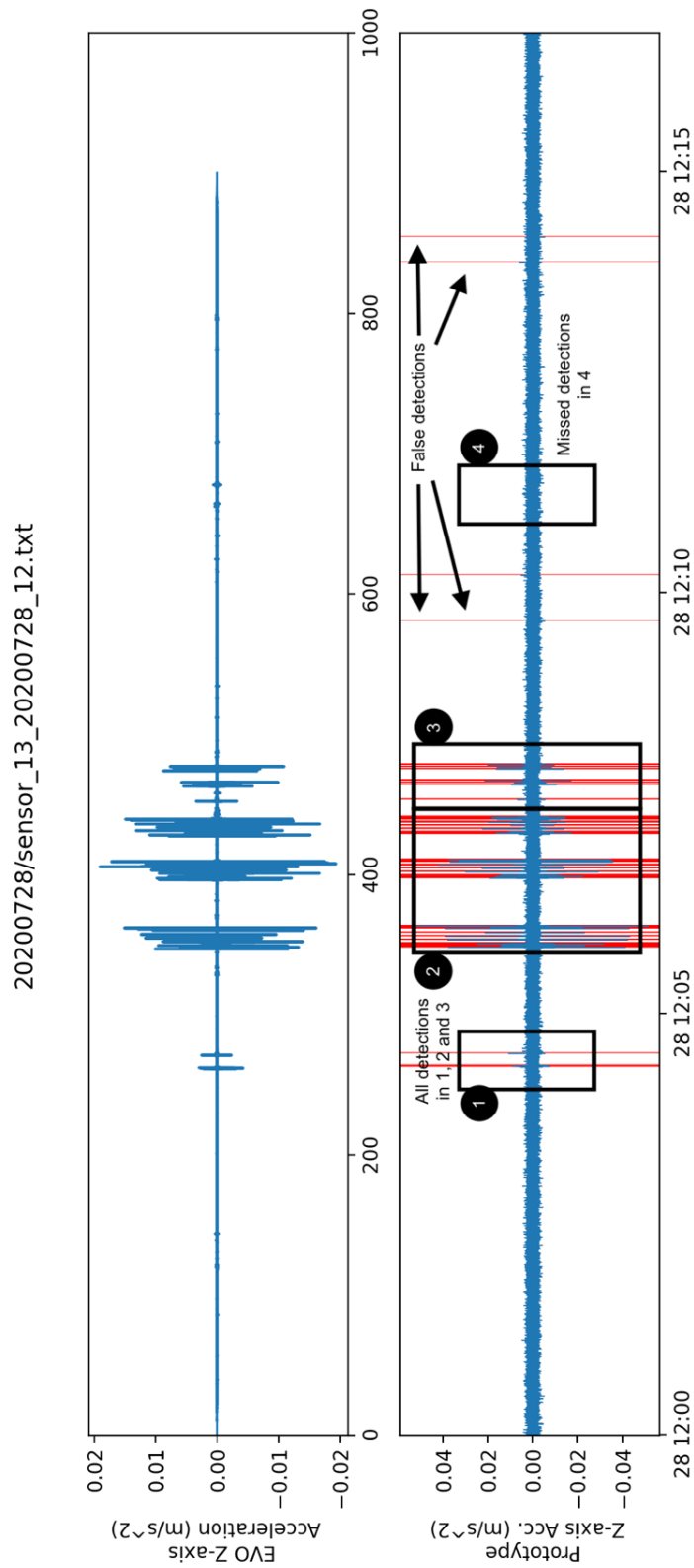


Figure 72 - Prototype “Sensor 13” with ADXL355 at 125Hz taken at 12h 2020-07-28 during the first 15 minutes. Detections are represented by vertical columns in red. The prototype detects signals (1), (2) and (3), but not (4). There are four false detections after signal (3).

Prototype “Sensor 17”

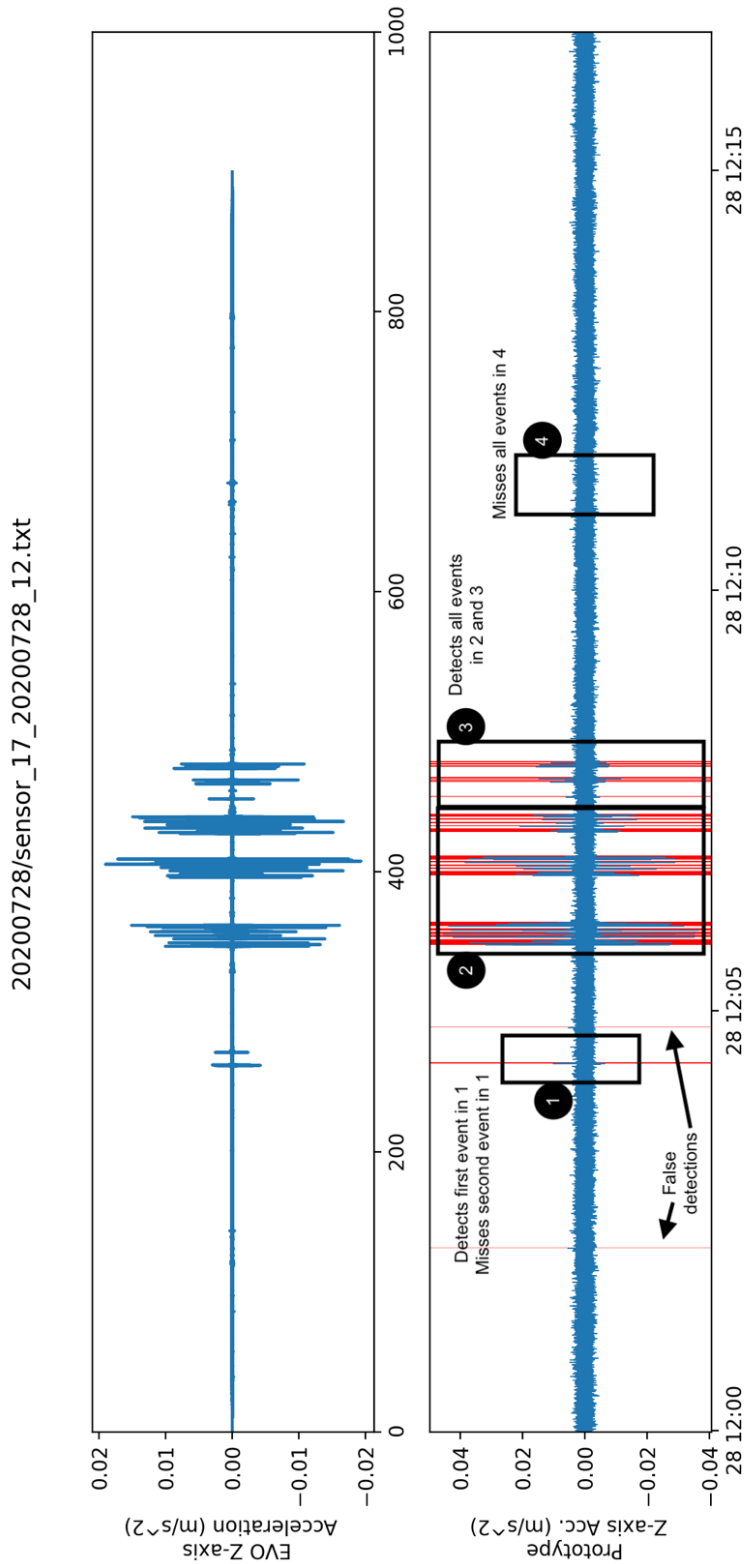


Figure 73 - Prototype “Sensor 17” with ADXL355 at 125Hz taken at 12h 2020-07-28 during the first 15 minutes. Detections are represented by vertical columns in red. The prototype detects signals (1) (partially), (2) and (3), but not (4). There is a false detection before and after signal (1).

Prototype “Sensor 15”

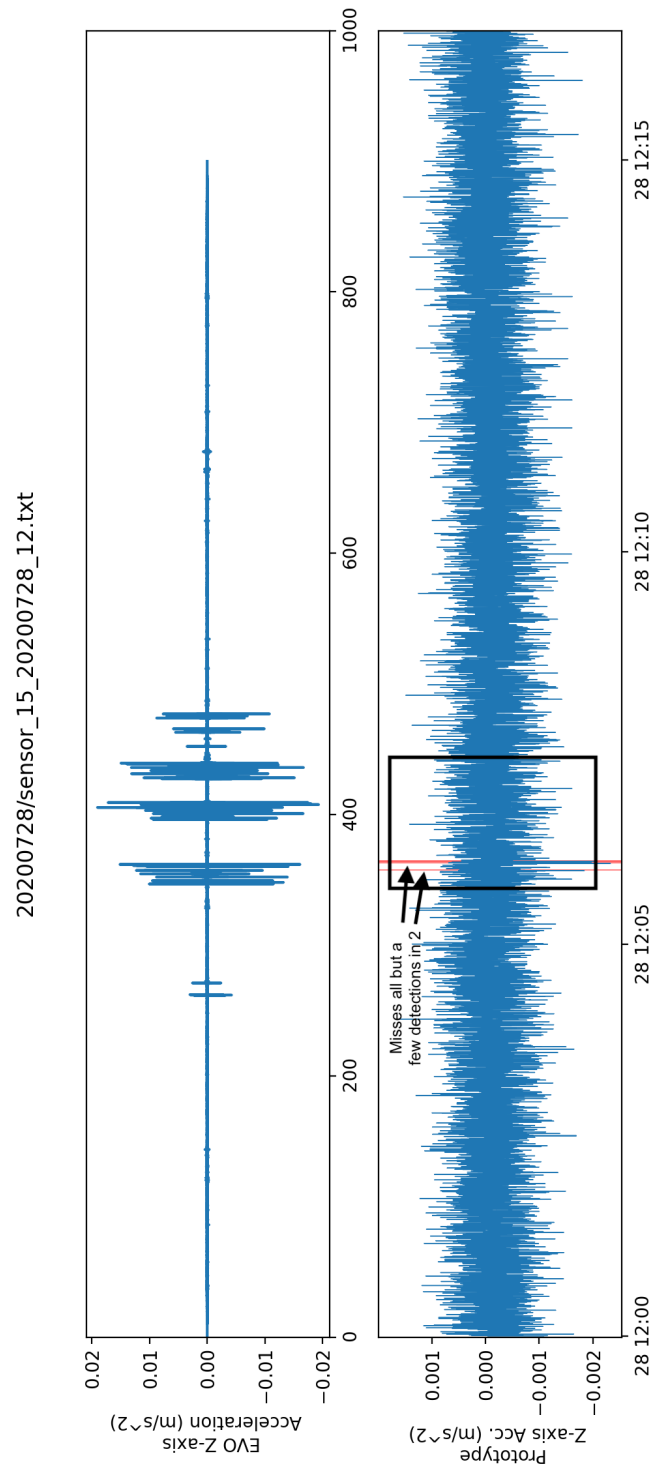


Figure 74 - Prototype “Sensor 15” with ADXL355 at 15Hz taken at 12h 2020-07-28 during the first 15 minutes. The sensor only shows two detections pertaining to signal (2), missing all others. The prototype only detects two (short) events pertaining to signal (2) missing all others. Given the strength of the signals, it is likely that the sampling frequency was not adequate to measure the signals of interest. This matter is further analysed in section 7.4.5.

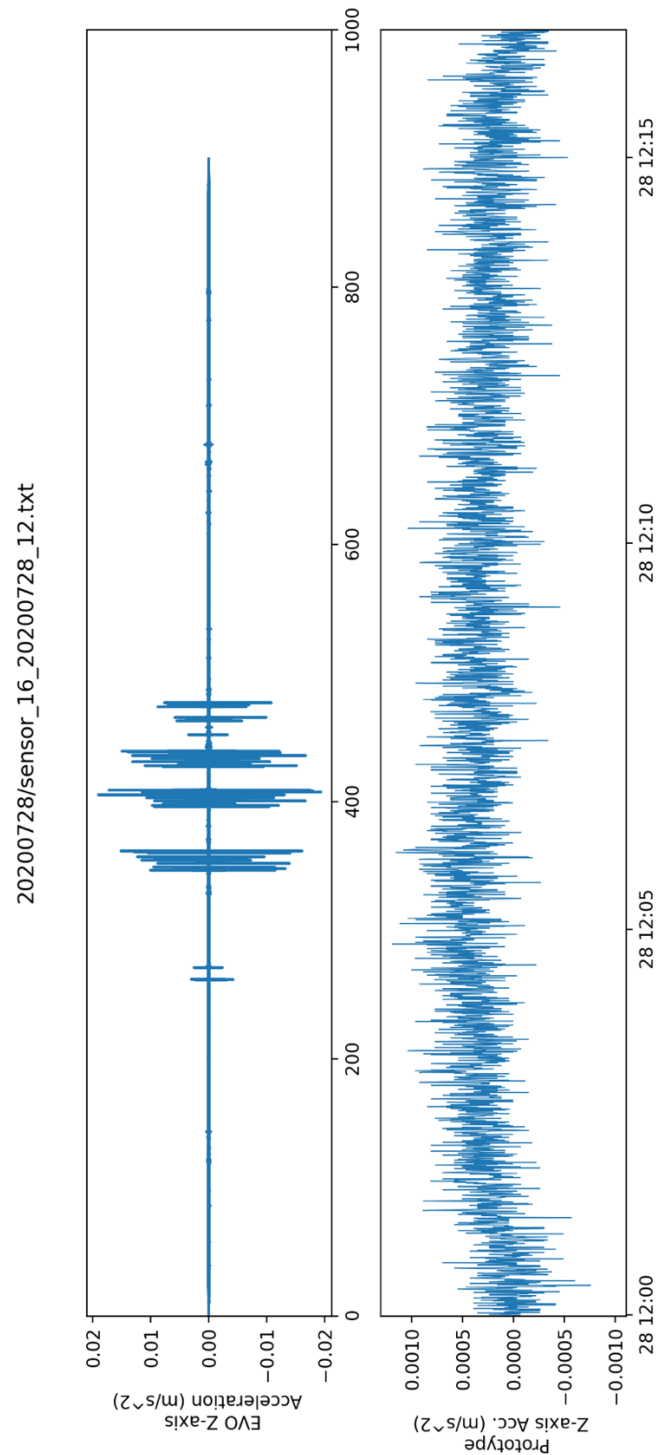
Prototype “Sensor 16”

Figure 75 - Prototype “Sensor 16” with ADXL355 at 4Hz taken at 12h 2020-07-28 during the first 15 minutes. The sensor does not show any detection. The prototype misses all signals. Given the strength of the signals, it is likely that the sampling frequency was not adequate to measure the signals of interest. This matter is further analysed in section 7.4.5. Moreover, a drift is visible in the magnitude value, indicating that the sensor operation is not adequate for use at this sampling rate.

Prototype “Sensor lis3dhh_0002”

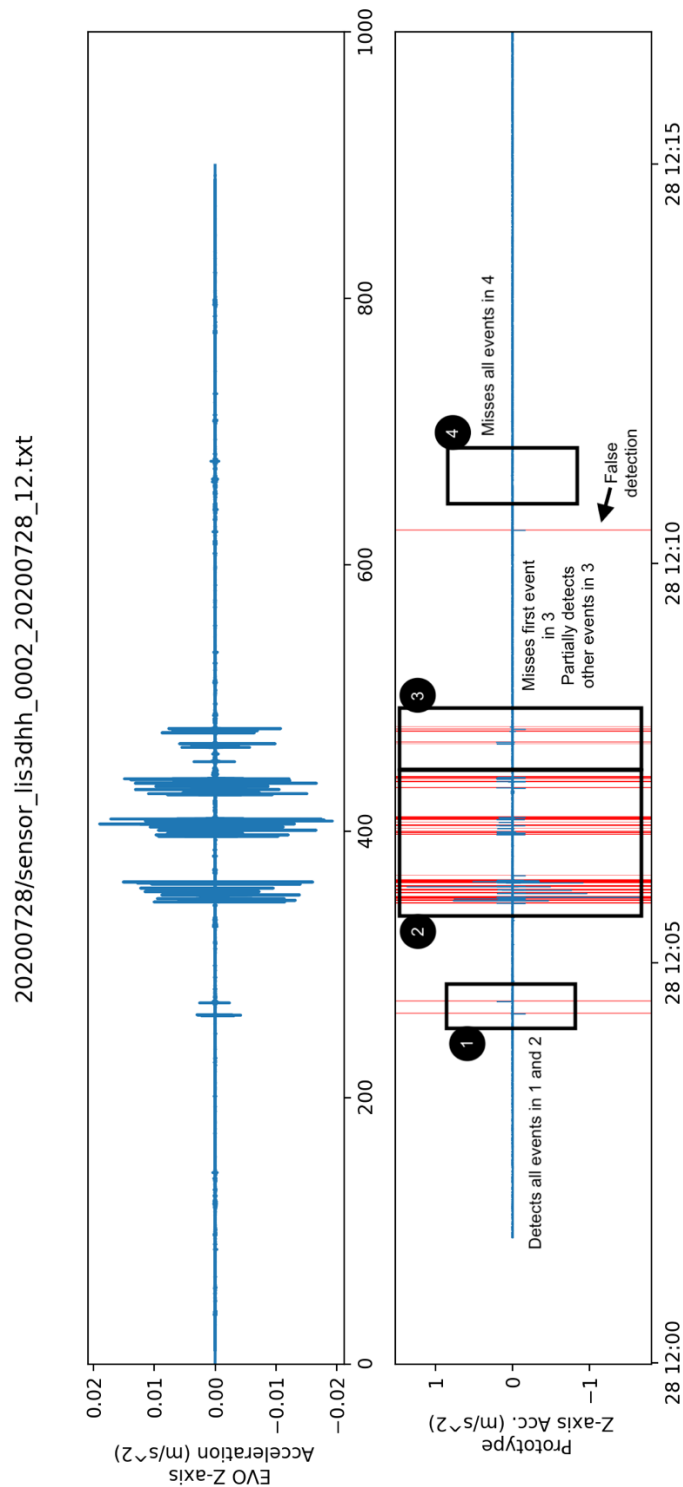


Figure 76 - Prototype “Sensor” with LIS3DHH at 100Hz taken at 12h 2020-07-28 during the first 15 minutes. Detections are represented by vertical columns in red. The prototype detects all signals (1), (2) and partially (3), but misses (4). There is also a false detection before (4). Moreover, the amplitude of the measurements is quite wide, when comparing with the EVO station and the previous sensors. The prototypes’ recorded amplitude is analysed in more detail in section 7.4.4.3.

7.4.4.3 Multiple Sensor Data Analysis

This subsection presents a comparative analysis between different prototypes in detecting signals. Therefore, only EVO station and prototypes 10, 13, 17 and lis3dhh_0002 are considered.

Sensors with ADXL355: Amplitude and Time

Measurements pertaining to 2020-07-28 at 12h (UTC time) for the three prototypes 10, 13 and 17 are presented in Figure 77 (Z-axis offset removed, observation of the three signals) and Figure 78 (time window pertaining to signal 2.1). Measurements include magnitude acceleration value and acceleration in axis X, Y and Z.

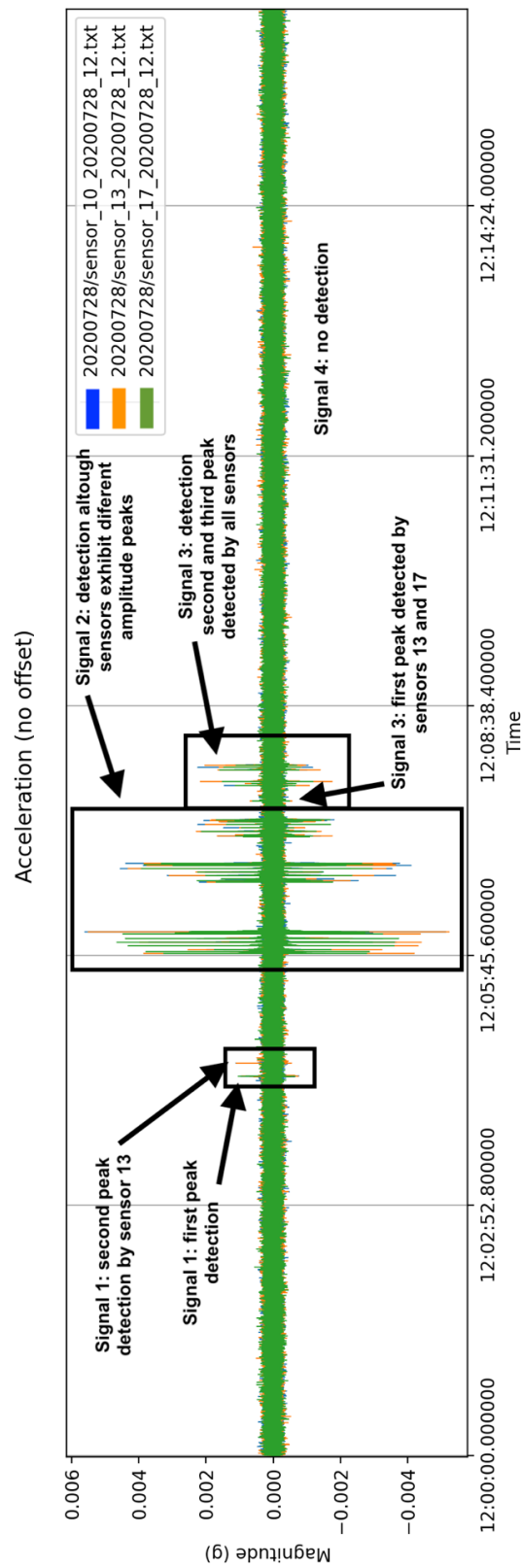


Figure 77 – Time series measurements for Sensors 10, 13 and 17 (using ADXL355 at 125Hz): time window of interest. The three sensors operate at the same frequency and yield similar measurements: however, differences are noted in recorded amplitude and in detection capability (see signals 1 and 3). No sensor detected signal 4.

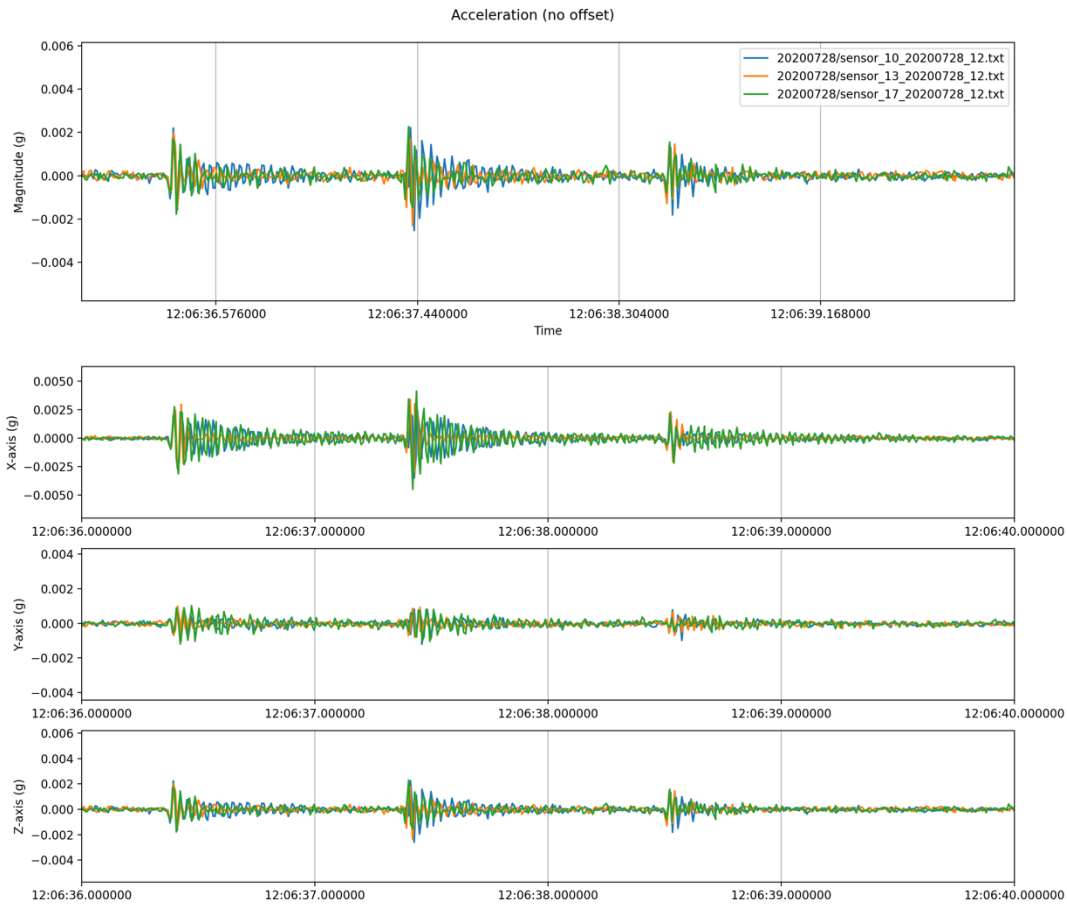


Figure 78 – Time series measurements for Sensors 10, 13 and 17 (using ADXL355 at 125Hz): time window of interest pertaining to signal 2.1. The three sensors operate at the same frequency and yield similar measurements; however, differences are noted in recorded amplitude and in detection capability (see signals 1 and 3). No sensor detected signal 4.

As expected, since the prototypes operate with the same sensor at the same frequency, they yield a similar output in amplitude, although a few “peaks” differ in intensity. It is also relevant to note that sensors 10 and 13 (but not 17) captured the second peak of signal (1) that occurred close to 12:05:00 (see Figure 77). Moreover, the first peak of signal (3) is recorded by sensor 13 and 17, but not by sensor 10.

Figure 79 provides a closer look into recorded signal close to 12:06:36 (signal (2.1)) allowing better observation of amplitude and attenuation over time.

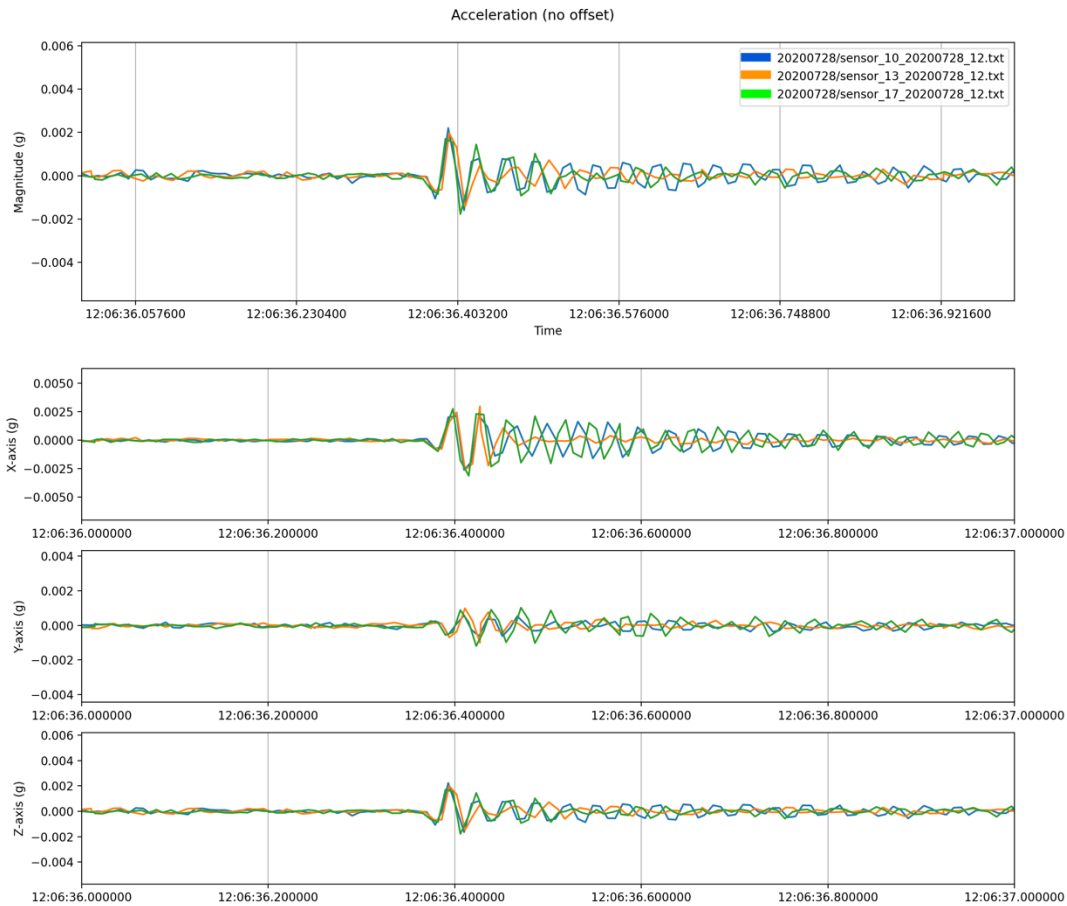


Figure 79 – Time series measurements for Sensors 10, 13 and 17 (using ADXL355 at 125Hz): time window of interest pertaining to first event in signal 2.1. The recorded initial amplitude is similar; however, it is noted different attenuation over time: sensor 13 exhibits higher attenuation over time than sensors 10 and 17. The highest difference is visible in the X-axis.

The data gathered from the three ADXL355 prototypes operating at 125Hz yield similar outputs in overall, concerning detection capability and amplitude over time. Concerning detection, minor differences were noted, with sensor 10 and 17 missing more detection events than sensor 13. The number of false detections was marginal. Differences are also noted in signal attenuation after the occurrence of an event: shown in Figure 79, sensor 13 exhibits higher attenuation over time than sensors 10 and 17.

Sensors with ADXL355 and LIS3DHH: Amplitude and Time

A prototype was also deployed using sensor LIS3DHH at 100Hz, yielding results in amplitude that differ significantly from the ADXL355 prototypes, as presented in Figure 80 and Figure

81. It is immediately visible that, when a signal occurs, LIS3DHH produces a response with a significant higher amplitude than ADXL355.

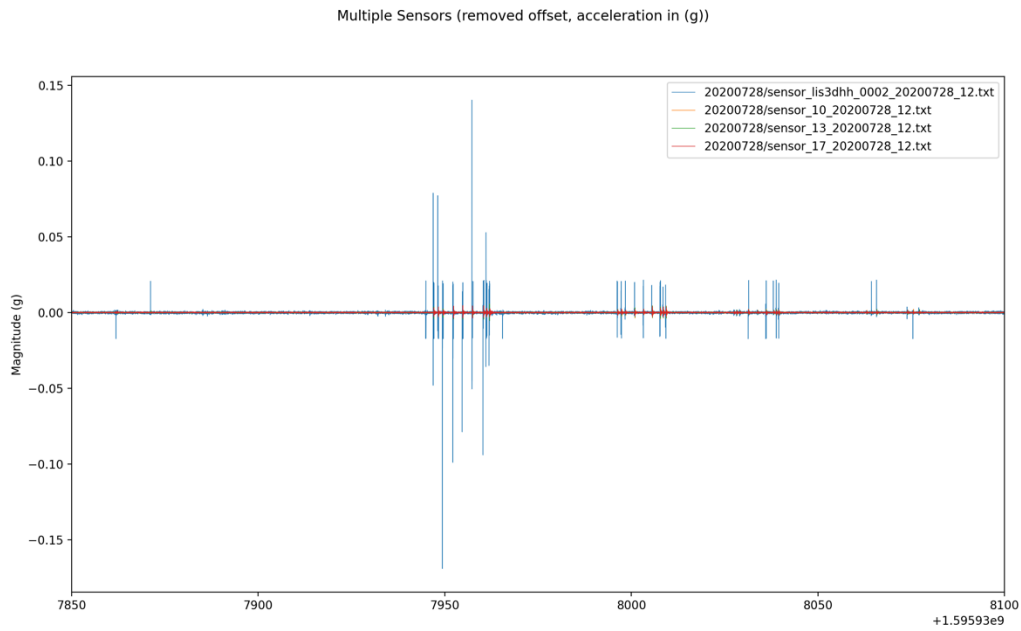


Figure 80 - Measurements for sensors LIS3DHH_0002 and ADXL (10, 13, 17): 15 minutes duration

Figure 81 allows a more detailed observation of amplitude and time difference between LIS3DHH and ADXL355.

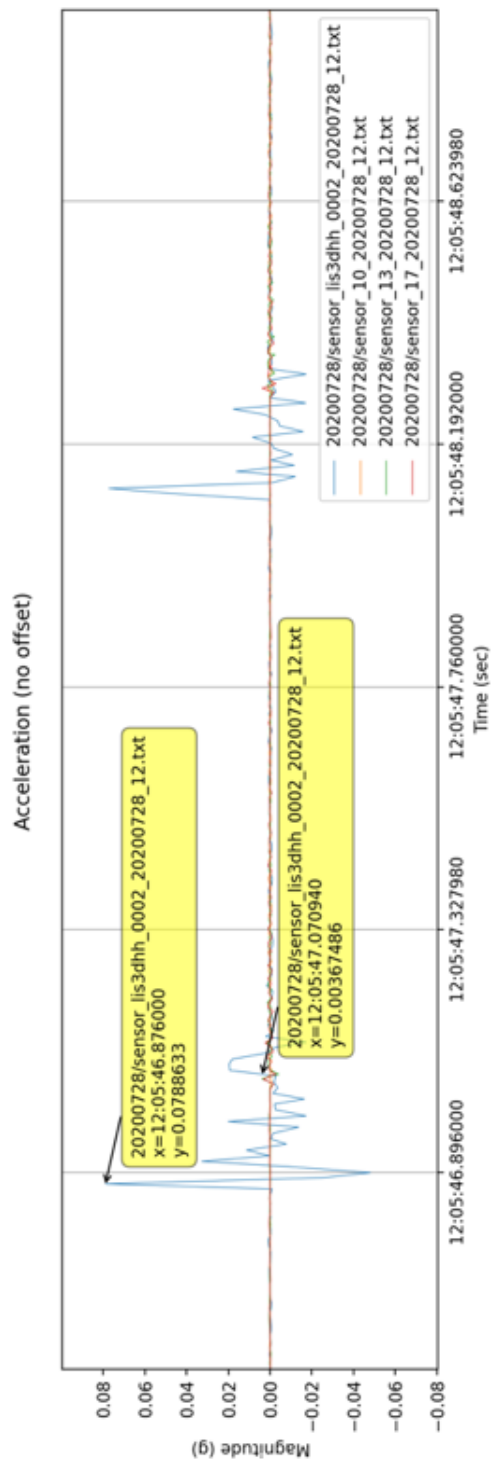


Figure 81 - Measurements for sensors LIS3DHH and ADXL355 (sensors 10, 13, 17): zoom in to observe amplitude and time difference. The annotations show a time and amplitude difference among prototypes pertaining to the same event. In addition to a time delay, LIS3DHH records a signal with an amplitude higher (more than 20x) than ADXL355.

Figure 81 further illustrates the high amplitude of LIS3DHH_0002 recorded signals, making observation of ADXL signals difficult. LIS3DHH_0002 exhibits a signal magnitude that is significantly higher than the ADXL355 sensors: the annotated box shows a magnitude value of 78.86mg and 3.67g for LIS and ADXL355 respectively. Thus, for the shown signal, LIS yields an amplitude that is more than 21 times higher than ADXL355.

Moreover, LIS3DHH_0002 recorded signals do not form a consistent waveform.

From the annotations in Figure 81, it is also visible that LIS3DHH_0002 has a time difference of about 195ms from the ADXL355 sensors. While NTP worked well for the ADXL355 sensors, it yields a time offset between LIS3DHH and ADXL355.

Sensors with ADXL355 and EVO: Amplitude and Time

A comparison between measurements obtained with EVO and ADXL355 is presented in Figure 82, Figure 83 and Figure 84.

It is noted that measurements obtained for ADXL355 are now converted to m/s^2 scale. The analysis measurements on Z-axis (vertical axis).

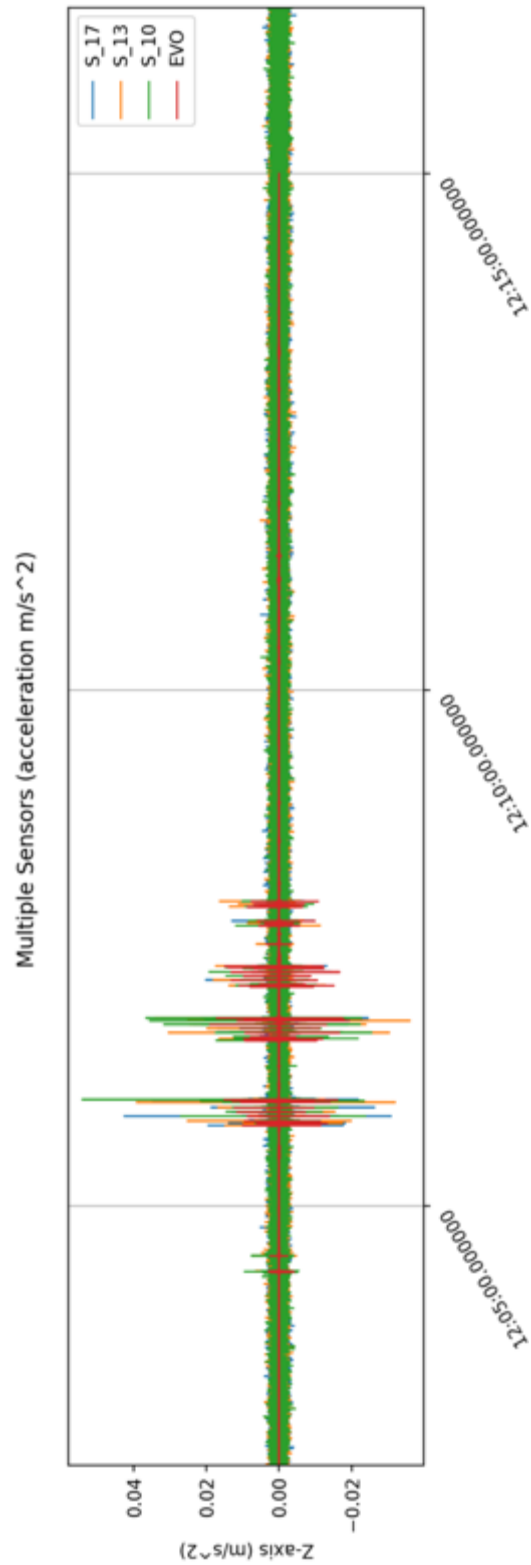


Figure 82 - Measurements for EVO and ADXL355 (sensors 10, 13 and 17). The following is noted: (a) ADXL355 self-noise is higher than EVO's; (b) signal (4) is barely visible and its amplitude is below ADXL355 self-noise (thus is not observable); (c) ADXL355 recorded amplitude is higher than EVO. In particular, signal (1) maximum amplitude is close to the ADXL355 self-noise level; however, sensors 10 and 13 are still able to detect them.

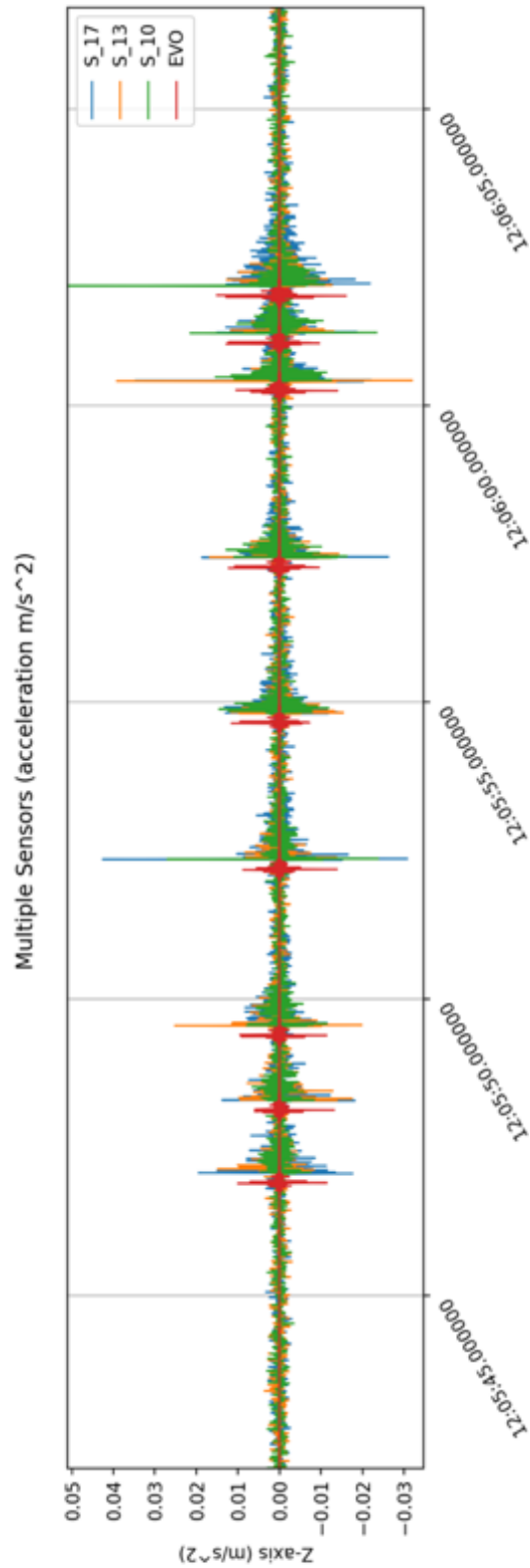


Figure 83 - Measurements for EVO and ADXL355 (sensors 10, 13, 17): close look in (2.1) signals of interest.

This view allows observing the increase in amplitude in ADXL recorded signal over EVO, as well as a time delay. It is noted that, in some events, ADXL magnitude can be several times (up to 5x) higher than EVO's. See next figure for a more in-depth analysis.

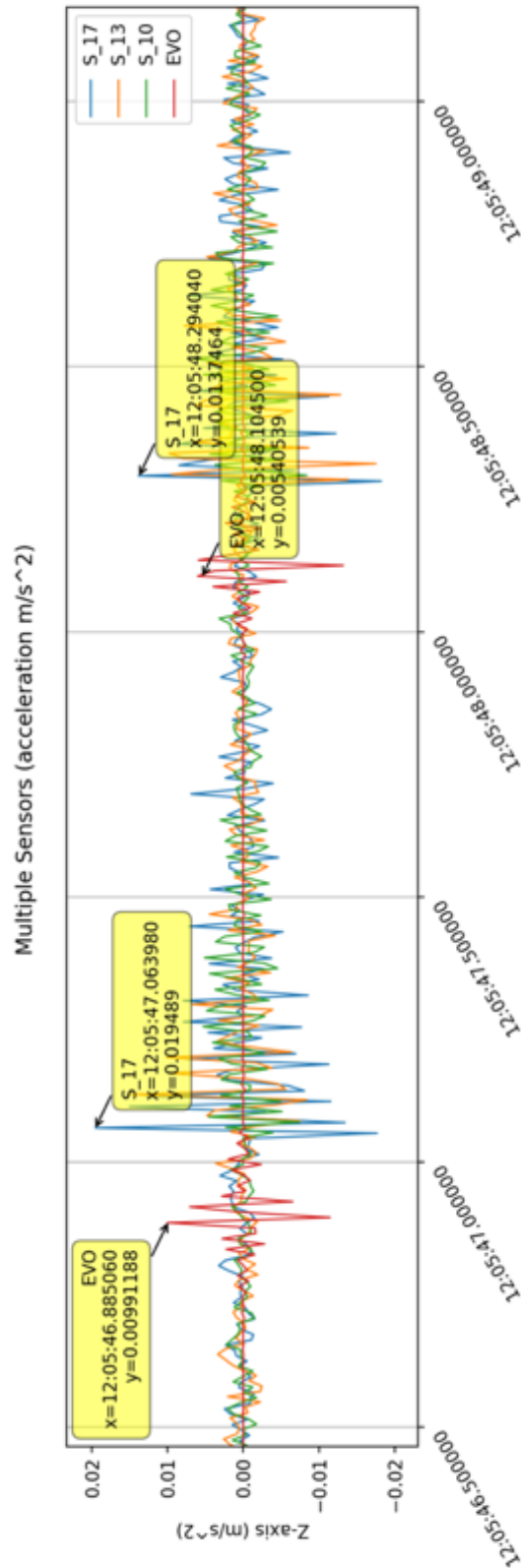


Figure 84 - Measurements for EVO and ADXL355 (sensors 10, 13, 17): zoom in to observe amplitude and time difference. The annotations show a time and amplitude difference among prototypes pertaining to the same event. Specifically, ADXL recorded amplitude is about 2x of EVO's. Moreover, ADXL measurements exhibit a time delay of about 200ms in relation to EVO's measurements.

In overall, comparing ADXL and EVO measurements, the following aspects are noted:

- EVO shows significantly lower noise than ADXL355. ADXL355 exhibits variations in the observed Z-axis while EVO seems to be stable.
- ADXL yields a higher signal amplitude than EVO. Looking into the annotations in Figure 84, it can be seen that the first peak reaches 0.0099m/s^2 for EVO and 0.0195m/s^2 for ADXL355 (sensor 17).
- Between ADXL355 sensors, slight differences are also observed in amplitude and damping: sensor 17 yields the highest amplitude of all; sensor 10 has the smallest damping. From Figure 83 however, it is visible that the maximum amplitude value differs across different sensors, thus this behaviour is not predictable. Future work should consider finding appropriate filters to produce consistent measurements.
- Although ADXL355 sensors seem to be well time synchronised, there is a time offset with EVO of about 200ms. Since EVO is synchronised using GPS, its time records are assumed to be correct, thus it is necessary to further analyse improvements or alternate (to NTP) time synchronisation mechanisms for the prototypes.

7.4.5 Frequency Analysis

In this subsection, a frequency analysis is presented using two techniques: the Discrete Fourier Transform (DFT) and a Spectrogram. In this analysis, only data collected from prototypes based on ADXL355 (sensors 10, 13 and 17) are presented.

The following transformations are applied to the measurements:

- ‘interp’ (linear interpolation) to resampling signals to 100 Hz.
- ‘detrend’ to remove mean and possible trends (or bias).
- ‘taper’ using the “Hann” window with maximum percentage of 5%.
- ‘bandpass’ filter using 0.5 Hz and 50 Hz as minimum and maximum frequency respectively. Since the sampling rate is 100Hz, the Nyquist frequency is 50Hz.

Results are presented next.

7.4.5.1 DFT Frequency Analysis

The DFT is presented for each axis (X, Y and Z) for sensors 10, 13 and 17 considering the time interval pertaining to the first event in (2.1.1), specifically between 2020-07-28T12:06:36 and 2020-07-28T12:06:37 (one second duration).

For comparison purposes, the EVO DFT is also presented.

These intervals were chosen in order to present a DFT containing signal information and not just noise. It is also noted that measurements obtained for ADXL355 are converted to m/s^2 scale.

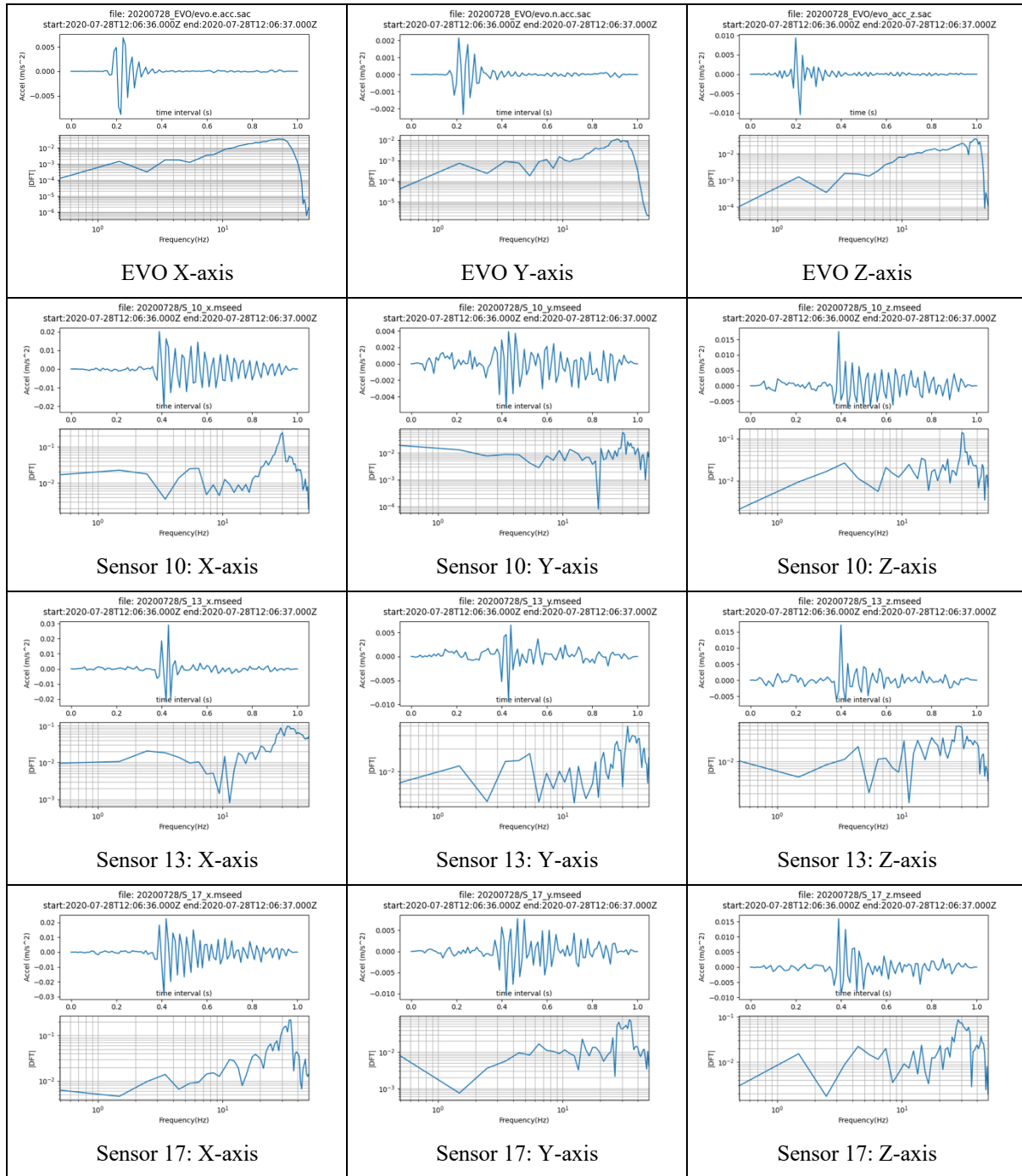


Figure 85 - DFT for time interval pertaining to first event in (2.1.1). EVO, sensor 10, sensor 13 and sensor 17 measurements are presented in the first, second, third and fourth row, respectively. The first column presents values recorded for the X-axis, the second column presents values recorded for the Y-axis and the third column presents values recorded for the Z-axis.

EVO registers in the Z-axis the signal with highest amplitude, followed by X-axis and then Y-axis. EVO measurements generate a regular waveform in each axis and, in overall, their resulting DFT increases with frequency from approximately 0.001 m/s² at 1Hz, reaching an

amplitude peak of about 0.04 m/s^2 close to 30-40Hz. EVO produces similar DTF in all 3-axis.

ADXL prototypes register in the X-axis the signal with highest amplitude, closely followed by Z-axis and then Y-axis. The measurements in the Y-axis exhibit a low amplitude, where it is also visible the presence of sensor self-noise before and after the signal, thus “distorting” the signal and the generated DFT.

The X-axis exhibits a clear response to the event; However, sensors 10 and 17 produce less attenuation in amplitude than EVO and sensor 13. Their DFT show a clear gain peak (close to 0.2 m/s^2) between 30 and 40 Hz. At lower frequencies, the resulting DTF is somewhat different between them: sensors 10 and 13 generate a close to flat response (at 0.02 and 0.01 m/s^2 respectively), while sensor 17 is below 0.01 m/s^2 . This could be a result of absence of signal (and thus prevalence of noise) at these frequencies.

The Z-axis also exhibits a clear response to the event and, once again, sensors 10 and 17 produce less attenuation in amplitude than EVO and sensor 13. The presence of sensor noise is also more visible than for the X-axis (resulting from a lower signal amplitude). Concerning the generated DFT, a gain peak is visible close to 30Hz, especially for sensor 10. However, in overall, the generated DTF is somewhat irregular.

It is also worth to mention that, looking into the time chart, comparing ADXL355 measurements with EVO, it is visible some amplitude excess, time delay and different attenuation factors, which corroborate the analyses done in section 7.4.4.3.

7.4.5.2 Spectrogram Analysis

This subsection presents a spectrogram analysis for the time interval pertaining to the first event of signal (2.1.1) specifically between 2020-07-28T12:06:36 and 2020-07-28T12:06:37 (one second duration) for sensors 10, 13 and 17. For comparison purposes, the EVO DFT is also presented.

The python library “obspy” was used to generate the spectrograms, scaled to show the values range of interest. In order to facilitate the interpretation, the measurement time series is presented on top of the spectrogram.

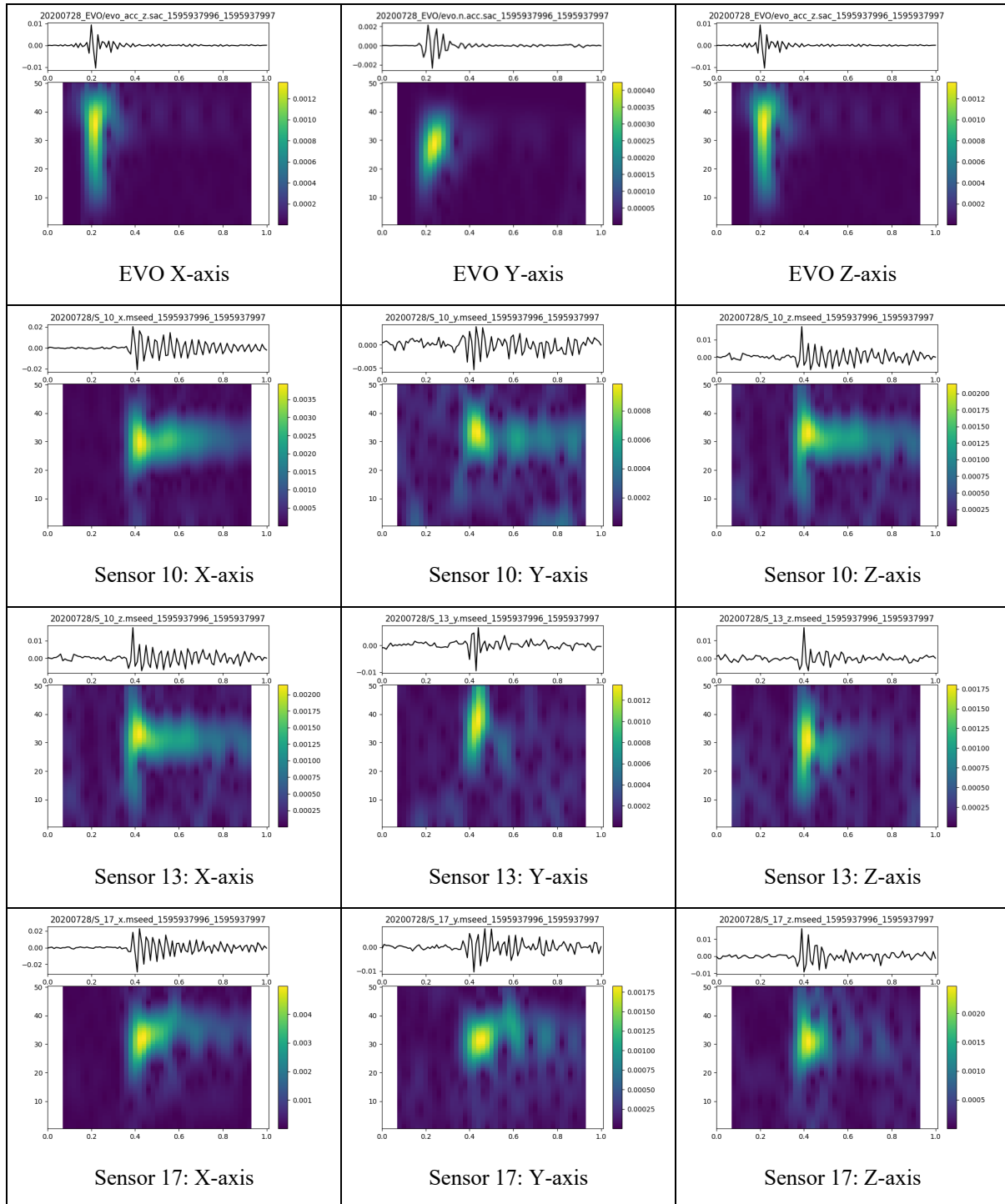


Figure 86 - Spectrograms related with the first event in signal (2.1.1) for sensors 10, 13 and 17 and EVO.

Sensors and EVO consistently show that frequencies between 30 Hz and 40 Hz are more dominant. Where the signal is stronger, EVO shows the presence of a wider range of frequencies (vertical plane of the spectrogram) than the ADXL sensors. The ADXL sensors however keep the presence of frequencies over a longer period of time (horizontal plan of the spectrogram) than EVO (ADXL has a lower signal attenuation factor than EVO). A time difference is also visible between ADXL sensors and EVO.

7.4.6 Probabilistic Power Spectral Density

A key aspect in seismology consists in understanding the noise characteristics of a sensor, which can be calculated based on the distribution of power spectral density. As mentioned in section 2, Peterson's **standard model of ambient earth noise** identifies a **new low noise model (NLNM)** and **new high noise model (NHNM)** (Peterson, 1993) establishing limits for electronic self-noise that should be present in seismometers. As mentioned before, a main limiting factor in the application of MEMS accelerometers in seismology is the presence of sensor noise, typically well above Peterson's NHNM.

In this section, the distribution of power spectral density is determined using "obspy" Probabilistic Power Spectral Densities (PPSD) (McNamara and Boaz, 2005) function for the EVO station and prototypes "Sensor 10" and "Sensor lis3dhh_0002". The PPSD is built by determining an instrument's amplitude response as a function of frequency, ideally in rest conditions, over multiple periods of time. The PPSD is obtained by "overlaying" the several periods and thus obtaining the probability function.

Figure 87 shows the PPSD obtained for the EVO station for one day (28-July-2020, using a 30-minute period forming a total of 47 segments). It shows EVO exhibiting measurements close to NLNM, which are consistent with the STS-2 datasheet (STS-2 Datasheet).

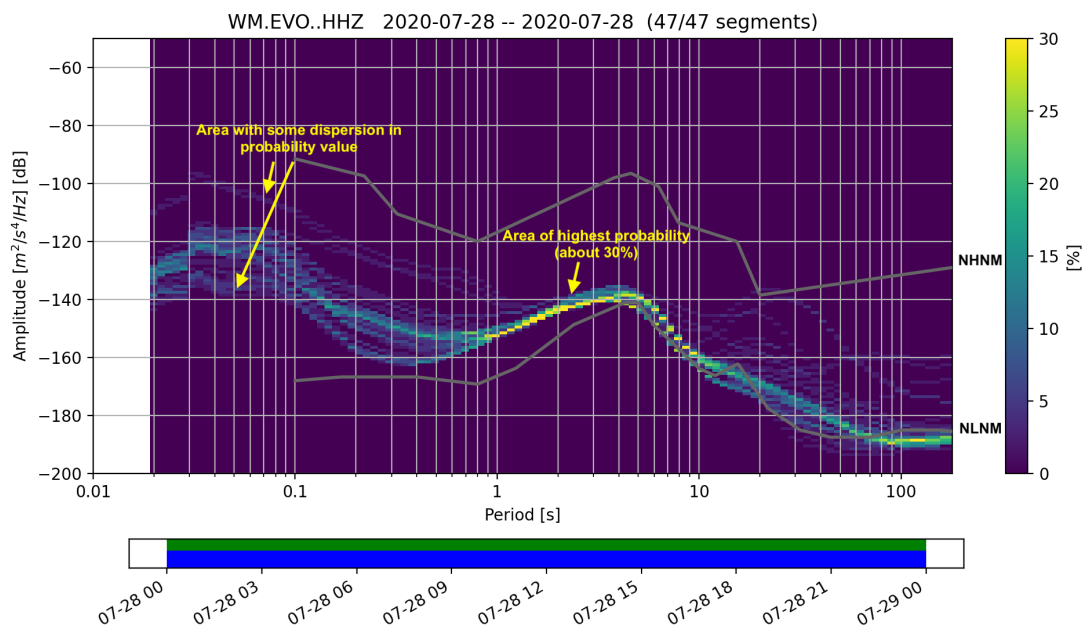


Figure 87 - EVO PPSD (time period 28-July-2020, 1 day). The lines pertaining to NHNM and NLNM are shown. It is also highlighted an area with high probability (centre annotation with yellow arrow indicating about 30% probability of occurrence) and another area (left annotation) where some dispersion in measurements is visible. Importantly, EVO measurements always stay below NHNM and are close to NLNM.

Figure 88 shows the PPSD obtained for the ADXL355 (Sensor 10) prototype for the period of one day (29-July-2020, using a 60-minute period forming a total of 24 segments). As expected and previously reported, the sensor exhibits a “high” electronic self-noise, thus being well above NHHM. It is noted that the PPSD value reaches -60dB after 0.4 seconds and is below -140dB after 100 seconds.

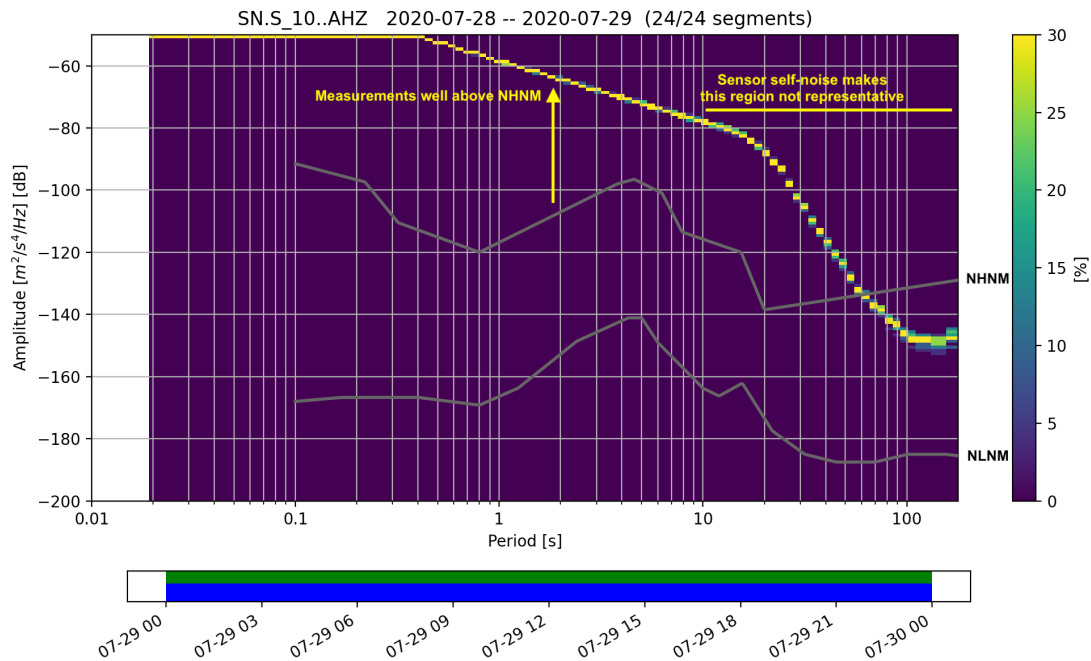


Figure 88 - Prototype “Sensor 10” PPSD (time period 29-July-2020, 1 day). The lines pertaining to NHHM and NLNM are shown. Sensor 10 measurements are well above NHHM for the region of interest of the sensor. The amplitude decreases above a 10 seconds period results from the sensor high-pass filter set to remove presence of sensor noise.

Figure 89 shows the PPSD obtained for the LIS3DHH (Sensor lis3dhh_0002) prototype for the period of one day (29-July-2020, using a 60-minute period forming a total of 24 segments). As expected and previously reported, (1) the sensor exhibits a “high” electronic self-noise, thus being well above NHHM and (2) LIS3DHH electronic self-noise is above ADXL355. It is noted that the PPSD value reaches -60dB after 4 seconds and is close -140dB after 100 seconds.

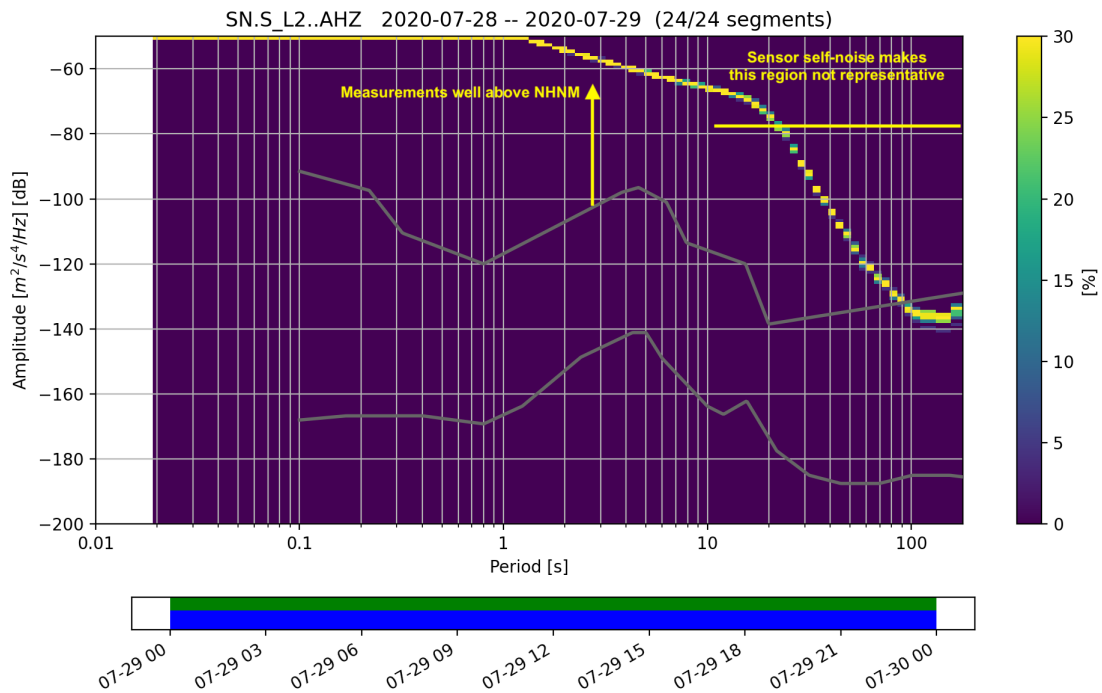


Figure 89 - Prototype “Sensor lis3dhh_0002” PPSD (time period 29-July-2020, 1 day). The lines pertaining to NHHM and NLNM are shown. Sensor 10 measurements are well above NHHM for the region of interest of the sensor. The amplitude decreases above a 10 seconds period results from the sensor high-pass filter set to remove presence of sensor noise.

The prototypes PPSD show the limitation of MEMS accelerometers in seismology: being well above Petterson’s NHHM, MEMS accelerometers’ applications should be limited to observation of strong motion and “high” frequencies (above 1Hz). In these particular cases, MEMS accelerometers will be better sources to use to reconstruct the signal, since they achieve higher amplitude ranges than seismometers (with “clip” levels around 0.5g).

7.4.7 Analysis from Recent Seismic Activity

During the writing of this thesis, it was possible to monitor and detect seismic activity using the developed prototypes, specifically:

- Event 1: Magnitude 3.4 (ML) with epicentre about 8 km east of Loures (Lisbon district), recorded 18-03-2021 at 9h51 (local time) (source: <https://www.ipma.pt/pt/geofisica/comunicados/>, accessed 27-March-2021).

- Event 2: Magnitude 2.5 (ML) with epicentre about 8 km north of Viana do Alentejo (about 10 km from EVO station) recorded 24-March-2021 at 14h30 (local time) (source: <https://www.ipma.pt/pt/geofisica/comunicados/>, accessed 27-March-2021).

The analysis of the prototypes' collected data related to the above events is presented next. Only the ADXL-based prototypes are used, namely: sensor_10, sensor_13 and sensor_17 (operating at 125 Hz). Where relevant, data from sensor_15 (operating at 15 Hz) and sensor_16 (operating at 4 Hz) is also presented.

The analysis includes:

- Recorded acceleration measurements (magnitude value and 3-axis) over time and detectability capability.
- DFT frequency analysis.
- Spectrogram analysis.

7.4.7.1 Event 1: Magnitude 3.4 (ML) recorded 18-March-2021 at 9h51 (local time)

IPMA reported a seismic event with 3.4 magnitude (ML) and epicentre 8 km east of Loures (Lisbon district) that occurred at the 18-March-2021 around 9h51 (local time)²⁵. The location of the event epicentre, as well as the prototypes location (SSN), is presented in Figure 90 (source: IPMA website, accessed 27-March-2021).

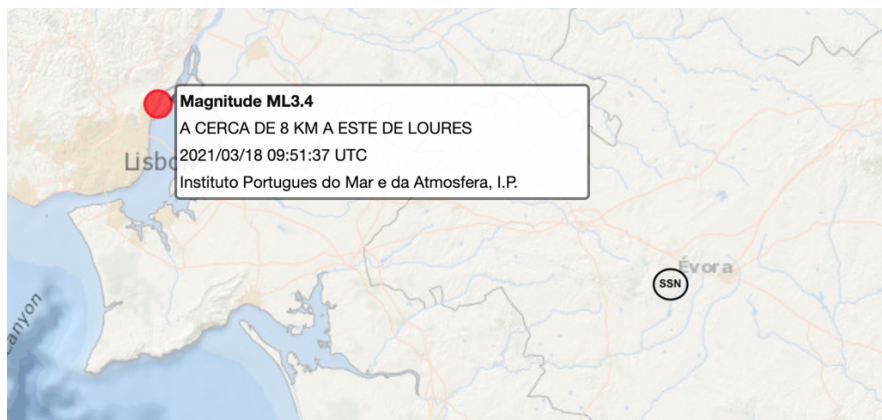


Figure 90 - Location of the seismic event with 3.4 magnitude (ML) with epicentre 8 km east of Loures (Lisbon district) reported by IPMA. The location of the prototypes is presented in the SSN circle. The prototypes are located at a distance of about 140 km from the epicentre.

²⁵ When the event occurred, Portuguese local time was the same as UTC time.

The event was recorded by EVO station, as presented in Figure 91, showing the arrival of the P-wave close to 9:51:54 (bottom).

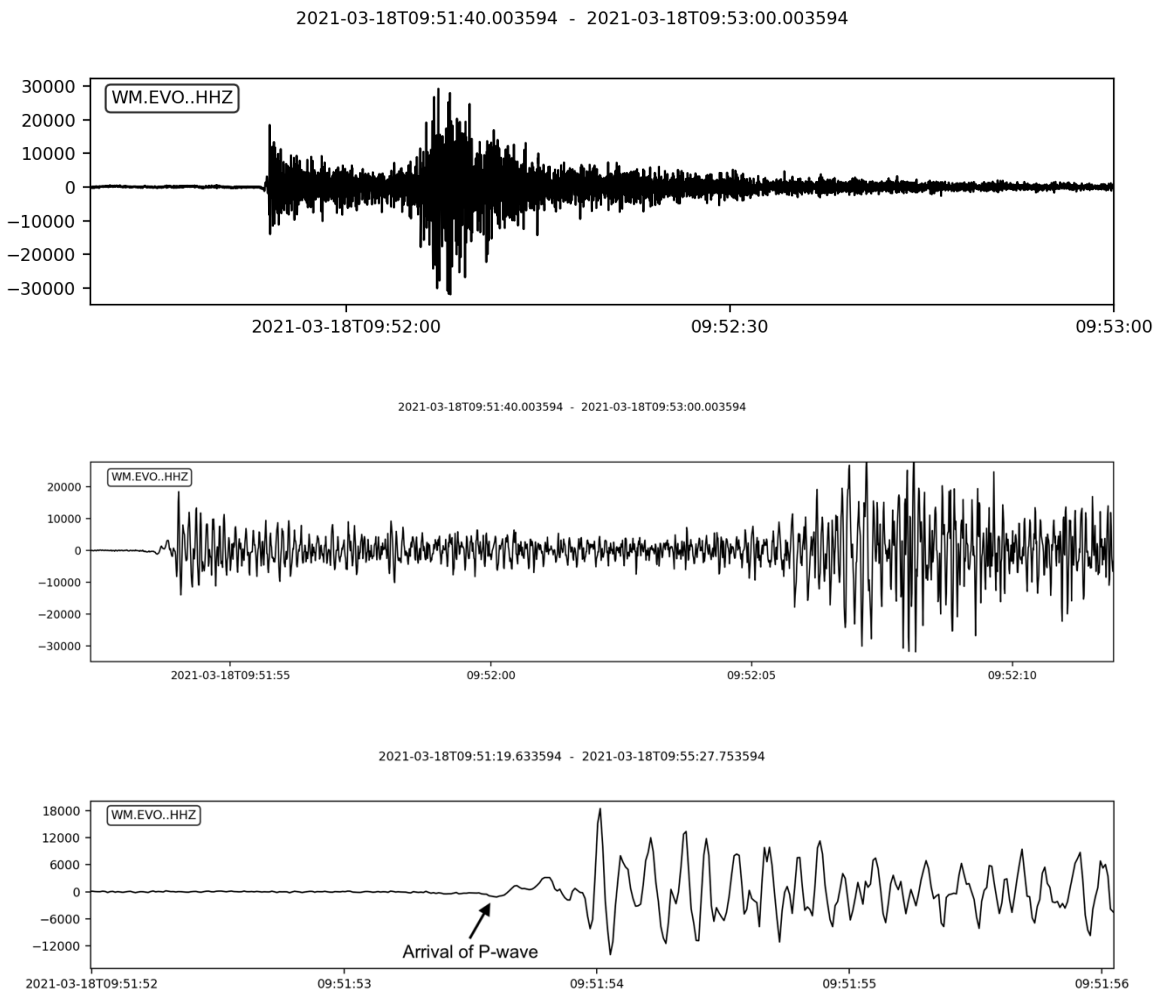


Figure 91 - EVO recording in the Z axis (HHZ) of a 3.4 magnitude event that occurred at 18-March-2021 for a 100 seconds time window (top), a 60 seconds time window (middle) and a 4-second window (bottom). The figure's Y-axis shows the raw amplitude value as recorded by EVO. The P-wave is detected close to 9:51:53 (bottom), followed by the start of the S-wave close to 9:52:05. At 9:53:00, EVO still records level of ground activity above what was recorded before the event.

7.4.7.1.1 Recorded signal and detectability of prototypes

Figure 92 shows the recorded accelerometer data for one hour (9:00:00 to 10:00:00 local time) for sensors 10, 13, 17 (operating at 125 Hz) and 15 (operating at 15 Hz). It is noted that sensor 16 (operating at 4 Hz) did not detect any event and therefore is excluded. The accelerometer data is the acceleration magnitude, calculated based on the 3-axis measurements, expressed as a function of g . The acceleration offset is removed by subtracting the acceleration mean value

over the time window. Detections are calculated using the detectability techniques described in section 5.7 for the applicable time window.

Sensors 10, 13, 17 and 15 Measurements

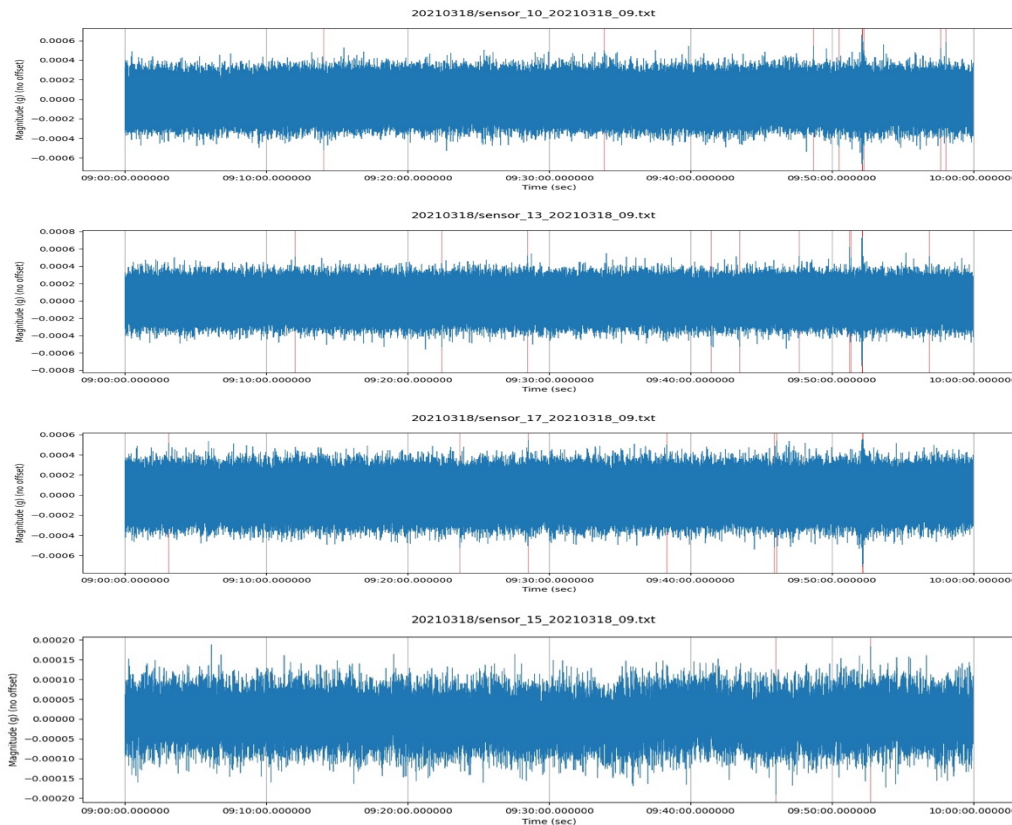


Figure 92 - Overview of acceleration measurements for sensors 10, 13, 17 and, for completeness, 15 over a one hour time window (9:00:00 to 10:00:00 local time). This figure supports the classification of true and false detections of events. Over the set of measurements from sensors 10, 13 and 17, there is only one ‘red’ vertical line that occurs around the same time and it corresponds to the time of the event.

7.4.7.1.2 Recorded signal and detectability over 70 seconds (9:51:50 and 9:53:30 local time)

Recorded accelerometer data is presented for the time-window of interest of 70 seconds (9:51:50 and 9:53:30 local time). Accelerometer data includes the acceleration value for each of the 3-axis. Acceleration is expressed as a function of g. The acceleration offset is removed by subtracting the acceleration mean value over the time window. Detections are calculated using the detectability techniques described in section 5.7 for the applicable time window. It is noted that, since the time window in this subsection differs from the previous one (that used a time window of one hour), detections might differ.

For the purpose of this analysis, only recordings of sensor 17 (operating at 125 Hz) for all 3 axes are shown in Figure 93. After it, recordings in the X-axis for sensors 10, 13, 17 (operating at 125 Hz), 15 (operating at 15 Hz) and 16 (operating at 4 Hz) are presented in Figure 94.

Sensor 17 Measurements

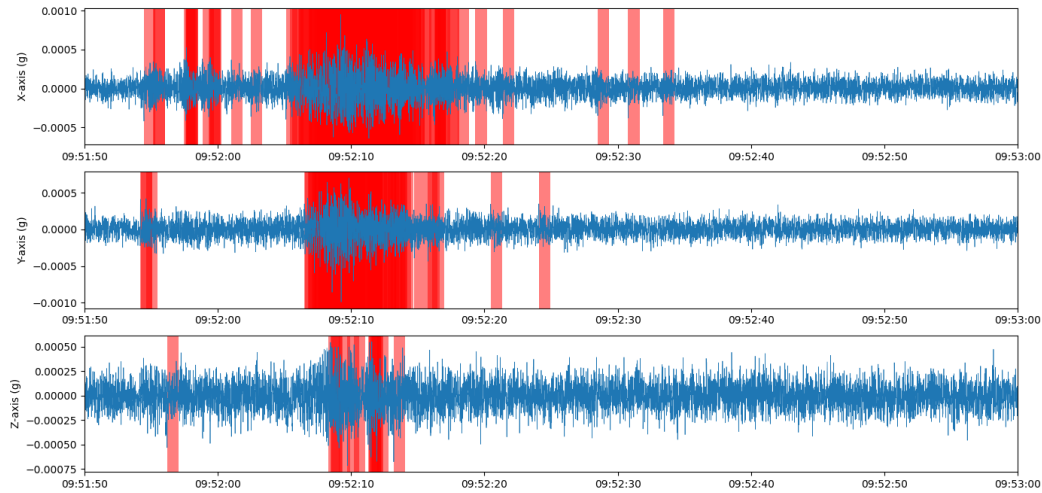


Figure 93 - Overview of acceleration measurements over the three axes for sensor 17 over a 70 seconds time window (9:51:50 and 9:53:20 local time). The X-axis recorded the highest amount of ground motion activity.

First detections start at about 9:51:54. The period with strongest activity starts at 9:52:05, continuing until 9:52:15 (the X-axis continues until 9:52:20). In overall, the presence of sensor noise does not allow observing the presence of weak signals after 9:52:20.

Sensors 10, 13, 17, 15 and 16 Measurements

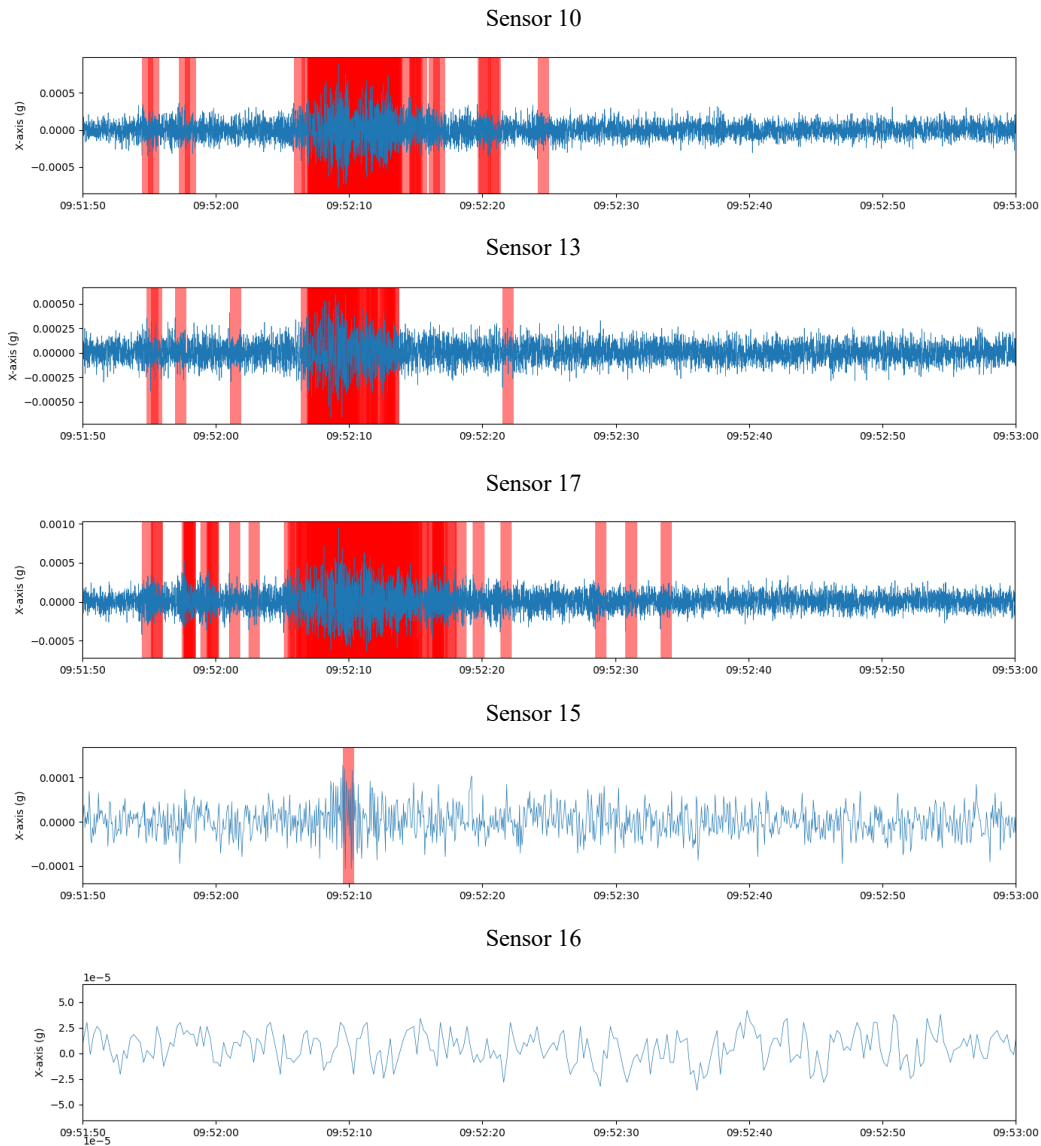


Figure 94 - Overview of acceleration measurements in the X-axis for sensors 10, 13, 17, 15 and 16 over a 70 seconds time window (9:51:50 and 9:53:20 local time). Detections are marked with a ‘red’ vertical rectangle.

Sensors 10, 13 and 17 perform a first detection at about the same time (9:51:54) and detect the periods of strongest activity. Sensor 13 (middle figure) exhibits a higher damping factor than sensors 10 and 17 (see section 7.4.4) thus has lower detection duration. For completeness, sensors 15 and 16 recordings are also shown, were only sensor 15 performs a single detection at 9:52:10, corresponding to the period of highest activity.

Discussion

IPMA’s reported seismic event with 3.4 magnitude (ML) had an epicentre at a distance of about 140 km from the prototypes. Based on the accelerometer data recorded by the ADXL-based prototypes (sensors 10, 13, 15, 16 and 17), it is shown that sensors 10, 13 and 17 (operating at

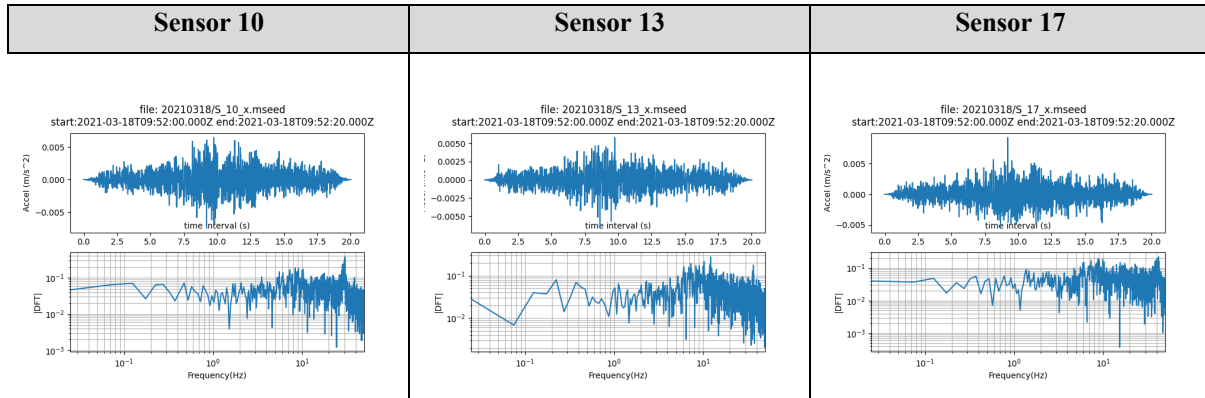
125 Hz) perform a first detection at about the same time (9:51:54) and detect the periods of strongest activity. Sensor 15 barely detected the event (the detection would likely be interpreted as a false positive) and sensor 16 missed the event.

Comparing the obtained empirical results with the conclusions in section 5.7 concerning detectability (which took a conservative approach), observations indicate that the ADXL prototypes operating at 125 Hz exhibit, in real world, better detectability in what regards range. However, the ADXL prototypes operating at lower frequencies did not. In what concerns the latter, it is hypothesized that the relevant seismic frequencies associated with the event occur at frequencies outside what the sensors can observe (i.e., above 7.5 Hz, considering that sensor 15 operates at 15 Hz).

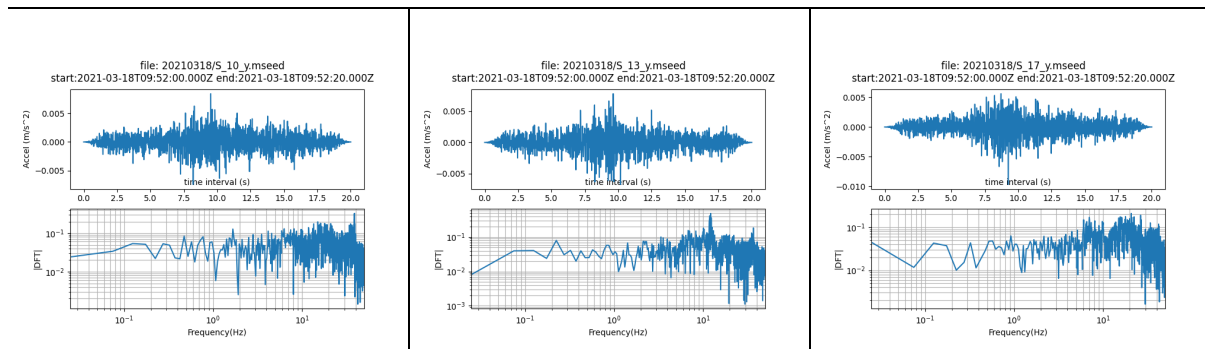
7.4.7.1.3 FFT

In this subsection, a frequency analysis is presented using the Discrete Fourier Transform (DFT). In this analysis, only data collected from prototypes based on ADXL355 (sensors 10, 13 and 17) are presented. This subsection follows a similar approach as the described in section 7.4.5.

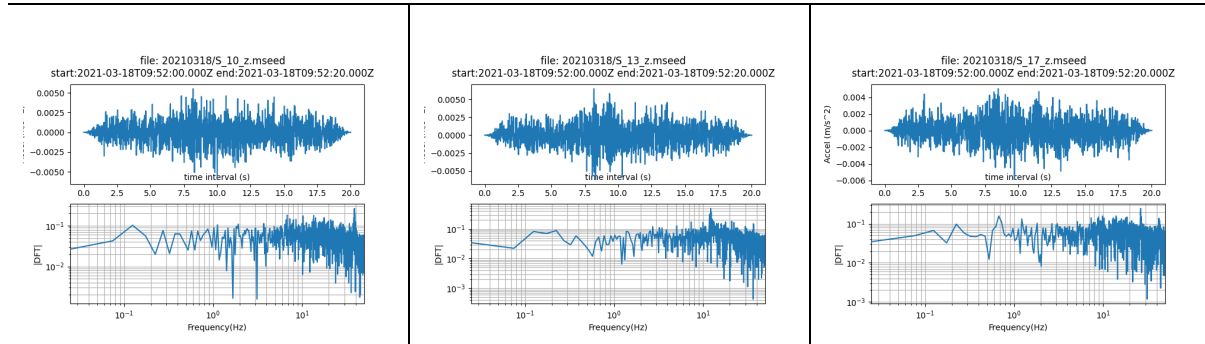
The DFT is presented for each axis (*X*, *Y* and *Z*) for sensors 10, 13 and 17, considering the time interval pertaining to the time window of 20 seconds (9:52:00 and 9:52:20 local time). Recorded measurements over time, considering the applicable time window, are also presented. It is also noted that measurements obtained for ADXL355 are converted to the m/s^2 scale.



In the X-axis, sensor 10 shows a peak close to 30 Hz, sensor 13 shows in addition a peak close to 10 Hz and sensor 17 shows a peak close to 40Hz.



In the Y-axis, sensor 10 shows a peak close to 40 Hz, sensor 13 shows in addition a peak close to 10 Hz, but sensor 17 does not show any significant peak (there is a gain fluctuation between 10 Hz and 40 Hz).



In the Z-axis, sensor 10 shows a peak close to 40 Hz, sensor 13 shows a peak close to 10 Hz (but none after it) and sensor 17 does not show any significant peak.

Figure 95 - DFT related with acceleration measurements from sensors 10, 13 and 17 for a time window of 20 seconds (9:52:00 and 9:52:20 local time). The first row refers to the X-axis, the second row to the Y-axis and the third row to the Z-axis. In overall, the DFT shows a somewhat flat response, where irregularities could be attributed to noise, except where clear peaks appear typically close to 10 Hz, 30 Hz and 40 Hz. Additional remarks are presented in the figures.

7.4.7.1.4 Spectrogram

This subsection presents a spectrogram analysis for a time window of 20 seconds. In this analysis, EVO generated spectrograms (using raw measurements) are used as reference to compare with those generated from prototypes based on ADXL355 (sensors 10, 13 and 17). This subsection follows a similar approach as the described in section 7.4.5.2.

EVO generated spectrograms

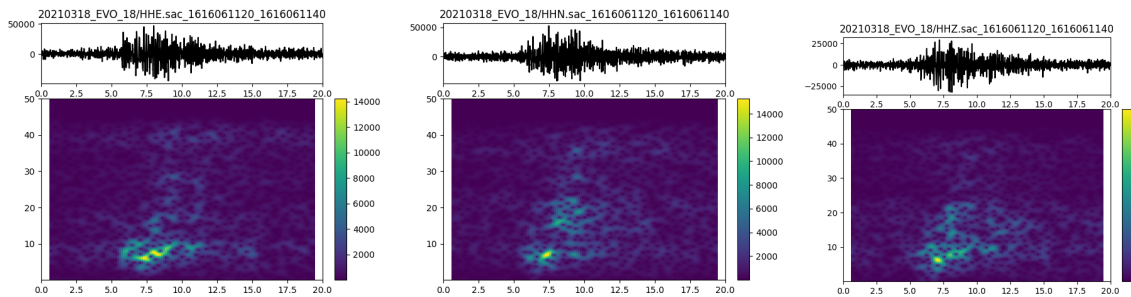
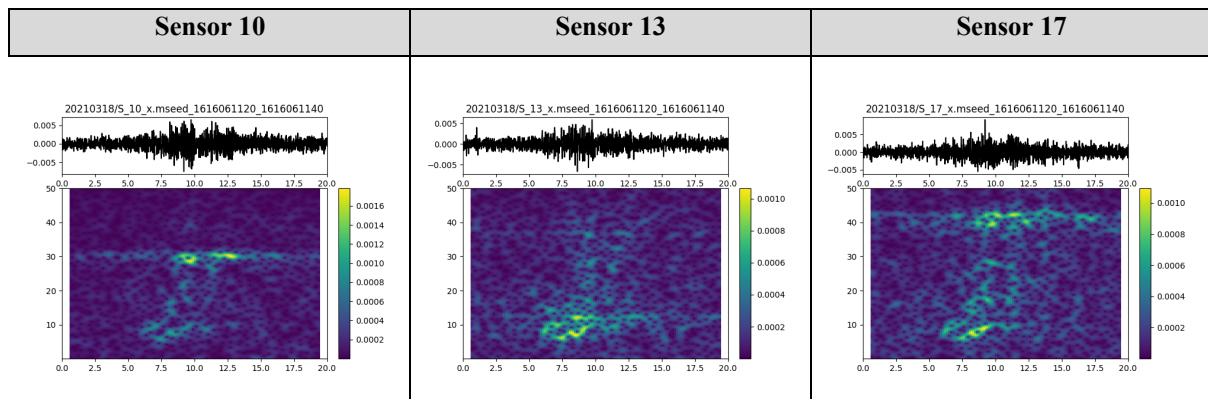
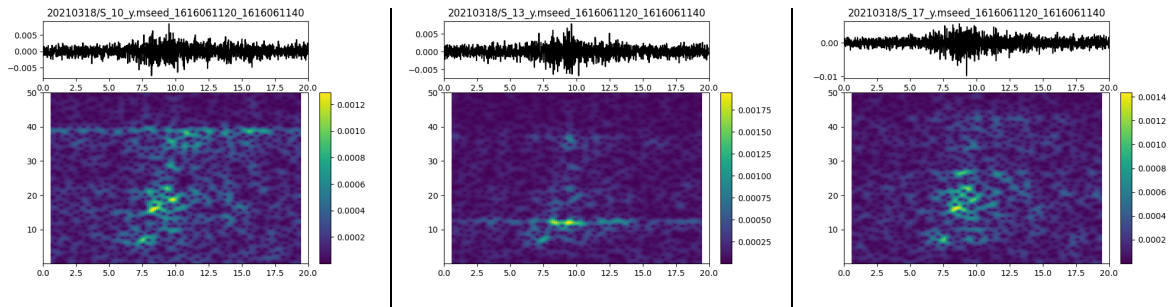


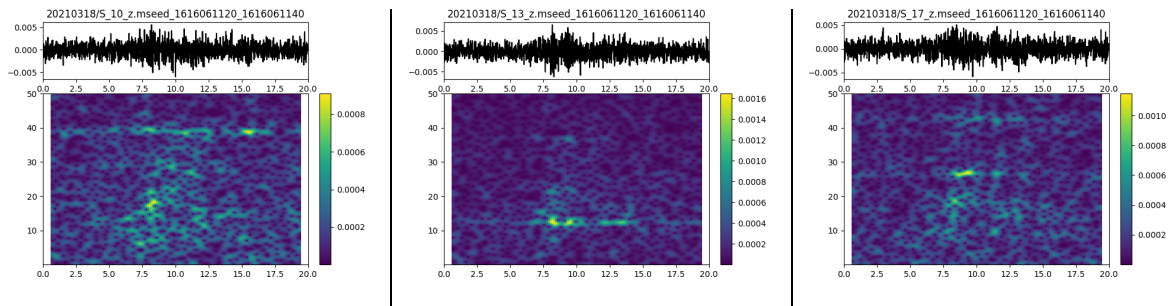
Figure 96 - Spectrograms related with EVO raw measurements for a time window of 20 seconds. The first column refers to EVO X-axis (HHE), the second column to EVO Y-axis (HHN) and the third column to EVO Z-axis (HHZ). In overall, the recorded signal show predominant frequencies around 10 Hz.



In the X-axis, close to the region of maximum signal intensity (10 seconds), sensor 10 dominant frequencies cluster around 30 Hz and slightly at 10 Hz (30 Hz is also dominant over time), sensor 13 dominant frequencies cluster around 10 Hz (10 Hz is also dominant over time) and sensor 17 dominant frequencies cluster around 10 Hz and 40 Hz (40 Hz is also dominant over time). The high dispersion in signal frequencies for sensors 13 and 17 spectrograms indicate presence of noise.



In the Y-axis, close to the region of maximum signal intensity (10 seconds), sensor 10 dominant frequencies cluster around 40 Hz and slightly at 10 Hz and 20 Hz (40 Hz is also dominant over time), sensor 13 dominant frequency is 10 Hz. Sensor 17's presence of signal frequencies range over 10 Hz and 30 Hz (there is no dominant frequency over time). The high dispersion in signal frequencies for sensors 10 and 17 spectrograms indicate presence of noise.



In the Z-axis, close to the region of maximum signal intensity (10 seconds), there is a dispersion of signal over several frequencies, especially for sensors 10 and 17. Sensor 13's dominant frequencies cluster around 10 Hz (10 Hz is also dominant over time).

Figure 97 - Spectrograms related with acceleration measurements from sensors 10, 13 and 17 for a time window of 20 seconds (9:52:00 and 9:52:20 local time). The first column refers to the X-axis, the second column to the Y-axis and the third column to the Z-axis. In overall, the recorded signal produces frequency gains predominantly around 10 Hz and 40 Hz. Additional remarks are presented in the figures.

Discussion

The analysis in the frequency domain provides additional insights concerning the observation of the event of interest. The spectrograms generated from EVO raw measurements reveal that the recorded signal show predominant frequencies around 10 Hz in all X-Y-Z axes. Compared with EVO, the ADXL sensor prototypes exhibit a higher dispersion of signal across several frequencies (being sensor noise a cause). Only sensor 13 shows a dominance of the 10 Hz frequency across all axis. Sensors 10 and 17 also exhibit signal present close to 30 Hz.

Given the frequency characteristics of the event, sensors 15 and 16, operating at 15 Hz and 4 Hz respectively (thus, according to the Nyquist theorem, can only observe up to 7.5 Hz and 2 Hz respectively), missed or barely detected the presence of any event.

It is also noted that sensors produced somewhat different frequency responses to the same signal, which is unexpected considering they use the same MEMS device (i.e., ADXL355) setup with the same parameters (e.g., same sample frequency).

7.4.7.2 Event 2: Magnitude 2.5 (ML) recorded 24-March-2021 at 14h30 (local time)

IPMA reported a seismic event with 2.5 magnitude (ML) and epicentre 8 km north-northwest of Viana do Alentejo (Évora district) that occurred at the 24-March-2021 around 14h30 (local time)²⁶. The location of the event epicentre, as well as the prototypes location (SSN), is presented in Figure 98 (source: IPMA website, accessed 27-March-2021).

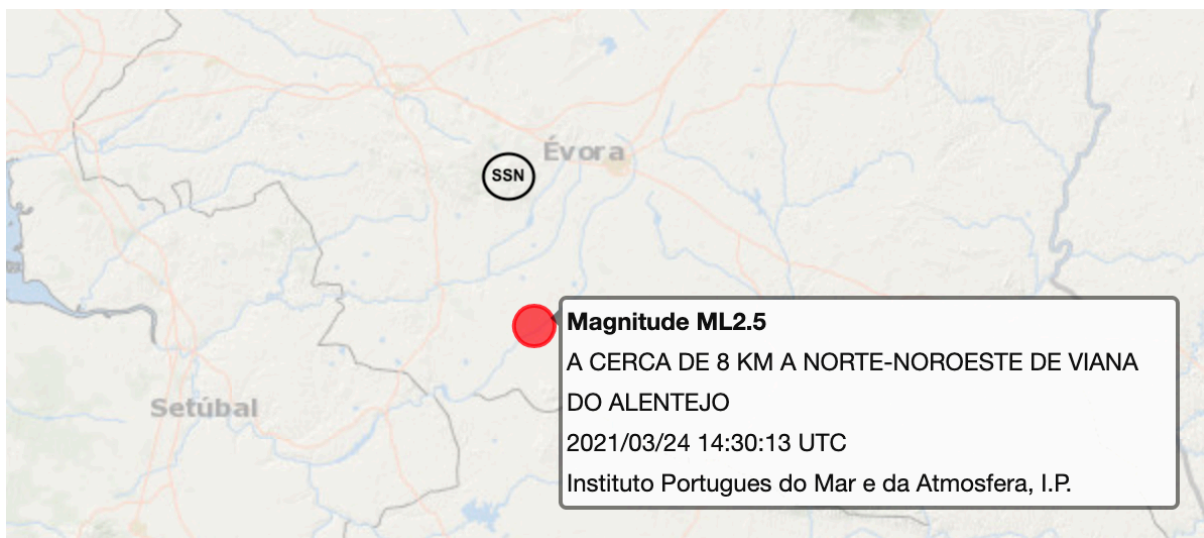


Figure 98 - Location of the seismic event with 2.5 magnitude (ML) with epicentre 8 km north-northwest of Viana do Alentejo (Évora district) reported by IPMA. The location of the prototypes is presented in the SSN circle. The prototypes are deployed at a distance of about 10 km from the epicentre.

The event was recorded by EVO station, as presented in Figure 99, showing the start of the event close to 14:29:39 (bottom) and an increase in ground motion activity after 14:29:41. It is noted that the event time recorded by the EVO station is before IPMA's reported time at 14:30:13. Subsequent analysis concluded that EVO time synchronisation (based on the GPS module) was not operating correctly.

²⁶ When the event occurred, Portuguese local time was the same as UTC time.

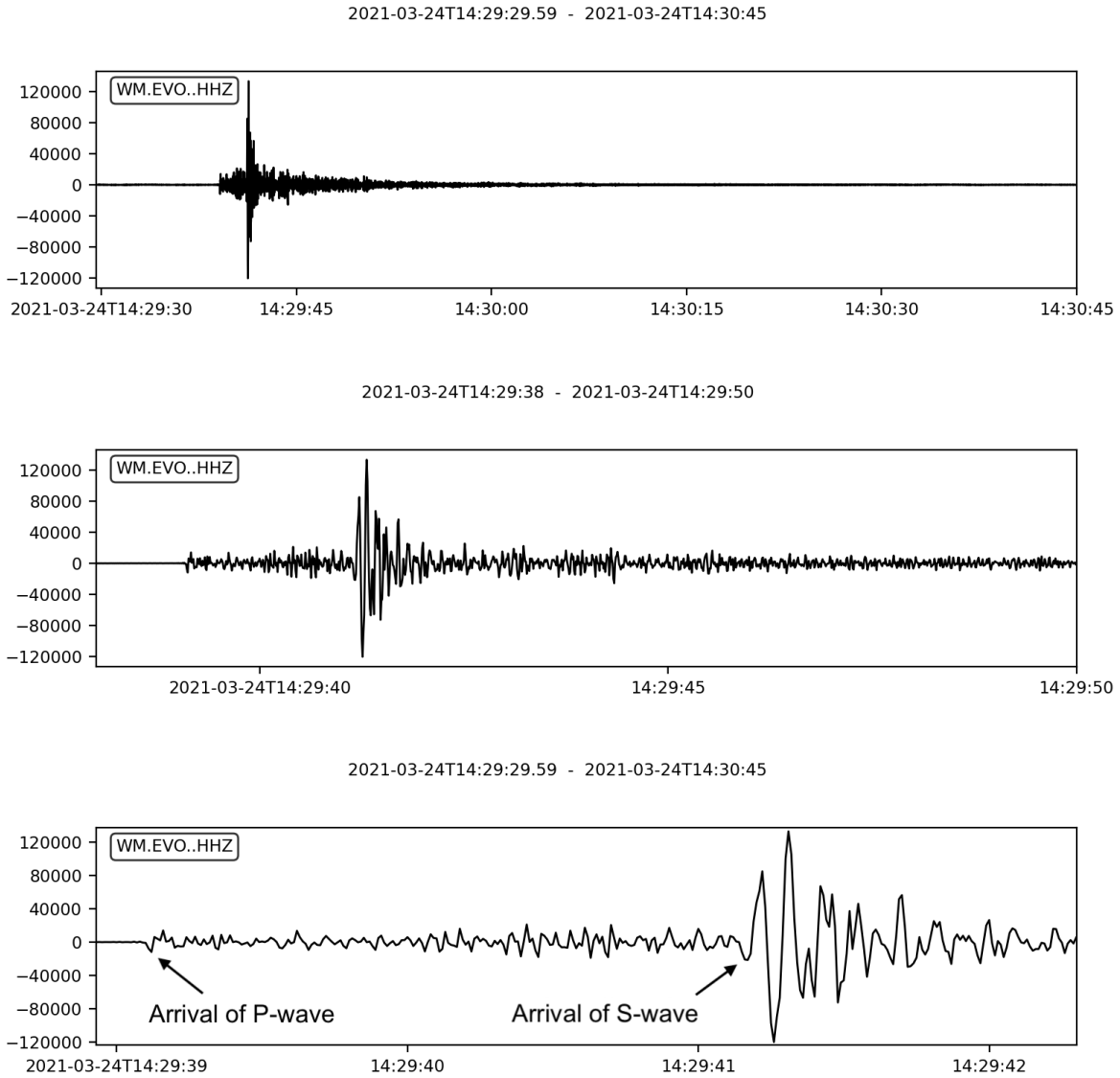


Figure 99 - EVO recording in the Z-axis (HHZ) of a 2.5 magnitude (ML) for a 45-seconds window (top), a 12-seconds time window (middle) and a 3-seconds window (bottom). The figure's Y-axis shows the raw amplitude value as recorded by EVO. The event starts with the arrival of the P-wave at 14:29:39 (bottom), followed by the S-wave at about 14:29:41. At 14:30:00 (top), EVO still records ground activity above what was present before the event.

7.4.7.2.1 Recorded signal and detectability over one hour (14:00:00 to 15:00:00 local time)

Figure 100 shows the recorded accelerometer data for one hour (14:00:00 to 15:00:00 local time) for sensors 10, 13, 17 (operating at 125 Hz) and 15 (operating at 15 Hz). It is noted that sensor 16 (operating at 4 Hz) did not detect any event and therefore is excluded. The accelerometer data is the acceleration magnitude, calculated based on the 3-axis measurements,

expressed as a function of g . The acceleration offset is removed by subtracting the acceleration mean value over the time window. Detections are calculated using the detectability techniques described in section 5.7 for the applicable time window.

Sensors 10, 13, 17 and 15 Measurements

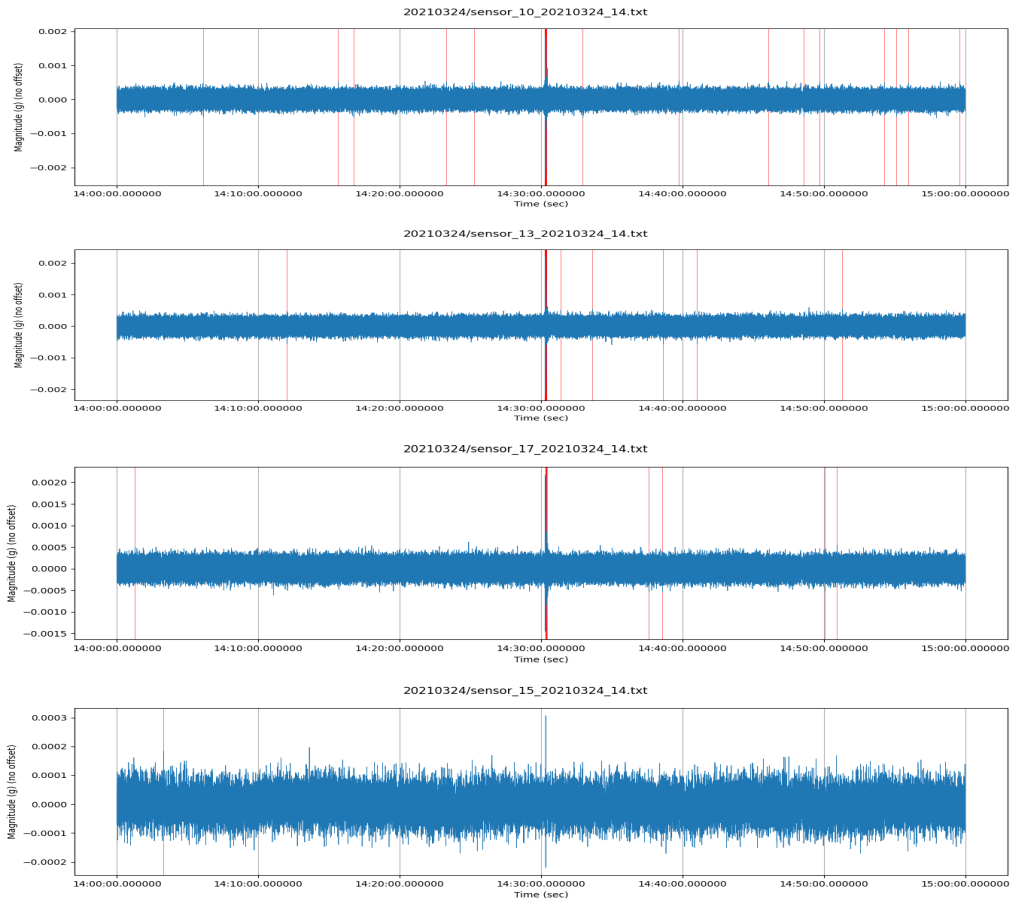


Figure 100 - Overview of acceleration measurements for sensors 10, 13, 17 and, for completeness, 15 over a one hour time window (14:00:00 to 15:00:00 local time). This figure supports the classification of true and false detections of events. Over the three set of measurements, there is only one ‘red’ vertical line that occurs at the same time and it corresponds to the time of the event.

7.4.7.2.2 Recorded signal and detectability over 20 seconds (14:30:15 and 14:30:35 local time)

Recorded accelerometer data is presented for the time-window of interest of 20 seconds (14:30:15 and 14:30:35 local time). Accelerometer data includes the acceleration value for each of the 3-axis. Acceleration is expressed as a function of g . The acceleration offset is removed by subtracting the acceleration mean value over the time window. Detections are calculated using the detectability techniques described in section 5.7 for the applicable time

window. It is noted that, since the time window in this subsection differs from the previous one (that used a time window of one hour), detections might differ.

For the purpose of this analysis, only recordings of sensor 17 (operating at 125 Hz) for all 3 axes are shown in Figure 101. After it, recordings in the X-axis for sensors 10, 13, 17 (operating at 125 Hz), 15 (operating at 15 Hz) and 16 (operating at 4 Hz) are presented in Figure 102.

Sensor 17

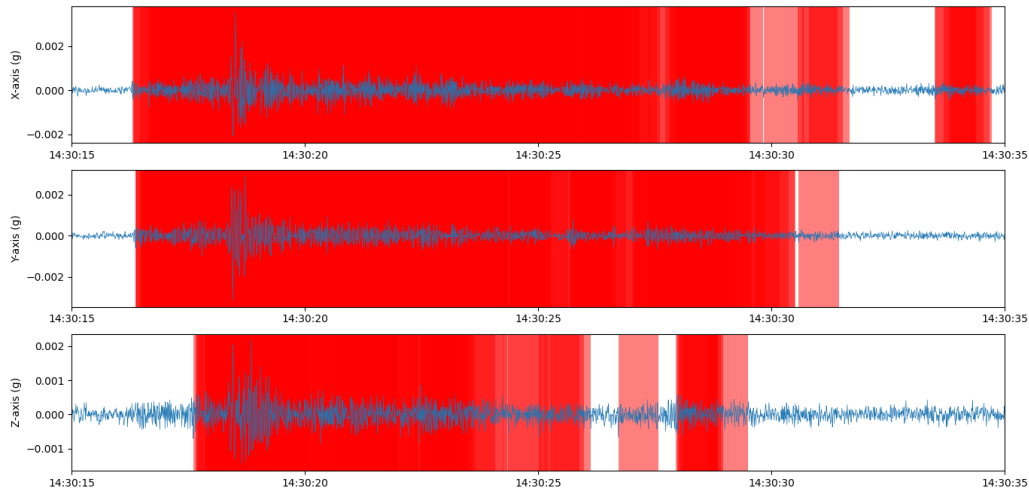


Figure 101 - Sensor_17 acceleration measurements over a 20-seconds time window (14:30:15 and 14:30:35 local time). Detections are marked with a 'red' vertical rectangle. The event is detected in all axes after 14:30:16, with strongest amplitude above 2mg for all axes. The X-axis exhibits the highest acceleration amplitude and detection over time.

Sensors 10, 13, 17, 15 and 16 Measurements

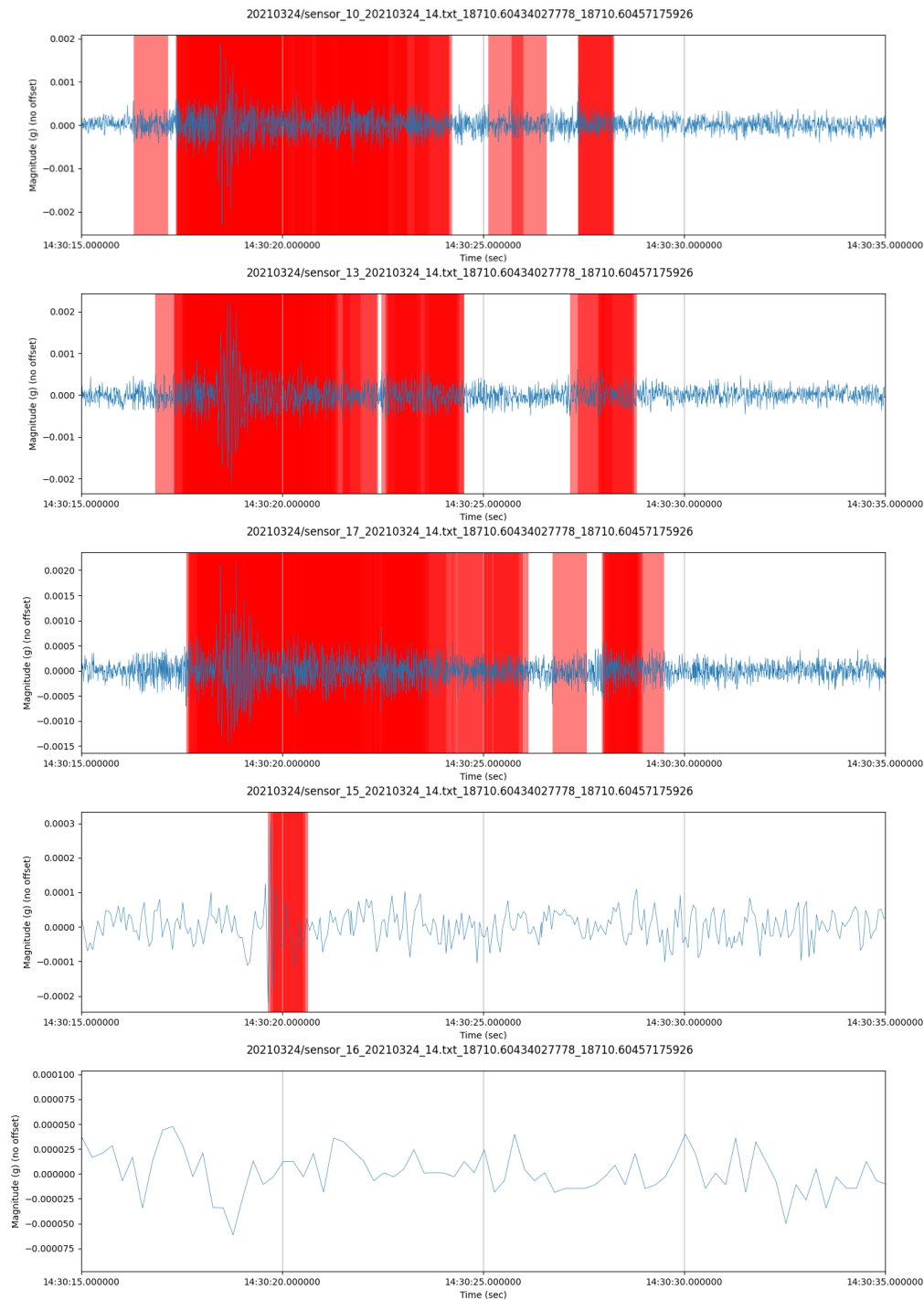


Figure 102 - Overview of acceleration measurements in the X-axis for sensors 10, 13, 17, 15 and 16 over a 20 seconds time window (14:30:15 and 14:30:35 local time). Detections are marked with a 'red' vertical rectangle. Sensor 10 performs the first detection, followed by sensors 13 and 17. After 14:30:17, all these sensors detect ground motion activity until about 14:30:25 (followed by periods of change in reported activity). After 14:30:30, no sensor reports any activity. Sensor 13 (middle figure) exhibits a higher damping factor than sensors 10 and 17 (see section 7.4.4) thus has lower detection duration. Sensor 15 only detect an event close to 14:30:20, while sensor 16 does not detect any event.

Discussion

IPMA's reported a seismic event with 2.5 magnitude (ML) had an epicentre at a distance of about 10 km from the prototypes. Based on the accelerometer data recorded by the ADXL-based prototypes (sensors 10, 13, 15, 16 and 17), it was shown that sensors 10, 13 and 17 (operating at 125 Hz) detect the event between 14:30:17 and 14:30:25 (over 8 seconds) and at 14:30:27 for about 1 second. Sensor 15 barely detects an event close to 14:30:20 over a short period of time (about 1 second). Sensor 16 misses the event.

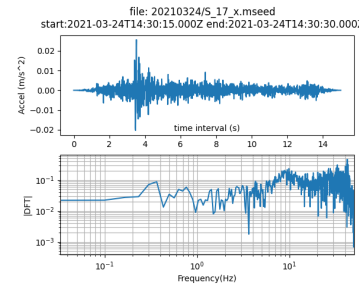
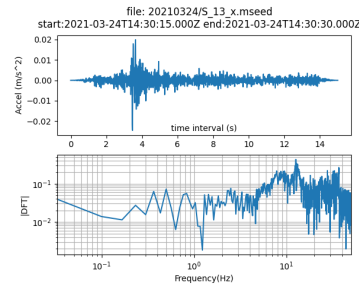
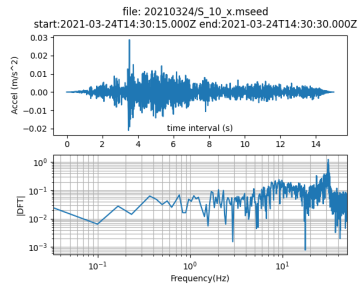
Comparing the obtained empirical results with the conclusions in section 5.7 concerning detectability, observations indicate that the ADXL prototypes operating at 125 Hz are capable to detect the event (as predicted), however, the ADXL prototypes operating at lower frequencies did not. In what concerns the latter, it is hypothesized that the relevant seismic frequencies associated with the event occur at frequencies outside what the sensors can observe (i.e., above 7.5 Hz, considering that sensor 15 operates at 15 Hz).

Moreover, it is important to note that the time of the event, as reported by IPMA, is at 14:30:13, while the EVO station identifies first activity occurring at 14:29:39 (with its strong activity recorded between 14:29:41 and 14:29:43). The sensor prototypes report the event as occurring between 14:30:17 and 14:30:25. Time differences between the EVO station and the prototypes was analysed in section 7.4.4.3, however these were well below one second. Given the gap between the EVO reported time of the event and IPMA's (that is closer to the sensor prototypes reported time), it is reasoned that the EVO reported time might be unsynchronised from UTC time. Indeed, subsequent analysis concluded that EVO time synchronisation (based on the GPS module) was not operating correctly.

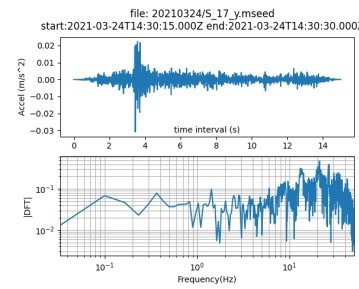
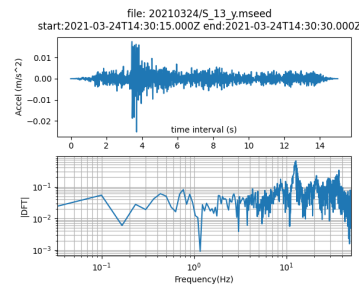
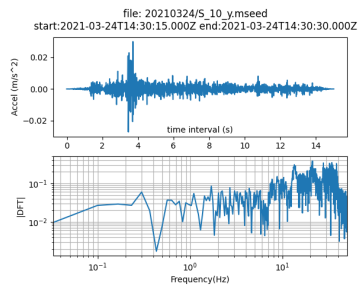
7.4.7.2.3 FFT

In this subsection, a frequency analysis is presented using the Discrete Fourier Transform (DFT). In this analysis, only data collected from prototypes based on ADXL355 (sensors 10, 13 and 17) are presented. This subsection follows a similar approach as the described in 7.4.5. The DFT is presented for each axis (X, Y and Z) for sensors 10, 13 and 17, considering the time interval pertaining to the time window of 15 seconds (14:30:15 and 14:30:30 local time). Recorded measurements over time, considering the applicable time window, are also presented. It is also noted that measurements obtained for ADXL355 are converted to the m/s^2 scale.

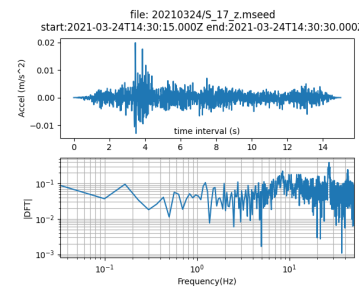
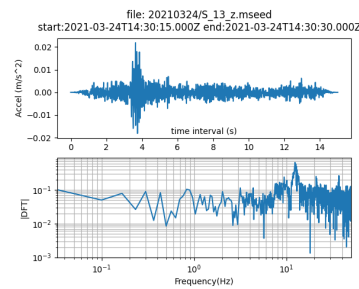
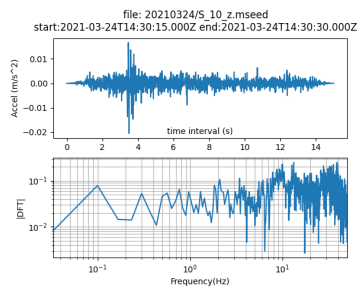
Sensor 10	Sensor 13	Sensor 17
------------------	------------------	------------------



In the X-axis, sensor 10 shows a peak close to 30 Hz, while sensors 13 and 17 does not show any relevant gain in any specific frequency.



In the Y-axis, sensor 10 shows a peak close to 10 Hz and another close to 40 Hz. Sensor 13 shows in addition a peak close to 10 Hz. Sensor 17 shows a peak close to 10 Hz and another close to 40 Hz.



In the Z-axis, sensor 10 shows a peak close to 40 Hz, sensor 13 a few peaks close to 10 Hz and 20 Hz and sensor 17 shows a peak close to 30 Hz.

Figure 103 - DFT related with acceleration measurements from sensors 10, 13 and 17 for a time window of 15 seconds (14:30:15 and 14:30:30 local time). The first row refers to the X-axis, the second row to the Y-axis and the third row to the Z-axis. In overall, the DFT shows a somewhat flat response, where irregularities could be attributed to noise, except where clear peaks appear typically close to 10 Hz, 20 Hz, 30 Hz and 40 Hz. Additional remarks are presented in the figures.

7.4.7.2.4 Spectrogram

This subsection presents a spectrogram analysis for a time window of 15 seconds. In this analysis, EVO generated spectrograms (using raw measurements) are used as reference to compare with those generated from prototypes based on ADXL355 (sensors 10, 13 and 17). This subsection follows a similar approach as the described in section 7.4.5.2.

EVO generated spectrograms

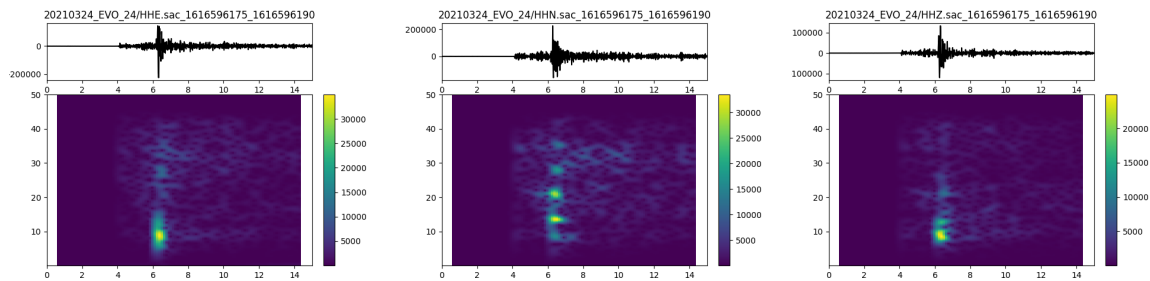
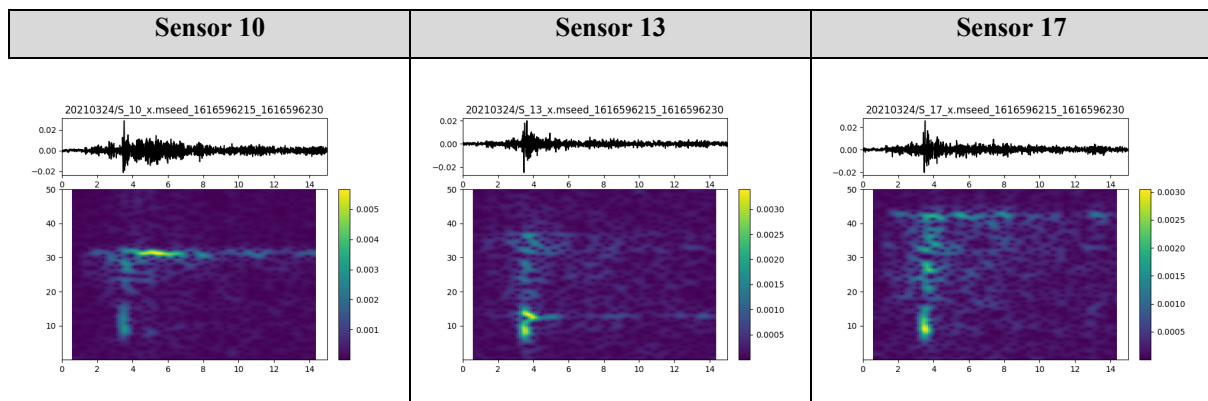
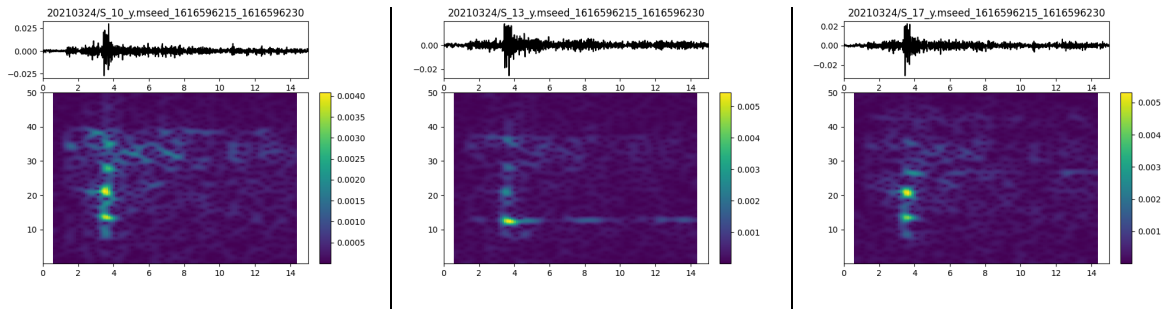


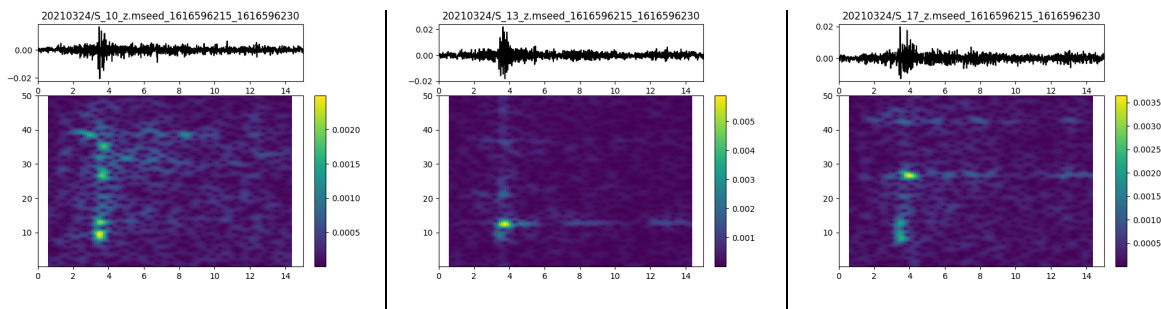
Figure 104 - Spectrograms related with EVO raw measurements for a time window of 15 seconds. The first column refers to EVO X-axis (HHE), the second column to EVO Y-axis (HHN) and the third column to EVO Z-axis (HHZ). In overall, the recorded signal show predominant frequencies around 10 Hz (in the X and Z EVO axes) and 10 Hz, 20 Hz, 30 Hz and 35 Hz in the Y-axis (EVO HHN).



In the X-axis, close to the region of maximum signal intensity (close to 4 seconds), sensor 10 dominant frequencies cluster around 10 Hz and 30 Hz (30 Hz is also dominant over time), sensor 13 dominant frequencies cluster around 10 Hz and spread up to 40 Hz (10 Hz dominates over time). Sensor 17 dominant frequencies cluster around 10 Hz there is spread up to 40 Hz (40 Hz is also dominant over time). The high dispersion in the presence of frequencies in for sensors 13 and 17 spectrograms indicate presence of noise.



In the Y-axis, close to the region of maximum signal intensity (close to 4 seconds), sensor 10 dominant frequencies are 10 Hz and 20 Hz, however there is a spread up to 40 Hz (40 Hz is also slightly dominant over time). Sensor 13 dominant frequency is 10 Hz (10 Hz is also dominant over time). Sensor 17 dominant frequencies are 10 Hz and 20 Hz, however there is no clear dominating frequency over time.



In the Z-axis, close to the region of maximum signal intensity (close to 4 seconds), sensor 10 dominant frequency is 10 Hz, however there is a wide dispersion of signal over other frequencies, indicating the presence of noise. Sensor 13 dominant frequency is 10 Hz (10 Hz is also dominant over time). Sensor 17 dominant frequency is close to 30 Hz (30 Hz is also dominant over time), followed by a small peak close to 10 Hz.

Figure 105 - Spectrograms related with acceleration measurements from sensors 10, 13 and 17 for a time window of 15 seconds (14:30:15 and 14:30:30 local time). The first column refers to the X-axis, the second column to the Y-axis and the third column to the Z-axis. In overall, the recorded signal produces frequency gains predominantly around 10 Hz, 20 Hz and 30 Hz. Additional remarks are presented in the figures.

Discussion

The spectrograms generated from EVO raw measurements reveal that the recorded signal show predominant frequencies around 10 Hz in the X and Z EVO axes (HHE and HHZ) and 10 Hz, 20 Hz, 30 Hz and 35 Hz in the Y-axis (HHN). Compared with EVO, the ADXL sensor prototypes exhibit a higher dispersion of signal across several frequencies (being sensor noise a cause); However, it is also visible a dominance of the 10 Hz frequency in X-axis (especially for sensors 13 and 17) and Z-axis (especially for sensors 10 and 13), and 10 Hz, 20 Hz, 30 Hz and 35 Hz in the Y-axis (HHN) for all sensors. It is noted that sensor 10 X-axis and sensor 17 Z-axis exhibit the presence of signal that is spread over several frequencies.

As in event 1 (described in 7.4.7.1), sensors 15 and 16, operating at 15 Hz and 4 Hz respectively (thus, according to the Nyquist theorem, can only observe up to 7.5 Hz and 2 Hz respectively), missed or barely detected the presence of any event.

As in event 1 (described in 7.4.7.1), it is also noted that sensors produced somewhat different frequency responses to the same signal, which is unexpected considering they use the same MEMS device (i.e., ADXL 355) setup with the same parameters (e.g., same sample frequency).

7.5 Conclusion

In this section, it was presented the results of field trials involving prototypes developed in section 5. Specifically, and for the purposes of this analysis, the following were used:

- 3 prototypes with sensor ADXL355 operating at 100Hz, named “sensor 10”, “sensor 13” and “sensor 17”.
- 1 prototype with sensor ADXL355 operating at 15Hz, named “sensor 15”.
- 1 prototype with sensor ADXL355 operating at 4Hz, named “sensor 16”.
- 1 prototype with sensor LIS3DHH operating at 100Hz, named “sensor lis3dhh_002”.

The prototypes were installed in the MITRA site that hosts the EVO station, a “Streckeisen STS-2/N” high performance station. The EVO station was used as reference instrument in comparing and assessing measurements obtained with the developed prototypes.

The prototypes were connected to a server hosted by the University of Évora. The sensors sent the measurement readings in real-time to the server using a Wi-Fi Access Point at MITRA.

The analysis covered the following aspects:

- Prototype generated file size volumes.
- Prototype sampling rate stability.
- Sensor measurement bias.
- Sensor noise characteristic.
- Sensor signal detection, in comparison with reference sensor EVO.
- Sensor frequency analysis.

The following is noted:

- The EVO station yields the lowest sensor noise from all sensors. Moreover, the EVO station exhibits the best sensitivity to detect signals.
- From the developed prototypes, the ADXL355 yields the best results.

- Given the characteristics of the generated signals, only prototypes operating at 100Hz (or above) sampling rate were able to detect them.
- ADXL35 yields a higher signal amplitude than EVO.
- Between ADXL355 sensors, slight differences are also observed in signal amplitude and attenuation: sensor 17 yields the highest amplitude of all; sensor 10 has the smallest attenuation. Future work should consider finding appropriate filters to produce consistent measurements.
- Although ADXL355 sensors seem to be well time-synchronised, there is a time offset with EVO of about 200ms. Since EVO is synchronised using GPS, its time records are assumed to be correct, thus it is necessary to further analyse improvements or alternate (to NTP) time synchronisation mechanisms for the prototypes.
- As shown by the generated PPSD, all prototypes exhibit self-noise well above Petterson's NHHM. This confirms that MEMS accelerometers applications should be limited to observation of strong motion and "high" frequencies (above 1Hz).

During this work, two seismic events were monitored and detected using the developed prototypes, specifically: one event of Magnitude 3.4 (ML) with epicentre about 8 km east of Loures (Lisbon district), recorded 18-03-2021 at 9h51 (local time), and one event of Magnitude 2.5 (ML) with epicentre about 8 km north of Viana do Alentejo (about 10km from EVO station) recorded 24-March-2021 at 14h30 (local time). These events allowed to demonstrate the sensors capabilities in detecting weak to moderate events at short and medium distances. Comparing with the EVO professional seismometer, however, the sensor prototypes exhibited a higher presence of sensor noise.

8 CONCLUSION AND FUTURE WORKS

In this thesis, it has been addressed the potential for high-density networks for seismic monitoring aiming to improve the resolution of the recorded seismic activity and consequently to improve the understanding of the physical processes that cause earthquakes, as well of obtaining more detailed seismic characterisation of studied regions.

It was identified that MEMS technology, used to produce small sized accelerometers, have a potential application in seismology. Indeed, MEMS accelerometers have enabled the deployment of high-density seismic networks capable to monitoring seismic activity with high spatial resolution. Example of high-density networks include CalTech's Community Seismic Network (CSN), MyShake Platform and SSN-Alentejo, currently in deployment phase.

In this context, this thesis described the work conducted to design and develop low-cost seismic sensor systems, based on low-cost MEMS accelerometers. This work included the conceptualisation of the architectural components that were implemented in four prototypes. Moreover, server-side components, necessary to operate and manage the sensor network, as well as provide visualisation tools for users, were also developed and described.

This work also included the field deployment and evaluation of selected prototypes, using a high-performance seismic station as the reference sensor for comparison. Moreover, during this work, two seismic events were monitored and detected using the developed prototypes. These events allowed to demonstrate the sensors capabilities in detecting weak to moderate events at short and medium distances.

The following main conclusions can be drawn from this work:

- The architecture herein defined has been demonstrated to be effective in the development and implementation of a high-dense seismic network, addressing both sensor-side and server-side components. The architecture delivers real-time sensor data globally accessible over the Internet. Moreover, the architecture is highly-scalable and supports distributing load over multiple processors and computers in a network.
- Low-cost MEMS accelerometers are effective in detecting strong motion events. From the assessed MEMS accelerometers, the ADXL355 is the best performing, being expected to detect earthquakes with $M=3$ and $M=5$ at a distance larger than 10 km and 100 km respectively.
- Low-cost MEMS accelerometers exhibit high levels of self-noise well above Peterson's NHNM, limiting their application in seismology to moderate and strong motion events.

- Low-cost MEMS accelerometers exhibit characteristics that complement seismometers, given their high range and high natural frequency. MEMS accelerometers can be installed next to seismometers, providing additional insights concerning seismic activity and seismology in general.

In order to improve the sensor network capabilities, a few areas for improvement are suggested to be addressed in future work:

- The used low-cost MEMS accelerometers exhibit higher amplitude values and lower damping than those recorded by the reference station EVO. Signal processing could be applied to make MEMS measurements closer to EVO.
- The sensor system measurements exhibit bias, which needs to be corrected before they can be used. Techniques for in-field calibration could be developed reducing burden for a large sensor network.
- Time synchronisation needs to be improved, either by using better techniques based on NTP or by incorporating highly accurate time sources like GPS.
- Combining multiple sensors to operate as a single logical sensor, improving overall data quality by performing data analytics and correlation and obtain a class-A sensor (comparable to traditional seismometers).

Despite their limitations, a network of MEMS accelerometers operating in real-time offers a wide range of applications (Manso *et al.*, 2020):

a) Seismic detection (strong motion) for near and "far" earthquakes (far being in the order of hundreds of kms), being less likely to saturate than comparing with traditional equipment. The network allows to study the seismic processes (earthquakes localizations and seismic source study, including the study of focal mechanisms) related to the occurrence of seismic events belonging to sedimentary basin structure.

b) Study of local events and characterize the structure of the seismogenic zone by performing waveform analysis of nearby small events (weak motions) and ambient noise. The network will enable the characterization of sedimentary basins structures, the location of near earthquakes, the identification of seismic sources by inverting the waveforms, the calculation of focal mechanisms, the performance of local seismic tomography and the study of the attenuation of seismic waves using ambient noise or seismic waveforms.

c) Analysis of the impact produced by human activity and cultural noise on buildings and monuments: *Urban seismic noise* is usually dominated by *traffic* and industrial activity with

peak frequencies below 25 Hz. A continuous exposure to urban tremors can cause a cumulative and progressive degradation on fragile buildings and monuments, which could cause irreparable damage in human heritage. If installed in buildings and monuments, the network produces information allowing to determine structural integrity risks.

d) *Shakemap* generation in near real-time. *Shakemaps* provide an estimate of *ground motion* amplitudes (maximum displacement, velocity or acceleration) caused by earthquakes. These maps can be used by civil protection authorities, decision-makers and local organizations (public or privates) for post-earthquake response, including assessing structural integrity risks in buildings and slopes. To be effective, these maps need to be *immediately* generated, thus requiring peak ground motion data in near real time.

e) Delivery to the scientific community of new open-access high-resolution seismic data for studying seismic-related phenomena and for developing methodologies useful to discriminate between natural and induced events.

f) Facilitation of access to education in seismology, resulting from open access to low-cost technology that can be installed in high schools and integrated in projects and activities.

While current MEMS accelerometers' performance limits their application in seismology, it is expected that next generation MEMS accelerometers will generate reduced electronic self-noise and will improve frequency response, especially for low frequencies (below Hz), thus capable of competing with traditional seismometers and eventually becoming the *de facto* technology in seismology.

9 BIBLIOGRAPHY

Addair T, Dodge D, Walter W, and Ruppert S (2014) Large-scale seismic signal analysis with Hadoop. *Computers & Geosciences* 66, 145–154

D'Alessandro, A., Luzio, D., & D'Anna, G. (2014). *Urban MEMS based seismic network for post-earthquakes rapid disaster assessment*. *Advances in Geosciences*, 40, 1-9.

D'Alessandro, A. Scudero, S. and Vitale, G. (2019) *A Review of the Capacitive MEMS for Seismology*. *Sensors* 2019, 19, 3093; doi:10.3390/s19143093

Allen R, Kong Q and Martin-Short R (2019) *The MyShake Platform: A Global Vision for Earthquake Early Warning*. *Pure Appl. Geophys.* <https://doi.org/10.1007/s00024-019-02337-7>

Anderson, D. P. (2004). *BOINC: A system for public-resource computing and storage rep.*, 5th IEEE/ACM International Workshop on Grid Computing, Pittsburgh, Pennsylvania, 8 November 2004.

ANSS (2008). *Instrumentation Guidelines for the Advanced National Seismic System*, Working Group on Instrumentation, Siting, Installation, and Site Metadata of the Advanced National Seismic System Technical Integration Committee U.S. Geol. Surv. Open-File Rept. 2008-1262, 41 pp.

Antonino D'Alessandro and Giuseppe D'Anna. (2013) *Suitability of Low-Cost Three-Axis MEMS Accelerometers in Strong-Motion Seismology: Tests on the LIS331DLH (iPhone) Accelerometer Short Note*. *Bulletin of the Seismological Society of America*, Vol. 103, No. 5, pp. 2906–2913, October 2013, doi: 10.1785/0120120287

Araújo A., Caldeira B., Martins A., Borges J., Araújo J., Moreira N., Maia M., Vicente S., Afonso P., Espanhol D., Bezzeghoud M. (2018) *Macrossismicidade associada ao sismo de Arraiolos do dia 15 de janeiro de 2018 com $M = 4.9$ e eventuais implicações na geometria da ruptura*. *Vulcânica – Revista Portuguesa de Vulcanologia*. Vol. II – 2018. ISSN 1646-3269.

Araújo A., B. Caldeira, A. Martins, J. Borges, N. Moreira, J. Araújo, M. Maia, S. Vicente, P. Afonso, D. Espanhol, M. Bezzeghoud, 2020. *Macrossismicity associated with the Arraiolos earthquake of January 15, 2018 with $M = 4.9$ and possible implications in the geometry of the rupture*. *Comunicações Geológicas* (2020) 107, Especial I, 35-3. ISSN: 0873-948X; e-ISSN: 1647-581X. https://www.lneg.pt/wp-content/uploads/2020/05/Volume_107.pdf

Atkinson, G. (2015). *Ground-Motion Prediction Equation for Small-to-Moderate Events at Short Hypocentral Distances, with Application to Induced-Seismicity Hazards*. *Bulletin of the Seismological Society of America*. March 2015. DOI: 10.1785/0120140142

Bezzeghoud M. and E. Buforn (1999). Source parameters of 1992 Melilla (Spain, Mw=4.8), 1994 Alhoceima (Morocco, Mw=5.8) and 1994 Mascara (Algeria, Mw=5.7) earthquakes and seismotectonic implications. *Bul. Seis. Soc. Am.*, 89, 2, 359-372. <https://pubs.geoscienceworld.org/ssa/bssa/article-abstract/89/2/359/120378/Source-parameters-of-the-1992-Melilla-Spain-MW-4-8?redirectedFrom=fulltext>

Bezzeghoud M., C. Adam, E. Buforn, J. F. Borges, B. Caldeira (2014). Seismicity along the Azores-Gibraltar region and global plate kinematics, *J. Seismol.*, 18, 205–220, <http://dx.doi.org/10.1007/s10950-013-9416-x>

Bird, P. (2003). An updated digital model of plate boundaries. *Geochemistry, Geophysics, Geosystems*, 4(3). <https://doi.org/10.1029/2001GC000252>

Borges, J., Fitas, A., Bezzeghoud, M., and Teves-Costa, P. (2001). Seismotectonics of Portugal and its adjacent Atlantic area. *Tectonophysics*, 337, 373-387. [https://doi.org/10.1016/S0040-1951\(00\)00291-2](https://doi.org/10.1016/S0040-1951(00)00291-2)

Borges J. F., M. Bezzeghoud, E. Buforn, C. Pro and A. Fitas (2007). The 1980, 1997 and 1998 Azores earthquakes and its seismotectonic implications. *Tectonophysics*, 435, 37-54. <https://doi.org/10.1016/j.tecto.2007.01.008>

Buforn E., M. Bezzeghoud, A. Udias and C. Pro (2004). Seismic source in the Iberian-African plate boundary. *Pure and Applied Geoph.*, 161, 3, 623 – 646. <https://doi.org/10.1007/s00024-003-2466-1>

Caldeira B, Carrilho F, Miranda M, Bezzeghoud M, Alves P, Silveira G, Villalonga F, Pena J, Matias L, Borges J, Vales D, Corela C and Madureira G (2007) Recent improvements in the Broadband seismic networks in Portugal. *EMSC Newsletters*, special issue, 22, 18-19

Carrilho F., S. Custódio, M. Bezzeghoud, C. Sousa Oliveira, C. Marreiros, D. Vales, P. Alves, A. Pena, G. Madureira, M. Escuer, G. Silveira, C. Corela, L. Matias, M. Silva, I. Veludo, Nuno A. Dias, A. Loureiro, José F. Borges, B. Caldeira, P. Wachilala, J. Fontiela, 2021. *The Portuguese National Seismic Network – Products and Services*. *Seismological Research Letter*, accepted.

Clayton R, Heaton T, Chandy M, Krause A, Kohler M, Bunn J, Guy R, Olson M, Faulkner M, Cheng M, Strand L, Chandy R, Obenshain D, Liu A and Aivazis M (2011) Community Seismic Network. *Annals of Geophysics*, 54, 6

Cochran E., Lawrence J., Christensen C., Chung A. (2009) *A novel strong-motion seismic network for community participation in earthquake monitoring*. *IEEE Instru. Meas. Mag.*, 12 (6), 8-15.

Custódio S, Dias N, Caldeira B, Carrilho F, Carvalho S, Corel, C, Díaz J, Narciso J, Madureira G, Matias L, Haberland C and WILAS Team (2014) Ambient Noise Recorded by a Dense Broadband Seismic Deployment

in Western Iberia. *Bulletin of the Seismological Society of America*, Vol. 104, No. 6, pp. 2985–3007, December 2014, doi: 10.1785/0120140079

Dominguez, L., Yildirim, B., Husker, A., Cochran, E., Christensen, C., Cruz-Atienza, V., and Lawrence, J. (2015) *The Red Atrapa Sismos (Quake-Catcher Network in Mexico): Assessing Performance during Large and Damaging Earthquakes*. *Seismological Research Letters* Volume 86, Number 3 May/June 2015. doi: 10.1785/0220140171

Dziewonski, A., Anderson, D. (1981) *Preliminary reference Earth model*. *Physics of the Earth and Planetary Interiors*, 25 (1981) 297— 356. Elsevier Scientific Publishing Company. doi:10.17611/DP/9991844

ECMA 2013. *The JSON Data Interchange Format*. ECMA International 2013. Available at: <https://www.ecma-international.org/publications/files/ECMA-ST-ARCH/ECMA-404%201st%20edition%20October%202013.pdf>

Evans J, Hamstr, R, Spudich P Jr, Kündig C, Camina P and Rogers J (2003) TREMOR: A Wireless, MEMS Accelerograph for Dense Arrays. U.S. Department of the Interior, U.S. Geological Survey. Open-file Report 03-159

Evans J, Allen R, Chung A, Cochran E, Guy R, Hellweg M, Lawrence J (2014) *Performance of Several Low-Cost Accelerometers*. *Seismological Research Letters* Volume 85, Number 1 January/February 2014.

Faulkner, M., Clayton, R., Heaton, T., Chandy, K., Kohler, M., Bunn, J., Guy, R., Liu, A., Olson, M., Cheng M. and Krause, A. (2014) *Community sense and response systems: your phone as quake detector*. *Communications of the ACM* Vol. 57, No. 7. <https://doi.org/10.1145/2622633>

Farine M, Thorburn N, and Mougnot D (2003) General Application of MEMS Sensors for Land Seismic Acquisition – Is it Time? Accessible at: <http://cseg.ca/assets/files/resources/abstracts/2003/218S0130.pdf>

Ferrão, C., Bezzeghoud, M., Caldeira, B., and Borges, J. (2016). *The Seismicity of Portugal and Its Adjacent Atlantic Region from 1300 to 2014: Maximum Observed Intensity (MOI) Map*. *Seismological Research Letters* Volume 87, Number 3 May/June 2016. doi: 10.1785/0220150217

Fette I., Melnikov A. (2011) RFC 6455 - The WebSocket Protocol. Internet Engineering Task Force.

Fraden, J. (2010). *Handbook of Modern Sensors*, Springer Science+Business Media, LLC 2010. DOI 10.1007/978-1-4419-6466-3_8

GEBCO Grid (2020), doi:10.5285/a29c5465-b138-234d-e053-6c86abc040b9

Grandin, R., Borges, J.F., Bezzeghoud, M., Caldeira, B. and Carrilho, F., 2007. *Simulations of strong ground motion in SW Iberia for the 1969 February 28 (MS = 8.0) and the 1755 November 1 (M ~ 8.5) earthquakes – I. Velocity model*, Geophys. J. Int., 171, 3, 1144– 1161, December 2007 doi: <http://dx.doi.org/10.1111/j.1365-246X.2007.03570.x>

Grandin, R., Borges, J.F., Bezzeghoud, M., Caldeira, B. and Carrilho, F., 2007. *Simulations of strong ground motion in SW Iberia for the 1969 February 28 (MS = 8.0) and the 1755 November 1 (M ~ 8.5) earthquakes – II. Strong ground motion simulations*, Geophys. J. Int., 171, 2, 807-822, November 2007. doi: <http://dx.doi.org/10.1111/j.1365-246X.2007.03571.x>

Inbal A., Clayton R., and Ampuero J. (2015) *Imaging widespread seismicity at midlower crustal depths beneath Long Beach, CA, with a dense seismic array: Evidence for a depth-dependent earthquake size distribution*. Geophysical Research Letters, 42, 15, 6314–6323

InvenSense Inc. *MPU-6000 and MPU-6050 Product Specification Revision 3.3*. Document Number: PS-MPU-6000A-00 Revision: 3.3 Release Date: 5/16/2012. www.invensense.com

Hamak I, Wachilala, P., Borges, J., Dias, N. A., Rio, I., Bezzeghoud, M. (2020). *Three-dimensional crustal image of Arraiolos aftershock sequence, earthquake of M=4.9, in Alentejo region, Portugal*. International Meeting 40 Years of the 1980 Azores Earthquake, online meeting, 6-7 October 2020, 58-62. Retrieved from <https://azores4080meeting.files.wordpress.com/2020/10/proceedingsbook-1.pdf>

Havskov J., and Alguacil., G. (2002). *Instrumentation in Earthquake Seismology*. Preliminary version, June 2002.

Havskov J., Ottemoller L. (2010) *Routine Data Processing in Earthquake Seismology*. Springer Science+Business Media B.V. ISBN 978-90-481-8696-9. DOI 10.1007/978-90-481-8697-6

Homeijer, B., Milligan, D., and Hutt, C. (2014) *A Brief Test of the Hewlett-Packard MEMS Seismic Accelerometer*. Open-File Report 2014–1047. U.S. Department of the Interior U.S. Geological Survey

International Seismological Centre (2020), on-line Bulletin, doi:10.31905/D808B830

ITU (2020). *Measuring digital development Facts and figures 2020*. Available at: <https://www.itu.int/en/ITU-D/Statistics/Documents/facts/FactsFigures2020.pdf>

Lainé J. and Mougénot D. (2014) *A high-sensitivity MEMS-based accelerometer*. The Leading Edge. November 2014. Special Section: Sensor technology and nanotechnology <http://dx.doi.org/10.1190/tle33111234>

Liu, A. (2013) *Sensor Networks for Geospatial Event Detection — Theory and Applications*. PhD Thesis. California Institute of Technology.

Mallon E. and Beddows P. (2014) Cutting Power to Secure Digital Media cards for Low Current Data Logging. Blog entry published on January 20, 2016. Available at: <https://thecavepearlproject.org/category/reducing-power-consumption/>

Matias, L., Rio, I., Waschilala, P., Vales, D., Borges, J., Dias, N., Carrilho, F., Caldeira, B., Custodio, S., Fontiela, J., Bezzeghoud, M., Araujo, A. and Corela, C. (2019) *The seismic sequence of Arraiolos, Portugal, in January 2018*. Geophysical Research Abstracts Vol. 21, EGU2019-9761, 2019. EGU General Assembly 2019.

Marco, M., Silva, H. and Bezzeghoud, M. (2011) *PLASMA - A high-performing and open platform for the integration of heterogeneous sensor networks*. Fifth Meeting of Post-Graduation in Physics and Earth Sciences of University of Évora. 21-22 September 2011.

Manso M, Bezzeghoud M, Caldeira B (2016) Design and Implementation of a Network Enabled High-Throughput MEMs-based Seismic Sensor. *Comunicações Geológicas*. 103, 1, 107-111. e-ISSN: 1647-581X Accessible at: https://www.lneg.pt/download/13472/11_Manso_et_al_ComGeo.pdf

Manso M., Bezzeghoud M., Caldeira B. (2017) Design and Evaluation of a High Throughput Seismic Sensor Network. Tools for Planning, Deployment and Assessment. 6th International Conference on Sensor Networks SENSORNETS, Porto, Portugal, 19 to 21 February.

Manso, M., Bezzeghoud, M., Borges, J., Caldeira, B., Abdelhakim A. (2020) *High-density seismic network for monitoring Alentejo region (Portugal) and Mitidja basin region (Algeria)*. Arab J Geosci 13, 976 (2020). <https://doi.org/10.1007/s12517-020-05972-w> (Published: 17 September 2020).

Manso, M. and Bezzeghoud, M. (2021) *On-Site Sensor Noise Evaluation and Detectability in Low Cost Accelerometers*. 10th International Conference on Sensor Networks SENSORNETS, Online streaming, 9 to 10 February, 2021.

NTP (2003). *The NTP Public Services Project*. Available at: <http://www.ntp.org/ntpfaq/NTP-s-algo.htm>. (Accessed: 5 September 2016)

Ousadou F., Bezzeghoud M. (2019) Seismicity of the Algerian Tell Atlas and the Impacts of Major Earthquakes. In: A. Bendaoud *et al.* (eds.), *The Geology of the Arab World—An Overview*, Springer Geology. 401-426

Palomeras I., Thurner S., Levander A., Liu K., Villasenor A., Carbonell R., Harnafi M. (2014) *Finite-frequency Rayleigh wave tomography of the western Mediterranean: mapping its lithospheric structure*. *Geochem. Geophys. Geosyst.*, 15(1), 140–160

Pakhomov, A., Pisano, D., Sicignano, A. and Goldburt, T. (2005) *Testing of New Seismic Sensors for Footstep Detection and Other Security Applications*. *Sensors, and C3I Technologies for Homeland Security and Homeland Defense IV*. Proceedings of SPIE Vol. 5778 (SPIE, Bellingham, WA, 2005) doi: 10.1117/12.604005

Peterson, J. (1993) *Observations and modeling of seismic background noise*. Open-File Report. USGS. DOI 10.3133/ofr93322

Pro. C., M. Bezzeghoud, E. Buforn, and Udias A. (2014). *Reply to Comment on “The earthquakes of 29 July 2003, 12 February 2007, and 17 December 2009 in the region of Cape Saint Vincent (SW Iberia) and their relation with the 1755 Lisbon earthquake”*. *Tectonophysics* 628 (2014) 246–247, <http://dx.doi.org/10.1016/j.tecto.2014.05.016>

Schiefer, M., Bono, R.. *Improved Low Frequency Accelerometer Calibration*. XIX IMEKO World Congress Fundamental and Applied Metrology September 6–11, 2009, Lisbon, Portugal

Scudero S., D'Alessandro A., Greco L., Vitale G. (2018) MEMS technology in seismology: A short review. Published in: 2018 IEEE International Conference on Environmental Engineering (EE). 12-14 March 2018. Milan, Italy. DOI: 10.1109/EE1.2018.8385252

SD Group. (2013) *SD Specifications, Part 1 - Physical Layer Simplified Specification*. Version 4.10, January 22, 2013. https://www.sdcard.org/downloads/pls/pdf/part1_410.pdf

Shearer, P. (2009) *Introduction to Seismology - Second Edition*. Cambridge University Press. ISBN-13 978-0-511-58010-9

Streckeisen. *STS-2 Portable Very-Broad-Band Triaxial Seismometer*. Product Datasheet. Available at: <https://streckeisen.swiss/assets/downloads/sts-2-datasheet.pdf>

Tunc S., Tunc B., Caka D., Ada S., Rademacher H. (2012) Does Broad-Band Seismometer Clip? American Geophysical Union, Fall Meeting 2012, abstract id. S51C-2446. December 2012

Veludo I., Dias A., Fonseca P., Matias L., Carrilho F., Haberland C., Villaseñore A. (2017) Crustal seismic structure beneath Portugal and southern Galicia (Western Iberia) and the role of Variscan inheritance. *Tectonophysics*, 717, 16 October 2017, 645-664.

Wachilala P., Borges J., Caldeira B., Matias L., Rio I., Bezzeghoud M. (2019) Characterization of the Region of Arraiolos, South Portugal – Period of January – May 2018. Ass. IUGG 2019, Montreal, Canada.

ANNEX - PAPERS AND PRESENTATIONS

As a result of the work conducting during the elaboration of this thesis, a number of presentations and papers were made as listed next:

[Presentation] M. Manso, M. Bezzeghoud, J. F. Borges and B. Caldeira (2016) *Low-Power Low-Cost Sensor Platform for Seismic and Environmental Monitoring*. Presentation at the “9a Asamblea Hispano-Portuguesa de Geodesia y Geofisica. Madrid”, 28-30 June 2016.

[Presentation] Manso M., Bezzeghoud M., and Caldeira, B. (2016) *Design and Implementation of a Network Enabled High-Throughput MEMs-based Seismic Sensor*. Workshop On Earth Sciences. Évora, Portugal, 8th to 10th December 2016.

[Journal Publication] Manso, M., Bezzeghoud, M., Caldeira, B. (2016) Contributor with article "Design and Implementation of a Network Enabled High-Throughput MEMs-based Seismic Sensor". *Comunicações Geológicas* (2016) 103, 1, 107-111 ISSN: 0873-948X; e-ISSN: 1647-581X. https://www.lneg.pt/download/13472/11_Manso_etal_ComGeo.pdf

[Conference Paper] Manso M., Bezzeghoud M. and Caldeira B. (2017) *Design and Evaluation of a High Throughput Seismic Sensor Network. Tools for Planning, Deployment and Assessment*. 6th International Conference on Sensor Networks SENSORNETS, Porto, Portugal, 19 to 21 February 2017. <https://doi.org/10.5220/0006127701290134>

[Conference Presentation] Manso, M., Bezzeghoud, M., Borges, J.F., Caldeira, B., Fontiela, J., Ayadi, A. (2019) *High-Density Seismic Network for monitoring Alentejo region (Portugal) and Mitidja basin region (Algeria)*. 2nd Conference of the Arabian Journal of Geosciences (CAJG). Sousse, Tunisia 25-28 November 2019.

[Journal Publication] Manso, M., Bezzeghoud, M., Borges, J., Caldeira, B., Ayadi, A. (2020) *High-density seismic network for monitoring Alentejo region (Portugal) and Mitidja basin region (Algeria)*. *Arab J Geosci* 13, 976 (2020). <https://doi.org/10.1007/s12517-020-05972-w> (Published: 17 September 2020).

[Conference Paper] Manso, M. and Bezzeghoud, M. (2021) *On-Site Sensor Noise Evaluation and Detectability in Low Cost Accelerometers*. 10th International Conference on Sensor Networks SENSORNETS, Online streaming, 9 to 10 February, 2021.

[Paper Publication] Bezzeghoud M., and Manso, M. (2021) *Monitoring the Earth: the Near-Future Developments in Seismology*. Academia Letters, Article 581. <https://doi.org/10.20935/AL581>

[Presentation] Manso M., Bezzeghoud M., Borges J., and Caldeira, B. (2016) *SSN-Alentejo: Towards High-Dense Seismic Network Deployments*. Jornadas do ICT. Faculdade de Ciências da Universidade do Porto. Portugal, 11-12 Fevereiro 2021.

The papers are included next.

Low-Power Low-Cost Sensor Platform for Seismic and Environmental Monitoring

M. Manso⁽¹⁾, M. Bezzeghoud⁽²⁾, J. F. Borges⁽²⁾ and B. Caldeira⁽²⁾

⁽¹⁾ Instituto de Ciências da Terra, Universidade de Évora, marco@marcomanso.com, Évora

⁽²⁾ Departamento de Física, Escola de Ciências e Tecnologia da Universidade de Évora

marco@marcomanso.com

ABSTRACT

The technology applied to sensors and sensor platforms has evolved in a strong and fast pace over the last years, resulting in increased performance, reduced energy consumption, improved connectivity, miniaturization and reduced cost. These innovations bring to scientific communities of experimenters promising prospects such as deployment of large sensor networks for high spatial resolution data collection.

In this paper, we present our first steps in developing a low-power low-cost sensor platform prototype fit for seismic and environmental monitoring purposes. We define the platform general architecture, which includes the platform's main functional components – that includes sensors, processor, communications, storage and other ancillary components – followed by our first implementation of the platform that realises the design, in the form of a functional prototype, where several components are selected and integrated. This prototype is capable to monitor temperature, relative humidity and ground acceleration (used to measure ground movement for seismology purposes). The prototype is demonstrated by showing our first experimental results, together with our results on energy consumption and cost. We conclude by presenting our main findings and future work.

Design and Implementation of a Network Enabled High-Throughput MEMs-based Seismic Sensor

Marco Manso

Instituto de Ciências da Terra, Universidade de Évora, Évora, PORTUGAL, marco@marcomanso.com

Mourad Bezzeghoud and Bento Caldeira

Departamento de Física, Escola de Ciências e Tecnologia da Universidade de Évora, mourad@uevora.pt, bafcc@uevora.pt

Abstract - The rapid technological evolution in sensors, sensor platforms and networking is enabling the deployment of large sensor networks for "live" monitoring of seismic activity with high spatial resolution. In this regard, this paper presents our work in designing and implementing a sensor system that operates autonomously, is network enabled and produces high data throughput (up to 200Hz). We describe the system deployment done to validate the sensor system and we present measurement results. By validating the sensor system, our work produced as well the necessary knowledge to plan the sensor network (i.e., recommended size per cluster) that will be deployed in next steps.

Key words - Seismic Network, Sensor Network, Seismology

INTRODUCTION

The technology applied to sensors and sensor platforms has evolved in a strong and fast pace over the last years, resulting in increased performance, reduced energy consumption, improved connectivity, miniaturization and reduced cost. These innovations bring to scientific communities and experimenters promising prospects such as the deployment of large sensor networks for "live" (online and real-time) monitoring of seismic activity with high spatial resolution.

In this regard, large scale high density sensor networks have been deployed aiming to bring to the field of seismology high resolution geo-referenced measurements: in 2001 and 2002, the California Institute of Technology (CalTech) deployed more than 5200 low-cost stations with an average spacing close to 100m with the purpose to better define the Long Beach Oil Field [5,7]; in addition, CalTech's established the Community Seismic Network (CSN), an earthquake monitoring system based on a dense array of low-cost acceleration sensors (more than 1000) aiming to produce block-by-block measurements of strong shaking during an earthquake (<http://csn.caltech.edu/about/>); the University of Southern California's (USC) Quake-Catcher Network (QCN) [1] began rolling out in the San Francisco

Bay Area comprising 6000 tiny sensors, being part of the densest networks of seismic sensors ever devoted to studying earthquakes [13]. These networks allowed measuring seismic activity with high resolution that, by correlating the signal with time and space, allowed, for example, producing "shake maps" directly from observations. High-density sensor networks can be relevant to other fields as well. Indeed, studies have taken place to demonstrate the detection of important geospatial events such as earthquakes and hazardous radiation, where sensor data correlation improved data quality and brought additional insights [6].

Inspired by these efforts, we leverage on recent technological developments to implement a high-throughput seismic sensor that provides "live" measurements using internet-enabled technologies and operates autonomously (i.e., do not require a computer or an external device to collect and transmit data).

This paper is structured as follows: in section 2 we describe the implementation of the sensor system; in section 3 we describe the deployment made to validate the sensor system, where we also present examples of collected measurements; in section 4 we conclude the paper and present next steps.

SENSOR SYSTEM IMPLEMENTATION

The sensor system purpose is to measure a physical quantity of interest that, in our case, is ground motion and transmit the output variable associated to the measure.

The sensor system we implement takes into account the following requirements:

- Uses sensors appropriate for purposes of measuring ground motion.
- Is able to connect to internet-based networks (e.g., supports 802.11/Wi-Fi standards family).
- Is based on low-cost platforms (to enable deployment of high density networks).
- Operates autonomously so that it can function over several weeks (or months) without requiring human intervention.

Following the general design in [9], the selected elements constituting the sensor system are presented in Table I.

TABLE I
 SENSOR IMPLEMENTATION ELEMENTS

Element	Architecture Component as in [9]
ESP8266 (ESP-01 model)	Acquisition and Processing Board (32-bit processor at 80MHz); Storage (on-chip SRAM); Networking (integrated TCP/IP protocol stack, Wi-Fi)
MPU-6050	Sensor: 3-axis 16-bit accelerometer (0.06mg resolution at 2g) Up to 200Hz measurement frequency
Internal clock synchronised with NTP	Real-Time Clock
3.3v Power Supply Board	Power Supply
I2C Bus	Data Interface (connecting the ESP8266 to the MPU-6050)

The ESP8266 is selected because it provides a fast and programmable microcontroller, embedded Wi-Fi capabilities and support of a wide range of libraries (via the Arduino community).

Time synchronisation is achieved by means of Network Time Protocol (provided by the server component running its own NTP server). NTP can keep time accuracy of all machines within the same subnet within one millisecond [11], which suffices for our application scenario.

Accelerometer Sensor Component

To measure ground motion, we rely on low-cost small size MEM (micro-electro-mechanical) accelerometer sensor technologies. These sensors are low cost, robust (capable to measure and/or sustain high acceleration values), capable of self-calibration (resulting from their ability to measure the gravity acceleration component) and requires low maintenance. For purposes of seismology, MEM-based accelerometers:

- provide adequate sensitivity, noise level, and dynamic range to be applicable to earthquake strong-motion acquisition ($M > 3$). However, their low sensitivity, due to the high level of instrumental self noise that increases as frequency decreases, limits their application in the study of low frequency weak-motion forces [2,3];
- are well fit to measure high frequency ($> 40\text{Hz}$) ground motion since their resonant frequency (typically above 1 kHz) is far above the seismic band pass;
- measure the gravity acceleration component that provides a useful reference for sensitivity calibration and tilt measurement;
- have high acceleration ranges (several gs) and are capable to sustain high acceleration (several hundred gs) without being damaged;
- when compared with seismometers, such as geophones, MEMs may have an advantage in detecting weak high

frequency signals, while geophones may have the advantage in detecting weak signals at low frequencies;

- can have useful applications such as earthquake early warning, seismic hazard map and security applications.

For this proof-of-concept, we select the MPU-6050 is a 3-axis MEM accelerometer that has the following specifications [8]:

- Accelerometer range: $\pm 2g$ (minimum)
- Accelerometer sample rate up to 1kHz
- 16-bit resolution (16384 LSB resolution per g at 2g)
- Power spectral density (PSD) (root mean square at 10Hz): $400\mu\text{g}/\sqrt{\text{Hz}}$ (well above the $10\text{ng}/\sqrt{\text{Hz}}$ peak of the Peterson Low Noise Model [12] thus unfit for measuring seismic activity weak signals at low frequencies)
- Operating current: $500\mu\text{A}$ (normal), $20\mu\text{A}$ (if sample rate at 5Hz), $5\mu\text{A}$ (sleep mode)
- I²C Digital Interface

The MPU-6050 is categorized as Class-C (resolution from about 12 to 16 bits, typically over 2g ranges) that have found applications in generating reliable pictures of regional seismicity and strong shaking [2].

The sensor system interconnections are presented in Figure 1. The pin connections between the components are presented in Table II. Note that the data interface used is the I²C Digital Interface and that the MPU module has pull-up resistors as required by the I2C bus.

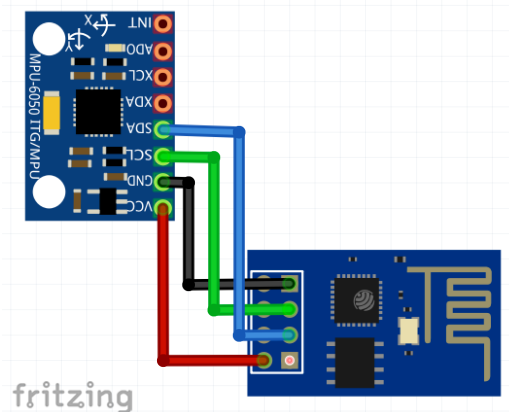


FIGURE 1
 SENSOR SYSTEM IMPLEMENTATION

TABLE II
 I²C PIN CONNECTIONS

Interface	ESP Pin	MPU Pin
I ² C SDA	Pin 0	SDA
I ² C SCL	Pin 2	SCL

DEPLOYMENT

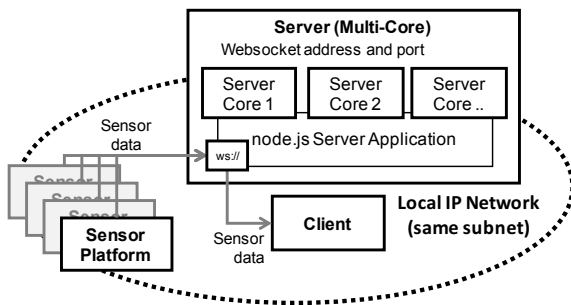
In this section we describe the deployment made to validate the sensor system. It comprises the following components:

- the **Sensor System** component (described in 2),
- the **Server** component, that is used to collect, store and process sensor data. It is also sends sensor data to subscribed clients.
- the **Client** component, that connects to the server component in order to visualise sensor data, and
- the **Network** component that enables data exchange between all components.

The design supports deployment of multiple sensors (measure events from different locations), multiple servers (manage specific sensor clusters, load balance sensor requests) and multiple clients.

Ultimately, components will be accessible globally over the World Wide Web (i.e., Internet) relying on many of the latter's components (e.g., routers and gateways). It is not the scope of this work to describe these thus, for simplicity purposes, the Internet and its components are treated as means to exchange information and are depicted as a cloud. A high-level of the system is presented in Figure 2. The server and client components are introduced next.

FIGURE 2
 SENSOR SYSTEM IMPLEMENTATION



I. Server Component

The server platform runs an HTTP server that can be accessed by sensors (to send measured data) and clients (to access sensor data). The server code is implemented in *node.js* since its event-driven and non-blocking I/O model delivers high performance and scalability. It is also highly integrated with Internet-based technologies and supports multi-core technology.

Furthermore, the server runs a NTP server allowing to synchronize sensors.

The server is implemented in a EliteBook Laptop. Its main characteristics are presented in Table III.

TABLE III
 SERVER IMPLEMENTATION

Server	Main Characteristics
EliteBook Laptop	Intel i7 2.13GHz Quad-Core Built-in Wi-Fi OS: Ubuntu 16.04 LTS 64-bit

II. Client Component

The client component allows visualising online sensor data in real-time. It connects to the server component and requests data from a specific sensor. The client code is implemented in Java Script, a technology supported by most Internet browsers. In this work we use Firefox.

III. Components Communications

The communications between all components (sensor(s), server(s) and client(s)) fully rely on Internet-based technologies. The base protocol will be the ubiquitous Internet Protocol (IP). Considering the need to support a high sensor throughput, producing measurements with a frequency up to 200Hz, the *websocket* protocol [4] is selected due to its capability to handle high data throughput and its easy integration with Internet-based technologies.

IV. Measurements

In order to validate the sensor system, we fixed the sensor system on top of a table. We produced an impulse response on the system and collected sensor measurements.

Example results are presented in Figures 3 (measurements presented in real-time via a web browser) and 4 (measurements stored in a file and later plotted in SciLab). The sensor successfully measured the surface motion over time, by recording the oscillations and associated (decreasing) amplitude and over time.

In Figure 5 we present sensor measurements while the sensor is at rest to show the presence of noise, which exhibits an amplitude of 100 units.

Through this deployment, we also calculated network-related parameters, first presented in [10], that will be relevant for next steps related with deployment of multiple sensor systems, namely:

- **Sensor Network Transmission Rate (SNTR)**, which provides the overall network sensor data transmission throughput and thus an indication of the required network capacity.
- **CPU Sensor Network Performance Index (CSNPI)**, which provides an indication of a server capability to handle network sensor data.

The system deployed in this work has the parameter values presented in Table IV. Based on the $n_{recommended}$ parameter, we know that we should deploy up to 40 sensors so that the server component CPU load is below 50%. We name this group of sensors and server a **cluster**.

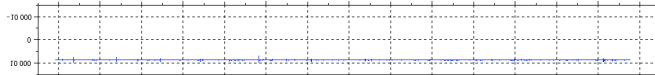
FIGURE 3

WEB CLIENT APPLICATION DISPLAYING ONLINE SENSOR MEASUREMENTS AT 200HZ OVER A 10 SECONDS WINDOW: EFFECT TO AN IMPULSE RESPONSE

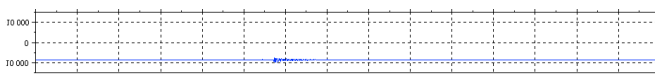


FIGURE 4

SCI-LAB PLOTS OF SENSOR MEASUREMENTS AT 200HZ (OFFLINE DATA): - OVER A 1 HOUR WINDOW



- OVER A 30 SECONDS WINDOW



- OVER A 11 SECONDS WINDOW

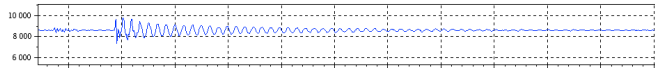


FIGURE 5

SENSOR NOISE (AMPLITUDE ~100 UNITS)

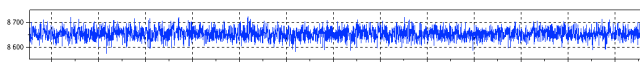


TABLE IV

PARAMETERS FOR SENSOR NETWORK PLANNING

Parameter as in (Manso et al., 2017)	Value (considers a sensor frequency of 200Hz)
SMsgSize	0.12KiB
SNTR	25KiB/s
CSNPI	1333 Ki/s
$n_{recommended}$	40 sensors (CPU at 50%, estimated transmitted network traffic of 960KiB/s)

CONCLUSION

In this paper we presented our work towards deploying an online high-throughput sensor system. Based on the described design and implementation, we presented real measurements collected by the sensor system, via a web-based client (in real-time) and the SciLab tool (offline). In addition, we also calculated network-related parameters for this particular deployment that will be useful for our next steps in the deployment of multiple sensors and clusters. Our next steps include field evaluation of sensor (single) and sensor network (collective) capabilities to measure seismic events.

In this regard, our first prototypes are based on Class C sensors, which limits their applicability in the field (e.g., detect strong shaking, detect signals with frequencies above 1Hz) thus our further experiments will include as well improved sensors, including Class A and Class B (as per USGS classification) seismic sensors.

REFERENCES

- [1] Clayton, R., Heaton, T., Chandy, M., Krause A., Kohler, M., Bunn J., Guy, R., Olson, M., Faulkner, M., Cheng, M., Strand, L., Chandy, R., Obenshain, D., Liu, A., Aivazis, M., 2011. *Community Seismic Network*. Annals of Geophysics, 54, 6.
- [2] Evans, J., Allen, R., Chung, A., Cochran, E., Guy, R., Hellweg, M., and Lawrence, J., 2014. *Performance of Several Low-Cost Accelerometers*. Seismological Research Letters, 85(1). pp. 147-158.
- [3] Farine, M. and Thorburn, N. and Mougnot, D. *General Application of MEMS Sensors for Land Seismic Acquisition – Is it Time?* At: <http://cseg.ca/assets/files/resources/abstracts/2003/218S0130.pdf>
- [4] Fette, I., Melnikov, A., 2011. *RFC 6455 - The WebSocket Protocol*. Internet Engineering Task Force.
- [5] Lin, Fan-Chi, Li, D., Clayton, R., Hollis D., 2013. *High-resolution shallow crustal structure in Long Beach, California: application of ambient noise tomography on a dense seismic array*. Geophysics, 78(4), Q45-Q56.
- [6] Liu, A., 2013. *Sensor Networks for Geospatial Event Detection – Theory and Applications*. PhD Thesis. California Institute of Technology.
- [7] Inbal, A., Clayton, R., and Ampuero, J., 2015. *Mapping Active Faults in Long Beach, California Using a Dense Seismic Array*. Geophysical Research Letters, 42, 6314-6323.
- [8] InvenSense Inc. *MPU-6000 and MPU-6050 Product Specification Revision 3.3*. Document Number: PS-MPU-6000A-00 Revision: 3.3 Release Date: 5/16/2012. www.invensense.com
- [9] Manso M., Bezzeghoud, M., Borges, J. and Caldeira, B., 2016. *Low-Power Low-Cost Sensor Platform for Seismic and Environmental Monitoring*. 9th Spanish-Portuguese Assembly of Geodesy and Geophysics, Madrid, Spain, 28th to 30th June.
- [10] Manso M., Bezzeghoud M. and Caldeira B. *Design and Evaluation of a High Throughput Seismic Sensor Network. Tools for Planning, Deployment and Assessment*. 2017
- [11] NTP (2003). The NTP Public Services Project. Available at: <http://www.ntp.org/ntpfaq/NTP-s-algo.htm>. (Accessed: 5 September 2016)
- [12] Peterson, J., *Observations and Modeling of Seismic Background Noise*, USGS Open- File Report 93-322, 1993
- [13] Science 2.0 (2011) *Quake Catcher Network - Citizen Science Tackles Seismology*. Available at: http://www.science20.com/news_articles/quake_catcher_network_citizen_science_tackles_seismology-80887. (Accessed: 29 January 2016)

Design and Implementation of a Network Enabled High-Throughput MEMs-based Seismic Sensor

Desenho e Implementação de uma Rede de Sensores Sísmicos Microelectromecânicos de Elevado Débito de Dados

M. Manso^{1*}, M. Bezzeghoud², B. Caldeira²

Artigo original
Original article

© 2015 LNEG – Laboratório Nacional de Geologia e Energia IP

Resumo: A rápida evolução tecnológica em sensores, plataformas de sensores e redes de computadores potencia a implantação de redes de sensores de elevada dimensão para a monitorização "ao vivo" e em tempo-real de actividade sísmica com elevada resolução espacial. Neste contexto, este artigo apresenta trabalho desenvolvido no desenho e implementação de um sistema sensor que opera autonomamente, em rede e tem a capacidade de produzir um elevado número de dados (até 200Hz). Descrevemos a instalação do sistema feita com o objectivo de validar o sistema sensor e apresentamos alguns resultados experimentais preliminares. Com base na validação do sistema sensor, o nosso trabalho produziu também conhecimento necessário para planificar adequadamente a rede de sensores que será implantada em trabalho futuro.

Palavras-chave: Rede sísmica, rede de sensores, sismologia

Abstract: The rapid technological evolution in sensors, sensor platforms and networking is enabling the deployment of large sensor networks for "live" and real-time monitoring of seismic activity with high spatial resolution. In this regard, this paper presents our work in designing and implementing a sensor system that operates autonomously, is network enabled and is capable to deliver high data throughput (up to 200Hz). We describe the system deployment done to validate the sensor system and we present preliminary experimental measurement results. By validating the sensor system, our work produced as well the necessary knowledge to properly plan the sensor network that will be deployed in next steps.

Keywords: Seismic Network, Sensor Network, Seismology.

¹ Instituto de Ciências da Terra, IIFA, Universidade de Évora, Colégio Luís António Verney, Rua Romão Ramalho 59, 7000-671 Évora.

² Instituto de Ciências da Terra, IIFA, Departamento de Física, Escola de Ciências e Tecnologia da Universidade de Évora, Departamento de Física, Rua Romão Ramalho, 59, 7000-671 Évora.

*Autor correspondente/Corresponding author: marco@marcomanso.com

1. Introduction

The technology applied to sensors and sensor platforms has evolved in a strong and fast pace over the last years, resulting in increased performance, reduced energy consumption, improved connectivity, miniaturization and reduced cost. These innovations bring to scientific communities and experimenters promising prospects such as the deployment of large sensor networks for "live" (online and real-time) monitoring of seismic activity with high spatial resolution¹.

In this regard, large scale high density sensor networks have been deployed aiming to bring to the field of seismology high resolution geo-referenced measurements: in 2001 and 2002, the California Institute of Technology (CalTech) deployed more than 5200 low-cost stations with an average spacing close to 100m with the purpose to better define the Long Beach Oil Field (Lin *et al.*, 2013; Inbal *et al.*, 2015); in addition, CalTech's established the Community Seismic Network (CSN), an earthquake monitoring system based on a dense array of low-cost acceleration sensors (more than 1000) aiming to produce block-by-block measurements of strong shaking during an earthquake (<http://csn.caltech.edu/about/>); the University of Southern California's (USC) Quake-Catcher Network (QCN) (Clayton *et al.*, 2011) began rolling out in the San Francisco Bay Area comprising 6000 tiny sensors, being part of the densest networks of seismic sensors ever devoted to studying earthquakes (Peterson, 1993). These networks allowed measuring seismic activity with high resolution that, by correlating the signal with time and space, allowed, for example, producing "shake maps" directly from observations. High-density sensor networks can be relevant to other fields as well. Indeed, studies have taken place to demonstrate the detection of important geospatial events such as earthquakes and hazardous radiation, where sensor data correlation improved data quality and brought additional insights (Liu, 2013). Additionally, we foresee the potential to identify precursor signals associated with earthquakes (Manso *et al.*, 2011), a capability that can be used for "early-warning" applications and thus to alert populations and reduce the time to respond to a disaster.

Inspired by these efforts, we leverage on recent technological developments to implement a high-throughput seismic sensor that provides "live" measurements using internet-enabled technologies and operates autonomously (i.e., do not require a computer or an external device to collect and transmit data).

This paper is structured as follows: in the next section we describe the implementation of the sensor system. Then, we describe the deployment made to test the sensor system - comprising server, client and network components - and we show collected preliminary measurements. We finalise by presenting our conclusions and planned future work.

¹ High spatial resolution herein refers to the capability to measure and observe seismic activity over time, where a high density of sensors (e.g.,

1000 times more than conventional seismic networks) is deployed and used to recreate a seismic wave in high detail at a given area.

2. Sensor System Implementation

The sensor system purpose is to measure the physical quantity of interest that, in our case is ground motion acceleration, and transmit the output variable associated to the measure. In this regard, it is important to consider the period associated with the type of seismic wave activity, presented in Table 1, that the sensor system should be able to properly sample (a subset or, optimally, the complete seismic activity range).

The sensor system we implement takes into account the following requirements:

- Uses sensors appropriate for purposes of measuring ground motion acceleration.
- Is able to connect to internet-based networks (e.g., supports 802.11/Wi-Fi standards family).
- Is based on low-cost platforms (to enable deployment of high density networks).
- Operates autonomously so that it can function over several weeks (or months) without requiring human intervention.

Following the general design in (Manso *et al.*, 2016), the components constituting the sensor system are the following: Acquisition and Processing Board, Storage, Networking, Sensor, Real-Time Clock (RTC) and Power Supply. These are presented in Table 2 and introduced next.

For the Acquisition and Processing Board, the ESP8266 is selected because it provides a fast and programmable microcontroller and integrates Storage (on-chip SRAM), Networking (via its embedded Wi-Fi capabilities) and RTC components as well. RTC time synchronisation, in particular, is achieved by means of Network Time Protocol (provided by the server component running its own NTP server). NTP can keep time accuracy of all machines within the same subnet within one millisecond (NTP, 2003), which suffices for our application scenario. The ESP8266 also supports a wide range of libraries, in large part provided by the Arduino community.

The sensor component is a central element of this work and is presented in more detail next.

Table 1: Typical period exhibited by seismic wave activity

Tabela 1: Período típico associado a actividade sísmica

Seismic Wave Period (Period in seconds and Frequency in Hz) based on (Shearer, 2009)					
0.001 to 0.1 s	0.1 to 10 s	10 to 100 s	100 to 10 ³ s	10 ³ to 10 ⁴ s	>10 ⁴ s
1000 to 10 Hz	10 to 0.1 Hz	0.1 to 0.01 Hz	0.01 to 10 ⁻³ Hz	10 ⁻³ to 10 ⁻⁴ Hz	<10 ⁻⁴ Hz
Body waves, earthqua kes (M < 2)	Body waves, earthqua kes (M > 2)	Surface waves, body earthqua kes (M > 6)	Surface waves, earthqua kes	Earth free oscillatio ns, earthqua kes	Earth tides

2.1. Accelerometer Sensor Component

To measure ground motion, we rely on low-cost small size MEM (micro-electro-mechanical) accelerometer sensor technologies. These sensors are low cost, robust (capable to measure and/or sustain high acceleration values), capable of self-calibration (resulting from their ability to measure the gravity

Table 2: Sensor Implementation Elements

Tabela 2: Elementos da Implementação do Sensor

Element	Architecture Component as in (Manso <i>et al.</i> , 2016)
ESP8266 (ESP-01 model)	Acquisition and Processing Board (32-bit processor at 80MHz); Storage (on-chip SRAM); Networking (integrated TCP/IP protocol stack, Wi-Fi)
MPU-6050	Sensor: 3-axis 16-bit accelerometer (0.06mg resolution at 2g) Up to 200Hz measurement frequency
Internal clock synchronised with NTP	Real-Time Clock
3.3v Power Supply Board	Power Supply
I2C Bus	Data Interface (connecting the ESP8266 to the MPU-6050)

acceleration component) and requires low maintenance. For purposes of seismology, these MEM-based accelerometers:

- provide adequate sensitivity, noise level, and range (measured in g) to be applicable to earthquake strong-motion acquisition ($M > 3$), thus also limiting the "resolution" capability. However, the high level of instrumental self noise that increases as frequency decreases limits their application in the study of low frequency weak-motion forces (Evans *et al.*, 2014; Farine *et al.*, 2003);
- are well fit to measure high frequency (>40Hz) ground motion since their resonant frequency (typically above 1 kHz) is far above the seismic band pass;
- measure the gravity acceleration component that provides a useful reference for sensitivity calibration and tilt measurement;
- have high acceleration ranges (several gs) and are capable to sustain high acceleration (several hundred gs) without being damaged;
- when compared with seismometers, such as geophones, MEMs may have an advantage in detecting weak high frequency signals, while geophones may have the advantage in detecting weak signals at low frequencies;
- can have useful applications such as earthquake early warning, seismic hazard map and security applications.

For this proof-of-concept, we select the MPU-6050, a 3-axis MEM accelerometer that has the following specifications (InvenSense, 2012):

- Accelerometer range: $\pm 2g$ (minimum);
- Accelerometer sample rate up to 1kHz;
- 16-bit resolution (16384 LSB resolution per g at 2g);
- Power spectral density (PSD): $400\mu g/\sqrt{Hz}$ (taking as reference the Peterson New Low Noise Model (approximately $10ng/\sqrt{Hz}$) (Peterson, 1993), this sensor's self-noise makes it unfit to measure weak seismic activity occurring at low frequencies);

- Operating current: 500µA (normal), 20µA (if sample rate at 5Hz), 5µA (sleep mode) and
- I2C Digital Interface

The MPU-6050 can be categorized as Class-C sensor (according to (USGS, 2008) given its resolution from about 12 to 16 bits, typically over 2g ranges) that have found applications in generating reliable pictures of regional seismicity and strong shaking (Evans *et al.*, 2014). Referring to Table 1, the MPU-6050 is expected to successfully measure surface waves, body waves and earthquakes exhibiting frequencies above 10Hz.

The sensor system interconnections are presented in Figure 1 and the pin connections between the components are presented in Table 3. Note that the data interface used is the I2C Digital Interface and that the MPU-6050 module has pull-up resistors as required by the I2C bus.

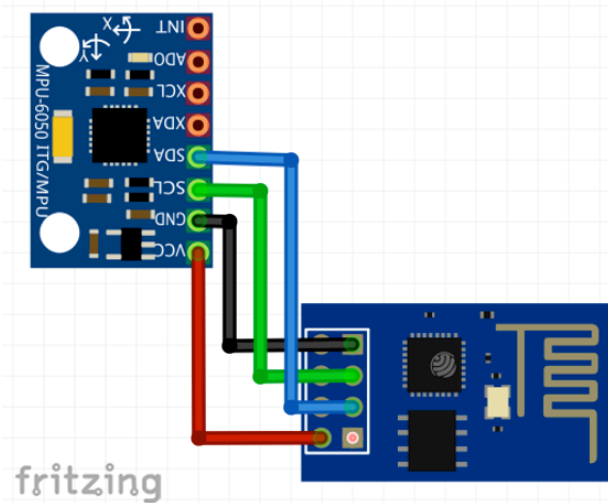


Figure 1. Sensor System Implementation

Figura 1. Implementação do Sistema Sensor

The software flowchart is depicted in Figure 2. It comprises two main parts:

- The "Initialisation" part is devoted to setup the system components, namely the I2C bus, network, accelerometer sensor and time (through NTP);
- The "Main Loop" main purpose is to periodically read accelerometer data and send it over the network. It verifies the network connection status and, if disconnected, attempts to reconnect the system to the network.

The data is sent over the network in "String" format comprising the following information: sensor identification (string), date (number aggregating year, month and day), time (number aggregating hours, minutes and seconds), milliseconds (number representing the milliseconds since program start), sequence number of sample (in our case is zero) and acceleration (3 numbers, each with a resolution of 16-bit and representing, respectively, the acceleration value in the X, Y and Z axis of the

Table 3: I²C PIN Sensor System Connections
Tabela 3: Ligações dos pinos I²C no Sistema Sensor

Interface	ESP Pin	MPU Pin
I ² C SDA	Pin 0	SDA
I ² C SCL	Pin 2	SCL

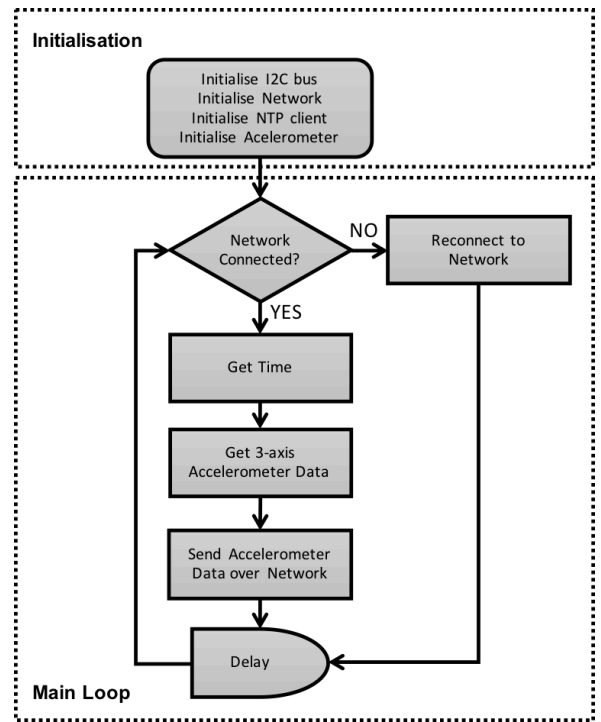


Figure 2 - Sensor System Flowchart

Figura 2 - Fluxograma do Sistema Sensor

sensor). An excerpt of data concerning a single sensor sample is presented below²:

```
/sensor_esp0004 20161020 040039
17455305 0 16168
1954 -3606
```

3. Deployment

In this section we describe the deployment made to test the sensor system. It comprises the following components:

- the Sensor System component (described in the previous section),
- the Server component, that is used to collect, store and process sensor data. It also sends sensor data to subscribed clients.
- the Client component, that connects to the server component in order to retrieve and/or visualise sensor data, and
- the Network component that enables data exchange between all components.

The design supports deployment of multiple sensors, servers and clients.

Ultimately, components will be accessible globally over the World Wide Web (i.e., Internet) relying on many of the latter's components (e.g., routers and gateways). It is not the scope of this work to describe them thus, for simplicity purposes, the Internet and its components are treated as means to exchange information and are depicted as a cloud.

² In this example, the accelerometer range was set to ±2g, thus a value of 16384 corresponds to 1g.

A high-level of the system is presented in Figure 3. The server and client components are introduced next.

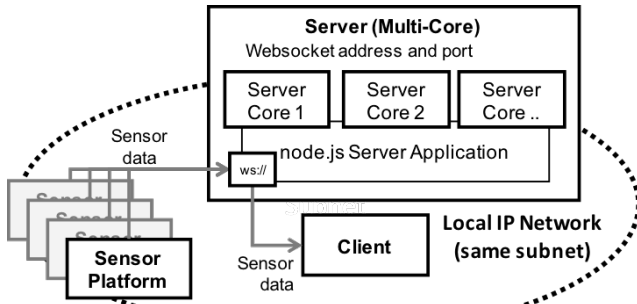


Figure 3 - Overall System Implementation

Figura 3 - Esquema de Alto Nível do Sistema

3.1. Server Component

The server platform runs an HTTP server that can be accessed by sensors (that send measured data) and clients (that access sensor data). The server code is implemented in node.js since its event-driven and non-blocking I/O model delivers high performance and scalability. It is also highly integrated with Internet-based technologies and supports multi-core technology.

Furthermore, the server runs a NTP server used to synchronize sensors.

The server is deployed in a EliteBook Laptop whose main characteristics are presented in Table 4.

Table 4: Server Implementation

Tabela 4: Implementação do Servidor

Server	Main Characteristics
EliteBook Laptop	Intel i7 2.13GHz Quad-Core Built-in Wi-Fi OS: Ubuntu 16.04.1 LTS (Xenial Xerus, Linux Kernel 4.4) 64-bit

3.2. Client Component

The client component allows collecting and/or visualising online sensor data in real-time. It connects to the server component and can request data from specific sensors. The client code used in this work is implemented in Javascript, a technology supported by most Internet browsers. In this work we use Firefox.

3.3. Components Communications

The communications between all components (sensor(s), server(s) and client(s)) fully rely on Internet-base technologies. The base protocol will be the ubiquitous Internet Protocol (IP). Considering the need to support a high sensor throughput, producing measurements with a frequency up to 200Hz, the websocket protocol (Fette and Melnikov, 2011) is selected due to its capability to handle high data throughput, exhibit low latency and its easy integration with Internet-based technologies.

3.4. Measurements

In order to validate the sensor system, we conducted a simple experiment where we fixed the sensor on top of a table, produced an impulse response input on the system (causing the table to oscillate) and collected sensor measurements using a 200Hz sampling frequency. Note that a single sensor operating in a single day generates more than 17 million samples (several Terabytes of network traffic data) and therefore strategies to reduce the volume of data transmitted (e.g., use of compression) and even preclude its transmission when data is irrelevant (e.g., no signal present) are highly recommended and will be addressed in future work.

Obtained results are presented in Figure 4 (measurements presented in real-time via a web browser) and Figure 5 (measurements stored in a file and later plotted in SciLab). The sensor measured surface motion recording surface acceleration over time.

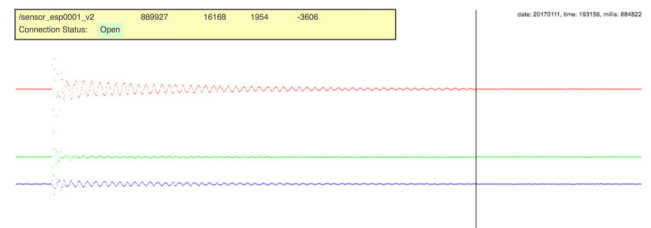


Figure 4: Web Client application displaying online sensor measurements at 200Hz over a 10 seconds window: effect to an impulse response

Figura 4: Aplicação de Cliente Web a apresentar medições do sensor a 200 Hz ao longo de uma janela temporal de 10 segundos

In this deployment, we also calculated parameters, first presented in (Manso *et al.*, 2017), that are relevant for our next steps in planning the deployment of networks comprising a large number of sensors. Namely:

- Sensor Network Transmission Rate (SNTR) represents the overall network sensor data transmission throughput per time and thus provides an indication of the required network capacity. SNTR is the amount of data (in KiB) transmitted per second and can be determined according to formula (1).

$$SNTR = \sum_{\text{All sensors}} SMsgSize \times SFreq(\text{sensor}) \quad (1)$$

Where:

- SMsgSize is the size (in KiB) required to transmit a single sensor measurement. It also includes protocol overheads (in our case, 0.12KiB per message).
- SFreq(sensor) is the measuring frequency (in Hz) of the respective sensor.
- CPU Sensor Network Performance Index (CSNPI), which provides an indication of a server capability to handle network sensor data. The CSNPI value can be determined for any server platform by conducting live measurements of server and sensors deployments. The CSNPI is a useful tool to

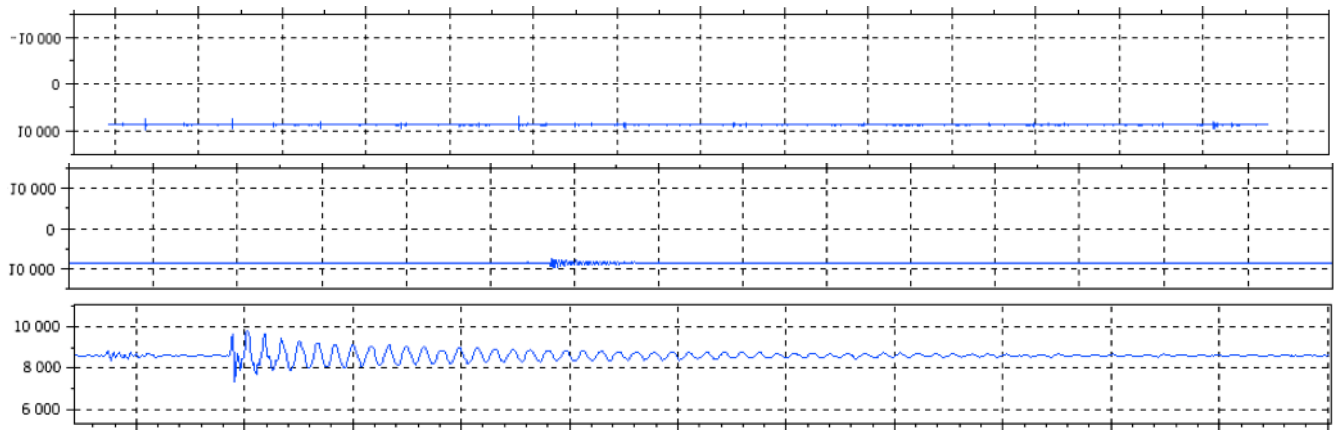


Figure 5. SciLab plots of recorded sensor measurements at 200Hz over a 60 minutes window (top), a 30 seconds window (middle) and 11 seconds window (bottom)

Figura 5. Gráficos no SciLab relativos a medições registadas do sensor a 200 Hz ao longo de uma janela temporal de 60 segundos (topo), 30 segundos (meio) e 11 segundos (baixo)

assist the design of a network involving a high number of high-throughput sensors and servers, providing a method to determine the recommended (and highest) number of connected sensors a server (or a cluster of servers) can support.

Once the CSNPI is empirically determined, the formula to determine the expected server CPU load when handling an arbitrary number of sensors (exhibiting a known SNTR) is presented in (2).

$$CPU_Load = \frac{SNTR}{CSNPI} \times 100\% \quad (2)$$

The system deployed in this work has the parameter values presented in Table 5. Based on the nrecommended parameter, we now know that we should deploy up to 35 sensors so that the server component CPU load is below 50%. We name this group of sensors and server a cluster.

Table 5: Parameters for Sensor Network Planning

Tabela 5: Parâmetros para o planeamento da Rede de Sensores

Parameter as in (Manso <i>et al.</i> , 2017)	Value (considers a sensor sample frequency of 200Hz)
SMsgSize	0.12KiB
SNTR	840KiB/s
CSNPI	1727 KiB/s
$n_{recommended}$	35 sensors (CPU at 50%, estimated transmitted network traffic of 840KiB/s)

4. Conclusion

In this paper we presented our work towards deploying an online high-throughput sensor system. Based on the described design and implementation, we demonstrated its successful deployment for testing purposes and presented real measurements - generated in controlled conditions - collected by the sensor

system, via a web-based client (in real-time) and the SciLab tool (offline). In addition, we also calculated the SNTR and CSNPT parameters for this particular deployment that will be useful for our follow up work in planning and deploying multiple sensors, servers and clusters. Furthermore, we will deploy our sensor system complementing existing seismic sensors in order to field evaluate them and produce evidence towards their usefulness in measuring seismic activity. In this regard, as per USGS classification (USGS, 2008), our first prototypes are based on Class C sensors, which limits their applicability in the field (e.g., detect strong shaking, detect signals with frequencies above 1Hz) thus our future experiments will include as well improved sensors, including Class A and Class B (as per USGS classification) seismic sensors.

References

- Clayton, R., Heaton, T., Chandy, M., Krause A., Kohler, M., Bunn J., Guy, R., Olson, M., Faulkner, M., Cheng, M., Strand, L., Chandy, R., Obenshain, D., Liu, A., Aivazis, M., 2011. Community Seismic Network. *Annals of Geophysics*, 54, 6.
- Evans, J., Allen, R., Chung, A., Cochran, E., Guy, R., Hellweg, M., and Lawrence, J., 2014. Performance of Several Low-Cost Accelerometers. *Seismological Research Letters*, 85(1). pp. 147-158.
- Farine, M., Thorburn, N. and Mougnot, D. General Application of MEMS Sensors for Land Seismic Acquisition - Is it Time? At: <http://cseg.ca/assets/files/resources/abstracts/2003/218S0130.pdf>
- Fette, I. and Melnikov, A., 2011. RFC 6455 - The WebSocket Protocol. Internet Engineering Task Force.
- Lin, Fan-Chi, Li, D., Clayton, R., Hollis D., 2013. High-resolution shallow crustal structure in Long Beach, California: application of ambient noise tomography on a dense seismic array. *Geophysics*, 78(4), Q45-Q56.
- Liu, A., 2013. Sensor Networks for Geospatial Event Detection — Theory and Applications. PhD Thesis. California Institute of Technology.
- Inbal, A., Clayton, R., and Ampuero, J., 2015. Mapping Active Faults in Long Beach, California Using a Dense Seismic Array. *Geophysical Research Letters*, 42, 6314-6323.
- InvenSense Inc. MPU-6000 and MPU-6050 Product Specification Revision 3.3. Document Number: PS-MPU-6000A-00 Revision: 3.3 Release Date: 5/16/2012. www.invensense.com
- Manso M., Silva H.G. and Bezzeghoud M. PLASMA, a high-performing and open platform for the integration of heterogeneous sensor networks. 2011. 5th Meeting of Post-Graduation in Physics and Earth Sciences of University of Évora (PGUE2011), Évora, Portugal, 21st September.
- Manso M., Bezzeghoud, M., Borges, J. and Caldeira, B., 2016. Low-Power Low-Cost Sensor Platform for Seismic and Environmental

- Monitoring. 9th Spanish-Portuguese Assembly of Geodesy and Geophysics, Madrid, Spain, 28th to 30th June.
- Manso M., Bezzeghoud M. and Caldeira B. Design and Evaluation of a High Throughput Seismic Sensor Network. Tools for Planning, Deployment and Assessment. 2017. 6th International Conference on Sensor Networks SENSORNETS, Porto, Portugal, 19 to 21 February.
- NTP (2003). The NTP Public Services Project. Available at: <http://www.ntp.org/ntpfaq/NTP-s-algo.htm>. (Accessed: 5 September 2016)
- Peterson, J., Observations and Modeling of Seismic Background Noise, USGS Open- File Report 93-322, 1993
- Science 2.0 (2011) Quake Catcher Network - Citizen Science Tackles Seismology. Available at: http://www.science20.com/news_articles/quake_catcher_network_citizen_science_tackles_seismology-80887. (Accessed: 29 January 2016)
- Shearer, P. In Introduction to Seismology, Second Edition. 2009. Cambridge University Press.
- USGS. Instrumentation Guidelines for the Advanced National Seismic System. Open-File Report 2008-1262.

Design and Evaluation of a High Throughput Seismic Sensor Network

Tools for Planning, Deployment and Assessment

Marco Manso¹, Mourad Bezzeghoud² and Bento Caldeira²

¹*Instituto de Ciências da Terra, Universidade de Évora, Évora, Portugal*

²*Departamento de Física, Escola de Ciências e Tecnologia da Universidade de Évora, Évora, Portugal*

Keywords: Seismic Network, Sensor Network, Seismology.

Abstract: The rapid technological evolution in sensors, sensor platforms and networking is enabling the deployment of large sensor networks for "live" monitoring of seismic activity with high spatial resolution. In this regard, this paper describes our work in developing an online "High Throughput Seismic Sensor Network". We present the architecture and implementation comprising seismic sensors and servers (running data collection services) connected through internet-enabled technologies. We validate and assess the system, as well as identify bottlenecks, by means of experimentation. Based on the collected empirical data, we were able to identify methods and tools to support effective planning and implementation of sensor networks based on two main indicators: Sensor Network Transmission Rate (SNTR), which provides the overall network sensor data transmission throughput and thus an indication of the required network capacity; and CPU Sensor Network Performance Index (CSNPI), which provides an indication of a server capability to handle network sensor data. As we progress in our work to field deploy seismic sensor networks, we will continue to use these tools to plan and deploy future sensor networks, as well as assess improvements and modifications along the way.

1 INTRODUCTION

The technology applied to sensors and sensor platforms has evolved in a strong and fast pace over the last years, resulting in increased performance, reduced energy consumption, improved connectivity, miniaturization and reduced cost. These innovations bring to scientific communities and experimenters promising prospects such as the deployment of large sensor networks for "live" (online and real-time) monitoring of seismic activity with high spatial resolution. Simultaneously, when considering the implementation of such networks that often require high data throughput, it becomes critical to address questions such as: What is the sensor network throughput and expected network load? What is the system required capacity to process all sensor data?

In this paper we present our work towards deploying an online "High Throughput Seismic Sensor Network" comprising several seismic sensors (real and simulated) and data collection services, all

of them connected using internet-enabled technologies. This paper is structured as follows: in section 2 we present related past and on-going work in this field; in section 3 we present our design and implementation (including equipment selection) of the system; in section 4 we describe experiments conducted with the aim to assess and validate the design and gather empirical data allowing to address the presented key questions and create methods and tools to support future planning decisions and assess improvements and modifications along the way; section 5 concludes the paper.

2 BACKGROUND

The deployment of large scale high density sensor networks aims to bring to the field of seismology high resolution geo-referenced measurements: in 2001 and 2002, the California Institute of Technology (CalTech) deployed more than 5200 low-cost stations with an average spacing close to

100m with the purpose to better define the Long Beach Oil Field (Lin *et al*, 2013; Inbal *et al*, 2015); in addition, CalTech's established the Community Seismic Network (CSN), an earthquake monitoring system based on a dense array of low-cost acceleration sensors (more than 1000) aiming to produce block-by-block measurements of strong shaking during an earthquake (<http://csn.caltech.edu/about/>); the University of Southern California's (USC) Quake-Catcher Network (QCN) (Clayton *et al*, 2011) began rolling out in the San Francisco Bay Area comprising 6000 tiny sensors, being part of the densest networks of seismic sensors ever devoted to studying earthquakes (Science 2.0). These networks allowed measuring seismic activity with high resolution that, by correlating the signal with time and space, allowed, for example, producing "shake maps" directly from observations. High-density sensor networks can be relevant to other fields as well. Indeed, studies have taken place to demonstrate the detection of important geospatial events such as earthquakes and hazardous radiation, where sensor data correlation improved data quality and brought additional insights (Liu, 2013).

Inspired by these efforts, we leverage on recent technological developments to realise a "High Throughput Seismic Sensor Network" comprising a large number of sensors capable of autonomous operation (i.e., do not require a computer or an external device to collect and transmit data), network using Internet-based technologies and be affordable (sensor cost inferior to €40). Affordability was proven by our first fully functional sensor prototype, presented in (Manso *et al*, 2016), that had a cost below €25.

3 DESIGN AND IMPLEMENTATION

In this section we present the system design of the seismic sensor network, that mainly comprises a **Sensor Platform** component (to measure the variable(s) of interest and transmit data), a **Server** component (to collect, store, process and visualise sensor data) and the **Network** component (to enable data exchange between sensors and server(s)). A large number of sensors is expected to be deployed. As such, a server cluster implementation is envisaged to ensure scalability and distribute load over multiple processors and computers.

Ultimately, system resources (sensors and servers) will be accessible globally over the World Wide Web (i.e., Internet) relying on many of the latter's components (e.g., routers and gateways). It is not the scope of this work to describe these thus, for simplicity purposes, the Internet and its components are treated as means to exchange information and are depicted as a cloud. It is also assumed that sensors are able to connect to servers. A general view of the system is presented in Figure 1. The sensor and server components are described next.

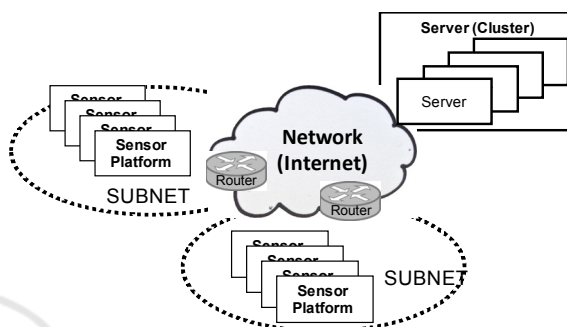


Figure 1: Seismic Monitoring System: General View.

3.1 Sensor Component

The sensor component purpose is to measure a physical quantity of interest, that, in our case is ground motion and transmit the output variable associated to the measure. Following the general design in (Manso *et al*, 2016), the selected elements constituting the sensor component are presented in Table 1.

Table 1: Sensor Implementation.

Element	Architecture Component as in (Manso <i>et al</i> , 2016)
ESP8266 (ESP-01 model)	Acquisition and Processing Board (32-bit processor at 80MHz); Storage (on-chip SRAM); Networking (Wi-Fi)
MPU-6050	Sensor: 3-axis 16-bit accelerometer (0.06mg resolution at 2g) Up to 200Hz measurement frequency
Internal clock synchronised with NTP	Real-Time Clock
3.3v Power Supply Board	Power Supply
I2C Bus	Data Interface (connecting the ESP8266 to the MPU-6050)

The ESP8266 is selected because it provides a fast and programmable microcontroller, embedded

Wi-Fi capabilities and support of a wide range of libraries (via the Arduino community).

Time synchronisation is achieved by means of Network Time Protocol (provided by the server component running its own NTP server). NTP can keep time accuracy of all machines within the same subnet within one millisecond (NTP, 2003), which suffices for our application scenario.

For sensor measurement purposes, we use a 3-axis accelerometer. We select the low cost MPU-6050 because it provides a good resolution (16-bit), high frequency measurements (up to 200Hz) and incorporates an internal FIFO allowing to store up to 170 measurements. The FIFO also allows decoupling the sensing cycle (running in the MPU-6050) from the main processing and networking cycles (running in the ESP8266) reducing the risk of missing sensor samples. The MPU-6050 is categorized as Class-C (resolution from about 12 to 16 bits, typically over 2g ranges) that have found applications in generating reliable pictures of regional seismicity and strong shaking (Evans et al, 2014).

3.2 Server Component

The implemented server component collects and stores data received from sensors. It also runs a NTP server allowing to synchronize sensors.

The server runs an HTTP server that can be accessed by sensors over a local network or the Internet and used to send measured data. The server code is implemented in *node.js* since its event-driven and non-blocking I/O model delivers high performance and scalability. It is also highly integrated with Internet-based technologies and supports multi-core technology.

Two server platforms will be implemented. Their main characteristics are presented in Table 2.

Table 2: Server Implementations.

Server	Main Characteristics
Server PC (ServerPC)	Intel Core 2 Duo 64-bit (dual core) 2.33GHz Built-in Ethernet OS: Ubuntu Server 16.04.1 LTS (Xenial Xerus, Linux Kernel 4.4) 64-bit
Raspberry Pi 3 (Raspi3)	CPU: ARMv8 64-bit quad-core 1.2GHz Built-in Ethernet OS: Raspian (Debian Jessie, Linux Kernel 4.4) 32-bit

3.3 Server-Sensor Communications

The communications between sensors and server(s) fully rely on Internet-base technologies. The base protocol will be the ubiquitous Internet Protocol (IP). Considering the need to support a high sensor throughput, which produces measurements with a frequency up to 200Hz, the *websocket* protocol (Fette and Melnikov, 2011) is selected due to its capability to handle high data throughput and its easy integration with Internet-based technologies.

4 EXPERIMENT

In this section we describe a set of experiments conducted to assess the network system based on collected empirical data. The derived analysis and observations allow developing methods and tools to support planning and design of future deployments.

4.1 Setup

We are interested in evaluating the system comprising sensors exhibiting high data throughput (up to 200Hz sensor data frequency, i.e., the highest frequency of the selected accelerometer).

The experiment setup is depicted in Figure 2. In this setting, all components are part of the same local network. Multiple sensors are deployed. The server component is accessible via the *websocket* protocol. To collect sensor data, the server runs a *node.js* application that is capable to distribute, as needed, sensor requests across all available CPU cores (i.e., load balancing), thus fully exploiting its processing capabilities.

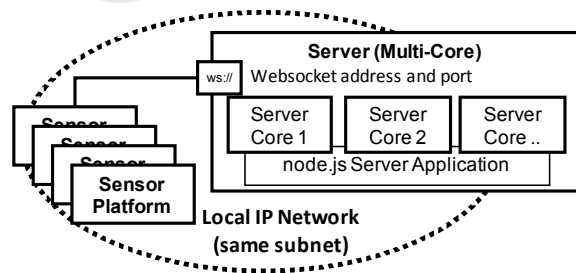


Figure 2: Experiment Setup.

The sensors used in this experiment are simulated and mimic the actual throughput of the sensor component described in Table 1.

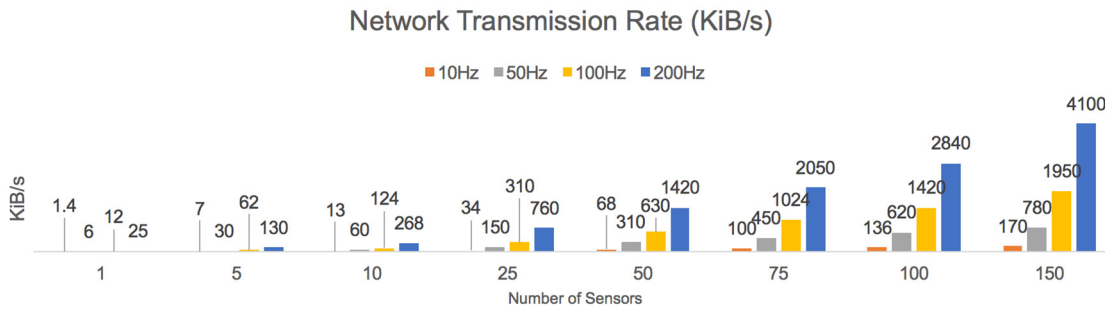


Figure 3: Network Transmission Rate measured per number of sensors per frequency. It is important to note that measurements pertaining to 100 and 150 sensors at 200Hz and 150 sensors at 100Hz were obtained using formula (1).

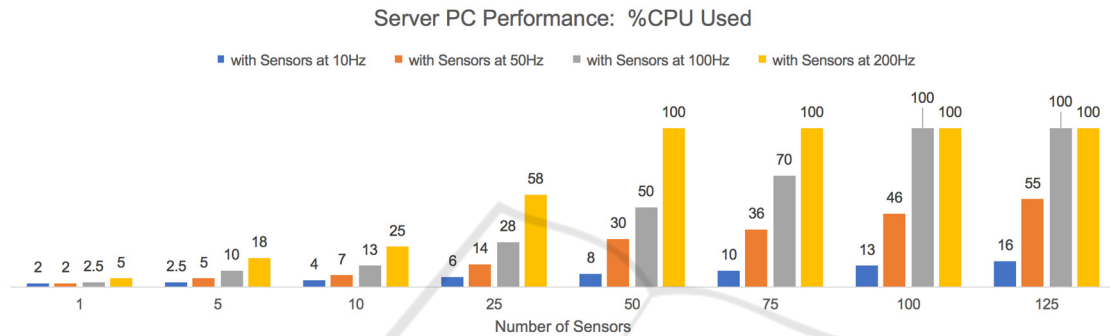


Figure 4: ServerPC Performance measured based on the percentage of CPU allocated to process sensors' requests.

4.2 Measurements

4.2.1 Network Transmission Rate

We start by measuring the actual network transmission rate as a function of the number of sensors and their measurement frequency. For this purpose, we used the "System Monitor" tool provided by Ubuntu, thus these measurements are only approximate and are presented in Figure 3.

As expected, the transmission rate increases proportionally with the number of sensors and their frequency. This relation can be approximately described and generalised according to formula (1).

$$SNTR = \sum_{\text{All sensors}} SMsgSize \times SFreq(sensor) \quad (1)$$

Where:

- *SNTR* (Sensor Network Transmission Rate) is the amount of data (in KiB) transmitted per second.
- *SMsgSize* is the size (in KiB) required to transmit a single sensor measurement. It also includes protocol overheads (in our case, 0.14KiB per message).

- *SFreq(sensor)* is the measuring frequency (in Hz) of the respective sensor.

It can be verified that the formula provides predictions that are close to the measured values, as exemplified below:

- 10 sensors at 10Hz produce 13KiB/s against 14KiB/s given by the formula;
- 75 sensors at 200Hz produce 2050KiB/s against 2100KiB/s given by the formula;
- 100 sensors at 200Hz produce 2080KiB/s against 2800 KiB/s given by the formula;
- 10 sensors at 100Hz produce 124KiB/s against 140 KiB/s given by the formula
- 25 sensors at 200Hz produce 760KBi/s against 700KiB/s given by the formula.

The SNTR is useful to determine the server workload (as presented next) and the network capacity requirements.

4.2.2 Server Performance

The server performance is assessed based on the percentage of CPU (%CPU) allocated to process all sensors' request, which varies according to the number of sensors and their sample frequency (both used to determine the *SNTR*). The lower the %CPU the better is the server performance. Average

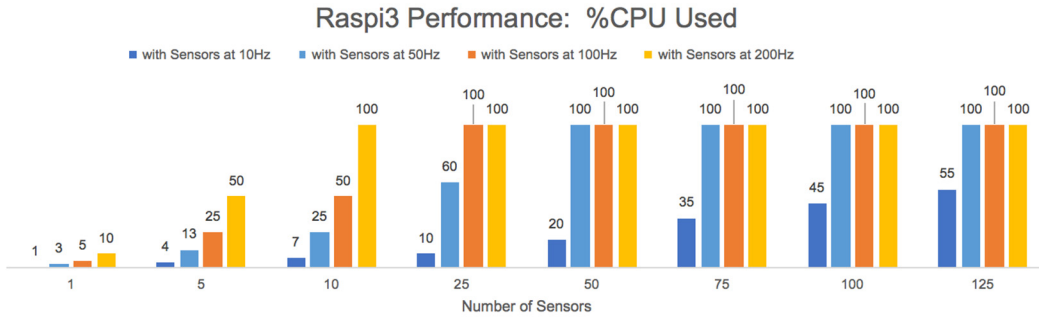


Figure 5: Raspi3 Performance measured based on the percentage of CPU allocated to process sensors' requests.

```
top - 22:12:17 up 1 day, 29 min, 4 users, load average: 0.86, 0.25, 0.08
Tasks: 154 total, 1 running, 153 sleeping, 0 stopped, 0 zombie
%Cpu(s): 16.7 us, 5.6 sy, 0.0 ni, 76.4 id, 0.0 wa, 0.0 hi, 1.4 si, 0.0 st
KiB Mem: 882780 total, 391408 used, 491372 free, 39128 buffers
KiB Swap: 102396 total, 0 used, 102396 free. 208028 cached Mem
```

PID	USER	PR	NI	VIRT	RES	SHR	S	%CPU	%MEM	TIME+	COMMAND
20724	pi	20	0	70288	18100	7752	S	30.6	2.1	0:08.61	nodejs
20720	pi	20	0	70452	17796	7844	S	18.3	2.0	0:05.66	nodejs
20721	pi	20	0	70448	18544	7840	S	18.3	2.1	0:21.74	nodejs
20722	pi	20	0	70456	17828	7844	S	17.8	2.0	0:05.74	nodejs
14835	root	20	0	0	0	0	S	5.9	0.0	0:01.63	kworker/u8+
78	root	-51	0	0	0	0	D	3.0	0.0	0:31.53	irq/92-mmc1
22094	pi	20	0	5112	2520	2140	R	1.0	0.3	0:00.83	top

Figure 6: Example of CPU Usage Provided by Top in Raspberry Pi 3.

allocations above 60% should be avoided to ensure a *healthy* server.

We present in Figure 6 an example visualisation of the %CPU allocation provided by the top application running on the *Raspi3*. It is visible the 4 instances of *nodejs* handling sensor requests. At the moment the snapshot was taken, the overall CPU usage was 22.3% CPU. Note that applications not related with the monitoring system also consume resources (*top* included).

Next, we present measurements for the two server platforms we selected.

(a) ServerPC Performance

The *ServerPC* performance measurements are presented in Figure 4. As expected, increasing the number of sensors and/or sensors' frequency increases the %CPU. Based on the performance measurements, we see that the relation is proportional and can be approximately described according to the following formula:

$$CPU_Load = \frac{SNTR}{1310} \times 100\% \quad (2)$$

Where:

- *CPU_Load* is the percentage of CPU (%CPU) allocated to process all sensors' request.
- *SNTR* is described in (1).

- 1310 is the value that characterises this server capability to handle network sensor data (units are KiB/s). We name this value the "CPU Sensor Network Performance Index" (CSNPI).

From Figure 4, the recommended maximum number of connected sensors to a single *ServerPC* (i.e., %CPU less than 60%) are 25, 50 and 125 if, respectively, a frequency of 200Hz, 100Hz and 50Hz are used. Adapting formula (2) to (2.1), we can infer that a single *ServerPC* may support in good *health* about 560 homogeneous sensors at 10Hz.

$$n_{\text{recommended}} = \frac{CPU_Load_{\text{recommended}} \times 1310}{SMsgSize \times SFreq \times 100} \quad (2.1)$$

Where $n_{\text{recommended}}$ is the maximum number of sensors recommended.

(b) Raspi3 Performance

The *Raspi3* performance measurements are presented in Figure 5.

Similar to the *ServerPC*, a relation can be established and described according to formula (2), however with the CSNPI that characterises the specific platform, obtained from the performance measurements. The formula for the *Raspi3* is presented in (3).

$$CPU_Load = \frac{SNTR}{280} \times 100\% \quad (3)$$

The variables in (3) are the same as in (2). Note that the Raspi3 CSNPI value is almost 5 times smaller than the ServerPC CSNPI, thus one can conclude that it copes with 5 times less sensors.

From Figure 5 the recommended maximum number of connected sensors to a single *Raspi3* are 5, 10 and 25 and 125 if, respectively, a frequency of 200Hz, 100Hz, 50Hz and 10Hz are used.

(c) Generalisation

The formula to determine the expected server CPU load when handling an arbitrary number of sensors (exhibiting a known *SNTR*) is presented in (4), which is a generalisation from (2) and (3).

$$CPU_Load = \frac{SNTR}{CSNPI} \times 100\% \quad (4)$$

The CSNPI value can be determined for any server platform and, as demonstrated herein, is a useful tool to assist the design of a network involving a high number of high-throughput sensors and servers, providing a method to determine the recommended (and highest) number of connected sensors a server (or a cluster of servers) can support, based on a sensors message size and frequency.

5 CONCLUSIONS

In this paper we presented our work towards deploying an online "High Throughput Seismic Sensor Network". An architecture has been described comprising seismic sensors and servers (running data collection services) connected through internet-enabled technologies. Experiments were conducted that successfully validated the design across different system configurations, as well as identify its limitations. The experiments also gathered important empirical data that allowed us to create methods and tools to support future planning decisions towards deploying real sensor networks. For this purpose, two network-related indicators are proposed:

- **Sensor Network Transmission Rate (SNTR)**, which provides the overall network sensor data transmission throughput and thus an indication of the required network capacity.
- **CPU Sensor Network Performance Index (CSNPI)**, which provides an indication of a server capability to handle network sensor data.

Based on these indicators, we are now able to determine the recommended number of sensors to deploy based on network and server capabilities. Conversely, we can also determine the network and server requirements based on the number of sensors we aim to deploy.

Our next steps include the evaluation of the sensor network capability to respond to seismic events and their field deployment involving a large number of components (thus a high network throughput is expected). Thus we will rely on the above tools for proper planning and implementation.

Furthermore, we will use these tools and methods to measure and empirically validate the effects of system- and component-level improvements (such as message compression to reduce size, use more efficient communications protocols, modify network protocol parameters, incorporation of message brokers). System- and component-level improvements will be addressed in future work.

REFERENCES

- Clayton, R., Heaton, T., Chandy, M., Krause A., Kohler, M., Bunn J., Guy, R., Olson, M., Faulkner, M., Cheng, M., Strand, L., Chandy, R., Obenshain, D., Liu, A., Aivazis, M., 2011. *Community Seismic Network*. *Annals of Geophysics*, 54, 6.
- Evans, J., Allen, R., Chung, A., Cochran, E., Guy, R., Hellweg, M., and Lawrence, J., 2014. *Performance of Several Low-Cost Accelerometers*. *Seismological Research Letters*, 85(1). pp. 147-158.
- Fette, I., Melnikov, A., 2011. *RFC 6455 - The WebSocket Protocol*. Internet Engineering Task Force.
- Inbal, A., Clayton, R., and Ampuero, J., 2015. *Mapping Active Faults in Long Beach, California Using a Dense Seismic Array*. *Geophysical Research Letters*, 42, 6314-6323.
- Lin, Fan-Chi, Li, D., Clayton, R., Hollis D., 2013. *High-resolution shallow crustal structure in Long Beach, California: application of ambient noise tomography on a dense seismic array*. *Geophysics*, 78(4), Q45-Q56.
- Liu, A., 2013. *Sensor Networks for Geospatial Event Detection — Theory and Applications*. PhD Thesis. California Institute of Technology.
- Manso M., Bezzeghoud, M., Borges, J. and Caldeira, B., 2016. *Low-Power Low-Cost Sensor Platform for Seismic and Environmental Monitoring*. 9th Spanish-Portuguese Assembly of Geodesy and Geophysics, Madrid, Spain, 28th to 30th June.
- NTP (2003). The NTP Public Services Project. Available at: <http://www.ntp.org/ntpfaq/NTP-s-algo.htm>. (Accessed: 5 September 2016).
- Science 2.0 (2011) *Quake Catcher Network - Citizen Science Tackles Seismology*. Available at: http://www.science20.com/news_articles/quake_catcher_network_citizen_science_tackles_seismology-80887. (Accessed: 29 January 2016).



High-density seismic network for monitoring Alentejo region (Portugal) and Mitidja basin region (Algeria)

Marco Manso¹ · Mourad Bezzeghoud² · José Borges² · Bento Caldeira² · Abdelhakim Ayadi³

Received: 17 May 2020 / Accepted: 2 September 2020
© Saudi Society for Geosciences 2020

Abstract

The seismic sensor network Alentejo (SSN-Alentejo) brings a new approach in seismological survey based on networked low-cost sensors and acquisition systems. It is developed by the Earth Sciences Institute (*Instituto de Ciências da Terra*, University of Evora) to bring the most dense seismic sensor network ever deployed in Portugal. By combining high-sensitive sensors with low-cost sensors, this novel network aims to improve the characterisation of seismic activity in the region, by augmenting existing sensing and monitoring capabilities, enabling the opportunity to observe, for the first time in Portuguese territory, real-time monitoring of the seismic activity in high resolution. In this study, we start by describing the seismicity along the occidental border between the Eurasian-Nubian plates, including the two regions of our interest: the Arraiolos region, in Portugal, and the Mitidja basin, in Algeria. We then present our work in designing and implementing a high-density sensor network, including low-cost sensor systems and server platforms. The conducted tests have proven the feasibility of the overall platform, including its detectability capability. Future work includes the deployment of the sensor network in the Alentejo region. Since seismogenic zones such as the Mitidja or Chelif basins in Algeria will also benefit from having a high-density network, we will also seek collaboration with Algerian institutions.

Keywords High-density seismic network · Seismic sensors · MEMS · Accelerometers · Seismology

Introduction

Seismic events can be extreme and severe threats to humanity, causing a heavy death toll, serious destruction and damage. Being no exception, the Iberian Peninsula and the North of Africa—part of the Ibero-Maghrebian region between the Gulf of Cadiz and Algeria—share the Eurasian-Nubian plate boundary that corresponds to a well-defined narrow band of

seismicity, where large earthquakes occur (Ousadou and Bezzeghoud 2019).

Helping to understand these phenomena, seismic networks have been deployed in increasing number, filling in the gaps in the global coverage and improving our understanding of the physical processes that cause earthquakes. Portugal, in particular, has made a significant effort to develop the Broadband Portuguese seismic network integrating seismological stations from various institutions supporting real-time monitoring of the earthquake activity (Caldeira et al. 2007). Between 2010 and 2012, the WILAS (West Iberia Lithosphere and Asthenosphere Structure) project integrated a temporary network of 20 sensors in the Portuguese national network resulting in a total of 55 stations spaced on average by 50 km (Veludo et al. 2017; Custódio et al. 2014). These stations continuously recorded measurements at frequencies up to 100 Hz, thus collecting a large volume of high-quality data of densely distributed broadband stations that can be used to image the Earth's inner structure with unprecedented resolution (Palomeras et al. 2014). More recently, the Arraiolos seismic network (in Alentejo) was deployed comprising 14 broadband stations (CMG 6TD, 30s) of the Institute of Earth

This paper was selected from the 2nd Conference of the Arabian Journal of Geosciences (CAJG), Tunisia 2019

Responsible Editor: Abd El-aziz Khairy Abd El-aal

✉ Marco Manso
marco@marcomanso.com

¹ Instituto de Ciências da Terra, Universidade de Évora, Evora, Portugal

² Departamento de Física (ECT), Instituto de Ciências da Terra (IIFA), Universidade de Évora, Evora, Portugal

³ Centre de Recherche en Astronomie Astrophysique et Géophysique, Algiers, Algeria

Sciences of Evora, Portugal (Instituto de Ciências da Terra or ICT), and temporarily extended with 21 short-period stations (CDJ, 2.0 Hz) of the Dom Luiz Institute of Lisbon, Portugal (Instituto Dom Luiz or IDL) within a 20-km radius (Wachilala et al. 2019).

Continuing the trend to increase seismic monitoring resolution by deploying more seismic stations, the United States deployed several very-high-density seismic networks with the capability of recording the propagation of seismic activity in high resolution. This methodology allowed displaying seismic wave propagations in space and time (i.e., evolutive *Shakemaps*): in 2001 and 2002, the California Institute of Technology (CalTech) deployed more than 5200 stations spaced by 100 m with the main purpose of conducting seismic survey to better define the Long Beach Oil Field (Inbal, Clayton and Ampuero 2015). In addition, the CalTech established the Community Seismic Network (CSN), an earthquake monitoring system based on a dense array of low-cost acceleration sensors (more than 1000) aiming to produce block-by-block strong shaking measurements during an earthquake (see <http://csn.caltech.edu/>, last accessed 2020/08/14). The University of Southern California's (USC) Quake-Catcher Network (QCN) began rolling out 6000 tiny sensors in the San Francisco Bay Area, being part of the densest networks of seismic sensors ever devoted to study earthquakes in real time (see <https://quakecatcher.net/>, last accessed 2020/08/14).

High-density networks also present several challenges for the state of the practice in seismology. According to Addair et al. (2014), the traditional techniques used in seismology use a processing paradigm that was developed in the 1980s when average computer processing power was a tiny fraction of what is commonly available now. The huge data volume generated by high-density networks demands for research on the application of data-intensive processing techniques like big data and artificial intelligence (e.g., clustering, pattern matching and correlation) in seismology. We expect that a high-dense network-enabled seismic network operating in the principle of “live” data brings the opportunity to explore new applications in seismology, including real-time earthquake detection, more accurate characterisation (high resolution) of strong earthquake motion and the generation of *Shakemaps* in near real time.

This chapter addresses the seismotectonic context of the regions of interest, namely, the region of Arraiolos, which is located in the north of Evora (Portugal) and the Ibero-Maghreb region, specifically the zones of the Mitidja basin, in Algeria, and the development of a high-dense seismic sensor and, in particular, SSN-Alentejo. It presents the design of the seismic network system, including the sensor platform component and the implementation of the server platform, followed with an analysis of the seismic activity detectability of the sensor platform. The chapter finalises by presenting the

planned deployment of the large-density network in Portuguese territory and the rationale for its deployment in the Mitidja basin (Algeria), involving a collaboration with Algerian institutions.

Seismotectonic context

Along the border between the Eurasian-Nubian plates, in the section that extends from the islands of the Azores to the Strait of Gibraltar and the Ibero-Maghreb region, different tectonic contexts are distinguished. The interaction between Iberia and Africa results in a complex region located in the western part of the boundary between the Eurasian and Nubia plates. The seismic activity within the region thus results from the transition from an oceanic border (from the Azores to the Goringe Bank (NE Atlantic), to a continental limit where Iberia and Nubia collide (see Fig. 1).

The plate boundary is very well defined in the oceanic part, from the Azores islands along the Azores-Gibraltar fault to west of the Strait of Gibraltar (approximately 12° W). From 12° W to 3.5° E, including the Ibero-Maghreb region and extending to the western part of Algeria, the border is more diffuse and forms a wide area of deformation (e.g. Bezzeghoud and Buforn 1999; Borges et al. 2001; Buforn et al. 2004; Borges et al. 2007).

The characteristics of the seismicity recorded in the region suggests the division of the western part of the Eurasia-Nubia limit, from the Middle Atlantic crest in the west, to Algiers in the east, in six zones (see Buforn et al. 2004; Bezzeghoud et al. 2014): these zones are characterised by a faulting mechanism variability based on seismicity and focal mechanisms (Bezzeghoud et al. 2014).

Specifically for this study, aiming towards a more detailed characterisation of the seismic activity in the area, we focus our analysis on two specific regions: the region of Arraiolos, which is located in the north of Evora (Portugal) (see Fig. 1, area A), and the Ibero-Maghreb region, specifically the Mitidja basin region, in Algeria (see Fig. 1, area B).

Arraiolos Region, Portugal In the Arraiolos region, located north of Evora in Portugal, an earthquake occurred on the 15th of January 2018 with a $ML = 4.9$ located at a depth of 11 km. This was the biggest recorded earthquake in the area. A mapping of the seismic activity registered in the area between 1961 and 2018 is illustrated in Fig. 2.

This seismic event has raised a number of interesting questions about the tectonic characterisation of this region.

The seismic activity in the Arraiolos region has been historically moderate, being assumed to be generated by the slow plate movement of Iberia. Geological and seismological studies have been conducted in the region (Wachilala et al. (2019), Araújo et al. (2018); Matias et al. (2019); however, the

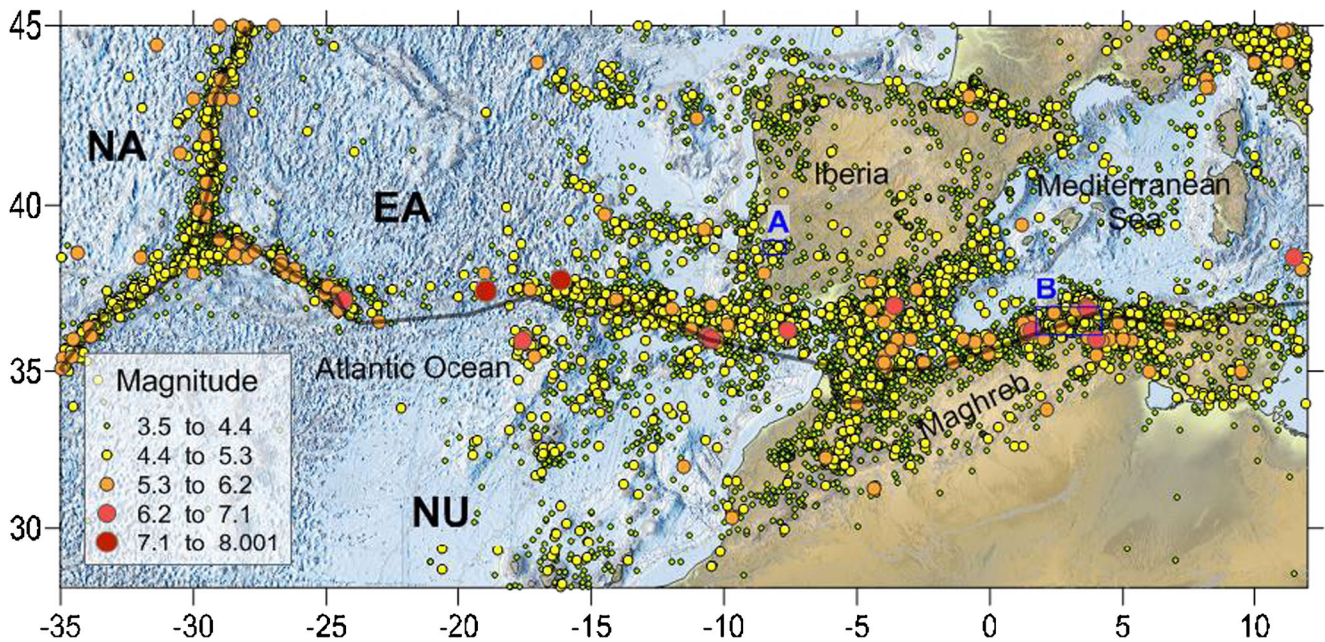


Fig. 1 Map of the seismic activity along the western border of the Eurasian (EU) and Nubian (NU) plates, between 1926 and 2020. NA = North American plate. The two regions of interest are shown with two letters: A (Arraiolos) and B (Mitidja basin). Seismicity data is from the

International Seismological Centre (2020). Bathymetry and topography data are from the GEBCO Grid (2020) The limit between the Eu and Nu plates is provided by Bird (2003)

seismotectonic interpretations have been difficult to derive from the existing tectonic knowledge and seismic data. The known mapped faults in the region do not seem to be linked to the recently observed seismic activity, and thus the identification of its probable associated faults is yet to be resolved. Given the increased—previously unknown—degree of seismotectonic complexity of the region, it becomes necessary to improve the seismic and tectonic knowledge of this region by, as envisaged by SSN-Alentejo, deploying additional seismic sensors, increasing the resolution of the recorded seismic

activity and, consequently, producing a more detailed seismic characterisation of the region.

Mitidja Basin Region, Algeria In the Ibero-Maghreb region, the Tell Atlas of Algeria is known to be formed by a complex system of faults. The Mitidja basin experienced several disastrous earthquakes such those of Algiers 1365 and 1716, Blida 1825, Mouzaia 1867 and more recently Tipasa-Chenoua 1989 and Zemmouri 2003. According to several studies (Buforn et al. 2004; Ousadou and Bezzeghoud 2018), the Tell Atlas,

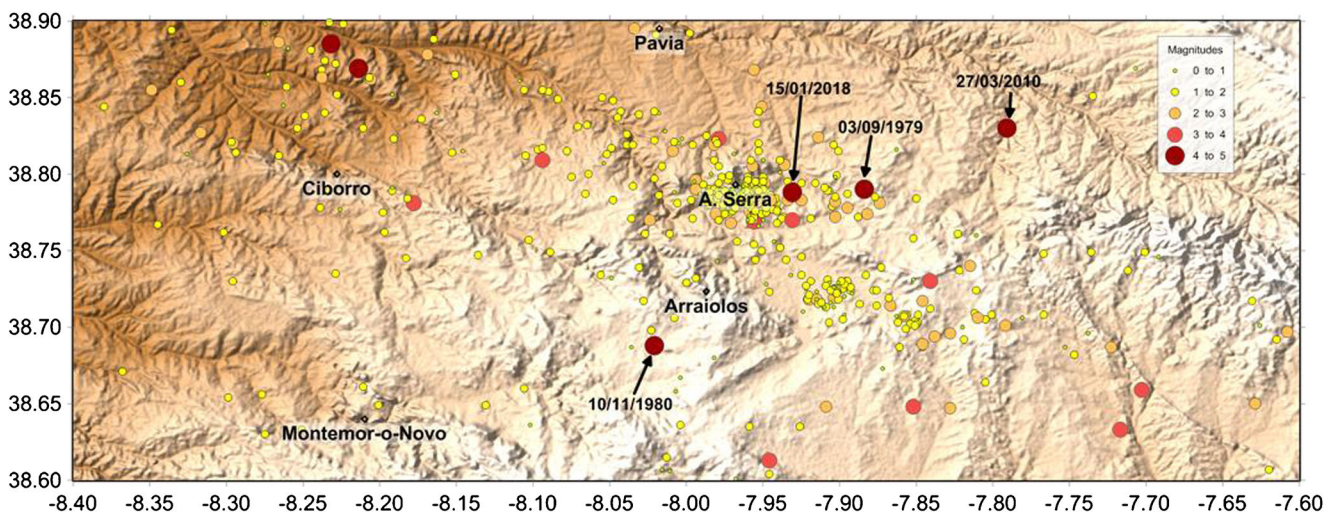


Fig. 2 Map of the recorded seismic activity in the Arraiolos Region, Portugal, between 1961 and March 2018, which marked some of the main shocks in the region, including the recent seismic sequence associated with the 15 January 2018 shock ($M = 4.9$). Seismicity source: IPMA (Portugal) catalogue

along the thrust system accommodates 2–3 mm/year shortening of the 5–6 mm/year obtained for the global plate movement. The Mitidja basin region yields a very active seismic activity, as depicted in Fig. 3 (bottom) for the period 1910–2020. Therefore, having the capability to provide a better characterisation of seismic activity through high-resolution mapping from a high-density network, as in SSN-Alentejo, will improve the seismic and tectonic knowledge of this

region. This basin is bounded by two important fault systems: the south Mitidja basin and the Sahel fault in the north. In this seismotectonic framework (Fig. 3), both western and eastern edges of the Mitidja basin experienced destructive earthquakes (e.g. Ayadi and Bezzeghoud 2015; Maouche et al. 2011; Benfedda et al. 2017), with the 1989 Tipasa earthquake (Mw 6.0) (Bounif et al. 2003) and the 2003 Zemmouri earthquake, respectively (Santos et al. 2015; Ayadi et al. 2003).

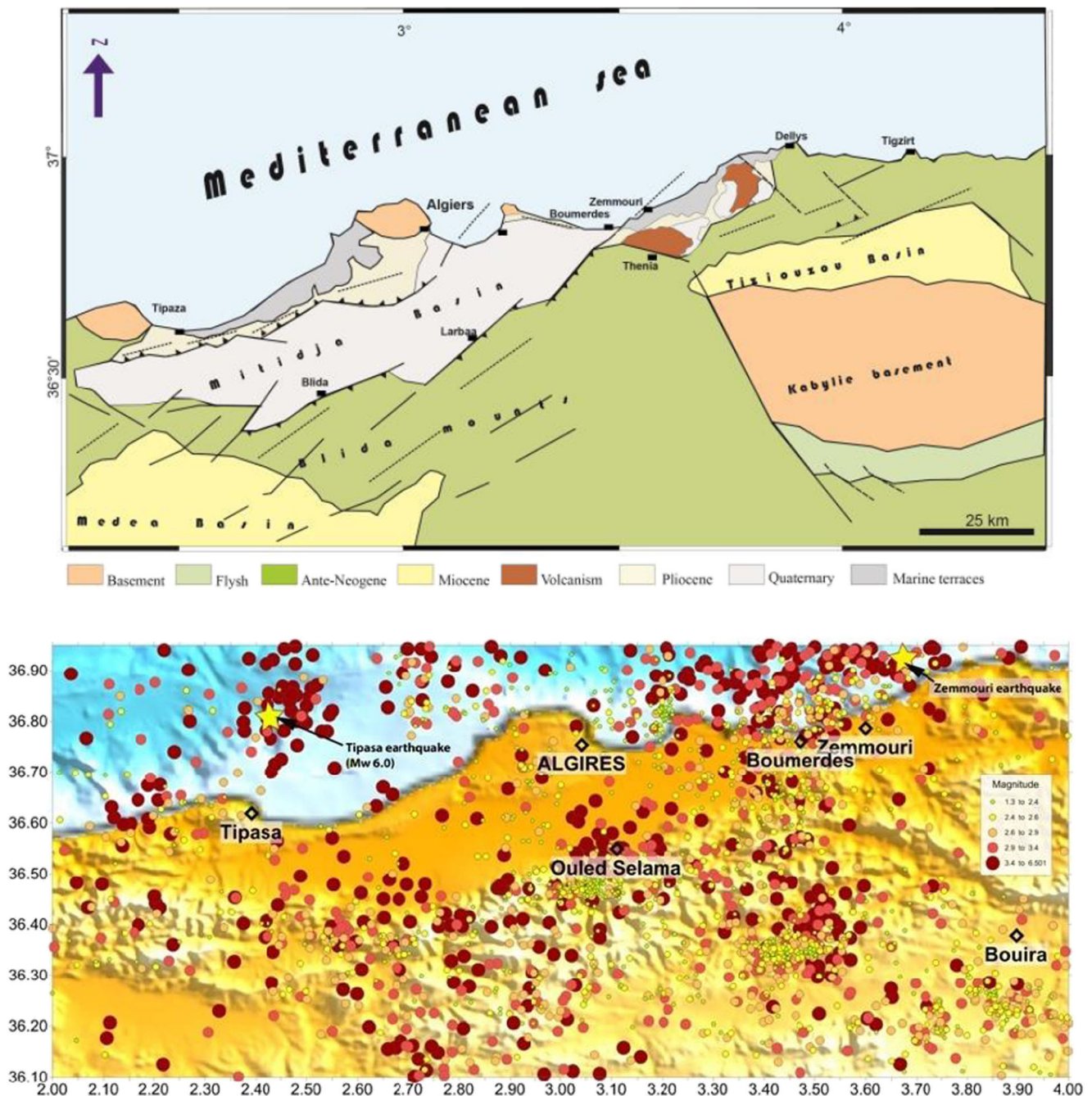


Fig. 3 Top: geological and tectonic background of the Mitidja basin bounded by thrust fault systems (adapted from Ayadi et al. 2003); bottom: seismicity map of Mitidja basin region, Algeria, between 1910 and June 2020. The figure shows a high number of moderate to strong

earthquakes distributed over a densely populated region such as Algiers. The 1989 Tipasa (Mw 6.0) and the 2003 Zemmouri earthquakes are highlighted by yellow stars. Seismicity source: International Seismological Centre (2020), online Bulletin

SSN-Alentejo: high-density seismic networks

In the last years, sensors and sensing network technology evolved at a fast pace, resulting in improved performance (resolution, sensibility and processing capacity), operation (energy efficiency, operation time) and connectivity (broadband communications), at significant cost reduction. Low-cost microelectromechanical (MEM) accelerometers, in particular, demonstrated the capability of generating relevant data for seismic analysis in dense deployment contexts (Lainé and Mougénot 2014).

The seismic sensor network Alentejo (SSN-Alentejo) developed by ICT brings the most dense seismic sensor network ever deployed in Portugal. This novel network aims to improve the characterisation of seismic activity in the region and to improve earthquakes' assessment.

Between 2020 and 2021, the SSN-Alentejo will deploy a monitoring network of 60 sensors to generate significant volumes of live data and advance seismology knowledge. The sensors will be distributed in a mesh configuration spaced on average 10 km and covering an area of about 5000 km². The density proposed for the network abides to the findings of Clayton et al. (2011). Furthermore, as recommended by Evans et al. (2003), the project opts for a cost-effective network configuration, combining high-performing broadband stations and low-cost sensors.

The seismic network design

The seismic network system for SSN-Alentejo was built by a team of researchers of the ICT. It was designed to operate with *live* data (generated by seismic sensors) and be highly scalable (support a high number of sensors). The design identifies three main functional elements: *producers* of seismic data (i.e. *sensors*), *servers* that collect and store seismic data and *consumers* of seismic data (i.e. users or *clients*). The network is an underlying element that provides connectivity between elements. The system is assumed to be always connected and available.

A general view of the seismic network is shown in Fig. 4, illustrating several connected sensors, clients and servers.

A goal of the seismic network is to provide global access to its resources (i.e. sensors and servers) via the *Internet*. It therefore will rely on many of the latter's components (e.g. routers and gateways).

The sensor and server components are described next.

Sensor platform component

Recent developments in microelectromechanical systems (MEMS) have enabled the mass production of small-size accelerometers with potential applications in numerous areas, including seismology. Capacitive accelerometers, in

particular, are highly popular due to reduced cost, their simple structure and the ability to integrate the sensor close to the readout electronics. When subjected to an acceleration, the inertial mass shifts cause a proportional change in capacitance. By measuring the capacitance change, the acceleration can be calculated.

The application of MEMS accelerometers to seismology has met a number of applications (Scudero et al. 2018):

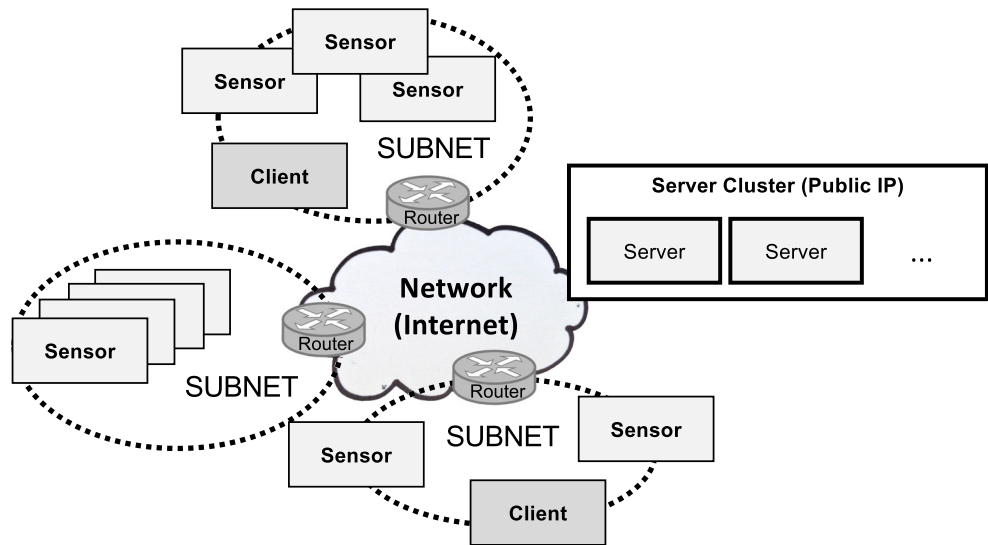
- i MEMSs for seismological study and earthquake observation
- j MEMS-based seismic monitoring networks
- k MEMSs for seismic surveys

Early applications explored the presence of MEMS accelerometers in computers (specifically in hard disc drives) that, connected to a distributed computing network, could be used to build a network of sensors to detect and monitor earthquakes, like the QCN (Cochran et al. 2009). As the underlying technologies to build connected MEMS systems become more accessible and affordable, dense seismic networks using dedicated MEMS sensors are being deployed, as the case of CSN and the urban MEMS seismic network in the Acireale Municipality (Sicily, Italy) (D'Alessandro et al. 2014).

In order to properly exploit its data, it is important to take into account MEMS benefits and limitations, as summarised next (Farine et al. 2003; Evans et al. 2014; Manso et al. 2017). MEMS accelerometers:

- Provide adequate sensitivity, noise level, and range (measured in g) to be applicable to earthquake strong-motion acquisition ($M > 3$), thus also limiting the "resolution" capability. However, the high level of instrumental self-noise that increases as frequency decreases limits their application in the study of low-frequency weak-motion forces
- Are well fit to measure high-frequency (> 40 Hz) ground motion since their resonant frequency (typically above 1 kHz) is far above the seismic band pass
- Measure the gravity acceleration component, thus providing a useful reference for sensitivity calibration and tilt measurement
- Have high acceleration ranges (several g) and are capable to sustain high acceleration (several hundred g) without being damaged
- When compared with broadband seismometers, MEMS may have an advantage in detecting weak high-frequency signals, while the broadband seismometers have the advantage in detecting weak signals at low frequencies
- Can have useful applications such as earthquake early warning, seismic hazard assessment map and security applications.

Fig. 4 General view of the seismic network



Analysis of MEMS accelerometers Seismology is most interested in measuring weak ground motion at low frequencies (e.g. distance teleseismic events), while sometimes dealing with moderate to large local events that exhibit medium and strong ground motion at high frequencies. The type of instruments used in seismology, their main purpose and scope is presented in Table 1.

It is quite challenging for a single seismometer to cope with a wide range of signals, inevitably having to set compromises between sensitivity and range: even broadband seismic sensors with a 160-dB dynamic range will clip in the presence of a magnitude 9 earthquake whose maximum dynamic range is around 220 dB (Tunc et al. 2012). Installing strong-motion accelerometers helps overcoming this limitation and thus provides valuable measurement data for seismologists.

Based on Havskov and Ottemoller (2010)

In this regard, when selecting MEMS accelerometers for seismological purposes, the following parameters should be taken into account:

- **Range:** Specifies the minimum and maximum acceleration values it can measure. It is often represented relative to g (e.g. ± 2 g).

- **Resolution:** Specifies both (i) the degree to which a change can be detected and (ii) the maximum possible value that can be measured. In the case of a digital sensor, it is expressed in bits. For example, a sensor with 16 bits resolution is able to quantify 65,536 possible values. If the scale is set to ± 2 g (hence, a 4 g range), the minimum possible change that can be detected is about 61 μ g.
- **Sensitivity:** Specifies the ratio of the sensor's electrical output to mechanical input, thus representing the smallest absolute amount of change that can be detected by a measurement. It is typically used in analogue sensors. It can be measured in V/g or in counts/g.
- **Noise density:** Accelerometers are subject to noise produced by electronic and mechanical sources. Since they have a small inertial mass, noise increases at low frequencies. The noise density is often represented in terms of power spectral density (PSD) and is expressed as $g/\sqrt{\text{Hz}}$. It varies with the measurement bandwidth: when multiplied by it, the resulting value represents the minimum acceleration values that can be resolved.
- **Bandwidth:** Specifies the frequency range that the sensor operates in. It is limited to the natural resonance frequency

Table 1 Seismology instruments: purpose and characteristics

Seismology instrumentation	Passive short-period (SP) sensors	Active BB sensors	MEMS accelerometers
Main purpose	Local earthquakes. Global observations of P waves	Suited for all seismological observations. Global observations	Retrieve unclipped observations near the earthquake (suitable for strong motion) Can replace SP sensors for local earthquakes Supports very high frequencies Not suited for low frequencies (< 1 Hz) and weak motion ($M < 2$).
Frequency Spectrum	Linear for velocity between 1.0 and 100 Hz	Linear for velocity between 0.01 and 50 Hz	Linear for acceleration in frequency band (e.g. 0–1000 Hz) however is limited at low frequencies due to the presence of sensor noise

of the mechanical structure of the accelerometer itself, which is typically very high (> kHz).

- *Sample rate*: Specifies the number of measurements (samples) per second.

Moreover, for purposes of high-dense deployments, other factors are also relevant:

- *Size*: Specifies the physical dimensions of the sensor. MEMS accelerometers are supplied embedded in small chips (order of mm).
- *Power consumption*: Specifies the required power to operate. Usually is very low (order of μA).
- *Cost*: Refers to the cost to purchase a MEMS accelerometer. Prices vary according to the sensor performance. Cost tends to decrease as new (improved) models are launched over time.

For the selection of MEMS accelerometers for SSN-Alentejo, target values were defined as presented in Table 2.

Moreover, in the context of high-dense networks, it is important to consider factors that impact the overall cost, including manufacturing and assembling aspects. As such, the assessment considers the following requirements:

- *Digital sensor*, facilitating direct data read (i.e. no need for an analogue-to-digital converter, no need for any signal pre-conditioning or pre-processing, signal is less exposed to external noise)
- *Cost* (for 3-axis measurements). Two other important parameters are intrinsic in most MEMS:
- *Size* (MEMS accelerometers are embedded in very small chips (in the order of mms))
- *Power* (MEMS accelerometers operate using small currents (in the order of mA or less))

Resorting to online resources and marketplaces, several MEMS accelerometers were analysed based on openly available information, such as product datasheets. The sensors

selected for prototyping and evaluation purposes are the following:

- Analogue ADXL355, a 3-axis digital sensor with 20-bit resolution, noise density (PSD) of $25 \mu\text{g}/\sqrt{\text{Hz}}$ and moderate cost (~ 35€). (source: <https://analog.com>)
- Freescale MMA8451Q with 14-bit resolution, noise density (PSD) of $99 \mu\text{g}/\sqrt{\text{Hz}}$ and low cost (~ 2€). (source: <https://www.nxp.com>)
- Invensense MPU-6050 with 16-bit resolution, noise density (PSD) of $400 \mu\text{g}/\sqrt{\text{Hz}}$ and low cost (~ 2€). (source: <https://www.invensense.com>)
- ST Electronics LIS3DHH with 16-bit resolution, noise density (PSD) of $45 \mu\text{g}/\sqrt{\text{Hz}}$ and low cost (~ 7€). (source: <https://www.st.com>)

Sensor platform implementation The sensor platform contains the sensor component as well as additional other components in order to achieve the functionalities required to operate in a network-enabled environment. The platform should incorporate microcontroller and processing capabilities in order to (i) deliver the capability to function autonomously (i.e. no need to connect to external computers to operate), (ii) connect to an IP-based network and be a low-cost platform (Manso et al. 2016).

The microchip ESP8266 (<https://www.espressif.com/en/products/hardware/socs>, last accessed 2020/08/14) is low-cost (each unit is below 5€) and covers several needs: it has a fast and programmable microcontroller (up to 160 MHz) and embedded Wi-Fi capabilities and supports a wide range of programming libraries (see <https://www.arduino.cc/en/reference/libraries>). Moreover, time synchronisation can be achieved by means of the Network Time Protocol (NTP). NTP can keep time accuracy of all machines within the same subnet within 1 ms (NTP 2003). The ESP8266 also contains a limited amount of flash memory (up to 3Mbits) that can be used to store sensor data.

The sensor platform based on ESP8266 has been demonstrated to work with several MEMS accelerometers (coping

Table 2 MEMS accelerometers: parameters and target values

Parameter	Target	Notes
Range	2 to 4 g	Increasing range reduces sensitivity. It is thus advisable to select a small value
Resolution	16-bit or above	-
Noise density	Below $100 \mu\text{g}/\sqrt{\text{Hz}}$ (below $400 \mu\text{g}/\sqrt{\text{Hz}}$ acceptable for prototyping and testing)	This is a critical parameter that is currently the main limiting factor in the application of MEMS in seismology. The target value reflects the current state of the art of the low-cost MEMS market
Bandwidth (and sample rate)	100 Hz or above	Increasing the bandwidth increases the noise density

with up to 200 samples per second), connect to an IP-based network (using the wireless Wi-Fi protocol) and stream data to a server component.

Server component

The server component main functions are to collect and store data received from sensors and to provide access of sensor data to clients (Manso et al. 2017).

Importantly, since a single server supports a limited number of sensors, servers can be deployed in a cluster configuration. In this way, several server instances can be deployed (as required) in order to be able to connect more sensors. Servers propagate information regarding registered sensors among other servers within the cluster as a mechanism to ensure that any server (and any client) can access any sensor.

The server component runs an HTTP server that can be accessed by sensors over a local network or the Internet and used to send measured data. In this regard, the *WebSocket* protocol (Fette and Melnikov 2011) is selected due to its capability to handle high data throughput and its easy integration with Internet-based technologies.

The server component also incorporates a HTTP web server module that allows clients (subscribers) to visualise, retrieve and/or process sensor data. Clients are fully decoupled from the server, can be implemented in different languages and can have different purposes.

The server code is implemented in node.js since it is event-driven and its non-blocking I/O model delivers high performance and scalability. It can also take advantage of multiple CPU cores and parallel processing in handling sensors and clients requests.

Visualisation and event detection tools

The SSN-Alentejo also delivers visualisation and data processing tools exploiting “live” sensor data. Users (*clients*) can use Internet browsers to access the SSN-Alentejo server and visualise the location of sensors, as well as their connection status.

Figure 5 illustrates a simulated scenario of 4 deployed sensors in Evora. Note that sensors are displayed as a circle over a map, thus allowing to visualise their location in space. A colour code is used as follows:

- Green: the sensor is connected and providing data.
- Orange: the sensor has triggered a seismological event.
- Blue: the sensor is registered but is not providing data.

The figure shows two connected sensors (green colour), one registered sensor (blue colour) and one sensor detecting an event (orange colour).

Visual artefacts, such as varying a sensor circle’s radius and/or colour based on MMI or other properties, and the use of spatial heat maps can be explored for improving the interpretation of the high-dense network measurements. Interesting implemented examples of the presentation of seismic-related information from high-dense networks are the following:

- Caltech’s experience with seismic sensor networks and CSN was employed to monitor campus buildings in the Los Angeles region. The system generates a map displaying the recorded peak acceleration in campus buildings in order to assess potential damage and risk of collapse (see: <http://csn.caltech.edu/lausd>).
- The MyShake platform is built on existing smartphone technology to detect earthquakes and issue warnings (Allen et al. 2019). The platform aggregates earthquake activity into clusters that are displayed over a map, allowing to visualise areas with high earthquake activity.

In a scenario of a high-dense network, it will be possible to register a large number of events containing time, location and intensity (MMI) of seismic events (and thus generate *Shakemaps*) as they occur. Referring recent research concerning the 4.9 ML seismic event in Arraiolos, Portugal (Marreiros et al. 2019), the generation of the associated *Shakemap* was delayed due to (1) the lack of availability of seismic data in real time and (2) the need to increase the observation points in space, by collecting feedback from human observers (thus, highly subjective). The SSN-Alentejo will fill the above gap by providing with high amounts of sensor data in quantified form.

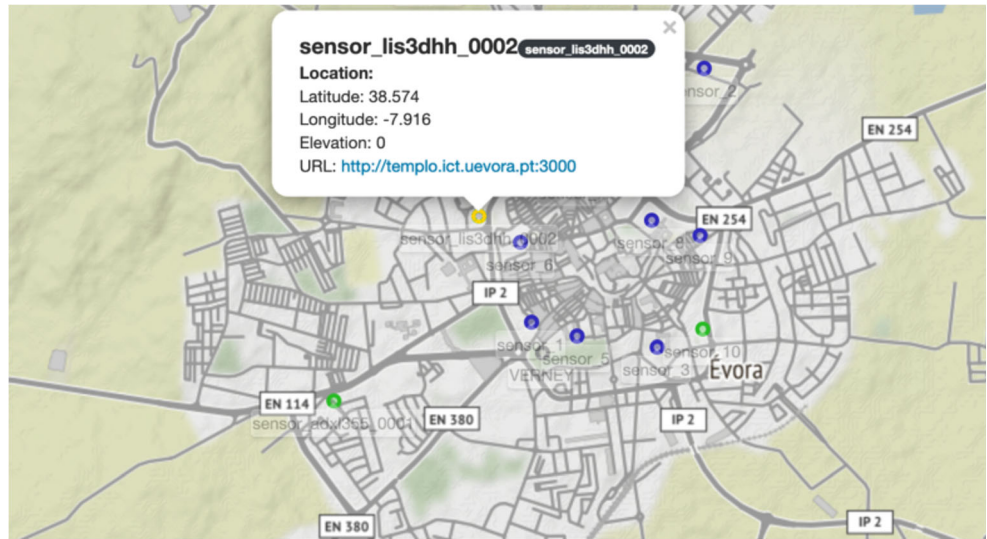
Detectability

In this subsection, we present an estimate of the detectability threshold of a seismic sensor prototype platform developed for the SSN-Alentejo, evidencing its relevant and applicability in the field.

The seismic sensor prototype platform, herein named SN.LIS3, used the LIS 3DHH accelerometer operating with a 100-Hz sampling frequency. The platform was deployed and connected to the SSN-Alentejo for several days. The sensor platform was at rest.

In order to estimate the detectability of SN.LIS3, a record of about 1 h and 30 min length was extracted from the SSN-Alentejo database. Date and time were chosen so that no significant seismic activity occurred and cultural noise was as small as possible (i.e. night). We applied a Butterworth low-pass filter with corner frequency in order to eliminate the high frequencies less present in the earthquake records. The result is illustrated in Fig. 6.

Fig. 5 Visualisation of a small sensor network deployment. The figure shows the sensors' location and connection status (green, connected; blue, registered; orange, activity detected). A sensor was coloured in orange because an event was being detected and recorded



Considering the average noise of the records and defining a criterion for detection signal/noise equal to 5, we estimate a detectability peak ground acceleration (PGA) threshold for SN.LIS3 of $4 \times 10^{-4} \text{ m/s}^2$.

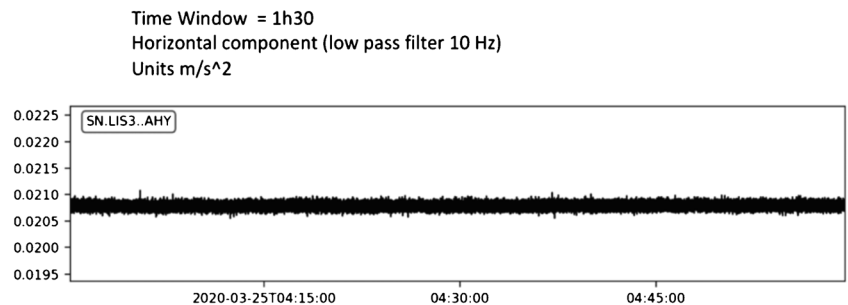
Considering a typical ground motion prediction equation (GMPE) proposed by Atkinson and Boore (2006), the SN.LIS3 detectability threshold, depending on the earthquake magnitude and epicentral distance, is depicted in Fig. 7.

Based on the calculated PGA threshold, we can conclude that:

- SN.LIS3 can detect a magnitude 3 earthquake having an epicentral distance less than 100 km.
- SN.LIS3 can detect a magnitude 4 earthquake having an epicentral distance less than 500 km.
- SN.LIS3 can detect a magnitude 5 earthquake having an epicentral distance less than 1000 km.

The detection capability is quite promising considering the seismic activity in the regions of interest (see Figs. 1, 2 and 3). Our future work will continue the performance analysis of the sensor prototypes using other accelerometers, such as the ADXL355 that is known to have a better signal-to-noise ratio.

Fig. 6 Time record of the horizontal component recorded by the seismic sensor platform prototype using LIS 3DHH

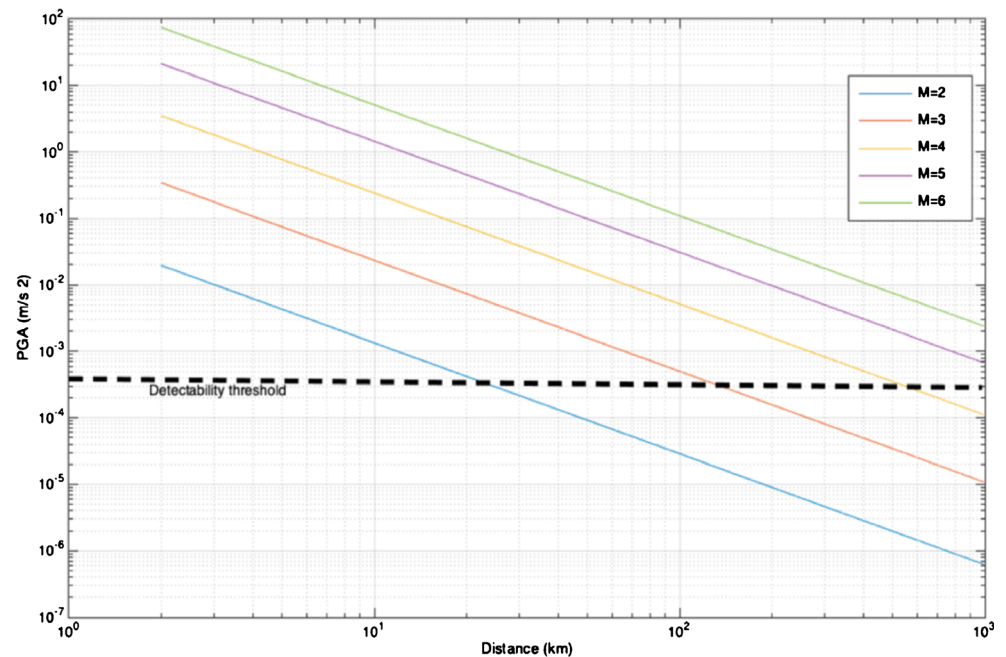


Applications

The SSN-Alentejo is composed by accelerometer sensors capable of recording ground motions depending on the event's magnitude and distance (see previous section "Detectability"). Moreover, saturation is unlikely to occur in these instruments because the limit of saturation is of the order of 1 g (9.8 m/s^2), unlike traditional seismometers that are designed to measure weak motions over narrow ranges. The network-enabled high-density seismic network generates data in real time and explores the accelerometers' good sensitivity, high resolution and generous bandwidth, enabling the following applications:

- a) Seismic detection (strong motion) for near and "far" earthquakes (far being in the order of hundreds of km), being less likely to saturate compared with traditional equipment. The network allows to study the seismic processes (earthquakes localizations and seismic source study, including the study of focal mechanisms) related to the occurrence of seismic events belonging to sedimentary basin structure.
- b) Study local events and characterise the structure of the seismogenic zone by performing waveform analysis of nearby small events (weak motions) and ambient noise. The network will enable us to characterise sedimentary basin structures,

Fig. 7 Detectability threshold for the SN.LIS3. PGA for magnitudes from $M = 2$ to $M = 6$ and epicentral distances to 1000 km, GMPE proposed by Atkinson and Boore (2006)



locate near earthquakes and get seismic source by inverting the waveforms, calculating focal mechanisms, performing local seismic tomography and studying the attenuation of seismic waves using ambient noise or seismic waveforms.

c) Analyse the impact produced by human activity and cultural noise on buildings and monuments: *Urban seismic noise* is usually dominated by *traffic* and industrial activity with peak frequencies below 25 Hz. A continuous exposure to urban tremors can cause a cumulative and progressive degradation on fragile buildings and monuments, which could cause irreparable damage in human heritage. If installed in buildings and monuments, the SSN-Alentejo produces information allowing to determine structural integrity risks.

d) *Shakemap* generation in near real-time. *Shakemaps* provide an estimate of *ground motion* amplitudes (maximum displacement, velocity or acceleration) caused by earthquakes. These maps can be used by civil protection authorities, decision-makers and local organisations (public or private) for post-earthquake response, including assessing structural integrity risks in buildings and slopes. To be effective, these maps need to be *immediately* generated, thus requiring peak ground motion data in near real time, as generated by the SSN-Alentejo.

e) Provide to the scientific community with new open-access high-resolution seismic data for studying seismic-related phenomena and for developing methodologies useful to discriminate between natural and induced events (Stabile et al. 2020; Serlenga and Stabile 2019; Havskov et al. 2012).

f) Facilitate access to education in seismology, resulting from open-access to low-cost technology that can be installed in high schools and integrated in projects and activities.

Conclusion

The SSN-Alentejo represents a reinforcement of sensing and monitoring capabilities, enabling the opportunity to explore for the first time in Portuguese territory the high-resolution observation of seismic activity. In particular for the identified two regions of interest, namely, Arraiolos (Portugal) and Mitidja basin (Algeria), we argued that there is a need to overcome the existing limitations in monitoring seismic activity by deploying additional seismic sensors, increasing the resolution of the recorded seismic activity and, consequently, producing a more detailed seismic characterisation of the region. This is a necessary step to improve the seismic and tectonic knowledge in the regions.

After the occurrence of the recent magnitude 4.9 earthquake in Arraiolos, a temporary network of about 40 stations was deployed for a few weeks (Fig. 8a) that has now been reduced to almost 15 permanent stations (Fig. 8b). The SSN-Alentejo will deploy 60 connected sensor platforms, increasing the regional seismic network to about 65 stations, enabling a high-resolution seismic characterisation (Fig. 8c). In addition, the SSN-Alentejo will be used to monitor ground motion activity (might be caused by natural and/or human activity) in high detail of Evora City, considering its high patrimonial value and cultural heritage. As it can be clearly visualised in Fig. 8, the SSN-Alentejo brings a significant increase in the monitoring of seismic activity in the area of interest.

The high-dense network-enabled seismic network operating in the principle of “live” data will bring the opportunity to explore new applications in seismology, including real-time earthquake detection, more accurate characterisation (high

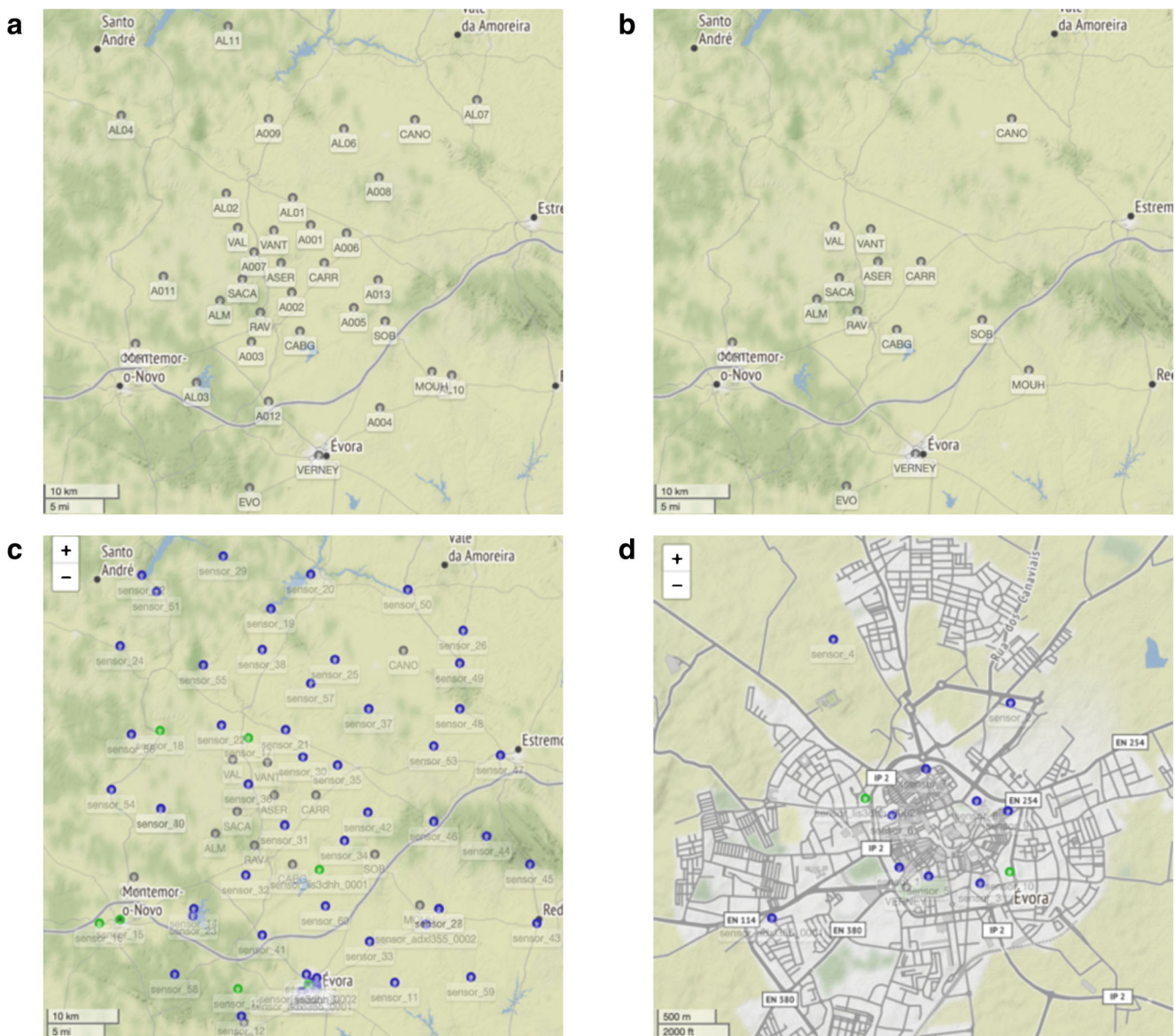


Fig. 8 Different phases of the seismic network in Alentejo (includes the Arraiolos region) and the SSN-Alentejo planned deployment. (a) Temporary seismic network deployed in the Arraiolos region after the earthquake. About 60 connected stations. (b) Current seismic network in the Arraiolos region. Less than 15 connected stations. (c) SSN-Alentejo:

planned deployment of additional 60 sensors, resulting in about 75 stations in total. (d) SSN-Alentejo: planned deployment for the Evora City. Sensor density is increased to monitor ground motion activity that may impact cultural heritage and historical buildings

resolution) of strong earthquake motion and the generation of shakemaps in near real time.

Moreover, based on Addair’s findings (Addair et al. 2014), novel and redesigned algorithms exploiting parallel computational-intensive techniques will allow applying machine learning techniques and pattern matching-based processing that are much more sensitive than the power detectors used in current seismic systems, making them especially relevant in the presence of noise and weak signals such as those present in slowly deforming regions, namely, Alentejo (Fig. 8).

Importantly, these high-density networks bring, in general, enormous potential to better understand seismogenic zones such as the Mitidja or Chelif basins in Algeria. It is our aim to explore a deployment resorting to our close relationship with several Algerian institutions such as the Algiers and Oran universities as well as the Centre National de Recherche Appliquée en Génie Parasismique (CGS) and the Centre de Recherche en Astronomie Astrophysique et Géophysique (CRAAG).

Acknowledgements We would like to thank the editor and the anonymous reviewer for their thoughtful and constructive comments which helped to improve the manuscript.

Funding The SSN-Alentejo project is funded by the Science Foundation of Portugal (FCT) under grant number ALT20-03-0145- FEDER-031260.

References

- Addair T, Dodge D, Walter W, Ruppert S (2014) Large-scale seismic signal analysis with Hadoop. *Comput Geosci* 66:145–154
- Araújo A, Caldeira B, Martins A, Borges J, Araújo J, Moreira N, Maia M, Vicente S, Afonso P, Espanhol D, Bezzeghoud M (2018) Macrossismicidade associada ao sismo de Arraiolos do dia 15 de janeiro de 2018 com $M = 4.9$ e eventuais implicações na geometria da ruptura. *Vulcânica – Revista Portuguesa de Vulcanologia*. Vol. II – 2018. ISSN 1646–3269
- Atkinson G, Boore D (2006) Earthquake ground-motion prediction equations for eastern North America. *Bull Seismol Soc Am* 96:2181–2205
- Ayadi A, Bezzeghoud M (2015) Seismicity of Algeria from 1365 to 2013: maximum observed intensity map (MOI2014). *Seismol Res Lett* 86(1):237–244. <https://doi.org/10.1785/0220140075>
- Ayadi A, Maouche S, Harbi A, Meghraoui M, Beldjoudi H, Oussadou F et al (2003) Strong Algerian earthquake strikes near capital city. *EOS Trans Am Geophys Union* 84(50):561–568
- Allen R, Kong Q, Martin-Short R (2019) The MyShake platform: a global vision for earthquake early warning. *Pure Appl Geophys*. <https://doi.org/10.1007/s00024-019-02337-7>
- Benfedda A, Abbes K, Bouziane D, Bouhadad Y, Slimani A, Larbes S, Haddouche D, Bezzeghoud M (2017) The August 1st, 2014 (Mw 5.3) Moderate earthquake: evidence for an active thrust fault in the Bay of Algiers (Algeria). *Pure Appl Geophys* 174(3):1503–1511. <https://doi.org/10.1007/s00024-017-1481-6>
- Bezzeghoud M, Adam C, Buforn E, Borges JF, Caldeira B (2014) Seismicity along the Azores–Gibraltar region and global plate kinematics. *J Seismol* 18:205–220. <https://doi.org/10.1007/s10950-013-9416-x>
- Bird P (2003) An updated digital model of plate boundaries. *Geochem Geophys Geosyst* 4(3). <https://doi.org/10.1029/2001GC000252>
- Buforn E, Bezzeghoud M, Udias A, Pro C (2004) Seismic source in the Iberian–African plate boundary. *Pure and Applied Geoph* 161(3): 623–646. <https://doi.org/10.1007/s00024-003-2466-1>
- Bezzeghoud M. and E. Buforn (1999). Source parameters of 1992 Melilla (Spain, Mw = 4.8), 1994 Al Hoceima (Morocco, Mw = 5.8) and 1994 Mascara (Algeria, Mw = 5.7) earthquakes and seismotectonic implications. *Bul. Seis. Soc. Am.*, 89, 2, 359–372. <https://pubs.geoscienceworld.org/ssa/bssa/article-abstract/89/2/359/120378/Source-parameters-of-the-1992-Melilla-Spain-MW-4-8?redirectedFrom=fulltext>
- Bounif A, Bezzeghoud M, Dorbath L, Legrand D, Deschamps A, Rivera L, Benhallou H (2003) Seismic source study of the 1989, October 29, Chenoua (Algeria) earthquake from aftershocks, broad-band and strong ground motion records. *Ann Geophys* 46(4):625–646. <https://doi.org/10.4401/ag-4370>
- Borges JF, Fitas AJS, Bezzeghoud M, Teves-Costa P (2001) Seismotectonics of Portugal and its adjacent Atlantic area. *Tectonophysics* 337:373–387. [https://doi.org/10.1016/S0040-1951\(00\)00291-2](https://doi.org/10.1016/S0040-1951(00)00291-2)
- Borges JF, Bezzeghoud M, Buforn E, Pro C, Fitas A (2007) The 1980, 1997 and 1998 Azores earthquakes and its seismotectonic implications. *Tectonophysics* 435:37–54. <https://doi.org/10.1016/j.tecto.2007.01.008>
- Caldeira B, Carrilho F, Miranda M, Bezzeghoud M, Alves P, Silveira G, Villalonga F, Pena J, Matias L, Borges J, Vales D, Corela C, Madureira G (2007) Recent improvements in the broadband seismic networks in Portugal. *EMSC Newsletters* 22:18–19
- Clayton R, Heaton T, Chandy M, Krause A, Kohler M, Bunn J, Guy R, Olson M, Faulkner M, Cheng M, Strand L, Chandy R, Obenshain D, Liu A, Aivazis M (2011) Community seismic network. *Ann Geophys* 54:6
- Cochran E, Lawrence J, Christensen C, Chung A (2009) A novel strong-motion seismic network for community participation in earthquake monitoring. *IEEE Instru Meas Mag* 12(6):8–15
- Custódio S, Dias N, Caldeira B, Carrilho F, Carvalho S, Corel C, Diaz J, Narciso J, Madureira G, Matias L, Haberland C and WILAS Team (2014) Ambient noise recorded by a dense broadband seismic deployment in Western Iberia. *Bull Seismol Soc Am* 104(6):2985–3007, December 2014. <https://doi.org/10.1785/0120140079>
- D’Alessandro A, Luzio D, D’Anna G (2014) Urban MEMS based seismic network for post-earthquakes rapid disaster assessment. *Adv Geosci* 40:1–9
- Evans J, Hamstr R, Spudich P Jr, Kündig C, Camina P, Rogers J (2003) TREMOR: a wireless, MEMS accelerograph for dense arrays. U.S. Department of the Interior, U.S. Geological Survey. Open-file Report, pp 03–159
- Evans J, Allen R, Chung A, Cochran E, Guy R, Hellweg M, Lawrence J (2014) Performance of several low-cost accelerometers. *Seismol Res Lett* 85(1):147–158
- Farine M, Thorburn N, and Mougnot D (2003) General application of MEMS sensors for land seismic acquisition – is it time? Accessible at: <http://cseg.ca/assets/files/resources/abstracts/2003/218S0130.pdf>
- Fette I, Melnikov A. (2011) RFC 6455 - The WebSocket protocol. Internet Engineering Task Force.
- GEBCO Grid (2020), doi:<https://doi.org/10.5285/a29c5465-b138-234d-e053-6c86abc040b9>
- Havskov J, Ottemöller L (2010) Routine data processing in earthquake seismology. Springer Science+Business Media B.V., Berlin. ISBN 978-90-481-8696-9. <https://doi.org/10.1007/978-90-481-8697-6>
- Havskov J, Ottemöller L, Trnkoczy A, Bormann P (2012) Seismic networks, in: *New Manual of Seismological Observatory Practice (NMSOP-2)*, IASPEI, edited by: Bormann, P. GFZ German Research Centre for Geosciences, chap. 8. https://doi.org/10.2312/GFZ.NMSOP-2_CH865 pp
- Inbal A, Clayton R, Ampuero J (2015) Imaging widespread seismicity at midlower crustal depths beneath Long Beach, CA, with a dense seismic array: evidence for a depth-dependent earthquake size distribution. *Geophys Res Lett* 42(15):6314–6323
- International Seismological Centre (2020), on-line Bulletin, doi:<https://doi.org/10.31905/D808B830>
- Lainé J, Mougnot D (2014) A high-sensitivity MEMS-based accelerometer. In: *The Leading Edge, Special Section: Sensor technology and nanotechnology*. <https://doi.org/10.1190/tle33111234>
- Matias L, Inês I, Wachilala P, Vales D, Borges J, Dias N, Carrilho F, Caldeira B, Custodio S, Fontiela J, Bezzeghoud M, Araujo A, Corela C (2019) The seismic sequence of Arraiolos, Portugal, in January 2018. *Geophysical Research Abstracts*. Vol. 21, EGU2019-9761, 2019. EGU General Assembly 2019
- Manso M, Bezzeghoud M, Caldeira B (2017) Design and evaluation of a high throughput seismic sensor network. Tools for planning, deployment and assessment. 6th International Conference on Sensor Networks SENSORNETS, Porto, Portugal, 19 to 21 February.
- Manso M, Bezzeghoud M, Caldeira B (2016) Design and Implementation of a Network Enabled High-Throughput MEMS-based Seismic Sensor. *Comunicações Geológicas* 103(1):107–111
- Maouche S, Meghraoui M, Morhange C, Belabbes S, Bouhadad Y, Haddoum H (2011) Active coastal thrusting and folding, and uplift

- rate of the Sahel anticline and Zemmouri earthquake area (Tell Atlas, Algeria). *Tectonophysics* 509(2011):69–80. <https://doi.org/10.1016/j.tecto.2011.06.003>
- Marreiros C, Alves P, Caldeira B, Araújo A, Borges A, Bezzeghoud M, Carrilho F (2019) Os shakemaps do sismo de Arraiolos de 15 de janeiro de 2018 (ML 4.9). In: 11^a Congresso Nacional de Sismologia e Engenharia Sísmica (Sísmica 2019). IST, Lisboa, pp 1–12
- NTP (2003) The NTP Public Services Project. Available at: <http://www.ntp.org/ntpfaq/NTP-s-algo.htm>. Accessed 5 September 2016
- Ousadou F, Bezzeghoud M (2018) Seismicity of the Algerian tell atlas and the impacts of major earthquakes. In: Bendaoud A, Hamimi Z, Hamoudi M, Djemai S, Zoheir B (eds) *The geology of the Arab World—An Overview*. Springer Geology. Springer, Cham, pp 401–426
- Ousadou F, Bezzeghoud M (2019) Seismicity of the Algerian Tell Atlas and the impacts of major earthquakes. In: Bendaoud A et al (eds) *The Geology of the Arab World—An Overview*, Springer Geology, pp 401–426
- Palomeras I, Thurner S, Levander A, Liu K, Villasenor A, Carbonell R, Hamafi M (2014) Finite-frequency Rayleigh wave tomography of the western Mediterranean: mapping its lithospheric structure. *Geochem Geophys Geosyst* 15(1):140–160
- Santos R., B. Caldeira, M. Bezzeghoud, J.F. Borges (2015). The rupture process and location of the 2003 Zemmouri-Boumerdes earthquake (Mw 6.8) inferred from seismic and geodetic data, *Pure and Applied Geophysics*, 172, issue 9, 2421–2434, published on line: 23 November 2014, 10.1007/s00024-014-0978-5
- Scudero S, D'Alessandro A, Greco L, Vitale G (2018) MEMS technology in seismology: a short review. Published in: 2018 IEEE International Conference on Environmental Engineering (EE). 12–14 March. Milan, Italy, p 2018. <https://doi.org/10.1109/EE1.2018.8385252>
- Serlenga V, Stabile TA (2019) How do local earthquake tomography and inverted dataset affect earthquake locations? The case study of High Agri Valley (Southern Italy). *Geomat Nat Haz Risk* 10:49–78. <https://doi.org/10.1080/19475705.2018.1504124>
- Stabile TA, Serlenga V, Satriano C, Romanelli M, Gueguen E, Gallipoli MR, Ripepi E, Saurel J-M, Panebianco S, Bellanova J, Priolo E (2020) The INSIEME seismic network: a research infrastructure for studying induced seismicity in the High Agri Valley (southern Italy). *Earth Syst Sci Data* 12:519–538. <https://doi.org/10.5194/essd-12-519-2020>
- Tunc S., Tunc B., Caka D., Ada S., Rademacher H. (2012) Does broadband seismometer clip? American Geophysical Union, Fall Meeting 2012, abstract id. S51C-2446. December 2012
- Veludo I, Dias A, Fonseca P, Matias L, Carrilho F, Haberland C, Villaseñore A (2017) Crustal seismic structure beneath Portugal and southern Galicia (Western Iberia) and the role of Variscan inheritance. *Tectonophysics* 717(16):645–664
- Wachilala P, Borges J, Caldeira B, Matias L, Rio I, Bezzeghoud M (2019) Characterization of the region of Arraiolos, South Portugal – Period of January – May 2018. Ass. IUGG. Montreal, Canada, p 2019

On-site Sensor Noise Evaluation and Detectability in Low Cost Accelerometers

Marco Manso¹^a and Mourad Bezzeghoud²^b

¹*Instituto de Ciências da Terra, Universidade de Évora, Évora, Portugal*

²*Departamento de Física (ECT), Instituto de Ciências da Terra (IIFA), Universidade de Évora, Portugal*

Keywords: Accelerometers, Seismology, Environmental Monitoring, Noise.

Abstract: Seismic networks help understanding the phenomena related with seismic events. These networks are employing low-cost accelerometers in order to achieve high-density deployments enabling accurate characterisation (high resolution) of strong earthquake motion and early warning capabilities. In order to assess the applicability of low-cost accelerometers in seismology, it is essential to evaluate their noise characteristics and identify their detectability thresholds. In this paper, a method is proposed that provides an indication of sensor noise, being demonstrated on different sensors. The method is designed to adapt to a sensor's characteristics while on-site and in-operation, thus removing potentially related logistical and maintenance bottlenecks.

1 INTRODUCTION


Seismic events can be extreme and severe threats to humanity, causing a heavy death toll, serious destruction and damage. Helping to understand these phenomena, seismic networks have been deployed in increasing number, filling in gaps in the global coverage and improving our understanding of the physical processes that cause earthquakes.


For example, Portugal has made a significant effort to develop the Broadband Portuguese seismic network integrating seismological stations supporting real-time monitoring of the earthquake activity (Caldeira *et al.*, 2007). The Portuguese national network (Instituto Português do Mar e da Atmosfera - IPMA) is the seismic monitoring of all the Portuguese territory, from the Azores and Madeira archipelagos to the mainland territory, covering the extensive Azores-Gibraltar plate boundary segment. This national network also contributes to global monitoring efforts.

EMSO-PT (<http://emso-pt.pt/>), the Portuguese counterpart of the European Multidisciplinary Seafloor and water column Observatory (EMSO), is an infrastructure jointly funded by the Portuguese government and the European Commission that aims

to create and develop infrastructures for scientific and technological research within the scope of Marine Sciences. One the goals of EMSO-PT is to improve the national seismic monitoring network, thus allowing for the development of an Earthquake Early Warning System (EEWS), including those generated in the Atlantic region in and adjacent to the Portuguese territory. Considering the seismogenic Eurasia-Nubia plate boundary located south of mainland Portugal, current efforts by the *Instituto de Ciências da Terra* (ICT), University of Évora (UE) and IPMA aim to densify the seismic network in the extreme west of the Algarve.

A paradigm change occurred in the United States by deploying high density seismic networks with the capability to record the propagation of seismic activity in high resolution: The California Institute of Technology (CalTech) that established the Community Seismic Network (CSN), an earthquake monitoring system based on a dense array of low-cost acceleration sensors (more than 1000) aiming to produce block-by-block strong shaking measurements during an earthquake (see <http://csn.caltech.edu/>, last accessed 2020/08/14); The University of Southern California's (USC) Quake-Catcher Network (QCN) began rolling out

^a <https://orcid.org/0000-0003-0953-049X>

^b <https://orcid.org/0000-0002-4908-0422>

6000 tiny sensors in the San Francisco Bay Area, being part of the densest networks of seismic sensors ever devoted to study earthquakes in real time (see <https://quakecatcher.net/>, last accessed 2020/08/14).

Following this trend, the ICT and UE are developing the Seismic Sensor Network Alentejo (SSN-Alentejo) that brings the most dense seismic sensor network ever deployed in Portugal. This novel network plans to deploy 60 low-cost sensors distributed in a mesh configuration spaced on average 10 km and covering an area of about 5000 square kilometres (Manso *et al.*, 2020).

A high dense network-enabled seismic network operating in the principle of “live” data brings the opportunity to explore new applications in seismology, including real-time earthquake detection, more accurate characterisation (high resolution) of strong earthquake motion and the generation of *Shakesmaps* in near real-time.

The remainder of this paper is organised as follows. Section 2 presents the background for this work, describing the relevant characteristics of low-cost accelerometers. Section 3 presents an analysis of sensor noise based on measurements collected from accelerometers, describing a suitable method for on-site and while in-operation. The method is used to determine the sensor detectability threshold related with seismic activity. Section 4 concludes this paper.

2 BACKGROUND

In the last years, sensors and sensing network technology evolved at a fast pace, resulting in improved performance (resolution, sensibility and processing capacity), operation (energy efficiency, operation time) and connectivity (broadband communications), at significant cost reduction. Low-cost Micro-Electro Mechanical Systems (MEMS) accelerometers, in particular, demonstrated the capability to generate relevant data for seismic analysis in dense deployment contexts (Lainé and Mougnot, 2014).

MEMS technology has enabled the mass production of small size accelerometers. Capacitive accelerometers, in particular, are highly popular due to reduced cost, their simple structure, and the ability to integrate the sensor close to the readout electronics. When subjected to an acceleration, the inertial mass shifts cause a proportional change in capacitance. By measuring the capacitance change, the acceleration can be calculated.

In order to properly exploit its data, it is important to take into account MEMS benefits and limitations,

(Farine *et al.*, 2003; Evans *et al.*, 2014; Manso *et al.*, 2017) including: adequate sensitivity, noise level, and range (measured in g) to be applicable to earthquake strong-motion acquisition ($M > 3$), however, limited by the *high* level of instrumental self-noise especially affecting measurement of low frequency weak-motion forces; well fit to measure high frequency ($> 40\text{Hz}$) ground motion since their resonant frequency (typically above 1 kHz) is far above the seismic band pass; measure the gravity acceleration component thus providing a useful reference for sensitivity calibration and tilt measurement; have high acceleration ranges (several g) and can sustain high acceleration (several hundred g); complement broadband seismometers by detecting weak high frequency signals.

There is a wide range of low-cost accelerometers built for different purposes and exhibiting different characteristics. Concerning seismological applications, the following parameters should be taken into account: **Range:** Specifies the minimum and maximum acceleration values it can measure. It is often represented relative to g (e.g., $\pm 2\text{g}$); **Resolution:** Specifies both (i) the degree to which a change can be detected and (ii) the maximum possible value that can be measured. For example, a digital sensor with 16-bits resolution is able to quantify 65536 possible values. If the scale is set to $\pm 2\text{g}$ (hence, a 4g range) the minimum possible change that can be detected is about $61\mu\text{g}$; **Noise density:** Accelerometers are subject to noise produced by electronic and mechanical sources. Since they have a small inertial mass, noise increases at low frequencies. The noise density is often represented in terms of power spectral density (PSD) and is expressed as $\text{g}/\sqrt{\text{Hz}}$. It varies with the measurement bandwidth: when multiplied by it, the resulting value represents the minimum acceleration values that can be resolved; **Bandwidth:** Specifies the frequency range that the sensor operates in. It is limited to the natural resonance frequency of the mechanical structure of the accelerometer itself, which is typically very high ($> \text{kHz}$); **Sample rate:** Specifies the number of measurements (samples) per second.

This paper main focus is to observe the presence of sensor noise among several accelerometers. The most relevant parameter is therefore “Noise density”. Next, an analysis of sensor noise measured from different accelerometers is provided.

3 NOISE ANALYSIS OF LOW-COST ACCELEROMETERS

The main limiting characteristic of consumer-based MEMS accelerometers in seismological applications is the presence of sensor noise that is originated from the sensor’s electrical and mechanical components. Ultimately, the sensor noise determines the minimum resolution of the sensor. Typically, accelerometers’ manufacturers provide in the respective datasheets an indication of sensor noise via the parameter “power spectral density” (PSD) that is measured in g/\sqrt{Hz} . Multiplying the PSD value by the square root of the measurement bandwidth gives the root mean square (RMS) acceleration noise, which is the minimal resolvable value for acceleration (NXP, 2007). It is noted that noise increases with bandwidth.

In this chapter, an indication of sensor noise is measured by deploying and collecting acceleration data from several accelerometers while at rest position. The sensor noise assessment is made by calculating the standard deviation (eq. 1) of the signal (calculated using a “moving window” of 100 samples), after removing the DC value. The lower the standard deviation the lower the sensor noise.

$$\sigma = \sqrt{\frac{\sum (x_i - \mu)^2}{N}} \quad (1)$$

Where: i is the sample number, x_i is the measurement related with sample i , μ is the mean value and N is the sample size.

The environment where accelerometers are installed might be affected by external factors (e.g., traffic or seismic activity), which can be registered by accelerometers and should be excluded from the sensor noise analysis. In order to exclude these “signals” from “noise”, a threshold logic is defined and implemented as follows:

```

let  $\sigma(n)$  be the standard deviation related
with sample window n
let  $\sigma_{min}$  be the registered minimum
standard deviation for the running
period

if (  $\sigma(n) > \sigma_{min} \cdot Threshold$  ) then
    is signal
else
    is noise
endif
    
```

The first part of the analysis uses dedicated accelerometers operating at different bandwidth, while the second part compares the sensor noise in

dedicated accelerometers and consumer smartphones. Note that this analysis assumes a “quiet” environment, thus the presence of background environmental noise is not taken into account.

3.1 Sensor Noise in Dedicated Accelerometers

In this subchapter, an indication of sensor noise is measured in two dedicated accelerometers, namely:

- **Analog ADXL355**, a 3-axis digital sensor with 20-bit resolution, noise density (as PSD) of $25\mu g/\sqrt{Hz}$. (source: <https://analog.com>)
- **Invensense MPU-6050** with 16-bit resolution, noise density (as PSD) of $400\mu g/\sqrt{Hz}$. (source: <https://www.invensense.com>)

Based on the specifications, the ADXL355 sensor noise is substantially lower (16x less) than the MPU-6050. Moreover, sensors are setup to work at different bandwidth in order to observe its effect in sensor noise.

The results are presented next.

3.1.1 ADXL355 Measurements

The ADXL355 is setup to operate in three different sampling frequencies: 15Hz, 100Hz and 1KHz. The measured magnitude acceleration values subtracted by the average (in g) are presented in Figure 1. As it can be seen, the magnitude of the acceleration increases with the sampling frequency.

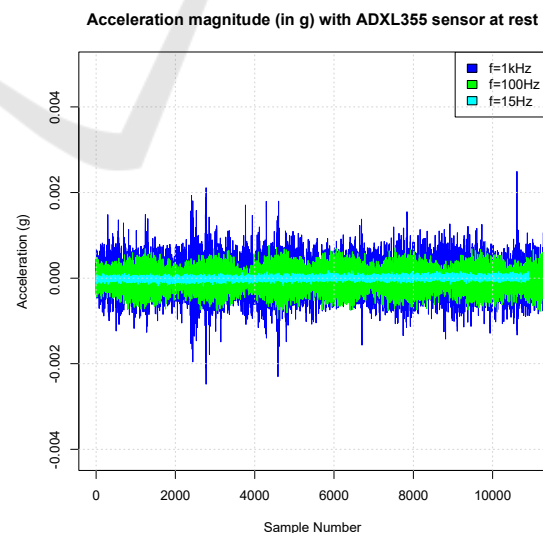


Figure 1: ADXL355 Measured Acceleration Magnitude for different sampling frequencies.

The measured standard deviation for ADXL-355 is presented in Figure 2 and Table 1. Two types are

considered for analysis: σ_{min} that represents the “sample window” with lowest sensor noise, and σ_{mean} that provides an indication of the average value of all included σ .

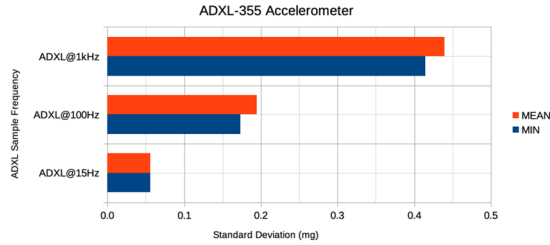


Figure 2: ADXL355 Measured Standard Deviation for different sampling frequencies.

Table 1: ADXL355 Measured Standard Deviation: minimum recorded value and mean value.

ADXL355	σ_{MIN} (mg)	σ_{MEAN} (mg)	Δ (mg)
1000 Hz	0.4143	0.4394	0.0252
100 Hz	0.1734	0.1950	0.0217
15 Hz	0.0555	0.0563	0.0008

As expected, increasing the sample frequency increases sensor noise, resulting in higher dispersion in measurements and thus in a higher standard deviation. The lowest standard deviation value (0.0555mg) was recorded at 15Hz (the lowest sample frequency used) and the highest standard deviation value (0.4143 mg) was recorded at 1KHz). This trend is also present in the difference between σ_{mean} and σ_{min} .

3.1.2 MPU-6050 Measurements

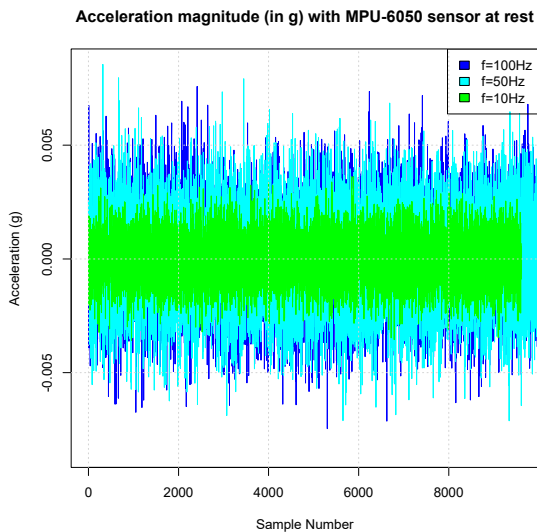


Figure 3: MPU-6050 Measured Acceleration Magnitude for different sampling frequencies

The MPU-6050 is setup to operate in three different sampling frequencies: 5Hz, 10Hz and 100Hz. The measured magnitude acceleration values subtracted by the average (in g) are presented in Figure 3. Once again, the magnitude of the acceleration increases with the sampling frequency.

The measured standard deviation for MPU-6050 is presented in Figure 2 and Table 1. As previously, the analysis considers σ_{min} and σ_{mean} .

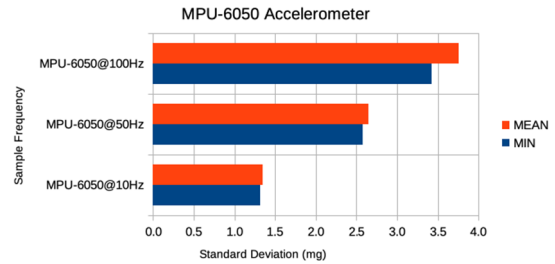


Figure 4: MPU-6050 Measured Standard Deviation for different sampling frequencies

Table 2: MPU-6050 Measured Standard Deviation: minimum recorded value and mean value.

MPU-6050	σ_{MIN} (mg)	σ_{MEAN} (mg)	Δ (mg)
100 Hz	3.4253	3.7606	0.3354
50 Hz	2.5713	2.6515	0.0802
10 Hz	1.3122	1.3472	0.0350

Again, sensor noise increases with the sample frequency: the lowest standard deviation value (1.3122 mg) was recorded at 10Hz (the lowest sample frequency used) and the highest standard deviation value (3.4253 mg) was recorded at 100Hz). This trend is also present in the difference between σ_{mean} and σ_{min} . Moreover, the standard deviation value can also be used to compare sensor noise between different accelerometers: Table 1 and Table 2 shows that, at a sampling frequency of 100Hz, the MPU-6050 standard deviation value is higher (about 20x higher) than ADXL-355, as expected from their respective datasheets.

A comparison between different accelerometers sensor noise is given next.

3.2 Sensor Noise in Smartphones and Dedicated Sensors

In this subchapter, an indication of sensor noise is measured for different accelerometers, including those present in consumer smartphones, operating at the same sampling frequency (100Hz) for purposes of comparing the associated sensor noise. The following devices were analysed:

- A TCL mobile phone
- A Xiaomi mobile phone
- A CAT mobile phone
- Invensense MPU-6050 (used in 3.1.2)
- ST LIS3DHH dedicated accelerometer
- Analog ADXL-355 (used in 3.1.1)

The results are presented next.

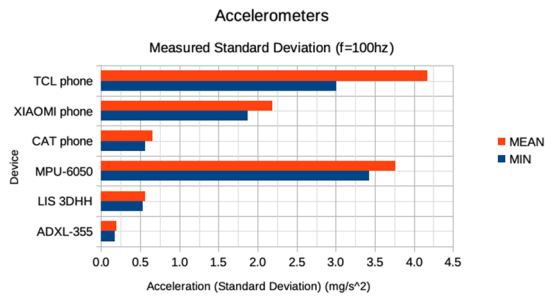


Figure 5: Measured Standard Deviation for several accelerometers operating at a sampling frequency of 100Hz.

Table 3: Measured Standard Deviation for several devices: minimum recorded value and mean value.

Accelerometers	σ_{MIN} (mg)	σ_{MEAN} (mg)
TCL phone	3.0115	4.1707
XIAOMI phone	1.8716	2.1893
CAT phone	0.5595	0.6563
MPU-6050	3.4253	3.7606
LIS 3DHH	0.5270	0.5634
ADXL-355	0.1734	0.1950

The developed method yields an indication of sensor noise, which is sensor specific. As shown in Figure 5 and Table , the dedicated accelerometer ADXL-355 yields the lowest minimum standard deviation (0.1734 mg), followed by the LIS 3DHH (0.5270 mg), the CAT phone (0.5595 mg). The TCL phone and the MPU-6050 yield the highest values, with 3.0115 mg and 3.4253 mg respectively. It is also pertinent to note the disparity between the mean and the minimum value of standard deviation for the TCL phone, indicating that the minimum value for standard deviation alone is not sufficiently robust to assess sensor noise in actual deployments.

3.3 Detectability Threshold Analysis

A potential application of accelerometers consists in measuring ground motion for seismological purposes. In this regard, accelerometers need to have the necessary sensitivity to detect and measure seismic events, which can have different magnitudes. Introduced in Manso et. al (2020), herein it is

presented in equation (2) an estimation of the detectability threshold ($DetecT$) of accelerometers, considering their noise level, as measured in 3.1 and 3.2, multiplied by C , a constant that is used to increase the assurance that measurements are above noise level:

$$DetecT = \sigma_{\text{accelerometer}} \cdot C \quad (2)$$

Considering a typical Ground Motion Prediction Equation (GMPE) proposed by Atkinson (2015) and resulting Peak Ground Acceleration (PGA), the accelerometers detectability threshold, depending on the earthquake magnitude and epicentral distance, is presented in Figure 6.

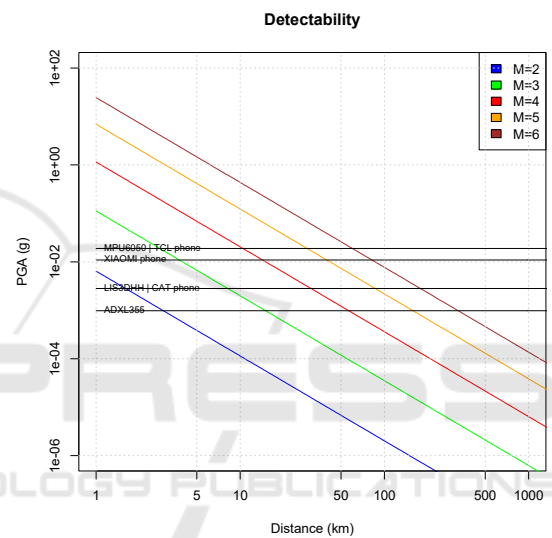


Figure 6: Accelerometers detectability threshold for accelerometers, depending on the earthquake magnitude and epicentral distance.

Using $C=5$ in (2), in a best case scenario, the ADLX-355 is the sensor with the lowest $DetecT$, being capable to detect earthquakes with $M=3$ and $M=5$ at a distance larger than 10 km and 100 km respectively. Both the MPU-6050 and TCL phone exhibit similar performance and should be able to detect earthquakes with $M=3$ and $M=5$ at a distance of about 2 km and 20 km respectively.

The ADXL-355 accelerometer exhibited the best performance based on the measured sensor noise, thus further analysis is presented. ADXL-355 detectability threshold changes with the chosen sampling frequency, as illustrated in Figure 7. For a $M=3$ event, the ADXL-355 would be able to detect it at a distance of about 30 Km if operating at a 15Hz frequency, or about 10 Km if operating at a 1000Hz frequency. For a $M=5$ event, the ADXL-355 at 15Hz would be able to detect it at a distance of about 300

Km. Therefore, applications where the sampling frequency can be lowered will benefit with increased detectability.

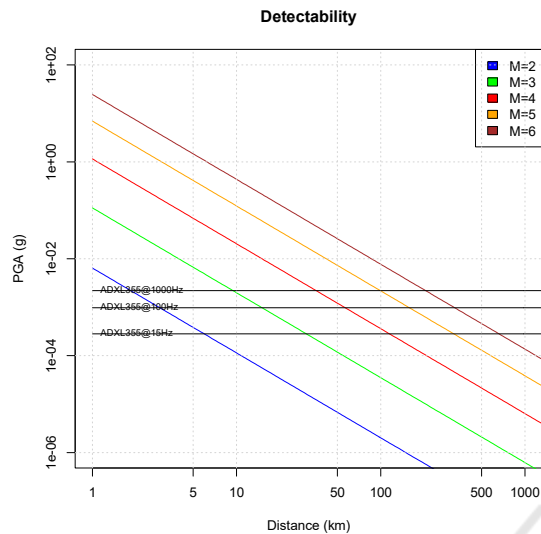


Figure 7: ADXL-355 accelerometer detectability threshold when using different sampling frequencies, depending on the earthquake magnitude and epicentral distance.

Although promising, these findings are preliminary for a more thorough analysis, considering the frequency domain, is required in order to properly assess the sensors detectability threshold.

4 CONCLUSION

Low-cost accelerometers have found numerous real-world applications, including in seismology and risk hazard assessment of buildings and human heritage. Being low-cost, it facilitates their widespread adoption enabling the deployment of high-density networking providing high resolution observation and massive amount of data that may feed intensive processing techniques like big data and artificial intelligence, applying machine learning techniques and pattern matching-based processing that are much more sensitive than the power detectors used in current seismic systems (Addair *et al.*, 2014), making them especially relevant in the presence of noise and weak signals.

This work conducted a preliminary analysis of sensor noise observed in different types of accelerometers, successfully developing a method to measure noise on-site and in-operation. The method produces an indication of sensor noise based on the measured standard deviation. It yields results consistent with sensors specifications (i.e., ADXL-

355, LIS 3DHH and MPU-6050) or, when not available, with the observations. Importantly, the method adapts to the sensor's characteristics (e.g., sensor noise), allowing to identify the occurrence of relevant events (i.e., presence of signal), without necessarily knowing *a-priori* the sensor specification (noise is calculated with the sensor in-operation). In addition, this method also adapts to changing circumstances, such as "noise" alterations caused by subtle changes in sensor characteristics (resulting from e.g., small displacements or temperature change). When considering a high-density deployment, logistic and maintenance aspects can represent serious bottlenecks unless the system supports adaptive capabilities, as those here described.

Next steps in this work involve a thorough analysis of the sensor noise characteristics including the frequency domain and against a reference sensor, thus understanding in more depth the applicability of low-cost accelerometers in real-work applications related with seismology, as well as their limitations.

ACKNOWLEDGEMENTS

The SSN-Alentejo project is funded by the Science Foundation of Portugal (FCT) under grant number ALT20-03-0145- FEDER-031260.

REFERENCES

- Addair T, Dodge D, Walter W, and Ruppert S (2014) *Large-scale seismic signal analysis with Hadoop*. Computers & Geosciences 66, 145–154
- Atkinson, G. (2015). *Ground-Motion Prediction Equation for Small-to-Moderate Events at Short Hypocentral Distances, with Application to Induced-Seismicity Hazards*. Bulletin of the Seismological Society of America. March 2015. DOI: 10.1785/0120140142
- Caldeira B, Carrilho F, Miranda M, Bezzeghoud M, Alves P, Silveira G, Villalonga F, Pena J, Matias L, Borges J, Vales D, Corela C and Madureira G (2007) *Recent improvements in the Broadband seismic networks in Portugal*. EMSC Newsletters, special issue, 22, 18-19
- Evans J, Allen R, Chung A, Cochran E, Guy R, Hellweg M, Lawrence J (2014) *Performance of Several Low-Cost Accelerometers*. Seismological Research Letters Volume 85, Number 1 January/February 2014.
- Farine M, Thorburn N, and Mougénot D (2003) *General Application of MEMS Sensors for Land Seismic Acquisition – Is it Time?* Accessible at: http://cseg.ca/assets/files/resources/abstracts/2003/218_S0130.pdf

- Lainé J. and Mougenot D. (2014) *A high-sensitivity MEMS-based accelerometer. The Leading Edge*. November 2014. Special Section: Sensor technology and nanotechnology.
<http://dx.doi.org/10.1190/tle33111234>
- Manso M., Bezzeghoud M., Caldeira B. (2017) *Design and Evaluation of a High Throughput Seismic Sensor Network. Tools for Planning, Deployment and Assessment*. 6th International Conference on Sensor Networks SENSORNETS, Porto, Portugal, 19 to 21 February.
- Manso, M., Bezzeghoud, M., Borges, J., Caldeira, B., Abdelhakim A. *High-density seismic network for monitoring Alentejo region (Portugal) and Mitidja basin region (Algeria)*. Arab J Geosci 13, 976 (2020).
<https://doi.org/10.1007/s12517-020-05972-w>
(Published: 17 September 2020).
- NXP (2007) *Accelerometer Terminology Guide - Quick Reference Guide*. Freescale Semiconductor. Rev 0, 05/2007.



*Monitoring the Earth: the Near-Future Developments in
Seismology*

Mourad Bezzeghoud
Marco Manso

University of Évora, Portugal

Seismology deals with the study of the activity of physical forces responsible for the origin of earthquakes and the seismic waves generated within the Earth. All structures located from the center of the Earth to its surface are the subject of study in this discipline. Seismology therefore pursues the understanding of the Earth's internal structure and the physical processes that cause earthquakes, resorting to advanced instruments for observation and measurements. This paper presents an overview of important milestones in the seismological field, followed by revolutions in the instrumentation and observation of seismological events.

The Earth

Earth is our natural habitat. Human beings and economic and social development depend on the planet's resources, which are not inexhaustible. In fact, the way resources will be managed during the 21st century will be decisive: only their moderate and rational exploitation will allow the Earth to host and sustain the 10 billion human population estimated for the end of this century. Developing a thorough knowledge and understanding of the functioning of our planet is therefore essential to develop our society in a harmonious and sustainable way. It is also our legacy to teach future generations our understanding of the Earth.

The Earth is a fascinating "entity" and discovering it from a physical point of view is an even greater adventure. Understanding its structure, its dynamics and its shape imposes answering questions across different domains, because several physical phenomena of different

scales are involved, from “astronomical” scale (e.g., interaction with other celestial bodies) to “atomic” scale (e.g., radioactive emission).

In the 20th century, the acquisition and analysis of massive amounts of observations and information was made possible by progresses in instrumentation, electronics and information technology. However, as opposed to Jules Verne’s novel “Journey to the Center of the Earth”, so far, knowing the interior of our planet is only possible through observations and records made on the surface, i.e., indirect observations.

The Physics of the Earth

Our knowledge of the Earth’s interior was still rudimentary at the beginning of the 20th century [1], especially when compared with the scientific advances obtained about the “infinitely small” (discovery of radioactivity by Becquerel in 1896; identification of the electron by Thomson in 1897; formulation of the quantum theory by Planck in 1900) and “infinitely large” (theory of gravitation by Newton in 1687; foundations of celestial mechanics by Laplace in 1799; formulation of the theory of general relativity by Einstein in 1915). Knowledge of the interior of the Earth mainly results from work conducted in the 20th century: in 1887 John Milne (1850-1913) identified the crust, Lord Rayleigh, Lord Rutherford and Emil Wiechert the mantle; the limit between the crust and the mantle was defined by Andrya Mohorovicic in 1909 (discontinuity of Mohorovicic/Moho); in 1906, Oldham’s remarkable work determined the size of the Earth’s outer core; Beno Gutenberg (1889-1960), in 1912 in his doctoral thesis, defined the boundary between the outer nucleus and the mantle. This interface between the asthenosphere and the endosphere is called Gutenberg’s Discontinuity; in 1926, Sir Harold Jeffreys (1891-1989) discovered that the outer core is liquid; in 1936 Inge Lehman (1888-1993) provided the key for the identification of the Earth’s inner core; inner core which, in 1946, is identified as solid by Keith Edward Bullen (1906–1976). In 1935, H. Jeffreys and K.E. Bullen published the famous travel time tables of the seismic waves that bear their names (Jeffreys-Bullen tables) and which served as a reference for seismologists and geophysicists for half a century. The previously mention discoveries about the structure of the Earth, from John Milde to K.E. Bullen, were based on the study of earthquakes and the propagation of seismic waves. It is also important to underline one of the great steps taken to understand internal geodynamics, due to the Irish Robert Mallet (1810-1881) and to the French, Alexis Perrey (1807-1882) and Count Fernand Jean Batiste Marie de Montessus de Ballore (1851-1923) who dedicated a significant part of their work to the collection of information regarding earthquakes that occurred throughout the planet. The revolutionary discovery of the ocean floor expansion in 1963 by Drummond Hoyle Matthews and his student Fred J. Vine, also in-

dependently brought by Lawrence Morley, were essential elements for the acceptance of the Plate Tectonics theory .

Recording earth motion and earthquakes - the first (r)evolution in high-density deployments

Seismic events can be extreme, and severe threats to humanity. Helping to understand these phenomena, seismic networks have been deployed in increasing number, filling in gaps in the global coverage and improving our understanding of the physical processes that cause earthquakes. Several countries have made significant efforts to deploy Broadband seismic networks incorporating seismological stations supporting real-time monitoring of the earthquake activity. However, these stations are installed several kilometers from each other, thus limiting the overall spatial resolution of the observations. It is important to highlight that the revolutionary contribution of broadband seismic instrumentation, in which principles of feedback accelerometers and zero-length leaf spring were implemented. Construction, functionality and measurement results of the first vertical STS-1 broad-band (BB) seismometer was published by Wielandt and Streckeisen [2] and the advancing the STS-1 to a novel digital Very-Broadband-Seismograph (VBB) was published by Wielandt and Steim [3].

A paradigm change occurred in the United States with the deployment of high density seismic networks with the capability to record the propagation of seismic activity in high resolution: The California Institute of Technology established the Community Seismic Network an earthquake monitoring system based on a dense array of low-cost acceleration sensors (more than 1000) aiming to produce block-by-block strong shaking measurements during an earthquake [4]. The University of Southern California's Quake-Catcher Network began rolling out 6000 tiny sensors in the San Francisco Bay Area, being part of the densest network of seismic sensors ever devoted to study earthquakes in real time [5].

A high dense network-enabled seismic network operating in the principle of "live" data brings the opportunity to explore new applications in seismology, including real-time earthquake detection, as well as the generation of Shakemaps (i.e., spatial representation of ground motion amplitudes).

Low-cost sensors: the second (r)evolution and the near-future developments

In the last years, sensors and sensing network technology evolved at a fast pace, resulting

in improved performance, operation and connectivity at significant cost reduction. Low-cost Micro-Electro Mechanical Systems (MEMS) accelerometers, in particular, demonstrated the capability to generate relevant data for seismic analysis in dense deployment contexts [6].

MEMS technology has enabled the mass production of small size accelerometers. Capacitive accelerometers, in particular, are highly popular due to reduced cost, their simple structure, and the ability to integrate the sensor close to the readout electronics. When subjected to an acceleration, the inertial mass shifts cause a proportional change in capacitance. By measuring the capacitance change, the acceleration can be calculated.

In order to properly exploit its data, it is important to take into account MEMS benefits and limitations [7-10]. MEMS accelerometers have adequate range (several times the standard gravity g), sensitivity and frequency response (typically around 1k Hz) but exhibit high-levels of instrumental self-noise. As such, they are especially fit to measure strong seismic activity ($M > 3$), high frequencies (> 40 Hz) and can measure the gravity acceleration component. Importantly, MEMS accelerometers complement broadband seismometers in what regards strong motion and high frequency measurements.

In Portugal, as part of the SSN-Alentejo project [11], the University of Évora is planning a deployment of up to 300 network-enabled stations in the Évora region, complementing the existing network that is comprised by 15 broadband stations. SSN-Alentejo will be used to monitor ground motion activity - caused by natural and/or human activity - in high detail, including in Évora city given its high patrimonial value and cultural heritage.

The network-enabled high-density seismic network generates data in real-time enabling the following applications [9]:

- Seismic detection (strong motion) for near and “far” earthquakes (far being in the order of hundreds of kms).
- Study of local events and characterize the structure of the seismogenic zone by performing waveform analysis of nearby small events and ambient noise.
- Analyze the impact produced by human activity and cultural noise on buildings and monuments: *Urban seismic noise* is usually dominated by *traffic* and industrial activity with peak frequencies below 25 Hz. A continuous exposure to urban tremors can cause a cumulative and progressive degradation on fragile buildings and monuments, which could cause irreparable damage in human heritage.
- Generation of *Shakemaps* that can be used by civil protection authorities for post-earthquake response, including assessing structural integrity risks in buildings and slopes.

- Provide to the scientific community with new open-access high-resolution seismic data.
- Facilitate access to education in seismology, resulting from open access to low-cost technology that can be installed in high schools and integrated in projects and activities.

Conclusion

Seismology is a relatively young scientific discipline, that has significantly evolved since the beginning of the 20th century, benefiting from significant advances in theories and technology. Broadband seismic networks brought the capability to perform real-time monitoring of the earthquake activity and subsequent high-density deployments allowed further increasing spatial resolution of the observations for a more accurate characterization (high resolution) of earthquake motion. Recent developments in low-cost MEMS accelerometers have found numerous real-world applications, including in seismology and risk hazard assessment of buildings and human heritage. Being low-cost, it facilitates their widespread adoption enabling the deployment of high-density networking providing high resolution observation and massive amount of data that may feed intensive processing techniques like big data and artificial intelligence, applying machine learning techniques and pattern matching-based processing that are much more sensitive than the power detectors used in current seismic systems [12] making them especially relevant in the presence of noise and weak signals.

The deployment of high-density network-enabled seismic networks represents an important step in our road towards understanding the functioning of the Earth, including its internal structure and physical processes that cause earthquakes, while at the same time contributing towards a safer and more sustainable society.

References

- [1] Bezzeghoud M. (2012) *Viagem ao interior da Terra*, in Ana Maria Silva, Araújo, A., Reis, A., Morais, M., Bezzeghoud, M (ed.) *Two Decades of Earth Science Research*. Centro de Geofísica de Évora Celebration of 20 Years. ISBN: 78-989-95091-4-6.
- [2] Wielandt E., Streckeisen G. (1982) *The leaf-spring seismometer: design and performance*, Bull. seism. Soc. Am., 72(6), 2349–2367.
- [3] Wielandt, E., Steim, J.M. (1986) *A digital very broad band seismographe*, Annales Geophysicae, 4, B, 3, 227-232.
- [4] See <http://csn.caltech.edu/>, accessed 2021/01/15
- [5] See <https://quakecatcher.net/>, accessed 2021/01/15
- [6] Lainé J. and Mougénot D. (2014). *The Leading Edge*. November 2014. Special Section: Sensor technology and nanotechnology. DOI: 10.1190/tle33111234
- [7] Evans J, Allen R, Chung A, Cochran E, Guy R, Hellweg M, Lawrence J (2014). *Performance of Several Low-Cost Accelerometers*. Seismological Research Letters, 85, 1, January/February 2014. DOI: 10.1785/0220130091
- [8] Farine M, Thorburn N, and Mougénot D (2003). *General applications of MEMS sensors for land seismic acquisition. Is it time?* The 2003 CSPG/CSEG convention. Canada.
- [9] Manso M., Bezzeghoud M., Caldeira B. (2017) *Design and Evaluation of a High Throughput Seismic Sensor Network - Tools for Planning, Deployment and Assessment*. In Proceedings of the 6th International Conference on Sensor Networks - Volume 1: SENSOR-NETS, ISBN 978-989-758-211-0, pages 129-134. DOI: 10.5220/0006127701290134
- [10] Manso, M., Bezzeghoud, M., Borges, J., Caldeira, B., Abdelhakim (2020) *High-density seismic network for monitoring Alentejo region (Portugal) and Mitidja basin region (Algeria)*. Arab J Geosci 13, 976. DOI: 10.1007/s12517-020-05972-w
- [11] See <https://www.uevora.pt/en/Research/projects?id=3812>, accessed 2021/01/15. The SSN-Alentejo project is funded by the Science Foundation of Portugal (FCT) under grant number ALT20-03-0145- FEDER-031260.
- [12] Addair T, Dodge D, Walter W, and Ruppert S (2014). *Large-scale seismic signal analysis with Hadoop*. Computers & Geosciences 66, 145–154. DOI: 10.1016/J.CAGEO.2014.01.014



SSN-Alentejo: Towards High-Dense Seismic Network Deployments

Marco Manso^{1*}, Mourad Bezzeghoud¹, José F. Borges¹, Bento Caldeira¹

¹ Departamento de Física (ECT), Instituto de Ciências da Terra (IIFA) da Universidade de Évora

*marco@marcomanso.com

Abstract

Seismic events can be extreme and severe threats to humanity, causing a heavy death toll, serious destruction and damage. Being no exception, the Iberian Peninsula and the North of Africa share the Eurasian–Nubian plate boundary that corresponds to a well-defined narrow band of seismicity, where large earthquakes occur. Helping to understand these phenomena, seismic networks have been deployed in increasing number, filling in gaps in the global coverage and improving our understanding of the physical processes that cause earthquakes. Deployments in very high density seismic networks - e.g., CalTech Community Seismic Network (<http://csn.caltech.edu/>) and USC Quake-Catcher Network (<https://quakecatcher.net>) - aimed to record the propagation of seismic activity in high resolution and displaying seismic wave propagations in space and time (i.e., evolutive Shakemaps). Recent developments in sensors and sensing network technology enabled cost-effective high-density deployments. Low-cost Micro-Electro Mechanical Systems (MEMS) accelerometers, in particular, demonstrated the capability to generate relevant data for seismic analysis in dense deployment contexts: MEMS accelerometers have adequate range (several times the standard gravity g), sensitivity and frequency response (typically around 1k Hz) but exhibit high-levels of instrumental self-noise. As such, they are especially fit to measure strong seismic activity ($M > 3$), high frequencies (> 40 Hz) and can measure the gravity acceleration component. Importantly, MEMS accelerometers complement broadband seismometers in what regards strong motion and high frequency measurements. In Portugal, planned for 2020 and 2021, the Seismic Sensor Network (SSN) Alentejo will deploy a monitoring network of 60 sensors to generate significant volumes of live data and improve the seismic and tectonic knowledge in the regions. The sensors will be distributed in a mesh configuration spaced on average 10 km and covering an area of about 5000 square kilometres. The density proposed for the network abides to the findings in other studies in that the project opts for a cost-effective network configuration, combining high-performing broadband stations and low-cost sensors.

In this work, we will present findings from SSN-Alentejo, including zones to be monitored, distribution of seismic sensors, detectability capability and comparability analysis with a reference station. Importantly, SSN-Alentejo will enable the application of novel data intensive processing techniques, like big data and artificial intelligence (e.g., clustering, pattern-matching and correlation) in seismology. SSN-Alentejo project is funded by the Science Foundation of Portugal (FCT) under grant number ALT20-03-0145- FEDER-031260.

Key words: High-Density Seismic Network, Seismic Sensors, MEMS accelerometers, Detectability